THESE

En vue de l'obtention du

DOCTORAT DE L'UNIVERSITE DE POLYNESIE FRANCAISE

Département : Science
Discipline : n°37 Météorologie, océanographie physique de l'environnement
Spécialité : Océanographie

Délivré par
Université de Polynésie Française

Présentée et soutenue le *13 septembre 2018* par :
Hirohiti RAAPOTO

Titre :
Processus physiques et biogéochimiques impliqués dans l'effet d'île aux Marquises

---

Ecole doctorale :
Ecole Doctorale du Pacifique (ED469)

Unité de recherche :
UMR 241 - Ecosystèmes Insulaires Océaniens

Directeur/trice(s) de Thèse :
Dr. Jean-Claude GAERTNER et Dr. Anne PETRENKO

Co-encadrante/t(s) de Thèse :
Dr. Elodie MARTINEZ et Dr. Andrea DOGLIOLI

Jury :

Pr. Pascal ORTEGA	UPF, GEPASUD	Président du jury
Pr. Paulo CALIL	FURG, IO	Rapporteur
Dr. Pierrick PENVEN	LOPS, IRD	Rapporteur
Dr. Jean-Claude GAERTNER	UMR EIO, IRD	Directeur de thèse
Dr. Anne PETRENKO	AMU, MIO	Co-directrice de thèse
Dr. Elodie MARTINEZ	LOPS, IRD	Examinatrice
Dr. Keitapu MAAMAATUAIAHUTAPU	UPF, GEPASUD	Examinateur

Remerciements

Tout d'abord, je souhaiterai remercier très chaleureusement une personne exceptionnelle qui a été un pilier pour moi durant ce travail de longue haleine. Je veux bien évidemment parler d'Elodie Martinez. Je tiens tout d'abord à la remercier de m'avoir fait confiance et de m'avoir proposé un sujet de thèse aussi passionnant. Je la remercie pour son aide et ses conseils mais surtout pour sa gentillesse et ses encouragements qui m'ont permis d'avancer malgré les difficultés et qui ont rendu ces années de thèse mémorables. Elodie, je ne pourrai jamais te remercier assez. Tu resteras pour moi un modèle tant sur le plan scientifique que sur le plan humain.

Ce travail n'aurait pas été possible sans le soutien financier de la Délégation à la Recherche de Polynésie Française (convention n°6841/MTS). Je tiens à les remercier ainsi que son représentant Jean-Yves Meyer et son prédécesseur Tea Frogier pour les ressources financières accordées à ce travail.

Je tiens à remercier Jean-Claude Gaertner d'avoir accepté d'être mon directeur de thèse. Je souhaiterais également dire un grand merci à deux personnes formidables qui m'ont encadré depuis Marseille : ma co-directrice de thèse Anne Petrenko et Andrea Doglioli. Je tiens à vous remercier pour votre aide et vos conseils mais aussi pour le temps que vous avez pris pour moi malgré la distance et vos emplois du temps déjà bien chargés. Ce fut un vrai plaisir de venir travailler au MIO avec vous. Je souhaite que l'on puisse continuer à travailler ensemble. Je tiens aussi à remercier Paulo Calil et Pierrick Penven pour avoir accepté d'être les rapporteurs de ma thèse et de prendre sur leur temps pour évaluer ce travail.

J'ai aussi une pensée toute particulière pour Christophe Maes que je remercie également pour son aide et sa réactivité. Bien que le projet de thèse que l'on avait déposé à la sortie de mon master n'ait pas été accepté, j'ai quand même eu la chance de pouvoir collaborer et travailler avec lui durant cette thèse. La thématique n'était pas la même mais ce fût une expérience enrichissante et amusante à la fois. Comme tu me l'as dit un jour : « le monde de l'océanographie est petit ! ».
Je remercie aussi la petite équipe d'océanographes de l'UMR EIO, avec qui j'ai pris plaisir à travailler, de m'avoir soutenu. Merci à Martine Rodier, Raphaëlle Sauzède et Clément Fontana pour ces échanges et conseils constructifs.

Je voudrais également remercier les personnes avec qui j'ai eu la chance de collaborer durant ce travail de thèse. En particulier, je remercie Keitapu Maamaatuaiahutapu pour ses bons conseils et sa contribution dans mon travail de thèse. Je souhaite également le remercier de m'avoir permis de me retrouver de l'autre côté de la salle de classe et de pouvoir enseigner et partager mon expérience avec les étudiants de l'université de Polynésie Française. J'espère pouvoir renouveler cette expérience de partage de connaissance avec la jeunesse polynésienne qui fut riche et captivante.

Je tiens à remercier Christophe Menkes et Jérôme Lefèvre pour leur aide et leur accueil au sein du centre IRD de Nouméa. Malgré que ma mission ne soit pas tombée au meilleur moment, j'ai pu compter sur leur soutien pour la mise en place du couplage des modèles physique et biogéochimique. Je les remercie également de m'avoir fourni les ressources informatiques pour le lancement des simulations et le bon déroulement de ma mission.

Je remercie également les membres du LOPS pour l'accueil et l'aide qu'ils m'ont apporté. J'ai une pensée particulière pour Gilles, Nicolas, Thomas, Claude, Pierrick, Gildas, Thierry, Gwenaelle et Tristan.

Je tiens à exprimer mes remerciements à tout le personnel du centre IRD de Tahiti représenté par Marc Taquet. Merci pour cet accueil et ce temps passé ensemble. Je remercie particulièrement Nicolas Maihota pour les conseils et discussions passionnantes sur la pêche qui m'ont permis de m'évader. Un grand merci à Françoise Hale pour son aide et sa réactivité pour tout ce qui concernait la partie administrative. Aussi, malgré la dispersion du personnel de l'IRD, si je devais garder une image du centre, ce serait celle des petits repas organisés sur l'ancien site de Arue. A Nicolas, Teva, Justin, Fabrice et Emile, je vous souhaite une bonne continuation. A Lisette, Rose, John et Joël je vous souhaite une bonne retraite.

Je remercie toutes les personnes qui m'ont aidé à la mise en place technique de mon travail de thèse en commençant par l'OSU Pythéas de Marseille qui m'a mis à disposition le cluster de calcul pour pouvoir lancer toutes mes simulations. Je remercie particulièrement Christophe Yohia et Maurice Libes pour leur aide technique. Je remercie également les services informatiques de l'université de Polynésie Française, du LOPS de Brest et du centre IRD de Tahiti pour avoir facilité mon installation sur les différents sites.

Je voudrais aussi remercier toutes les personnes qui m'ont accompagné, que j'ai rencontré et qui ont participé à la vie de ces années de thèses. Je pense particulièrement à tous mes collègues de bureaux qui se sont succédé et qui ont partagé mon espace vitale. A Marseille j'ai une pensée pour Louise, Sara, Andrea ainsi que les stagiaires, post-docs, ingénieurs que j'ai rencontrés. Je remercie mon amie de lycée Vaihiti que j'ai retrouvé à Nouméa pour ces petites soirées avec ses amis calédoniens. Je remercie également Chloé Martias que j'ai connu durant mon master et que j'ai pu revoir à Nouméa. Merci pour ces petites sorties terrains qui m'ont permis de découvrir de nouveaux paysages et de me déconnecter de mes simulations. Je souhaite enfin remercier toutes les personnes que j'ai pu fréquenter durant ma thèse à Tahiti : Sarah, Tepoe, Simon, Nicolas, Raimana, Camille, Kristelle, Tohei, Raihei, Yann, Heipoe, Oihana, Gaëlle, Vivien, Fabien, Tamatoa, Vehia, Brice et Florent. Merci pour ces échanges et moments passés et, notamment pour ces « vendredi gâteau » qui ont rendu ces journées plus agréables. Je remercie aussi mes anciens profs de licence Stéphanie, Taivini et Pascal pour leurs encouragements, le personnel de l'UMR, en particulier Phila, Mayalen, Aline, Chloé, Mélanie, Cécile et Nabila ainsi que tous les autres membres. Je souhaite remercier les doctorants des autres laboratoires de l'UPF que j'ai eu la chance de connaître durant les formations proposées par l'école doctorale : Maheata, Gaël, Franky, Vahine, Johnny, Ivan, Rony, Fang Zhao et Franco. Merci pour tous ces moments partagés ensemble. C'est toujours un plaisir de se revoir en dehors des horaires de bureau. Je tiens également à remercier les personnes rencontrées à Brest, avec qui j'ai eu la chance d'échanger et qui ont rendu mon séjour à Brest agréable : Yurui, Natalie, Solen, Elodie et Arthur.

Je tiens également à remercier Evans, Manoa et Huriau, membres de mon groupe de musique Heroes and Minivans, qui m'ont permis de m'évader tous les samedi après-midi et avec qui on a eu la chance de rencontrer et échanger avec des musiciens internationaux. Durant ces trois années de thèse, la musique aura joué un rôle important pour évacuer le stress accumulé mais aussi parfois pour m'éclairer dans ce travail de thèse. A présent que j'ai terminé mon doctorat, on pourra se focaliser sur l'ascension du groupe !

Je terminerai par remercier les personnes qui sont les plus chers à mes yeux. Je pense en particulier à mon épouse qui m'a soutenu et aidé pour arriver jusqu'ici. Je la remercie d'avoir fait preuve de patiente et de compréhension durant ces années de thèse. Je n'aurai, à présent, plus d'excuse pour esquiver les tâches ménagères. Je tiens également à remercier ma famille et ma belle-famille qui m'ont encouragé tout au long de ces années et en particulier mes parents

qui m’ont toujours soutenu, et à qui je dois mon épanouissement tant personnel que professionnel. Je souhaiterai également remercier mes amis et témoins Guillaume, Heiata, Tareva et Maimiti qui ont toujours su m’encourager à chaque visite.

Ainsi, à toutes les personnes que j’ai cité et celles que j’ai malencontreusement oublié, un grand Mauruuru !

Table des matières

Chapitre I

Contexte Générale

I.1. Le phytoplancton dans les océans

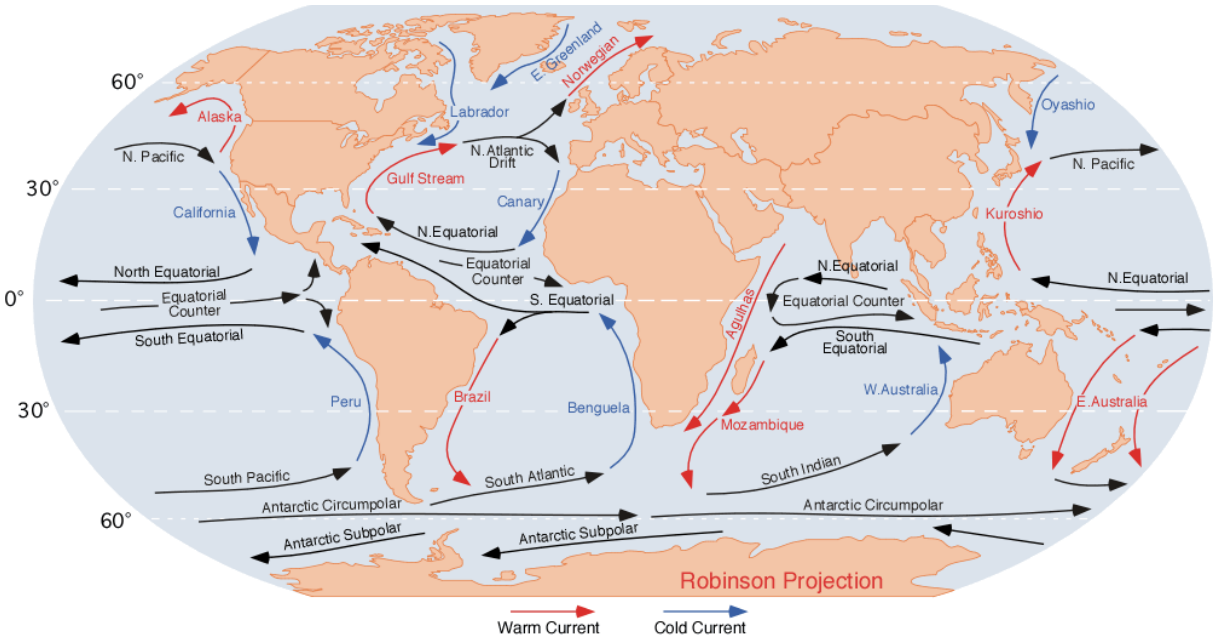

Figure I-1 : Carte globale représentant les courants de surface moyens. Les courants chauds sont représentés en rouge et les courants froids en bleu. Source : www.physicalgeography.net

Le phytoplancton est constitué de l'ensemble du plancton végétal, c'est-à-dire des microorganismes photosynthétiques qui sont libres, passifs et en suspension dans la colonne d'eau. Il s'agit de cellules, colonies ou filaments qui ne peuvent se déplacer et dont les mouvements dépendent de ceux de l'environnement aquatique et/ou qui sont mobiles (flagellés) mais dont les déplacements sont restreints. Pour se développer, le phytoplancton a besoin de lumière et de sels nutritifs. A l'échelle des bassins océaniques, les vents créent des flux horizontaux dans la couche de surface (transport d'Ekman) qui induisent des différences de distributions de nutriments [*Williams and Follows*, 2003] :

• Les gyres subtropicaux présentent une circulation anticyclonique (Figure I-1), caractérisés en leur centre par un downwelling (plongée d'eau) et un approfondissement de la thermocline (Figure I-2). Ce profil de la thermocline se reflète dans la distribution de nutriments par un approfondissement de la nutricline (zone de fort gradient vertical en nutriment séparant les eaux pauvres de surface des eaux riches en profondeur). Il en découle généralement de faibles concentrations en Chlorophylle (Chl, indicateur de la biomasse phytoplanctonique) et de Production Primaire (PP) au niveau des gyres subtropicaux (en bleu sur la Figure I-5 - gauche).

• Dans la bande équatoriale, les Alizées entraînent un transport d'Ekman des masses d'eaux de surfaces, des deux côtés de l'équateur vers les pôles (Figure I-2). Ces vents entrainent également un transport des masses d'eaux vers le large à partir des bords est des bassins océaniques. Ces déplacements d'eaux induisent un phénomène d'upwelling (remontée d'eau) le long de la zone équatoriale et des côtes situées à l'est des bassins. Ces systèmes d'upwelling équatoriaux et côtiers apportent les nutriments nécessaires au développement du phytoplancton dans la zone euphotique, augmentant ainsi la production locale (en vert-jaune-orange sur la Figure I-5 -gauche) [*Williams and Follows*, 1998; *Yoder and Kennelly*, 2003].

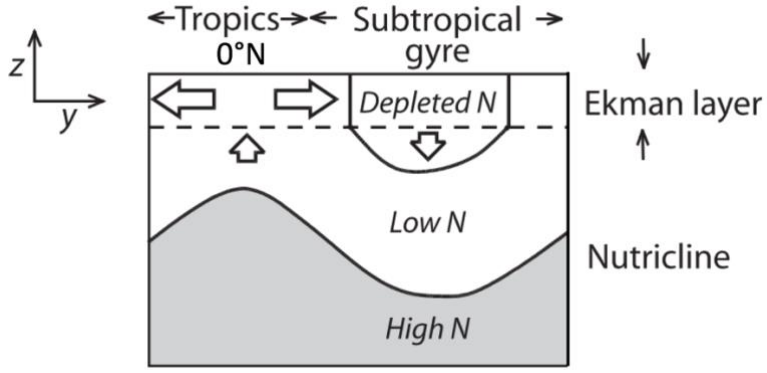

Figure I-2: Schéma des transports d'Ekman le long d'une section verticale méridienne à l'intérieur d'un bassin adapté de Williams et Follows (2003). La divergence des transports d'Ekman horizontaux induit un upwelling et une remonté de la nutricline au niveau de l'équateur, mais aussi un downwelling et un approfondissement de la nutricline dans la gyre subtropicale.

Dans les gyres subtropicaux, la température des eaux de surface est élevée durant l'été. La stratification est alors relativement forte et le système est limité en nutriments en surface. Le refroidissement hivernal des eaux de surfaces et le renforcement des vents induisent un mélange convectif. L'augmentation de l'épaisseur de la couche de mélange peut alors entrainer un transfert de nutriments vers la couche euphotique, et un enrichissement en phytoplancton [*Menzel and Ryther*, 1961].

La croissance du phytoplancton repose sur la disponibilité de nutriments et d'énergie radiative. Les rayonnements solaires pénètrent l'océan et sont partiellement absorbés par la couche supérieure. La croissance du phytoplancton est ensuite contrôlée par les processus physiques tels que la circulation induite par le vent, le mélange vertical et/ou les phénomènes d'upwelling qui viennent influencer la disponibilité des nutriments en surface.

A l'échelle interannuelle, la circulation océanique est gouvernée par les vents et la circulation thermohaline qui contrôlent la profondeur de la thermocline permanente et ainsi la profondeur de la nutricline. Par conséquent, les changements de la profondeur de la thermocline permanente peuvent moduler la variation de la biomasse phytoplanctonique, comme c'est le cas dans le Pacifique pendant les évènements El Niño [*Wilson and Adamec*, 2001; *Messié and Chavez*, 2012]. Le phénomène ENSO (El Niño Southern Oscillation) est un phénomène couplé océan/atmosphère ayant lieu dans le Pacifique central et qui affecte les températures de surface de la mer, les vents et les précipitations à grande échelle (Figure I-3). Ce phénomène caractérisé par des anomalies de température de surface de la mer présente une phase chaude (El Niño) et une froide (La Niña). Au niveau de la bande équatoriale, on observe en condition normale, les alizés qui soufflent d'est en ouest dans le Pacifique équatorial créant des courants de même direction le long de l'équateur [*McPhaden MJ*, 1993; *McPhaden*, 1999]. On note alors une remontée des eaux profondes et froides à l'est de la bande équatoriale, au niveau de l'Amérique du sud et une accumulation d'eau chaude à l'ouest (Figure I-3 milieu). Durant les phases El Niño, les alizés faiblissent. Les masses d'eaux chaudes s'accumulent alors au centre et à l'est du Pacifique équatorial avec un approfondissement de la thermocline (Figure I-3 gauche). Durant les phases La Niña, les alizés se renforcent et il en résulte une accentuation de l'accumulation d'eau chaude à l'ouest du bassin mais aussi de la remonté de la thermocline et nutricline à l'est (Figure I-3 droite). Ainsi, la biomasse phytoplanctonique à l'est et au centre de la bande équatoriale augmentent grâce à cet apport accru de sels nutritifs [*Radenac et al.*, 2001, 2012; *Masotti et al.*, 2011; *Shi and Wang*, 2014]. Toutefois, il s'agit ici d'une explication simplifiée du phénomène ENSO dans la bande équatoriale seulement. En effet, le phénomène ENSO est plus complexe et a des conséquences à l'échelle du bassin Pacifique mais aussi à l'échelle globale.

Dans l'Océan Pacifique, la variabilité de la profondeur de la thermocline et nutricline est aussi influencée par les phases de l'Oscillation Inter-décennale du Pacifique (IPO - Interdecadal Pacific Oscillation) [*Power et al.*, 1999; *Salinger et al.*, 2001; *Folland et al.*, 2002]. L'IPO est lui aussi un phénomène couplé océan/atmosphère qui impacte le bassin Pacifique avec des périodes d'oscillation variant de 15 à 30 ans. Lors de la phase positive de l'IPO, les températures dans le Pacifique tropicale sont plus chaudes que la normale et plus froide dans le Pacifique tropical nord et sud (Figure I-4a). Durant la phase négative, la tendance est inversée avec des

eaux plus froides que la normale dans les régions tropicales et plus chaudes dans les régions tropicales (Figure I-4b).

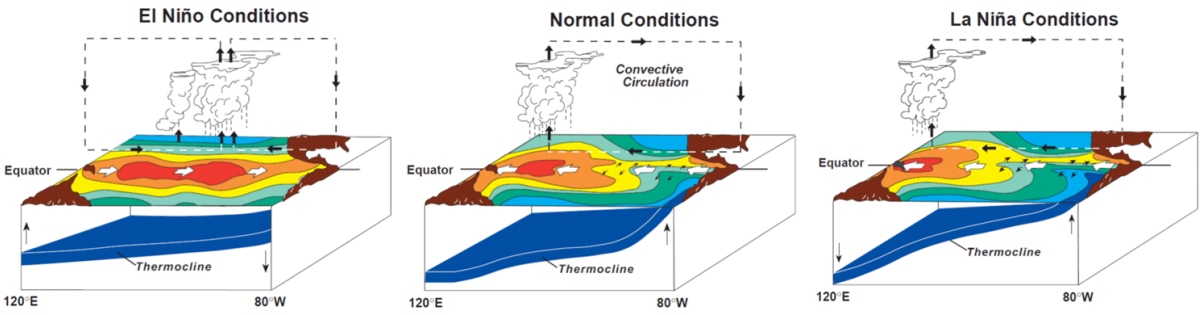

Figure I-3: Représentation schématique des conditions (gauche) El Niño, (milieu) normale et (droite) La Niña du phénomène ENSO. Les flèches noires indiquent la direction du vent et les flèches blanches la direction des courants de surface. (Source : McPhaden, 2015*)*

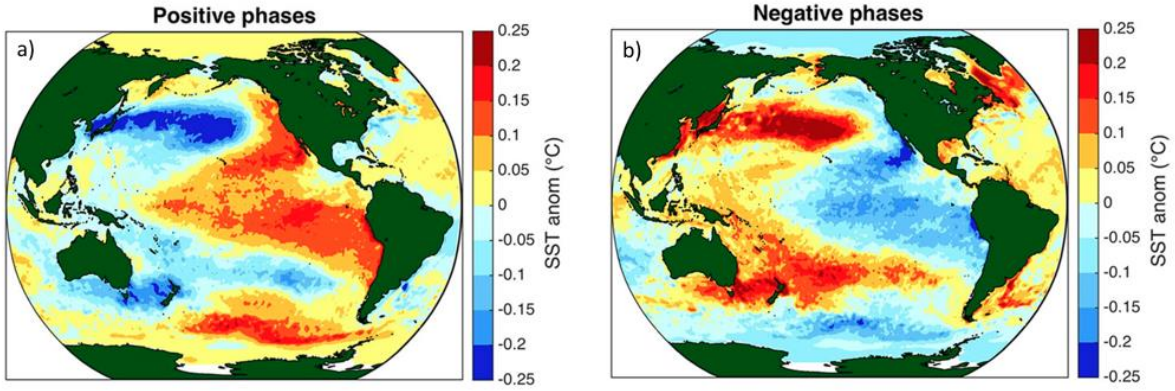

Figure I-4: Composites d'anomalies de température de surface de la mer durant les phases (a) positive et (b) négative de l'IPO, issues des données HadISST2.1 sur la période 1870-2007. (Source : Henley et al., 2015*)*

Le phytoplancton a un rôle des plus importants dans l'océan puisqu'il alimente la chaine alimentaire océanique et affecte les concentrations de O_2 et de CO_2 océanique et atmosphérique par le processus de photosynthèse. Ce processus est la principale source d'acquisition d'énergie pour les organismes phytoplanctonique via l'assimilation de sels nutritifs et de carbone (sous forme de CO_2) sous l'action de la lumière. En effet, grâce à la photosynthèse, le phytoplancton est capable de séquestrer le dioxyde de carbone atmosphérique par le mécanisme de « pompe biologique » [*Tian et al.*, 2000]. Ces organismes autotrophes fixent le carbone inorganique dans

les eaux de surface, le transforment en carbone organique, puis le transportent de la zone euphotique vers les eaux profondes.

Certains des éléments nutritifs, grâce à leurs fortes concentrations dans l'eau de mer, sont toujours biodisponibles pour le phytoplancton (carbone, hydrogène, oxygène, soufre, potassium, calcium...). Les trois éléments nutritifs principaux appartenant aux macro-nutriments sont les nitrates, phosphates et silicates. Les concentrations de ces macronutriments peuvent être importantes dans l'océan (de l'ordre de 1 à 100 μmol kg^{-1}). Cependant, ils sont généralement totalement consommés dans les eaux de surface par les organismes autotrophes et ils limitent ainsi la production primaire.

En plus de ces macro-nutriments indispensables au développement du phytoplancton, d'autres éléments, des métaux, sont nécessaires pour leur croissance. Ces micro-nutriments, tels que le fer, le cobalt, le cuivre, le zinc, sont généralement moins abondants dans l'océan (concentrations inférieures ou de l'ordre du nmol L^{-1}). Ces éléments essentiels pour le développement du phytoplancton permettent de faire fonctionner le métabolisme des cellules. Par exemple, le fer est utilisé dans de nombreux composés intermédiaires permettant le transfert d'électron aussi bien dans les processus de respiration que de photosynthèse. Il joue notamment un rôle essentiel dans la fixation d'azote et dans la synthèse de la chlorophylle-a. Ce dernier est un des pigments chlorophylliens et est le pigment majoritaire impliqué dans la photosynthèse.

I.2. Les Marquises : une oasis au milieu du désert

La présence d'îles en plein océan perturbe la vision très simplifiée des schémas grandes échelles de circulations océaniques et atmosphériques présentée ci-dessus. Les vents et les régimes d'écoulements ainsi que les flux de chaleur sont redistribués dans le sillage des îles et peuvent causer l'approfondissement de la couche de mélange et/ou de la pycnocline à travers différents processus physiques (i.e. tourbillons, upwelling côtier). Ces événements peuvent entraîner un enrichissement nutritif qui déclenche des efflorescences phytoplanctoniques. Cette augmentation locale de l'activité biologique est appelée « Island Mass Effect » (IME ; *Doty and Oguri*, 1956), soit « Effet d'Ile » en français (EI).

A première vue, l'impact des EI sur les flux de carbone paraît négligeable en comparaison des flux de carbone à l'échelle globale. Toutefois, les îles sont des endroits importants, dénommés "hotspots" avec une terminologie anglophone, pour les ressources et la biodiversité marine [*Hernández-León et al.*, 2001]. Elles jouent également un rôle important pour la survie alimentaire des populations locales [*Bell et al.*, 2009; *Lehodey et al.*, 2011].

C’est dans ce contexte que se situe l’archipel des Marquises localisé au nord-est de la Polynésie française, au centre du Pacifique Sud (218°-222°E/8°-11°S - Figure I-5 et Figure I-7). Ces îles sont un “hotspot” en termes de biodiversité marine, endémisme et ressources marines pour les populations locales (AAMP, 2012). Les îles Marquises sont dispersées sur une surface de 100 000 km² et s'élèvent rapidement sur la plaine abyssale située à 4000 m de profondeur. Situées dans une zone tropicale voire proche équatoriale, les îles Marquises sont sous l'influence océanique du Courant Equatorial Sud (SEC - South Equatorial Current). Ce courant de surface, forcé par les alizés, s'écoule vers l’ouest/sud-ouest. Les îles représentent des obstacles de 10 à 40 km de large qui vont ainsi perturber l’écoulement du SEC.

Du point de vue biogéochimique, les eaux environnantes des îles Marquises constituent la frontière sud des eaux mésotrophes de la région d'upwelling équatorial (Chl >0.2mg.m^{-3}) et des eaux oligotrophes (Chl<0.1 mg.m^{-3}) du reste de la Polynésie française (Figure I-5). Les eaux équatoriales et Marquisiennes sont riches en macro-nutriment (*i.e.,* phosphate et nitrate) mais relativement pauvre en Chl, on parle de région « High Nutrient Low Chlorophyll » (HNLC) (Biogeosciences special issue on BIOSOPE cruise, 2008 ; *Martinez et al.*, 2016). La géométrie et la localisation des îles Marquises sont des facteurs déterminants dans la perturbation du SEC et donc dans le renforcement ou non de la productivité biologique locale.

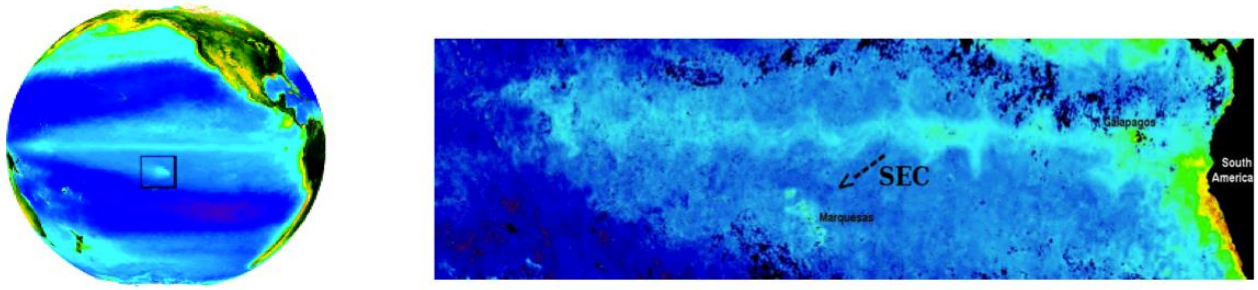

Figure I-5: (gauche) Moyenne de concentration en chlorophylle (Chl) sur la période 1997-2010 dans l’océan Pacifique à partir des données satellites issues du capteur radiométrique SeaWiFS. La boîte noire délimite l’archipel des Marquises. (droite) Panache de Chl dans le Pacifique équatorial et aux Marquises en 2002. La flèche indique le Courant Equatorial Sud (SEC pour « South Equatorial Current »), courant dominant aux Marquises.

L'effet d'îles aux Marquises est remarquable pour plusieurs raisons (Figure I-5) :

- De fortes valeurs de Chl (>0.2 mg m^{-3}) au voisinage des îles sont observées tout au long de l'année, exceptée en période El Niño [*Martinez et Maamaatuaiahutapu*, 2004].
- Le panache de Chl en aval du SEC, à l'ouest de l'archipel est fortement étendu au regard de la taille des îles (jusqu'à 800 km en novembre 1998 ; Figure I-6).
- Les mécanismes physico-chimiques à l'origine de cet enrichissement biologique sont toujours débattus.
- Un très fort niveau d'endémisme des espèces océaniques (proche de 20%, comme à Hawaii ou en mer rouge) a été rapporté (AAMP, 2012), motivant le dépôt d'inscription de l'archipel au patrimoine mondial de l'humanité de l'UNESCO.
- C'est une région riche en grands pélagiques (thonidés, dorades coryphènes), notamment en juvéniles, source majeure de l'alimentation des polynésiens.

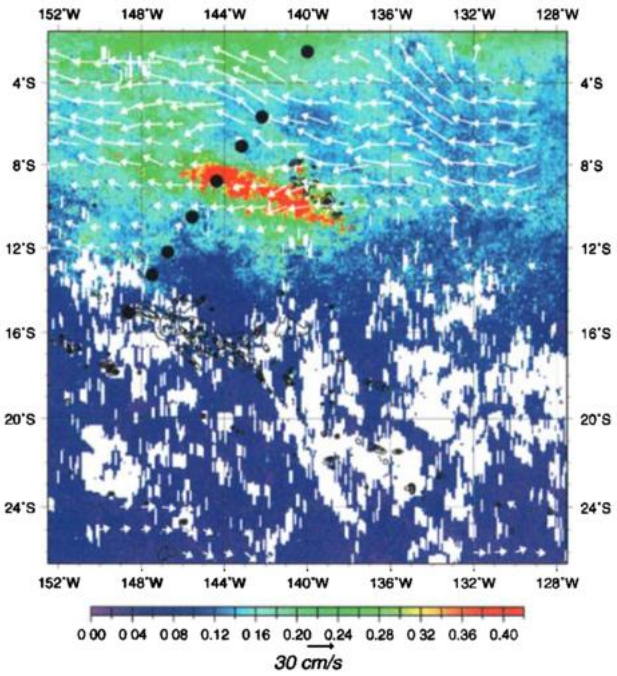

Figure I-6: Concentration de chlorophylle-a (mg m^{-3}) en novembre 1998 issues du capteur radiométrique SeaWiFS. Les courants géostrophiques correspondant déduit de des données altimétriques sont représentés par les flèches blanches. (Source : Signorini et al., 1999*)*

Figure I-7: Carte représentant l'ensemble des îles composant l'archipel des Marquises (Source : http://blogs.oregonstate.edu/marquesas/map-of-the-marquesas-islands/)

L'EI de l'archipel des Marquises est d'autant plus remarquable que ces îles sont géographiquement isolées. D'une part, elles sont éloignées de toutes perturbations pouvant être causées par la présence de régions côtières proches (*e.g.,* pollution). De plus, le nombre d'habitants peu élevé (environ 8000 répartis sur les cinq îles principales), permet de considérer l'impact anthropique local comme quasi nul dans la zone d'étude. Ainsi, la variabilité du phytoplancton observée dans l'archipel est représentative des cycles naturels et non liée à des processus d'eutrophisation.

Bien que remarquable, l'environnement océanique pélagique de ces îles a été peu étudié. La majorité des connaissances biologiques et biogéochimiques des eaux environnantes des Marquises proviennent de deux campagnes océanographiques : BIOSOPE (BIogeochemistry

and Optics South Pacific Experiment) menée en 2004 (*Claustre et al.*, 2008b, et les références présentes dans cette issue spéciale), et "Pakaihi I te Moana" (« Respect de l'Océan » en Tahitien) en 2012 [*Rodier and Martinez*, 2012; *Martinez et al.*, 2016]. Cependant, les données issues de ces campagnes ou d'observations satellites [*Signorini et al.*, 1999; *Legeckis et al.*, 2004; *Martinez et Maamaatuaiahutapu*, 2004] n'ont pas suffi pour caractériser et comprendre l'EI aux Marquises, du point de vue des processus impliqués aux échelles saisonnières et interannuelles.

Par ailleurs, dans l'Annexe A, l'utilisation des observations satellites a permis d'aborder certains processus physiques et biogéochimiques à l'échelle régionale (de l'équateur aux Marquises), et souligner l'importance des phénomènes dits de méso-échelles (< 100 km). Dans la bande équatoriale, les Alizées engendre un déplacement des eaux de surface vers les pôles de part et d'autre de l'équateur, créant ainsi une zone de divergence, c'est l'upwelling équatorial. On observe alors la remontée d'eaux riches en nutriments et notamment en fer (Figure I-5). Un apport de nutriments de ces eaux équatoriales par la propagation d'ondes d'instabilités tropicales (Tropical Instability Waves - TIW) vers les Marquises vient ainsi influencer les concentrations de Chl dans la zone. Dans leur étude, *Legeckis et al.* [2004] ont émis l'hypothèse que les TIWs permettraient de transporter ces eaux riches vers l'archipel des Marquises durant les événements La Niña. Cependant l'augmentation de Chl ne sont, en réalité, corrélées qu'avec les évènements de 1998 et 2010. Il apparait également que les TIWs peuvent influencer la forme du panache de Chl dans l'archipel. Cependant, la dynamique générée par la présence des îles Marquises au milieu de l'écoulement du courant équatorial sud apparait comme jouer un rôle prédominant dans l'enrichissement de l'archipel.
(**Annexe A** : Martinez, E., Raapoto, H., Maes, C., & Maamaatuaiahutapu, K. (2018). Influence of Tropical Instability Waves on Phytoplankton Biomass near the Marquesas Islands. *Remote Sensing*, 10(4), 640)

En effet, la présence d'îles au milieu d'un courant marin représente un obstacle pour l'écoulement et génère une circulation complexe dans leur sillage. Plusieurs processus physiques peuvent alors être observés tels que l'accélération du courant sur les flancs des îles et la génération de tourbillons dans leur sillage [*Pattiaratchi et al.*, 1987; *Heywood et al.*, 1996; *Hasegawa et al.*, 2004]. Dans leur étude, *Hasegawa et al.* [2009] ont montré à l'aide d'un modèle numérique que la circulation générée autour des îles pouvait permettre l'enrichissement des eaux et la formation d'un EI. C'est dans ce même contexte que nous utiliserons un modèle

de dynamique océanique régional pour vérifier si l'écoulement du SEC dans l'archipel pourraient, lui aussi, permettre la génération de l'EI Marquisien.

I.3. Objectifs et méthodologie

Les processus impliqués dans l'EI marquisien sont complexes et encore mal connus. L'objectif de cette thèse est d'identifier et comprendre les cycles saisonniers de la dynamique océanique et phytoplanctonique dans l'archipel des Marquises.

Ainsi, ce travail de thèse consistera à, 1) faire des tests de sensibilités sur plusieurs configurations pour identifier la plus réaliste, et 2) utiliser celle-ci pour caractériser l'activité méso-échelle de l'archipel, et 3) mettre en place un modèle couplé physique-biogéochimique pour la zone de l'archipel. Les jeux de données utilisés pour forcer le modèle sont issus de données climatologiques, c'est à dire des moyennes mensuelles. Ainsi, en plus des processus, la variabilité saisonnière de la dynamique océanique et phytoplanctonique sera étudiée. Ainsi, nous proposons un travail articulé sur 3 axes :

- *Mise en place d'une configuration de dynamique océanique réaliste*

Les données satellites ne fournissent pas d'information sur la verticale et ont une résolution spatiale et temporelle insuffisante pour caractériser l'activité méso-échelle. D'autre part, les observations *in situ* sont quasi inexistantes dans cette région. Ainsi, pour atteindre les objectifs de la thèse et étudier l'EI aux Marquises suivant les 4 dimensions (2 horizontales, verticale et temporelle) avec une résolution spatio-temporelle adéquate, le modèle de dynamique océanique ROMS (Regional Ocean Modeling System – [*Marchesiello et al.*, 2001]) a été configuré pour la zone. Le modèle ROMS, largement utilisé dans la communauté scientifique, est particulièrement adapté à cette étude. En effet, la version ROMS_AGRIF développée par l'IRD permet l'utilisation d'un emboîtement de grilles avec des résolutions spatiales de plus en plus fines. Ainsi, plusieurs simulations numériques utilisant différentes conditions initiales et forçages ont été mises en place. Ces simulations ont été configurées en utilisant différents jeux de données climatologiques (i.e., champs moyens) mensuelles. Puis les différentes sorties de modèle ont été comparées avec des observations satellites et *in-situ* pour déterminer la configuration la plus réaliste.
(**Chapitre II** : H. Raapoto, A. M. Doglioli, A. Petrenko & E. Martinez. Prêt à être soumis dans *Journal of Oceanography*)

- *Étude de la dynamique océanique méso-échelle de l'archipel*

Le manque de données mais aussi la faible résolution temporelle et spatiale des observations disponibles ne permet pas, à ce jour, de caractériser l'environnement physique de l'archipel des Marquises. Or, plusieurs processus physiques peuvent intervenir dans l'enrichissement biologique observé, et cet axe vise à les déterminer grâce au modèle de dynamique océanographique ROMS. En particulier, la configuration la plus réaliste déduite de l'axe précédent est utilisé pour déterminer le rôle respectif des vents et des courants dans la dynamique de l'archipel et dans la génération de tourbillons dans le sillage des îles. Ces derniers peuvent être générés par la contrainte topographique sur les courants océaniques [e.g., *Jiménez et al.*, 2008], sur les vents [e.g., *Chavanne et al.*, 2002] ou par un mélange de ces deux processus [*Kersalé et al.,* 2011].

(**Chapitre III** : Raapoto, H., Martinez, E., Petrenko, A., Doglioli, A. M., & Maes, C. (2018). Modeling the wake of the Marquesas archipelago. *Journal of Geophysical Research*: Oceans, 123(2), 1213-1228.)

- *Étude de l'Effet d'île des Marquises*

L'apport d'eaux riches en sels nutritifs dans la zone éclairée de surface est nécessaire au phytoplancton pour se développer autour des îles. Les processus nécessaires à cet enrichissement et à la génération de l'effet d'île observé aux Marquises est étudié dans ce dernier axe. En se basant sur les travaux des axes précédents, le modèle de dynamique océanique qui a été couplé, dans cette partie, au modèle biogéochimique PISCES (Pelagic Interaction Scheme for Carbon and Ecosystem Studies). L'impact de l'apport de Fer dans l'archipel est ici évalué grâce à la mise en place de plusieurs simulations contraintes par les mêmes forçages physiques mais des forçages biogéochimiques différents. Ces derniers permettent de révéler des processus capables de générer une forte activité biologique dans l'archipel, ainsi que de caractériser leur variabilité saisonnière.

(**Chapitre IV** : H. Raapoto, E. Martinez, A. Petrenko, A. M. Doglioli, R. Sauzède, K Maamaatuaihutapu, C. Menkes, T. Gorgues. Prêt à être soumis dans *Journal of Geophysical Research : Ocean*)

Chapitre II

A high-resolution ocean circulation nested model for the Marquesas Archipelago

H. Raapoto[1], A. M. Doglioli[2], A. Petrenko[2] and E. Martinez[1]

[1] IRD, UPF, ILM, Ifremer, Écosystèmes Insulaires Océaniens (EIO), Tahiti, French Polynesia.

[2] Aix Marseille Univ, Université de Toulon, CNRS, IRD, OSU PYTHEAS, Mediterranean Institute of Oceanography MIO, UM 110, 13288, Marseille, Cedex 09, France.

Prêt à être soumis dans *Journal of Oceanography*

RESUME

L'écoulement des courants marins autour de petites îles océaniques tel que l'archipel des Marquises peut générer des circulations océaniques complexes. Cependant, très peu de mesures ont été réalisées autour de ces îles et l'utilisation d'un modèle océanique est essentielle pour étudier les la génération et la dynamique du sillage de ces îles. Dans cette étude, 7 simulations avec emboitement de grilles ont été réalisées en utilisant le modèle ROMS (Regional Oceanic Modelling System) afin de déterminer la configuration la plus réaliste pour la région. Les différences entre les sorties de modèle et les mesures satellites ont été quantifiées en utilisant des indices de différences. Ainsi, nous nous sommes intéressé aux moyennes annuelles et aux cycles saisonniers de paramètres thermohalins et dynamiques. Pour la température et la salinité, toutes les configurations sont proches des observations. A l'inverse, les énergies cinétiques et énergies cinétiques tourbillonaires présentent des écarts significatifs. Les simulations utilisant les forçages de surface et aux bords de plus haute résolution génèrent de plus grandes énergies et permettent d'obtenir les résultats les plus proches des observations. Cette simulation optimale sera celle choisie pour la continuité de l'étude (chapitre III et IV).

ABSTRACT

Currents around small oceanic islands such as the Marquesas archipelago present complex oceanic circulation. Only few measurements are available for the area and the use of a model is essential to properly investigate physical processes in these island wakes. In this study, we implement 7 simulations using the nested method of the Regional Oceanic Modelling System code in order to determine the most realistic configuration for the archipelago. We quantify the differences between model outputs and independent remote sensing observations using different indexes. Both annual mean and seasonal variability are investigated for thermohaline and dynamical parameters. For temperature and salinity, all configurations are close to the observations, while some biases are observed for kinetic and eddy kinetic energy. Boundary and surface forcing with the highest resolution allow a high production of energy and present the closest results to the observations.

II.1. Introduction

Ocean circulation flowing around steep islands generates complex island wakes. Numerous studies have assessed these fine scale dynamical processes using different approaches. Remote sensing can reveal the interesting features of these transitory circulation difficult to detect using conventional in-situ instrumentation. For instance, to identify island wakes in the Bristol channel, Pattiaratchi et al. (1987) used remote sensing imagery considering suspended sediment in the surface water as a passive tracer. Caldeira et al. (2002) used Sea Surface Temperature (SST) from AVHRR data to reveal warm wake south of the Madeira Island with eddies and fronts generated in the region. Hasegawa et al. (2004 and 2008) took advantage of in-situ measurements to investigate processes in the water column leeward small islands lying in the Kuroshio. They used a 3D velocity survey and a towed free fall instrument to observe vigorous turbulence leeward the islands revealing strong secondary circulations. Other studies investigate dynamical processes in island wakes using laboratory experiments. Teinturier et al. (2010) investigated destabilizations of an island wake flow in a shallow-water configuration while Stegner (2014) characterized the different regimes thanks to a deep-water configuration. Then, the modeling approach allows to break down, uncouple and identify the physical processes occurring in island wakes. Previous numerical studies of flow past isolated obstacles in the ocean have focused on the eddy shedding process [*Wolanski et al.*, 1984; *Dietrich et al.*, 1996; *Heywood et al.*, 1996]. Increasing the incident current rises the Reynolds number and allows the generation of a Von Karman wake [*Von Karman and Sears*, 1938]. Dong et al. (2007) modelled the flow around an idealized island in deep water and investigated wake instability and eddy activity. They showed the relations between wake instabilities and non-dimensional numbers (Reynolds number, Rossby number and Burger number). Jiménez et al. (2008) developed a barotropic model to study the relative importance of wind and topographic forcing around the island of Gran Canaria. They revealed that wind acts as an additional source of vorticity and allows eddy shedding at lower intensity of current. Using different resolutions of wind forcing, Calil et al. (2008) and Kersalé et al. (2011) tend to find the same results for the eddy generation processes in the Hawaiian archipelago. Therefore, the investigation of the dynamical processes around oceanic islands, and particularly those which have never been investigated before, requires giving a particular attention to the different physical forcings.

In the present study, we focus on the circulation around the Marquesas Islands (Figure II-1). This archipelago (144°W-137°W; 8°S-11°S) is located in the northern part of French Polynesia,

central South Pacific, where the South Equatorial Current (SEC) flows south-westward. It is composed by a dozen of small steep islands with mountains up to 1224 m. The main five islands are Nuku Hiva (339 km^2), Ua Pou (105 km^2) and Ua Huka (83 km^2) in the northern part of the archipelago, and Hiva Oa (320 km^2) and Fatu Hiva (85 km^2) in the southern part [*Maury et al.*, 2014]. An intense biological activity referred as an Island Mass Effect (IME - Doty and Oguri, 1956) occurs in this archipelago and is revealed by the chlorophyll-a concentration (Chl) plume observed leeward the islands on satellite ocean colour observations [*Signorini et al.*, 1999]. Nevertheless, while Martinez and Maamaatuaiahutapu (2004) associated the occurrence of the Chl blooms with an intensification of the SEC, the relevant processes involved are not elucidated yet. A wind curl dipole is generated leeward the archipelago [*Martinez et al.*, 2009], and oceanic cyclonic eddies associated with such atmospheric features can induce a nutrient enrichment of the upper layer (and consequently of Chl) leeward the concerned islands [*Hasegawa et al.*, 2009; *Andrade et al.*, 2014]. Therefore, meso and sub-mesoscale dynamics are suspected to play a key role in both the archipelago circulation and IME. However, the very few existing studies on the Marquesas did not mention any eddy features probably due to the too coarse spatial resolution of the satellite products used [*Signorini et al.*, 1999; *Legeckis et al.*, 2004; *Martinez and Maamaatuaiahutapu*, 2004].

To start investigating the physical fine-scale processes occurring in the Marquesas, the implementation of a high-resolution model is required since currently there is a severe lack of observations in this area and the spatial resolution of satellite observations and global oceanic circulation models are too coarse. Available climatologies used to initialize and force numerical models are built on various datasets with different spatial resolutions that could induce differences when modeling the ocean circulation around these small islands. Hence, the present work investigates several high resolution numerical simulations forced with different monthly climatologies, and compares different model outputs with independent satellite products. The aim is to evaluate the impact of the different forcings on the fine scale dynamics and to determine the best simulation to set up a coupled biological-physical simulation of this archipelago in the future.

The paper is organized as follows: Section 2 introduces the high resolution numerical model, the different simulations and the remotely sensed data used. Section 3 presents the modeling results and their comparisons with satellite observations. These results are then discussed in section 4. Our conclusions are drawn in Section 5.

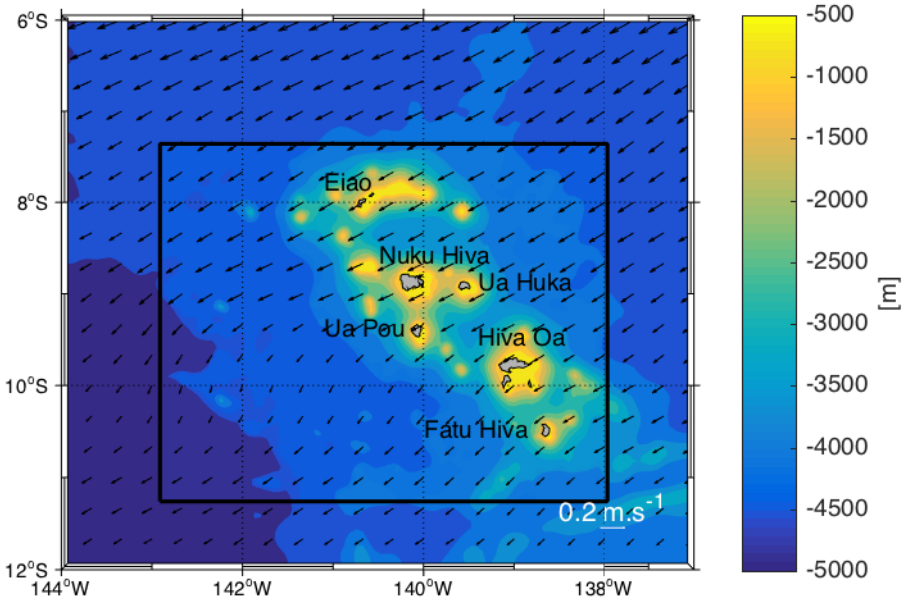

Figure II-1: Bottom topography from the 2-arc minute topography/bathymetry dataset ETOPO2 (in m) used in the model configurations. The vectors are the mean current obtained from the Ocean Surface Current Analysis – Real time (OSCAR) product (time averaged over Oct-1992 to Jun-2015 in m s^{-1}). The parent grid is delimited by the frame of the figure while the child grid is delimited by the black box.

II.2. Data and methods

In the present study, 7 simulations based on the same high-resolution model built with different forcings with various spatial resolutions are set up. The model outputs are then compared with different independent remote sensed products to determine the most realistic configuration.

II.2.1.Numerical Model

The model is based on the Regional Ocean Modeling System (ROMS)-AGRIF (Adaptive Grid Refinement in Fortran) code provided by Debreu et al. (2012) and Penven et al. (2007). The ROMS model is a split-explicit, free surface and terrain-following vertical coordinate oceanic model [*Shchepetkin and McWilliams*, 2003, 2005]. All runs are based on the AGRIF version which is especially suitable to study regional scale since it can manage an arbitrary number of fixed grids and embedding levels. In this study, we configure and compare the 1-way *vs*. 2-way

embedding procedure. In the 1-way, the parent grid provides the boundary conditions for the child grid. Using the two-way method, the solution of the child grid is used to improve the larger scale parent grid solution, allowing a smooth, continuous interfacing between grid levels [*Debreu and Blayo*, 2008; *Debreu et al.*, 2012]. Here, we tested the 1 way vs. 2-way method for the simulation using lowest spatial resolution data and implemented the 2-way for the other simulations. We defined the same two embedded grids for all simulations: 1) the parent grid extends from 137°W to 144°W and 6°S to 12°S; 2) the child grid extends from 138°W to 143°W and 7.3°S to 11.3°S (Figure II-1). The grid refinement rate is 3, implying a 1/15° (~7km) and 1/45° (~2.5 km) grid resolutions for the parent and child grids, respectively. This allows a sufficient sampling of the island topography and of the fine-scale dynamics, as the first baroclinic Rossby radius of deformation is about 120 km in this region according to Chelton et al. (1998). The internal (external) time stepping is set to 3600 (600) s for the parent grid and 1200 (200) s for the child grid. Both grids have 32 vertical levels and the vertical s-coordinate is stretched for the boundary layer resolution. The topography is derived from the 2' resolution ETOPO2 database provided by NOAA-NGDC [*Smith and Sandwell*, 1997]. The bathymetry field has been filtered to keep the slope parameter < 0.25 [*Beckmann and Haidvogel*, 1993]. The K-profile parameterization (KPP) vertical mixing scheme from Large et al. (1994) is used to parameterize vertical mixing processes.

All the external forcing of the ROMS simulations are based on monthly climatologies. At the surface, the heat and fresh water fluxes are extracted on a ½° grid from the Comprehensive Ocean-Atmosphere dataset (COADS) [*da Silva et al.*, 1994]. Two monthly climatologies are used for the wind forcing: the ½° spatial resolution COADS dataset (averaged over 1945-1989) and the ¼° spatial resolution QuikSCAT (QSCAT) dataset (averaged over 1999-2009) [*Lungu and Callahan*, 2006]. ROMS is connected to the lateral boundaries by an active, implicit and upstream-biased radiation condition [*Marchesiello et al.*, 2001]. The boundary conditions and initial state are based on: 1) the objectively analysed World Ocean Atlas (WOA) 2009 available on a 1° grid resolution [*Antonov et al.*, 2010; *Locarnini et al.*, 2010] ; 2) the more recent WOA 2013 product with a ¼° grid resolution [*Locarnini et al.*, 2013; *Zweng et al.*, 2013]; 3) the CSIRO Atlas of Regional Seas (CARS) 2009 climatology on a ½° grid [*Ridgway et al.*, 2002]. The inflow boundary conditions are nudged toward temperature, salinity, and geostrophic velocity fields. The nudging timescale for inflow and outflow are set to 1 (3) day and 1 (1) yr for the tracer (momentum) fields, respectively. The geostrophic velocity is referenced to the 1000 m depth. The explicit lateral viscosity is null all over the domain, except in the sponge

layer. The width of the nudging border is 50 km and the maximum viscosity value for the sponge layer is set to 1000 m^2 s^{-1}.

We run 7 simulations, 1 using the one-way nesting method and 6 using the two-way nesting method. Table II-1 summarizes the different simulations set up. These simulations are run over 10 years with outputs averaged every 2 days. After 2 years, the KE and the other variables reach the equilibrium. We have decided to remove the first three years of spin up and the outputs from years 4 to 10 are investigated.

		Boundary conditions			
		WOA 2009 (1°)		CARS 2009 (1/2°)	WOA 2013 (1/4°)
		1 Way	2 Way		
Surface Forcing	QSCAT (1/4°)		W09-Q	CARS-Q	W13-Q
	COADS (1/2°)	W09-C-1W	W09-C	CARS-C	W13-C

Table II-1: Summary of the acronyms of the numerical implementations performed according to the method and the forcings used. The spatial resolution of the products is indicated underneath their names.

II.2.2. Remote sensing data

The monthly climatologies used to initiate and force the ROMS simulations are built on *in situ* measurements. Thus, to avoid biases when comparing our ROMS outputs with observations, we use independent remote sensing products. First, the numerical results are compared with SST from the Advanced Very High Resolution Radiometer (AVHRR) [*Hastings and Emery*, 1992]. This dataset is available on a weekly basis with a 9 km spatial resolution. The time period used in this study extends from January 2004 to December 2014.

Second, a comparison is performed with Sea Surface Salinity (SSS) from the Soil Moisture and Ocean Salinity (SMOS) data [*Olmedo et al.*, 2016]. SMOS SSS is available from May 2010 to April 2017 with a spatial and temporal resolution of 0.25° and 9 days, respectively.

Third, the dynamics in the archipelago is then investigated through the Kinetic Energy (KE_g) and the Eddy Kinetic Energy (EKE_g) calculated from the surface geostrophic velocity fields provided by AVISO from 1993 to 2016. These daily fields are available on a 0.25° grid.

II.2.3. Model-observation comparison metrics

Hereafter, we compare SST, SSS, KE_g and EKE_g at -10 m from ROMS with their corresponding satellite derived observations. For these four parameters, the annual mean and its standard deviation are computed over the last seven years of the ROMS simulations and over all the available time period for satellite observations.

To quantify the spatial differences between the results of each simulation *vs*. observations, first we interpolate the high spatial resolution ROMS outputs to the spatial grid of the respective remote sensing products. Then, we investigate the spatial differences using normalized root-mean-square errors ($NRMSE_{xy}$) between the ROMS outputs and the observations:

$$NRMSE_{xy} = \frac{\sqrt{\frac{1}{n}\sum_{i=1}^{n}\left(\langle V_{ROMS,i}\rangle_T - \langle V_{SAT,i}\rangle_T\right)^2}}{\frac{1}{n}\sum_{i=1}^{n}\langle V_{SAT,i}\rangle_T} * 100$$

where n is the total number of grid cells, $\langle V_{ROMS,i}\rangle_T$ and $\langle V_{SAT,i}\rangle_T$ are the annual averages of ROMS outputs and satellite observations, respectively.

We also investigate the seasonal variability of the 4 parameters calculating 1) their monthly climatology (over year 4 to 10 for model outputs and over the whole time period for observations), then 2) their spatial average on the child grid. The associated standard deviations are computed over the monthly averages for these two cases.

To quantify the differences over the seasonal variability, we use the same methodology as the $NRMSE_{xy}$. The Temporal normalized root-mean-square errors ($NRMSE_t$) is defined as:

$$NRMSE_t = \frac{\sqrt{\frac{1}{m}\sum_{i=1}^{m}\left(\langle V_{ROMS,i}\rangle_{XY} - \langle V_{SAT,i}\rangle_{XY}\right)^2}}{\frac{1}{m}\sum_{i=1}^{m}\langle V_{SAT,i}\rangle_{XY}} * 100$$

where m is the number of considered years, $\langle V_{ROMS,i}\rangle_{XY}$ and $\langle V_{SAT,i}\rangle_{XY}$ are the spatial averages over the archipelago from ROMS over years 4-10 and from the satellite observations over their entire time series, respectively.

$NRMSE_{xy}$ and $NRMSE_t$ are used to point out differences between model outputs and observations. The lower the index, the better the agreement between model ouputs and observations.

II.3. Results

II.3.1.Sea Surface Temperature

The SST annual average derived from AVHRR reveals the presence of warm water in the south-western part of the archipelago (Figure II-2a) corresponding to the imprint of the western Pacific warm pool (Yan et al., 1992). Contrastingly, the north-east region shows the cold water imprint of the equatorial upwelling. This spatial pattern is well reproduced by all the ROMS simulations (Figure II-2b-h). The $NRMSE_{xy}$, quantifying the spatial pattern differences between model outputs and remote sensed observations, is always less than 1%, varying from 0.26% (0.07°C) for W09-Q to 0.56% (0.15°C) for CARS-C (Table II-2). These small biases obtained between the 7 simulations, and particularly the CARS-based ones, are induced by the different extent and magnitude of the incursions of cold (warm) waters in the north-east (south-west). The inter-annual variability of the AVHRR SST data set induces standard deviations with a north/south gradient and a minimum variability in the west (Figure II-3a) stronger than in the 7 ROMS simulations (Figure II-3b-h). The simulated standard deviations differ from observations with a weak north-east/south-west gradient.

The SST seasonality from satellite and ROMS are close, with warmer waters in April and colder ones in September (austral summer and winter, respectively - Figure II-4). Thus, the seasonal variability from model outputs remains in the range of the standard deviations of AVHRR (grey shade), highlighting the robustness of the modelled SST. The $NRMSE_t$ vary from 0.34 % for the W09 simulations to 0.57 % for the W13 ones (Table II-2). This higher difference can be explained by colder waters occurring in May and November in the outputs of W13-Q and W13-C runs. Simulations using CARS product (CARS-Q and CARS-C) present a delay of approximatively one month in comparison with AVHRR. Whatever the boundary conditions are (i.e., WOA 2009, 2013 and CARS), the differences in SST annual averages, SST standard deviations, as well as SST seasonality, between the simulations using COADS *vs*. QSCAT as surface forcing remain very small. Moreover, the reproduction of the satellite SST spatial and seasonal patterns is very performant for all simulations regarding $NRMSE_{xy}$ and $NRMSE_t$, which are both always lower than 1%.

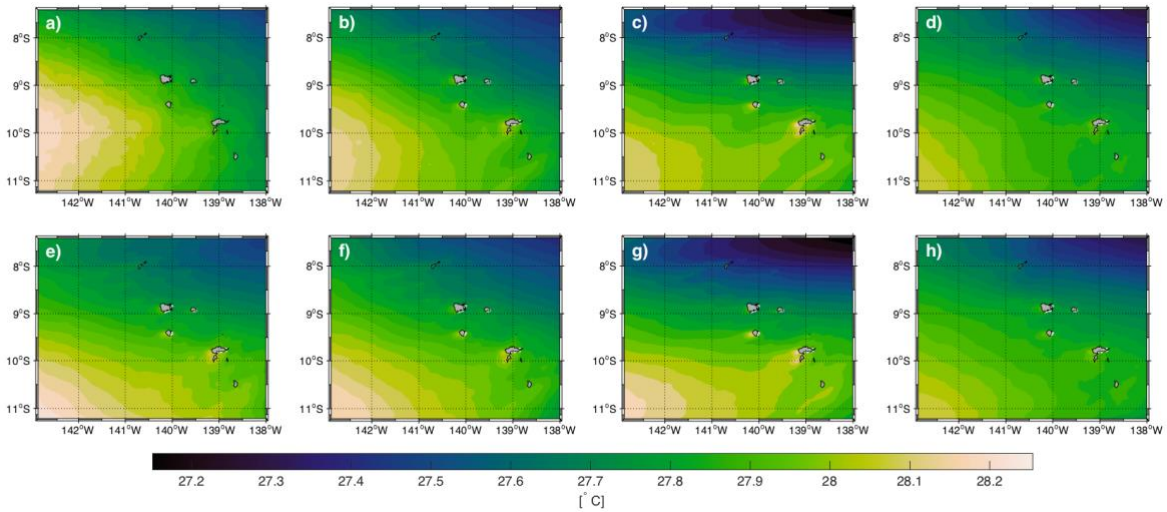

Figure II-2: Mean SST over the child grid area from (a) AVHRR (time averaged from Jan-2004 to Dec-2014), (b) W09-Q, (c) CARS-Q, (d) W13-Q, (e) W09-C-1W, (f) W09-C, (g) CARS-C and (h) W13-C. Model outputs are time averaged over year 4 to 10.

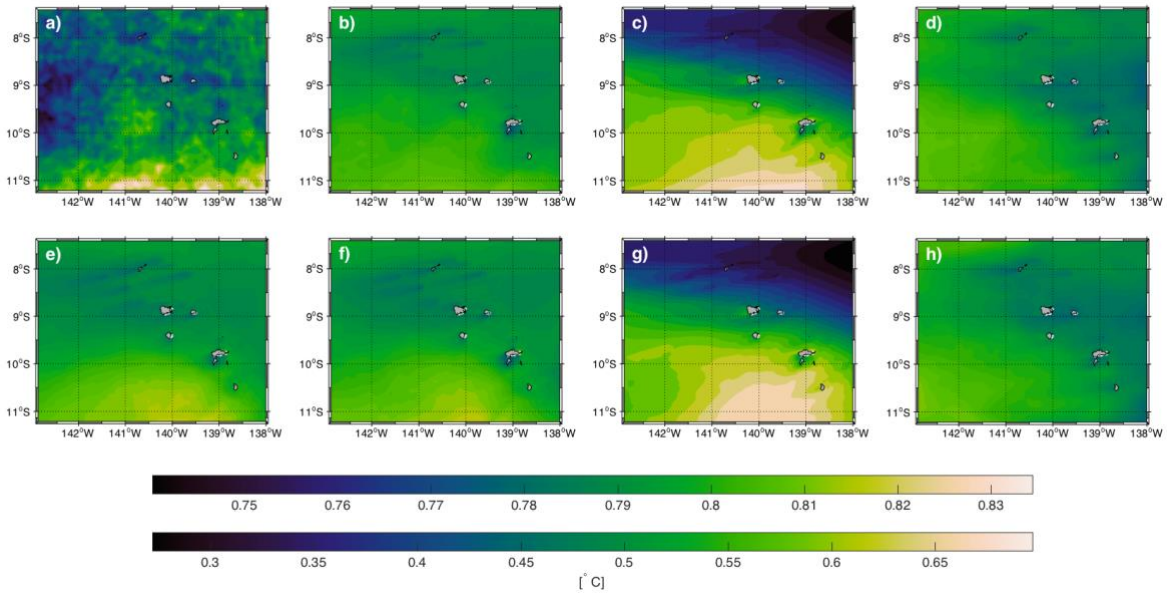

Figure II-3: Standard deviations of the SST over the child grid area from (a) AVHRR (Jan-2004 to Dec-2014), (b) W09-Q, (c) CARS-Q, (d) W13-Q, (e) W09-C-1W, (f) W09-C, (g) CARS-C and (h) W13-C (for year 4 to 10). The upper color bar is associated with the remote sensing standard deviation (a) while the one below is associated with the model outputs (b-h).

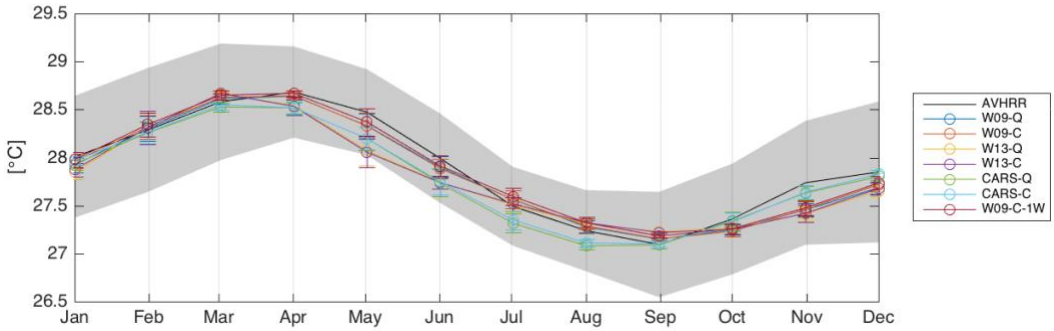

Figure II-4: Seasonal variability of the SST over the child grid area from AVHRR and the 7 runs. The grey shaded area represents the standard deviation from the monthly climatology of the remote sensing observations.

		1W-WOA2009	WOA2009	CARS 2009	WOA 2013
$NRMSE_{xy}$	QSCAT		0.29	0.66	0.45
	COADS	0.34	0.33	0.66	0.46
$NRMSE_t$	QSCAT		0.42	0.52	0.69
	COADS	0.40	0.41	0.48	0.70

Table II-2: SST $NRMSE_{xy}$ and $NRMSE_t$ values calculated for the SST for the 7 numerical implementations.

II.3.2.Sea Surface Salinity

The north/south gradient of SSS observed in the SMOS data (Figure II-5a) is well reproduced within all simulations (Figure II-5b-h). Simulations built with WOA 2009 present saltier waters in the whole archipelago while the salinity range in CARS 2009 simulations is larger. However, these biases with observations remain small with $NRMSE_{xy}$ varying from 0.16 % to 0.33 % for simulations W13-Q and W09-C, respectively (Table II-3). The standard deviation from SMOS presents higher values than ROMS, likely due to the inter-annual variability of the satellite dataset from which the climatology is performed (Figure II-6). Its spatial pattern presents a dipole extending over the islands with the strongest variability in the southern region of the archipelago. Nevertheless, note that the color bar limits used for this figure is likely overstressing this pattern. Indeed, at a larger scale, the archipelago is located within a high and low transient variability area [*Talley*, 2002]. All the standard deviations from model outputs present a different pattern from the remote sensing observations, highlighting a south-east/north-west gradient.

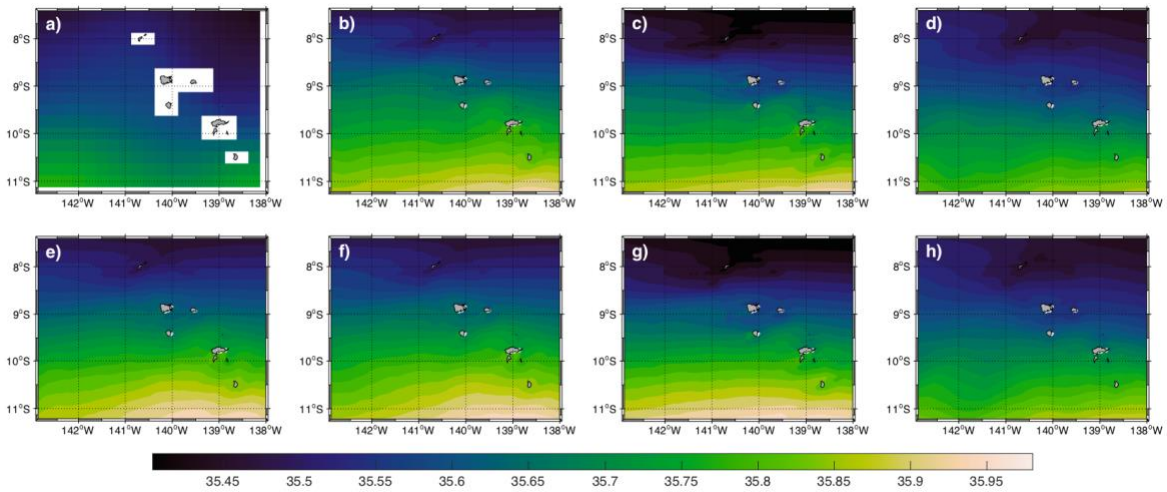

Figure II-5: Mean SSS over the child grid area from (a) SMOS (time averaged from May-2010 to Apr-2017), (b) W09-Q, (c) CARS-Q, (d) W13-Q, (e) W09-C-1W, (f) W09-C, (g) CARS-C and (h) W13-C. Model outputs are time averaged over year 4 to 10.

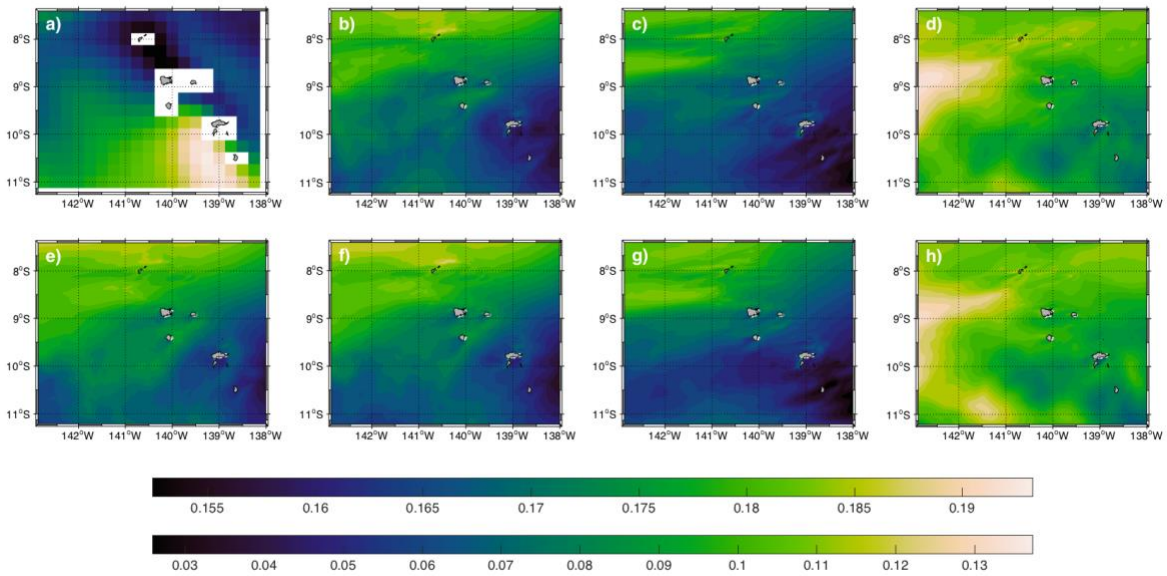

Figure II-6: Standard deviations of SSS over the child grid area from (a) SMOS (May-2010 to Apr-2017), (b) W09-Q, (c) CARS-Q, (d) W13-Q, (e) W09-C-1W, (f) W09-C, (g) CARS-C and (h) W13-C (for year 4 to 10). The upper color bar is associated with remote sensing standard deviation (a) while the one below is associated with the model outputs (b-h).

The SSS seasonalities from satellite and ROMS outputs particularly differ in austral winter: SMOS data show saltier water while ROMS reveal minimum values (Figure II-7). Thus, the increase of salinity in the second half of the year is quasi-linear. Nevertheless, here again, the $NRMSE_t$ remains small from 0.25 % for CARS-Q to 0.35 % for W13-Q, revealing good performances from the model outputs (Table II-3). Similarly to SST, changes in boundary conditions induce a stronger impact on ROMS SSS than changes in surface forcing.

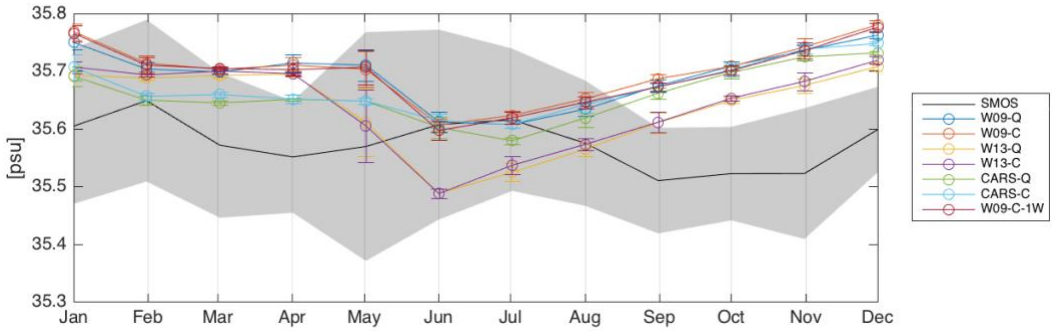

Figure II-7: Seasonal variability of SSS over the child grid area from SMOS and the 7 runs. The grey shaded area represents the standard deviation from the monthly climatology of the remote sensing observations.

		1W-WOA2009	WOA2009	CARS 2009	WOA 2013
$NRMSE_{xy}$	QSCAT		0.35	0.31	0.19
	COADS	0.37	0.38	0.36	0.22
$NRMSE_t$	QSCAT		0.38	0.31	0.29
	COADS	0.39	0.40	0.33	0.30

Table II-3: SSS $NRMSE_{xy}$ and $NRMSE_t$ values calculated for the 7 numerical implementations.

II.3.3.Surface geostrophic Kinetic Energy

To investigate the surface dynamics within the archipelago, we first compute KE_g. KE_g annual mean from AVISO is high north of the islands (i.e. from the equator) and weakens southward (Figure II-8a). This spatial distribution is reproduced in the 7 simulations although some differences appear in KE_g amplitude (Figure II-8b-h). Indeed, the energy in the simulations is enhanced when the spatial resolution of both boundary conditions and surface forcing increase. The KE_g grows with increased spatial resolution. The differences between the model outputs and the remote sensing derived KE_g are large in comparison with those of the thermohaline

parameters. According to the $NRMSE_{xy}$, the simulations forced with WOA 2013 data are the closest to AVISO with an index equal to 36.36 % for the one with boundary condition from COADS (Table II-4). The simulations forced with WOA 2009 differ the most with a $NRMSE_{xy}$ = 58.63 % mainly due to a too low production of energy. The standard deviation of energy is elevated where KE_g is already high (Figure II-9b-h). The inter-annual variability of the initial satellite dataset allows a high spatial variability of the KE_g (Figure II-8a). Simulations using WOA 2009 and CARS 2009 present low spatial variability while simulations using WOA 2013 present a high spatial variability on the Marquesas archipelago, and particularly south-westward the islands.

The seasonality of the AVISO KE_g is weak but with a strong variability (Figure II-10). The seasonal variabilities of KE_g in simulations built with WOA 2009 and CARS 2009 are weak both in values and amplitudes. Contrastingly, simulations built with WOA 2013 exhibit a stronger KE_g, even exceeding the AVISO one from May to August. Finally, when considering the $NRMSE_t$, the seasonal variability from simulations built with CARS 2009 are the closest to AVISO (~30 %, Table II-4). Differences induced by the different surface forcings (i.e., COADS *vs*. QSCAT) are weak when considering the $NRMSE_{xy}$ and $NRMSE_t$ which are substantially close for all the simulations.

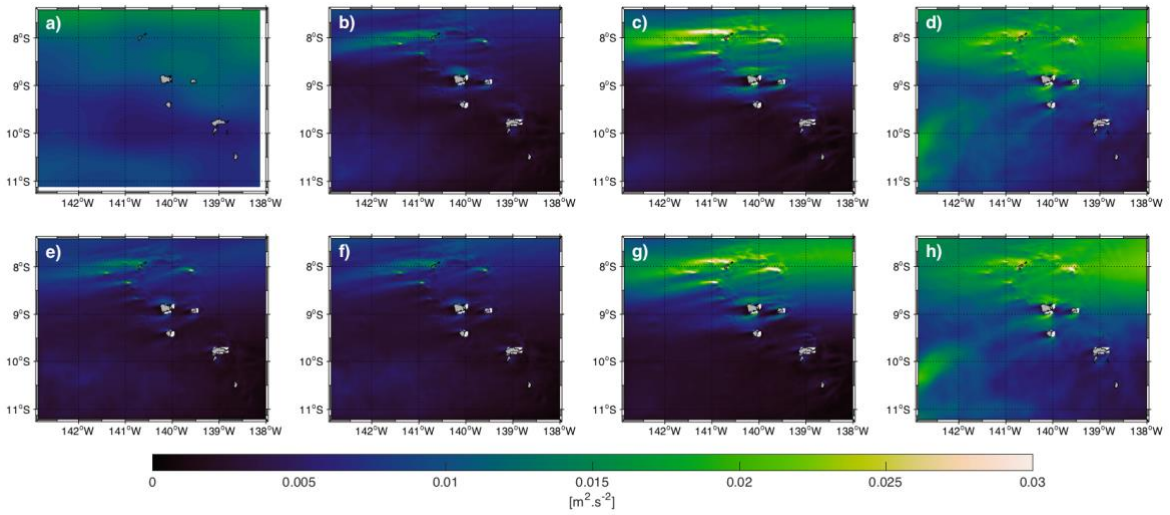

Figure II-8: Mean KE_g over the child grid area from (a) AVISO (time averaged from 1993 to 2016), (b) W09-Q, (c) CARS-Q, (d) W13-Q, (e) W09-C-1W, (f) W09-C, (g) CARS-C and (h) W13-C. Model outputs are time-averaged over year 4 to 10.

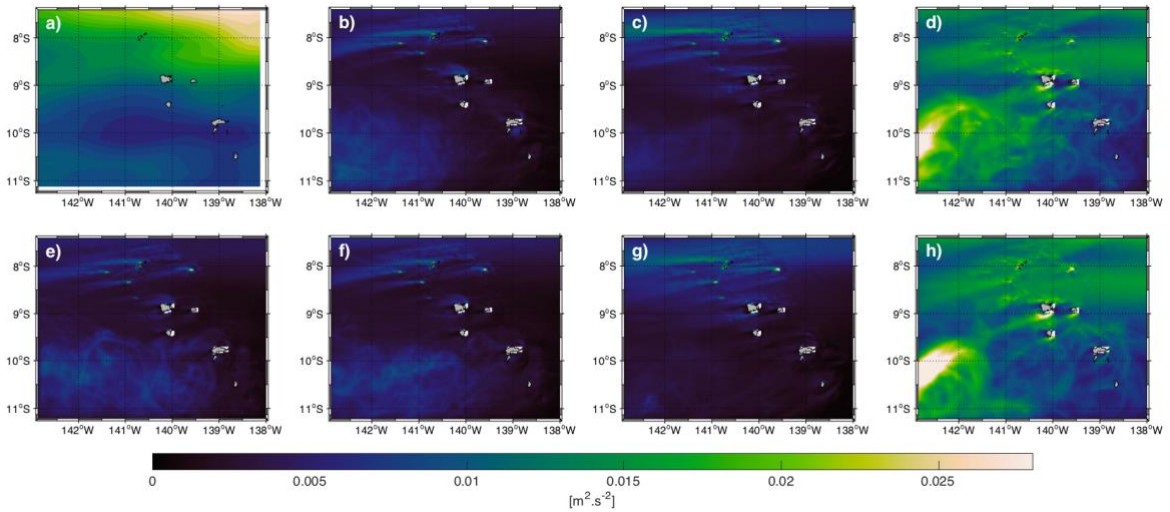

Figure II-9: Standard deviations of KE_g over the child grid area from (a) AVISO (1993 to 2016), (b) W09-Q, (c) CARS-Q, (d) W13-Q, (e) W09-C-1W, (f) W09-C, (g) CARS-C and (h) W13-C (for year 4 to 10).

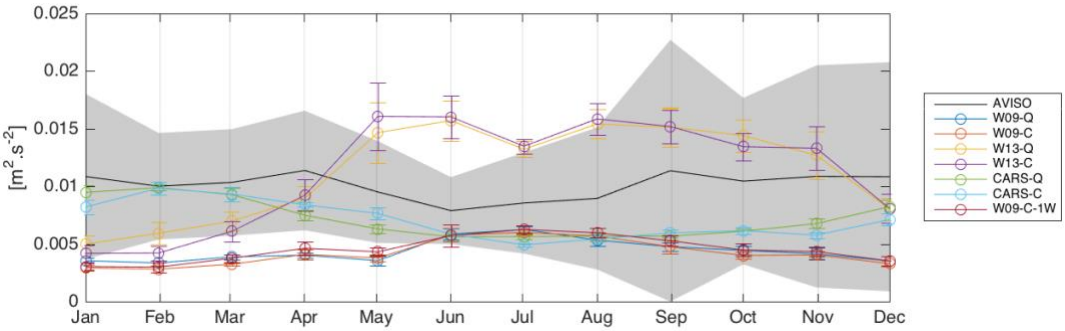

Figure II-10: Seasonal variability of KE_g over the child grid area from AVISO and the 7 runs. The grey shaded area represents the standard deviation from the monthly climatology of the remote sensing observations.

		1W-WOA2009	WOA2009	CARS 2009	WOA 2013
$NRMSE_{xy}$	QSCAT		58.00	53.49	36.72
	COADS	55.20	58.63	52.90	36.36
$NRMSE_t$	QSCAT		59.35	32.36	46.22
	COADS	58.25	61.48	33.61	51.15

Table II-4: KE_g $NRMSE_{xy}$ and $NRMSE_t$ values calculated for the 7 numerical implementations.

II.3.4.Surface geostrophic Eddy Kinetic Energy

An important feature of currents encountering oceanic islands is the generation of turbulent flow. Here, we investigate the eddy activity by computing the EKE_g. As for KE_g, the annual mean and standard deviations of EKE_g from AVISO are strong in the northern and south-western parts of the archipelago (Figure II-11a and Figure II-12a). The EKE_g annual means from simulations using WOA 2009 and CARS 2009 at their boundaries are extremely weak (<20 $cm^2.s^{-2}$), except in the south-westward part of the archipelago, when compared with satellite data (Figure II-11b-c, e-g). They strongly differ from AVISO with the highest $NRMSE_{xy}$ reaching up to 82.80 % for the simulation with CARS boundary conditions and forced by COADS (Table II-5). Contrastingly, the simulations using WOA 2013 allow the generation of EKE_g northward and south-westward the Marquesas, but also leeward the islands (Figure II-11d, h). These simulations are the closest to AVISO with $NRMSE_{xy}$ = 31.65 % for the simulation W13-C while $NRMSE_{xy}$ is higher than 75.09 % for simulations using WOA 2009 and CARS.

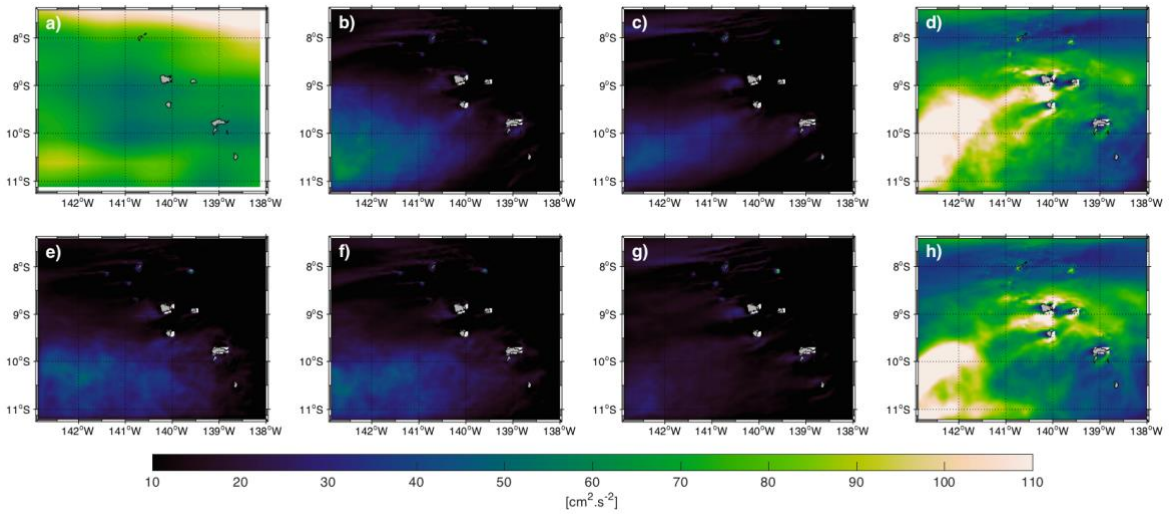

Figure II-11: Mean EKE_g over the child grid area from (a) AVISO (time averaged from 1993 to 2016), (b) W09-Q, (c) CARS-Q, (d) W13-Q, (e) W09-C-1W, (f) W09-C, (g) CARS-C and (h) W13-C. Model outputs are time averaged over year 4 to 10.

EKE_g is about 80 $cm^2.s^{-2}$ all year round with a weak seasonality but a strong spatial variability, that increases during austral spring and summer (Figure II-13). Here again, both simulations forced with WOA 2013 present the closest seasonality to AVISO with $NRMSE_t$ values equal

to 34.90 % and 31.65 % for W13-Q and W13-C, respectively (Table II-5). Even if the seasonality in W13 simulations is higher than in satellite observations, it remains in the range of the AVISO rms, while other simulations present low EKE_g all over the year with high $NRMSE_t$ up to 85 %.

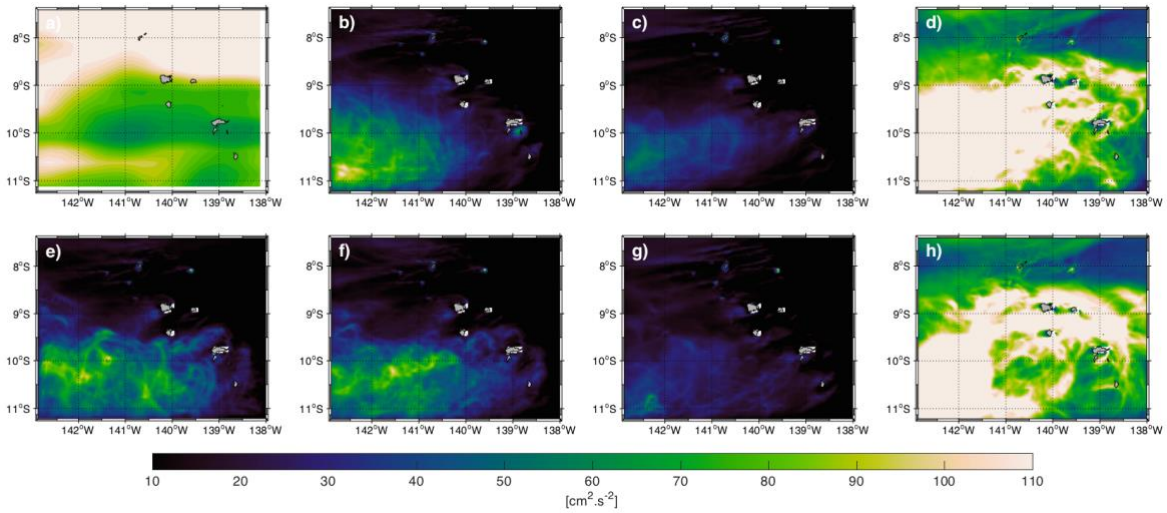

Figure II-12: Standard deviations of EKE_g over the child grid area from (a) AVISO (1993 to 2016), (b) W09-Q, (c) CARS-Q, (d) W13-Q, (e) W09-C-1W, (f) W09-C, (g) CARS-C and (h) W13-C (for year 4 to 10).

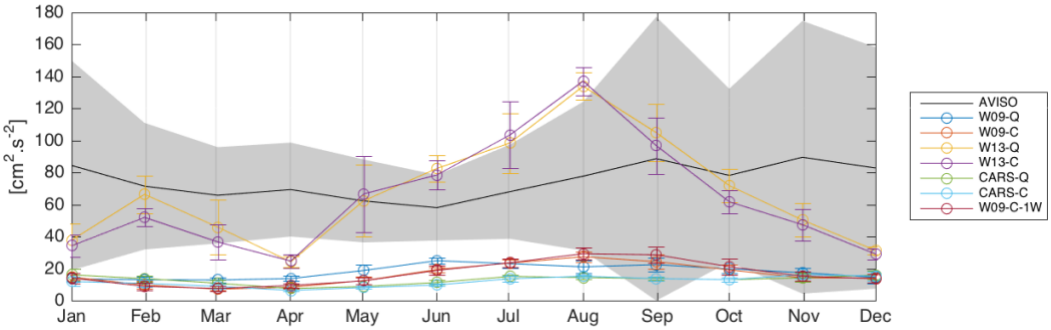

Figure II-13: Seasonal variability of EKE_g over the child grid area from AVISO and the 7 runs. The grey shaded area represents the standard deviation from the monthly climatology of the remote sensing observations.

		1W-WOA2009	WOA2009	CARS 2009	WOA 2013
$NRMSE_{xy}$	QSCAT		77.27	81.30	34.90
	COADS	75.09	78.33	82.80	31.65
$NRMSE_t$	QSCAT		77.51	83.53	45.46
	COADS	78.61	79.55	84.75	48.87

Table II-5: EKE_g $NRMSE_{xy}$ and $NRMSE_t$ values calculated for the 7 numerical implementations.

II.4. Discussion

Results from the 7 ROMS simulations set up with several initial/lateral boundary conditions and surface forcings have been compared with available satellite observations to determine the most suitable numerical implementation. We used spatial and temporal indexes to quantify the differences between ROMS and satellite observations.

The climatological boundary conditions used to set up the different simulations (i.e., monthly temperature and salinity 3D fields) have a direct impact on the ROMS thermohaline outputs. Particularly, forcing database and their spatial resolution can explain the differences observed in the spatial patterns of the model outputs (Figure II-2 and Figure II-5). The SST time series from runs using CARS 2009 and WOA 2013 present the largest differences with remote sensing data (Figure II-4). As seen in the Results section, simulations using CARS products present a delay of one month. Yet, SST in the archipelago from the initial CARS database also presents this 1-month delay comparing to AVHRR SST (not shown). This means that this lag is connected to the CARS product itself. Differences are also observed during May and June with a cooling observed in the runs forced with WOA 2013. This is induced by the high KE_g observed at the same period, probably indicating an incursion of cold waters from the north (Figure II-4 and Figure II-10).

The Marquesas archipelago is located between the fresh Pacific Equatorial Water [*Emery*, 2001] in the north and the saltier South Pacific Tropical Water [*O'Connor et al.*, 2005] in the south, as seen in Figure II-5. The temporal variation of these two water masses may explain the pattern of the standard deviation obtained in Figure II-6. When comparing seasonality of SSS from ROMS with ISAS13 *in situ* measurements (product based on Argo profiling floats), both are well correlated (not shown). This result was expected since Argo data are included in WOA and CARS products. But the comparison of SSS seasonal variability from ROMS and remote sensed data shows different patterns, likely highlighting the coarse spatial resolution of remote sensing in such specific localized areas (Figure II-7). In the second half of the year, SSS from

model outputs all presents a linear increase probably induced by the ROMS dynamics. Indeed, the SSS from WOA 2009, 2013 and CARS 2009 do not present this pattern.

Martinez and Maamaatuaiahutapu (2004) reported that surface currents are correlated with Chl increase in the Marquesas archipelago so that it is particularly important to investigate the robustness of the dynamical parameters. Besides, Kersalé et al. (2011) demonstrated the need of to take into account the cumulative effect of three forcings (wind, inflow current and topography) to correctly reproduce the mesoscale circulation around the Hawaiian archipelago. Here, we show that the used boundary conditions induce large differences on dynamical parameters such as KE_g and EKE_g. Particularly, the higher the resolution is, the higher the energy produced. A coarser topography of the Marquesas islands was also tested (not shown). In that case, the topography spatial resolution was not sufficient to let Ua Huka and Ua Pou emerge and hence no wake was observed leeward these islands. In the 7 implementations presented here, the smallest islands such as Eiao and Fatu Hiva did not emerged either, highlighting the need to use an even finer topography to model more realistic dynamics.

As previously mentioned, the SEC is the main current entering the area of the Marquesas archipelago. On the northern part of the area, KE_g is mainly induced by this current (Figure II-8). At the open boundaries, ROMS simulations are forced by geostrophic currents induced by modeled larger scale circulation while at the surface, wind forcing induces Ekman transport. The effect of the boundary conditions on the surface inflow current is here investigated by computing the latitudinal gradient of density at the eastern boundary where the SEC enters the parent grid for the month of January (Figure II-14). Since the WOA 2009 data have the lowest spatial resolution (1°), its corresponding density gradient is small. On the other hand, WOA 2013, with the highest resolution (1/4°), presents the highest density gradient. This induces a high input of surface KE_g from geostrophic current with WOA 2013 boundary conditions. In the same way, this dataset with an eddy permitting resolution enhances the fine scale dynamics and particularly the surface EKE_g within the archipelago (Figure II-11). Furthermore, the intensification of the SEC induced by the WOA 2013 boundary conditions generates an intense island wake.

The different ROMS simulations of the present study highlight large differences in the thermohaline and dynamical structures induced by the different boundary conditions used. While the spatial resolution of COADS is not sufficient to consider the presence of the Marquesas Islands, spatial patterns start appearing when using QSCAT winds to force ROMS [*Martinez et al.*, 2009]. However, the use of either of these two surface forcings only weakly impact the model outputs. Nevertheless, Dong and McWilliams (2007) and Jiménez et al.

(2008) demonstrated that wind can play a key role in island wakes. Indeed the wind curl generated leeward the islands can act as a source of vorticity for eddy generation. In our case, the Marquesas islands have diameters around 25 km. Both wind products used here are too coarse spatially to adequately reproduce the atmospheric circulation, explaining their close results. Nonetheless, Calil et al. (2008) showed that higher resolution wind forcing produce substantially more realistic EKE patterns. Hence, despite our results not finding a clear advantage at using QSCAT, we advise, in order to investigate physical processes in an archipelago with small islands such as the Marquesas archipelago, to use the wind product with the highest resolution, here QSCAT.

To investigate the maximum possibilities for the best simulation, we ran both 1-way and 2-way methods with the coarser forcing. As seen in all figures according to the $NRMSE_{xy}$ and $NRMSE_t$, results from the child grid in W09-C-1W and W09-C are practically identical. Indeed, most of the differences are observed in the parent coarser grid since the 2-way method uses the child grid results to improve the child/parent interface (not shown).

Otherwise, our results suggest that the overall best agreement between the remote sensing observations and the model outputs are obtained when the boundary conditions are calculated from the more recent, higher resolution climatology WOA2013 and the wind forcing provided by the higher resolution QSCAT field.

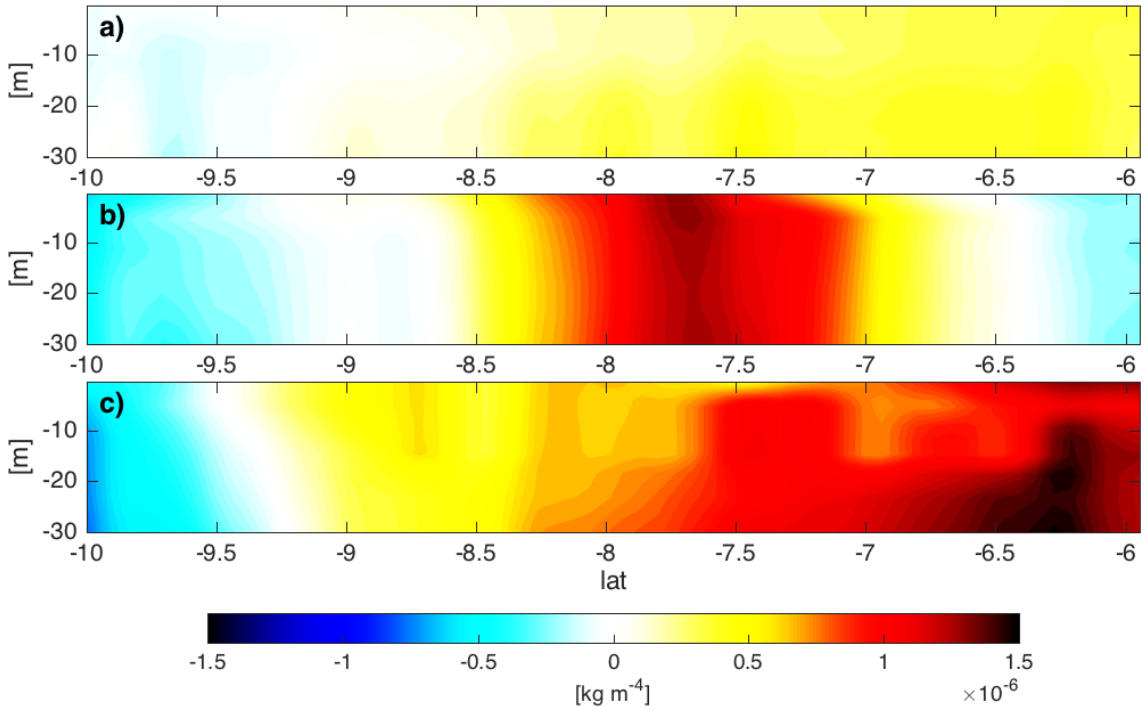

Figure II-14: Latitudinal gradient of density in January at the eastern boundary of the parent grid for (a) WOA 2009, (b) CARS 2009 and (c) WOA 2013.

II.5. Conclusion

Modeling the fine scale dynamics around steep and small islands such as the Marquesas archipelago is a challenge. Indeed, very few measurements are available around these isolated islands and the spatial resolutions of global circulation models are too coarse to investigate fine-scale dynamical processes. In this study, we ran 7 different simulations and compare them with independent remote sensing data to determine the most realistic simulation. We used indexes ($NRMSE_{xy}$ and $NRMSE_t$) to quantify the differences between model results and observations. For the thermohaline parameters, all model outputs reveal annual mean and seasonal variability of SST and SSS consistent with satellite observations. But dynamical parameters such as KE_g and EKE_g may differ not negligibly from one simulation to another. The largest differences are observed between runs using different boundary conditions. Comparing the model outputs, the higher resolution of WOA 2013 induces higher density gradient along latitude and inflow currents at the eastern child grid boundary. This implies a more realistic level of energy for the W13 simulations. However, simulations using different surface wind forcings exhibit similar results, indicating that the resolutions of the wind products (QSCAT and COADS) are not sufficient to properly consider the impact of these islands on the atmospheric circulation.

QSCAT being the most recent product and having a higher resolution than COADS, W13-Q is recommended, among the 7 ones presented here, as the best configuration to investigate dynamical processes in the Marquesas archipelago.

This study is the first step in the investigation of the Marquesas IME. It allows studying the fine scale dynamics of the islands wake [*Raapoto et al.*, 2018] and to lay the foundation for an in-depth determination of the physical processes potentially at the origin of the biological enhancement. A coupled physical-biogeochemical simulation using W13-Q is actually under way to further investigate the processes at the origin of the Marquesas biological enhancement.

Acknowledgements

We thank the government of French Polynesia for the financial support of the moana-maty project (convention 6841/MTS) including the PhD grant of H. Raapoto. We also thank the OSU Pytheas that provided the cluster support.

References du Chapitre II

Andrade, I., Sangrà, P., Hormazabal, S., Correa-Ramirez, M., 2014. Island mass effect in the Juan Fernández Archipelago (33°S), Southeastern Pacific. Deep. Res. Part I Oceanogr. Res. Pap. 84, 86–99. doi:10.1016/j.dsr.2013.10.009

Antonov, J., Seidov, D., Boyer, T., Locarnini, R., 2010. World Ocean Atlas 2009, vol. 2: Salinity, edited by: Levitus. S., NOAA Atlas NESDIS.

Beckmann, A., Haidvogel, D.B., 1993. Numerical Simulation of Flow around a Tall Isolated Seamount. Part I: Problem Formulation and Model Accuracy. J. Phys. Oceanogr. doi:10.1175/1520-0485(1993)023<1736:NSOFAA>2.0.CO;2

Caldeira, R.M.A., Groom, S., Miller, P., Pilgrim, D., Nezlin, N.P., 2002. Sea-surface signatures of the island mass effect phenomena around Madeira Island, Northeast Atlantic. Remote Sens. Environ. 80, 336–360. doi:10.1016/S0034-4257(01)00316-9

Calil, P.H.R., Richards, K.J., Jia, Y., Bidigare, R.R., 2008. Eddy activity in the lee of the Hawaiian Islands. Deep. Res. Part II Top. Stud. Oceanogr. 55, 1179–1194. doi:10.1016/j.dsr2.2008.01.008

Chelton, D.B., deSzoeke, R. a., Schlax, M.G., El Naggar, K., Siwertz, N., 1998. Geographical Variability of the First Baroclinic Rossby Radius of Deformation. J. Phys. Oceanogr. 28, 433–460. doi:10.1175/1520-0485(1998)028<0433:GVOTFB>2.0.CO;2

da Silva, A.M., Young, C.C., Levitus, S., 1994. Atlas of surface marine data 1994, vol. 4, Anomalies of fresh water fluxes. Noaa atlas nesdis 9, 308.

Debreu, L., Blayo, E., 2008. Two-way embedding algorithms: A review. Ocean Dyn. 58, 415–428. doi:10.1007/s10236-008-0150-9

Debreu, L., Marchesiello, P., Penven, P., Cambon, G., 2012. Two-way nesting in split-explicit ocean models: Algorithms, implementation and validation. Ocean Model. 49–50, 1–21. doi:10.1016/j.ocemod.2012.03.003

Dietrich, D.E., Bowmanb, M.J., Lin, C.A., Mestas-nunezd, A., 1996. Numerical studies of small island wakes in the ocean. Geophys. Astrophys. Fluid Dyn. 83, 195–231. doi:10.1080/03091929608208966

Dong, C., McWilliams, J.C., 2007. A numerical study of island wakes in the Southern California Bight. Cont. Shelf Res. 27, 1233–1248. doi:10.1016/j.csr.2007.01.016

Dong, C., McWilliams, J.C., Shchepetkin, A.F., 2007. Island Wakes in Deep Water. J. Phys. Oceanogr. 37, 962–981. doi:10.1175/JPO3047.1

Doty, M.S., Oguri, M., 1956. The Island Mass Effect. ICES J. Mar. Sci.

doi:10.1093/icesjms/22.1.33

Emery, W.J., 2001. Water Types and Water Masses. Encycl. Ocean Sci. Second Ed. doi:10.1006/rwos.2001.0108

Hasegawa, D., Lewis, M.R., Gangopadhyay, a., 2009. How islands cause phytoplankton to bloom in their wakes. Geophys. Res. Lett. 36, 1–4. doi:10.1029/2009GL039743

Hasegawa, D., Yamazaki, H., Ishimaru, T., Nagashima, H., Koike, Y., 2008. Apparent phytoplankton bloom due to island mass effect. J. Mar. Syst. 69, 238–246. doi:10.1016/j.jmarsys.2006.04.019

Hasegawa, D., Yamazaki, H., Lueck, R.G., Seuront, L., 2004. How islands stir and fertilize the upper ocean. Geophys. Res. Lett. 31, 1–4. doi:10.1029/2004GL020143

Hastings, D.A., Emery, W.J., 1992. The advanced very high resolution radiometer (AVHRR): a brief reference guide. Photogramm. Eng. Remote Sensing. 58, 1183–1188.

Heywood, K.J., Stevens, D.P., Bigg, G.R., 1996. Eddy formation behind the tropical island of Aldabra. Deep. Res. Part I Oceanogr. Res. Pap. 43, 555–578. doi:10.1016/0967-0637(96)00097-0

Jiménez, B., Sangrà, P., Mason, E., 2008. A numerical study of the relative importance of wind and topographic forcing on oceanic eddy shedding by tall, deep water islands. Ocean Model. 22, 146–157. doi:10.1016/j.ocemod.2008.02.004

Kersalé, M., Doglioli, a. M., Petrenko, a. a., 2011. Sensitivity study of the generation of mesoscale eddies in a numerical model of Hawaii islands. Ocean Sci. 7, 277–291. doi:10.5194/os-7-277-2011

Legeckis, R., Brown, C.W., Bonjean, F., Johnson, E.S., 2004. The influence of tropical instability waves on phytoplankton blooms in the wake of the Marquesas Islands during 1998 and on the currents observed during the drift of the Kon-Tiki in 1947. Geophys. Res. Lett. 31, 1–4. doi:10.1029/2004GL021637

Locarnini, R.A., Mishonov, A. V., Antonov, J.I., Boyer, T.P., Garcia, H.E., Baranova, O.K., Zweng, M.M., Paver, C.R., Reagan, J.R., Johnson, D.R., Hamilton, M., Seidov, D., 2013. World Ocean Atlas 2013. Vol. 1: Temperature. S. Levitus, Ed.; A. Mishonov, Tech. Ed.; NOAA Atlas NESDIS 73, 40. doi:10.1182/blood-2011-06-357442

Locarnini, R., Mishonov, A., Antonov, J., Boyer, T., Garcia, H., 2010. World Ocean Atlas 2009, vol. 1, Temperature, edited by S. Levitus, 184 pp. US Gov. Print. Off.

Lungu, T., Callahan, P.S., 2006. QuikSCAT science data product user's manual: Overview and geophysical data products. D-18053-Rev A, version 3, 91.

Marchesiello, P., McWilliams, J.C., Shchepetkin, A., 2001. Open boundary conditions for long-

term integration of regional oceanic models. Ocean Model. 3, 1–20. doi:10.1016/S1463-5003(00)00013-5

Martinez, E., Ganachaud, A., Lefevre, J., Maamaatuaiahutapu, K., 2009. Central south pacific thermocline water circulation from a high-resolution ocean model validated against satellite data: seasonal variability and el niño 1997-1998 influence. J. Geophys. Res. Ocean. 114, 1–16. doi:10.1029/2008JC004824

Martinez, E., Maamaatuaiahutapu, K., 2004. Island mass effect in the Marquesas Islands: Time variation. Geophys. Res. Lett. 31, 1–4. doi:10.1029/2004GL020682

Maury, R.C., Guille, G., Hervé, G., Catherine, C., Legendre, C., Rossi, P., Blais, S., Pallares, C., Sébastien, D., Marabal, A., 2014. Géologie des Marquises : des volcans boucliers intra-océaniques effondrés issus d ' un point chaud atypique Géologie des Marquises : des volcans boucliers intra-océaniques effondrés issus d ' un point chaud atypique. Géologie la Fr. 1, 111–135.

O'Connor, B.M., Fine, R.A., Olson, D.B., 2005. A global comparison of subtropical underwater formation rates. Deep. Res. Part I Oceanogr. Res. Pap. 52, 1569–1590. doi:10.1016/j.dsr.2005.01.011

Olmedo, E., Martinez, J., Umbert, M., Hoareau, N., Portabella, M., Ballabrera-Poy, J., Turiel, A., 2016. Improving time and space resolution of SMOS salinity maps using multifractal fusion. Remote Sens. Environ. 180, 246–263. doi:10.1016/j.rse.2016.02.038

Pattiaratchi, C., James, A., Collins, M., 1987. Island wakes and headland eddies: A comparison between remotely sensed data and laboratory experiments. J. Geophys. Res. Ocean. 92, 783–794. doi:10.1029/JC092iC01p00783

Penven, P., Marchesiello, P., Debreu, L., Lefèvre, J., 2007. Software tools for pre- and post-processing of oceanic regional simulations. Environ. Model. Softw. 23, 660–662. doi:10.1016/j.envsoft.2007.07.004

Raapoto, H., Martinez, E., Petrenko, A., Doglioli, A.M., Maes, C., 2018. Modeling the Wake of the Marquesas Archipelago. J. Geophys. Res. Ocean. doi:10.1002/2017JC013285

Ridgway, K.R., Dunn, J.R., Wilkin, J.L., 2002. Ocean interpolation by four-dimensional weighted least squares - Application to the waters around Australasia. J. Atmos. Ocean. Technol. 19, 1357–1375. doi:10.1175/1520-0426(2002)019<1357:OIBFDW>2.0.CO;2

Shchepetkin, A.F., McWilliams, J.C., 2005. The regional oceanic modeling system (ROMS): a split-explicit, free-surface, topography-following-coordinate oceanic model. Ocean~Model. 9, 347–404. doi:10.1016/j.ocemod.2004.08.002

Shchepetkin, A.F., McWilliams, J.C., 2003. A method for computing horizontal pressure-

gradient force in an oceanic model with nonaligned vertical coordinate. J. Geophys. Res. 108, 1–34. doi:10.1029/2001JC001047

Signorini, S.R., McClain, C.R., Dandonneau, Y., 1999. Mixing and phytoplankton bloom in the wake of the Marquesas Islands. Geophys. Res. Lett. 26, 3121–3124. doi:10.1029/1999GL010470

Smith, W.H., Sandwell, D., 1997. Global Sea Floor Topography from Satellite Altimetry and Ship Depth Soundings. Science (80-.). 277, 1956–1962. doi:10.1126/science.277.5334.1956

Stegner, A., 2014. Oceanic Island Wake Flows in the Laboratory, in: von Larcher, T., Williams, P.D. (Eds.), Modeling Atmospheric and Oceanic Flows: Insights from Laboratory Experiments and Numerical Simulations. John Wiley & Sons,Inc., Hoboken, New Jersey, pp. 265–276. doi:10.1002/9781118856024.ch14

Talley, L.D., 2002. Salinity Patterns in the Ocean. Earth Syst. Phys. Chem. Dimens. Glob. Environ. Chang.

Teinturier, S., Stegner, A., Didelle, H., Viboud, S., 2010. Small-scale instabilities of an island wake flow in a rotating shallow-water layer. Dyn. Atmos. Ocean. 49, 1–24. doi:10.1016/j.dynatmoce.2008.10.006

Von Karman, T., Sears, W.R., 1938. Airfoil Theory for Non-Uniform Motion. J. Aeronaut. Sci. 5, 379–390. doi:10.2514/8.674

Wolanski, E., Imberger, J., Heron, M.L., 1984. Island wakes in shallow waters. J. Geophys. Res. 89, 553–569. doi:10.1029/JC093iC02p01335

Yan, X., Ho, C., Zheng, Q., Klemas, V., 1992. Temperature and Size Variabilities of the Western Pacific Warm Pool. Science (80-.). 258, 1643–1645.

Zweng, M.M., Reagan, J.R., Antonov, J.I., Mishonov, A.V., Boyer, T.P., Garcia, H.E., Baranova, O.K., Johnson, D.R., Seidov, D., Bidlle, M.M., 2013. World Ocean Atlas 2013, Volume 2: Salinity, NOAA Atlas NESDIS. doi:10.1182/blood-2011-06-357442

Conclusion du Chapitre II

Au travers de cette étude, nous avons révélé l'importance que pouvait avoir différents forçages en entrée du modèle sur la dynamique océanique de l'archipel des Marquises. Bien que toutes les simulations mises en place montrent de très bonnes performances pour les structures moyennes et la variabilité saisonnière des paramètres thermohalins, de grandes différences sont notables pour les paramètres dynamiques. L'utilisation des produits de forçages océaniques et atmosphériques à plus haute résolution spatiale permettent la modélisation de courants de surface ayant une énergie du même ordre de grandeur que celle des observations satellites. Cependant, il est à noter que les courants marins mesurés par satellite restent l'un des paramètres les plus difficiles à quantifier et peuvent présenter une incertitude assez grande. Notre analyse montre donc que les forçages ayant la plus haute résolution spatiale (i.e. WOA 2013 et QuikSCAT) permettent d'obtenir les sorties de modèle les plus proches des observations satellites. Cette phase de validation/comparaison est donc une étape essentielle pour la suite de l'étude de l'effet d'île qui a lieu dans l'archipel des Marquises.

Cette analyse qui représente la première partie de ce travail de thèse a permis de mettre en place une base solide pour une étude plus approfondie des processus physiques impliqués dans l'archipel. Comme indiqué précédemment, les nutriments sont essentiels pour le développement du phytoplancton. L'écoulement des courants autour de petites îles océaniques tel que les îles Marquises peuvent générer des circulations complexes dans leur sillage. Des turbulences sont générées et peuvent permettre aux eaux profondes, plus riches en sels nutritifs, de remonter jusqu'à la couche euphotique. Ainsi, dans le chapitre suivant, une étude plus détaillée de la dynamique dans l'archipel des Marquises a été réalisée. Un intérêt particulier a été porté sur l'un des processus physiques pouvant entraîner un enrichissement biologique : la génération et la propagation de tourbillons dans l'archipel. Cette étude a été réalisée à partir de la simulation la plus réaliste déterminée de ce chapitre II.

Chapitre III

Modeling the wake of the Marquesas archipelago

H. Raapoto[1], E. Martinez[1], A. Petrenko[2], A. M. Doglioli[1] and C. Maes[3]

[1] IRD, UPF, ILM, Ifremer, Écosystèmes Insulaires Océaniens (EIO), Tahiti, French Polynesia.

[2] Aix Marseille Univ, Université de Toulon, CNRS, IRD, OSU PYTHEAS, Mediterranean Institute of Oceanography MIO, UM 110, 13288, Marseille, Cedex 09, France.

[3] Université Brest, Ifremer, CNRS, IRD, Laboratoire d 'Océanographie Physique et Spatiale (LOPS), IUEM, Brest, France.

Publié dans *Journal of Geophysical Research: Oceans*

Raapoto, H., Martinez, E., Petrenko, A., Doglioli, A. M., & Maes, C. (2018). Modeling the wake of the Marquesas archipelago. *Journal of Geophysical Research: Oceans, 123*(2), 1213-1228.

RESUME

Dans cette étude pionnière, un modèle à haute résolution (~2,5 km) a été mis en place pour étudier la dynamique à fine échelle dans l'archipel des Marquises. La robustesse de la configuration est évaluée en comparant les sorties du modèle avec des mesures satellites et in situ. Nos résultats indiquent la présence d'eaux chaudes derrière plusieurs îles avec la génération d'énergie cinétique tourbillonnaire (*EKE*) sur leurs flancs. Une analyse des conversions d'énergies a été réalisée à l'échelle de l'archipel et révèle une contribution du vent, ainsi que des instabilités baroclines et barotropes dans la variabilité de *l'EKE*. L'utilisation d'un algorithme de détection automatique des tourbillons basé sur la géométrie de l'écoulement a permis de révéler la génération de tourbillons cycloniques et anticycloniques dans le sillage des plus grandes îles. L'activité tourbillonnaire dans l'archipel est maximale durant l'hiver austral ainsi que celle du stress du vent et de *l'EKE*. La majeure partie des tourbillons générés ont un rayon entre 20 et 30 km avec une dominance de tourbillons cycloniques. Des vitesses verticales importantes, associées à la séparation de l'écoulement induite par la topographie, sont observées à proximité des îles. Les tourbillons piégeant les eaux côtières sont advectés au large, dans le sillage des îles. L'ensemble de cette dynamique à fine échelle pourrait expliquer le fort enrichissement biologique dans l'archipel.

ABSTRACT

In this study, a high-resolution (~2.5 km) numerical model was set up to investigate the fine-scale activity within the region of the Marquesas archipelago. This has never been performed before. The robustness of the model results is assessed by comparison with remote sensing and in situ observations. Our results highlight regions of warm waters leeward of the different islands with high eddy kinetic energy (*EKE*) on their sides. The analysis of energy conversion terms reveals contributions to *EKE* variability by wind, baroclinic and barotropic instabilities. The use of a geometry-based eddy detection algorithm reveals the generation of cyclonic and anticyclonic eddies in the wake of the largest islands, with both an inshore and offshore effect. Maximum eddy activity occurs in austral winter following the seasonality of both wind stress and *EKE* intensity. Most eddies have a radius between 20 and 30 km and are generally cyclonic rather than anticyclonic. Significant vertical velocities are observed in the proximity of the islands, associated with topographically-induced flow separation. Eddy trapping inshore waters are advected offshore in the wake of the islands. The overall influence of these fine-scale dynamics could explain the strong biological enhancement of the archipelago.

III.1. Introduction

The Marquesas archipelago (144°W-137°W; 8°S-11°S) is located in the northern part of French Polynesia, central South Pacific, where the South Equatorial Current (SEC) flows south-westward (Figure III-1a). It is composed by a dozen of small volcanic islands with mountains up to 1224 m, rugged steep cliffs and no surrounding coral reefs (*Savanier et al.*, 2006; Figure III-1b). The main five islands are Nuku Hiva (339 km^2), Ua Pou (105 km^2) and Ua Huka (83 km^2) in the northern part of the archipelago, and Hiva Oa (320 km^2) and Fatu Hiva (85 km²) in the southern part. Despite their relatively small area coverage, a remarkable plume of chlorophyll-a (Chl, a proxy of phytoplankton biomass) can be observed leeward of the islands in the open ocean from satellite derived ocean color [*Signorini et al.*, 1999; *Martinez and Maamaatuaiahutapu*, 2004]. Such biological enhancement is referred to as an island mass effect (IME) [*Doty and Oguri*, 1956]. While several physical processes can be involved in the present IME, such as coastal upwelling, Ekman pumping, eddies or internal waves [*Heywood et al.*, 1990, 1996; *Barton*, 2001; *Sangrà et al.*, 2001; *Palacios*, 2002], the IME dominant mechanisms have not been elucidated yet for the Marquesas archipelago.

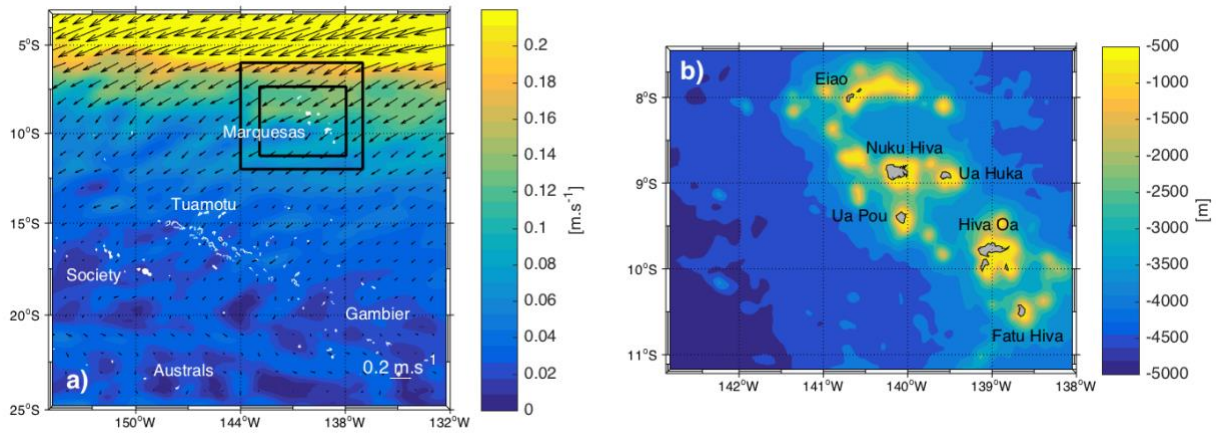

Figure III-1: (a) Mean surface current from the satellite derived Ocean Surface Current Analysis – Real time (OSCAR) product (time averaged over Oct-1992 to Jun-2015, in m s^{-1}) over French Polynesia. The islands are represented in white, as well as the name of the five archipelagos. The black boxes show the parent and child grids implemented in the ROMS configuration. (b) Bottom topography from the 2-arc minute topography/bathymetry dataset ETOPO2 (in m) around the archipelago used in the model configuration as well as the names of the main islands.

It is well known that oceanic currents encountering islands generate complex wakes. Several studies in other regions have assessed these island wakes and their forcing mechanisms using a remote-sensing [*Wolanksi et al.*, 1996; *DiGiacomo and Holt*, 2001], in situ data [*Hasegawa et al.*, 2004, 2008] or a modeling approach [*Dietrich et al.*, 1996; *Wolanksi et al.*, 1996; *Dong et al.*, 2007; *Jiménez et al.*, 2008; *Hasegawa et al.*, 2009]. An important distinction has to be made between shallow- and deep-water wakes. Shallow-water wakes occur when considering islands in shallow shelves or estuaries where near-shore bottom drag acts as the primary source of vorticity generation [*Wolanksi et al.*, 1996; *Alaee et al.*, 2004; *Neill and Elliott*, 2004]. Deep-water wakes occur leeward tall islands surrounding by a deep bathymetry - like in the Marquesas archipelago - where bottom influence can be neglected and topographic and wind forcing are the primary sources of vorticity generation. Topographic forcing refers to the detachment of the frictional layer around the island as a result of differential bottom stress imparted to the flow by the sloping sides of the island [*Dong et al.*, 2007]. Wind forcing refers to eddy generation as a consequence of Ekman pumping induced by wind shear in the island's wake [*Jiménez et al.*, 2008].

Eddy formation and propagation in island wakes could play a key role in the IME of the Marquesas archipelago. Indeed, a wind curl dipole has been reported in the archipelago [*Martinez et al.*, 2009] possibly forming oceanic cyclonic eddies and jets inducing an enrichment of the upper layer leeward the islands by mechanisms such as the ones proposed by *Hasegawa et al.* [2009] and *Andrade et al.* [2014]. Nevertheless, the previous studies on the Marquesas IME using satellite altimetry did not mention any eddy features [*Signorini et al.*, 1999; *Legeckis et al.*, 2004; *Martinez and Maamaatuaiahutapu*, 2004]. This is probably due to the coarseness of the Sea Level Anomaly (SLA) products used in these studies. However, some eddy activity does imprint the Sea Surface Temperature (SST). For example, on Nov. 17, 2015 (Figure III-2a) a SST dipole is observed leeward Nuku Hiva at (140.5W; 9°S), as well as a warm eddy further southwest, while a cool eddy is present at (141°W; 10.1°S) on Aug. 21, 2012 (Figure III-2b). In both cases, it is important to note that the size of the structures is of the same order than the island diameter (~30 km for Nuku Hiva). Such an eddy activity could possibly be at the origin of nutrient uplift from deep rich waters to the euphotic zone allowing the development of phytoplankton. Because the spatio-temporal resolution of satellite altimetry is too coarse to investigate the small scales of such aforementioned eddy activity around the Marquesas archipelago, recourse to high-resolution modeling taking into account the topographic forcing (i.e., the presence of the islands) has been done by the present study. Documenting the generation and characteristics of the oceanic eddies should be viewed as a

first step toward an explanation of the origin of the surface layer biological enrichment in this archipelago.

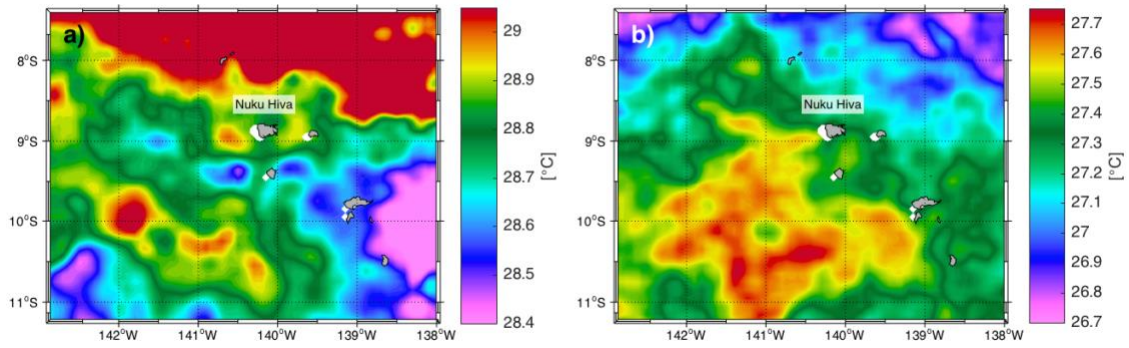

Figure III-2: SST (°C) from Geostationary Operational Environmental Satellite (GOES)/ Polar Operational Environmental Satellite (POES) in the Marquesas archipelago for (a) 2015-NOV-17 and (b) 2012-AUG-21.

The present work is organized as follows: Section 2 presents the data and the methodology. A comparison of the oceanic conditions between the model, satellite and *in situ* observations is performed in section 3. In this section, eddy properties generated leeward the islands are also characterized. Finally, section 4 concludes this study.

III.2. Data and Methods

III.2.1. Numerical model

Our model is based on the Regional Ocean Modeling System (ROMS)-AGRIF (Adaptive Grid Refinement in Fortran) code provided by *Debreu et al.* [2012] and *Penven et al.* [2007]. The ROMS model is a split-explicit, free surface and terrain-following vertical coordinate oceanic model [*Shchepetkin and McWilliams*, 2003; 2005]. The AGRIF version is especially suitable to study regional scale since it has the ability to manage an arbitrary number of fixed grids and embedding levels. We configure the two-way embedding procedure. It means that the parent grid provides the boundary conditions for the child grid, and that the solution of the child grid is used to improve the larger scale parent grid solution, allowing a smooth, continuous interfacing between grid levels [*Debreu and Blayo*, 2008; *Debreu et al.*, 2012]. Therefore, we defined two embedded grids: 1) the parent grid extends from 137°W to 144°W and 6°S to 12°S; 2) the child grid extends from 138°W to 143°W and 7.3°S to 11.3°S as shown in Figure III-1a.

The grid refinement rate is 3, implying a 1/15° (~7km) and 1/45° (~2.5 km) grid resolutions for the parent and child grids, respectively. This allows a sufficient sampling of the island topography and of the fine-scale dynamics, as the first baroclinic Rossby radius of deformation is about 120 km in this region according to *Chelton et al.* [1998]. The internal (external) time stepping is set to 3600 (600) sec for the parent grid and 1200 (200) sec for the child grid. Both grids have 32 vertical levels and the vertical s-coordinate is stretched for boundary layer resolution. The topography is derived from the 2' resolution ETOPO2 database provided by NOAA-NGDC [*Smith and Sandwell*, 1997]. The bathymetry field has been filtered to keep the slope parameter < 0.25 [*Beckmann and Haidvogel*, 1993]. The K-profile parameterization (KPP) vertical mixing scheme from *Large et al.* [1994] is used to parameterize vertical mixing processes.

All the external forcings of the ROMS simulations are based on monthly climatologies. At the surface, the heat and fresh water fluxes are extracted on a monthly ½° grid from the Comprehensive Ocean-Atmosphere dataset (COADS) [*da Silva et al.*, 1994]. The wind forcing is issued from the QuikSCAT monthly climatology calculated over 1999-2009, on a ¼° grid [*Lungu and Callahan*, 2006]. ROMS is connected to the lateral boundaries by an active, implicit and upstream-biased radiation condition [*Marchesiello et al.*, 2001]. The boundary conditions and initial state are based on the objectively analysed World Ocean Atlas 2013 (WOA13) monthly climatology on a ¼° grid [*Locarnini et al.*, 2013; *Zweng et al.*, 2013]. The inflow boundary conditions are nudged toward temperature, salinity, and geostrophic velocity fields. Following *Kersalé et al.*, [2011], the nudging timescale for inflow and outflow are set to 1 day and 1 yr for the tracer fields and 3 days and 1 yr for the momentum fields. The geostrophic velocity is referenced to the 1000 m depth. The explicit lateral viscosity is null all over the domain, except in the sponge layer. The width of the nudging border is 50 km and the maximum viscosity value for the sponge layer is set to 1000 $m^2\ s^{-1}$.

The high resolution ROMS simulation, hereafter referred to as W13Q, is run over 10 years with outputs averaged every 2 days. Integrated physical properties show that a statistical equilibrium is reached by the model after the first year of simulation. To avoid any impact of the spin up on the model output and to ensure the robustness of our findings, we decided to also entirely remove the third year and to focus our investigation on the outputs from year 4 to 10.

III.2.2. Datasets

We compared our numerical results with several datasets. The Moderate Resolution Imaging Spectroradiometer (MODIS) infrared SST measured from the Aqua satellite are available on a monthly basis with a spatial resolution of 4 km. We use the time period from July 2002 to June 2015 to compute the monthly climatology.

The 3-D monthly fields of temperature and salinity issued from the In Situ Analysis System (ISAS13) are based on Argo data [*Gaillard et al.*, 2016] and are available on a 0.5° grid from 2002 to 2012.

Monthly near surface current over 1992 to 2015 are obtained from the Ocean Surface Current Analysis – Real time (OSCAR) with a 1/3° spatial resolution [*Bonjean and Lagerloef*, 2002].

Finally we used reanalyzed currents from the global Hybrid Coordinate Ocean model and the Navy Coupled Ocean Data Assimilation (HYCOM+NCODA) [*Cummings and Smedstad*, 2013]. These velocity fields are available with a spatial resolution of 1/12.5° and a daily resolution from January 1st 2006 to December 31st 2012.

III.2.3. Non-dimensional numbers

The ocean dynamics in island wake is generally characterized by the recourse to non-dimensional numbers issued from geophysical fluid dynamics. The wake is typically controlled by the turbulent Reynolds number defined as:

$$Re = U_0 D/\nu$$

where U_0 is the unperturbed upstream velocity, D is the horizontal scale of the obstacle, and ν is the eddy viscosity [*Tomczak*, 1988]. To compute *Re* in the Marquesas Islands, we use an horizontal eddy viscosity value of $\nu = 100$ m^2 s^{-1} [*Heywood et al.*, 1990; *Jiménez et al.*, 2008]. In the archipelago, only the biggest island, Nuku Hiva, exhibits a Reynolds number ($Re \approx 50$) that exceeds the theoretical threshold of the Von Karman vortex street generation ($Re_{th} = 40$).

To consider the spatial scale and energy involved in island wake, we also consider the Burger number, representing the ratio between stratification and Earth's rotation, and defined as:

$$Bu = \left(\frac{R_d}{R}\right)^2$$

where R is the island radius and R_d the Rossby radius associated to the first baroclinic mode. Using the forcing data from WOA13, we found that the seasonality of R_d vary between120 and 130 km in the archipelago. When the island radius R is smaller than R_d ($Bu \geq 1$), a submesoscale

wake is generated with eddies having their radius in the order of R [*Stegner*, 2014]. This is always the case in the archipelago where the radius of the largest island is about 20 km.

Finally, we calculate the geometric shallow-water parameter $\alpha = \frac{h}{R}$, with h the mean thermocline depth. We obtained an alpha ranging between 0.01 and 0.03. These values are typical of mid-ocean isolated islands, such as Madeira [*Caldeira et al.*, 2002], Gran Canaria [*Sangrà et al.*, 2005] or Hawaii [*Calil et al.*, 2008], generating a deep-water wake.

III.2.4. Eddy detection and tracking

To detect eddies in our model experiment, the method based on the geometry of the flow field developed by *Nencioli et al.* [2010] is applied. This method is well established and used in several studies with different resolution [*Dong et al.*, 2012; *Liu et al.*, 2012; *Amores et al.*, 2013; *Mkhinini, N. et al.*, 2014]. It relies on the spatial definition of vortices defined as a region with a rotary flow around its center. In other words, a vortex is defined as a region with velocity vectors rotating around a center with a minimum speed. Its boundary is defined by the largest closed contour line of the local stream function around the center. The flexibility of the algorithm depends on two parameters: a, the number of grid points where the current increases, and b, the dimension of the area used to define the local minimum of velocity. These parameters set the minimum size of the detectable vortices and allow the algorithm to work on different grid resolution. Using the same protocol than *Nencioli et al.* [2010] and *Liu et al.* [2012], optimal performances of the algorithm have been obtained with $a = 2$; $b = 2$ for our model configuration and $a = 3$; $b = 2$ for the HYCOM reanalysis outputs.

Once eddies have been detected at each time step, we used the tracking method proposed by *Doglioli et al.* [2007] and *Nencioli et al.* [2010]: the position and sign of each eddy center are compared at successive time steps. An eddy track is identified when the eddy center at the next time step is found within a given searching area of the previous time step. The searching radius is the product of the averaged eddy center displacement speed and the time interval between two model outputs (i.e., 2 days). To avoid that eddies move further than the searching area within successive time steps (thus preventing track splitting), we added a constant of 20 cm s^{-1} corresponding to the eddy-center displacement speed and representing the mean velocity of the background current. Moreover, eddies with a shorter lifetime than 4 days are not considered to ensure the only detection of consistent structures only.

The dataset obtained after applying the detection includes: eddy center locations, eddy contours, polarities and radii. Time evolution of each eddy detected is also recorded and gives us information on their generation and ending.

III.2.5. Eddy Kinetic Energy budgets

The *EKE* is defined as the kinetic energy due to transient dynamic. Neglecting the vertical velocity contributions: $EKE = \frac{1}{2}(u'^2 + v'^2)$, where $u' = u - \bar{u}$ and $v' = v - \bar{v}$, with u and v the zonal and meridian components of the velocity at 10 m, $\bar{u}$ and $\bar{v}$ their temporal means from year 4 to 10. To consistently compare our numerical model results with the monthly satellite derived observations (OSCAR), we subsampled the W13Q current components at 10 m (u_m and v_m) by extracting one grid point every 5 grid points. Then, we used monthly averages to compute the monthly $EKE_m = \frac{1}{2}({u_m}'^2 + {v_m}'^2)$.

To quantify the relative importance of instability and eddy-mean interaction mechanisms on the *EKE* generation, we consider the different terms of energy budgets relative to the *EKE* generation [*Auad et al.*, 1991; *Marchesiello et al.*, 2003; *Liang et al.*, 2012]. The wind work, the barotropic and the baroclinic energy conversion [*Dong et al.*, 2007; *Halo et al.*, 2014; *Hristova et al.*, 2014; *Sun et al.*, 2016] are defined, respectively, as:

$$FeKe = -\frac{1}{\rho_0}\left(\overline{u'\tau_x{}'} + \overline{v'\tau_y{}'}\right)$$

$$KmKe = -\left(\overline{u'u'}\frac{\partial \bar{u}}{\partial x} + \overline{u'v'}\frac{\partial \bar{u}}{\partial y} + \overline{u'w'}\frac{\partial \bar{u}}{\partial z} + \overline{v'u'}\frac{\partial \bar{v}}{\partial x} + \overline{v'v'}\frac{\partial \bar{v}}{\partial y} + \overline{v'w'}\frac{\partial \bar{v}}{\partial z}\right)$$

$$PeKe = -\frac{g}{\rho_0}\overline{\rho'w'}$$

where τ_x and τ_y are the meridian and zonal component of the wind stress. The prime indicates the anomaly from the annual mean. g is the gravity, ρ is the density and ρ_0 = 1030 kg m^{-3}. The overbar denotes the temporal mean and the prime represents the anomaly deviation from the mean. The *FeKe* is the *EKE* generation due to transient wind. When positive, this term induces an energy input while, when negative, it implies a damping effect on the sea surface [*Xu and Scott*, 2008]. The *KmKe* is the energy conversion between mean currents and *EKE*. When its volume-integration is positive, it implies barotropic energy conversion. The *PeKe* is the energy conversion between available potential energy and *EKE* and indicates baroclinic instability when its volume-integration is positive [*Harrison and Robinson*, 1978]. Both *KmKe* and *PeKe* are vertically integrated over the surface layer (top 100 m) [*Hristova et al.*, 2014]. The

minimum depth in the model is set to 75 m. When the bathymetry is shallower than 100 m, conversion terms are integrated over the actual depth.

III.3. Results and Discussion

III.3.1. Thermohaline structures and seasonal variability

The Marquesas archipelago is characterized by a north-east/south-west SST gradient as shown by MODIS remote sensing data and W13Q (Figure III-3a and 3b). Colder water in the north-east (≤ 27.5°C) represents the imprint of the equatorial upwelling [*Wyrtki*, 1981] while warmer SST in the west (≥ 28°C) is the south-eastward imprint of the western Pacific warm pool [*Yan et al.*, 1992]. The high-resolution of MODIS reveals warm regions behind the islands likely due to areas zones of weak currents leeward the islands. These structures have also been observed leeward several islands elsewhere [*Caldeira and Marchesiello*, 2002; *Caldeira et al.*, 2002]. The maximum of the mean satellite SST over the archipelago is up to 28.6°C in April during the austral summer (Figure III-3c, black line). In austral winter (September), SST in the Marquesas region decreases down to 27°C. In this tropical region, the seasonal amplitude is around 2°C as confirmed by *in-situ* SST from ISAS13 (red line). All the aforementioned features appear in the same locations and with comparable amplitudes in our numerical experiment, although SST is slightly colder than satellite observations (0.05°C to 0.1°C; Figure III-3b vs. 3a; green line on Figure III-3c). Thus, SST seasonal climatology from the model shows a good agreement with *in situ* and satellite-derived temperature variability.

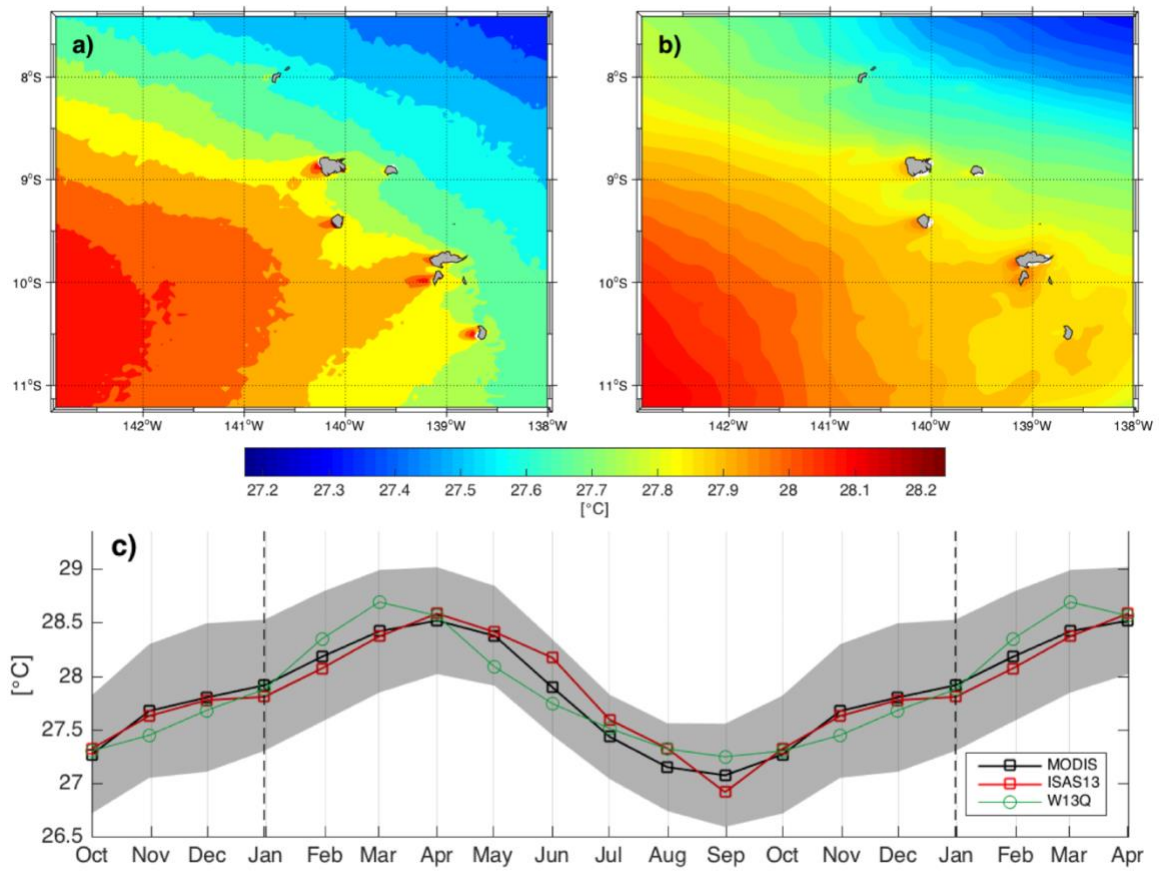

Figure III-3: Mean SST over the child grid area from (a) MODIS (time averaged from Jul-2002 to Jun-2015) and (b) W13Q at 10m (time averaged over year 4 to 10). (c) Monthly climatology averaged over the child grid area from MODIS (black), ISAS13 (red) and W13Q (green). The grey shaded area represents the spatial standard deviation from MODIS monthly climatology. Units are in °C.

Considering the haline structure, *in situ* data from ISAS13 show a SSS maximum in austral summer and a minimum in austral winter (35.7 and 35.5 psu +/- 0.01 psu), that are satisfactory reproduced by the model (Figure III-4a). The TS diagram issued from ISAS13 and W13Q illustrates the water masses within the archipelago (Figure III-4b). The South Pacific Tropical Water (SPTW) is characterized by a salinity maximum in subsurface (> 35.6 psu) [*O'Connor et al.*, 2005]. The Eastern South Pacific Central Water (ESPCW) and the Antarctic Intermediate Water (AAIW) are respectively defined by temperature ranges between 8 °C and 24 °C and between 2 °C and 10 °C. Their salinities are ranging between 34.4 psu and 36.4 psu and between

33.8 psu and 34.5 psu, respectively [*Emery*, 2001]. Only the SPTW is fresher in W13Q than with *in situ* measurements. The other water masses are quite well reproduced.

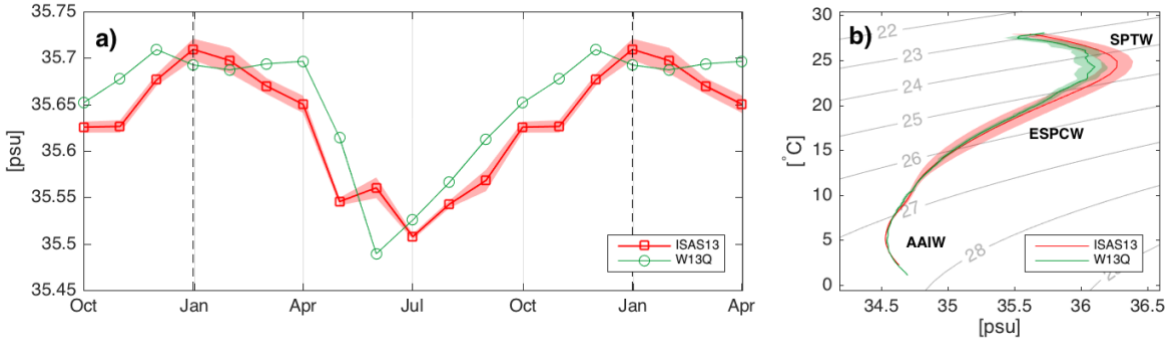

Figure III-4: (a) Time series of the monthly averaged salinity (in psu) at 10 m issued from ISAS13 (red) and W13Q (green). Red shaded area corresponds to the spatial standard deviation from ISAS13. (b) TS diagram from ISAS13 (red) and W13Q (green) monthly climatology and their standard deviations (red and green shades respectively).

III.3.2. Current structures

As shown in Figure III-1a, the SEC is the main surface current flowing around the Marquesas archipelago. Currents issued from W13Q present the same order of magnitude than the OSCAR ones, although with a more westward direction in the north (Figure III-5a). The spatial distribution of the mean current in the archipelago can be depicted in two regions: the southern part where the horizontal current is weak (8 cm s^{-1}), and the northern part where the SEC is stronger and reaches values of 20 cm s^{-1} as observed by *Martinez et al.* [2009]. The deviation of the SEC creates stronger currents on both sides of the islands and regions of weak current just behind the islands (Figure III-5b) [*Chang et al.*, 2013; *Karnauskas et al.*, 2017]. These shadow zones of weak currents are collocated with the warm areas as reported previously in *Figure* III-3b.

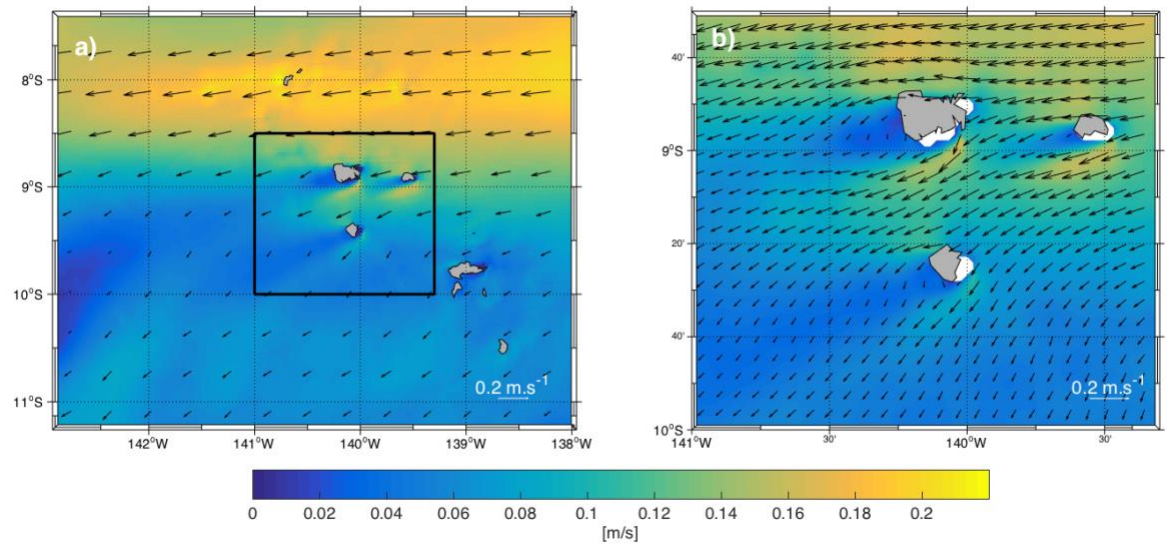

Figure III-5: (a) W13Q current at 10 m time averaged over year 4 to 10 and over the child domain. For clarity, only 1 vector out of 17 is represented. (b) Zoom of (a) over the Marquesas northern islands, as defined by the black box on a). For clarity, only 1 vector out of 3 is represented. Units are in m s^{-1}.

III.3.3. *EKE* generation and seasonal variability

In order to investigate the dynamical properties within the archipelago and more precisely the eddy field, we first focus on the *EKE* characterisation. The EKE_m obtained from OSCAR monthly currents show homogeneously low values around the archipelago (25 cm^2 s^{-2}) in Figure III-6a. In the northern and the south-western part of the archipelago, two areas are barely more active, the former corresponding to the southward imprint of the turbulent equatorial area [*Qiu and Chen*, 2004]. To compare the eddy activity from W13Q with the remote sensed one, we subsampled the model outputs to the same spatial and temporal resolution before computing EKE_m (Figure III-6b). High activity occurs in the northern and south-western part of the archipelago. Monthly W13Q also presents a high eddy activity west of Nuku Hiva. To fully take advantage of the high-resolution model, the annual mean of *EKE* is now directly computed from the W13Q two-day outputs (Figure III-6c). Thanks to the higher spatial and temporal resolution, the *EKE* at 10 m reaches up to 90 cm^2 s^{-2} (*vs.* 55 cm^2 s^{-2} in Figure III-6b). Island wakes characterized by a highly variable *EKE* pattern are highlighted westward the northern islands of Nuku Hiva, Ua Pou and Ua Huka. We could have also expected high activity leeward Hiva Oa (in the south), since its diameter is approximately the same as Nuku Hiva. However, the SEC being weaker windward this island, it does not produce a strong enough *EKE*.

Consistently, *EKE* patterns are more pronounced in the northern part of the archipelago where the mean current is stronger as seen on Figure III-5a. The *EKE* standard deviations are given in Figure III-6e and 6f. They reveal high activity where the mean *EKE* is already high and in good agreement with OSCAR *EKE* standard deviations (Figure III-6d).

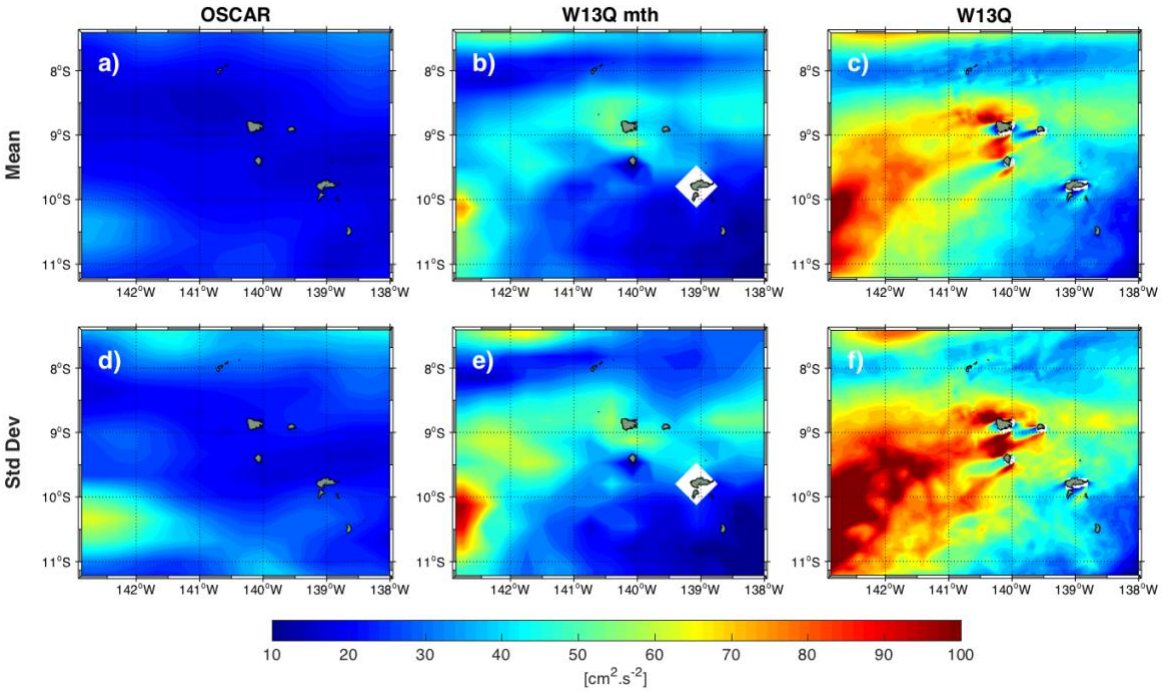

Figure III-6: Annual mean of EKE_m (in $cm^2 s^{-2}$) obtained from monthly averaged of (a) OSCAR surface currents and (b) W13Q currents at 10m. (c) is the annual mean of EKE derived from the W13Q 2-day outputs. Their standard deviations are represented in (d), (e) and (f), respectively.

In order to determinate the *EKE* origin, we now investigate the energy budget. For all the islands, the Burger number $Bu > 1$. Therefore, a significant amount of kinetic energy in the *EKE* origin is expected. This trend is observed in the barotropic energy conversion (Figure III-7a). The *KmKe* is particularly intense leeward Nuku Hiva where the *EKE* pattern is the strongest (Figure III-6c). It is mainly due to the fact that Nuku Hiva is the largest island and that it lies where the currents are the strongest. This implies a Re = 58 and, consequently, a possible Von Karman wake generation. *KmKe* and *PeKe* spatial patterns are close and are driven by the topography of the archipelago (Figure III-7a, b and Figure III-1b). The distribution of the baroclinic energy conversion is negative in average, which indicates an eddy dissipation toward the eddy potential energy [*Kang and Curchitser*, 2015]. The averaged energy

input from the wind (*FeKe*) presents smooth patterns because of the relatively low resolution of the wind stress used in the model (Figure III-7c). Values are weaker than the two previous parameters.

The *EKE* seasonality is superimposed with the different energy budget terms and their sum in Figure III-7d. *EKE* time series show a maximum activity in February, June and August, when the *KmKe* is also high. The latter remains positive all year round, indicating a constant flux towards *EKE*. *PeKe*, in a smaller proportion, also contributes to the high *EKE* activity in February. *PeKe* is responsible for the minimum value of *EKE* in April. The *EKE* variation on the second half of the year is explained by the *FeKe* variation, with a decreasing activity from August to December. The sum of these energy flux terms is relatively well correlated with the *EKE* variability. When this sum is positive (negative), an increase (decrease) of *EKE* is observed except during June where the energy budget seems too low to explain the *EKE* activity. According to *Chen et al.* [2016], the energy transfer through eddy-mean flow interactions could be imbalanced and compensated by advection. Indeed, currents are relatively intense in the archipelago during this time period. This could be at the origin of the decay observed in these time series. Although the spatial averaging reveals low values of *PeKe* and *FeKe* compared to some local maxima (Figure III-7a and b), these energy inputs seem to play an important role in the *EKE* seasonal variation, particularly at the beginning and the end of the year.

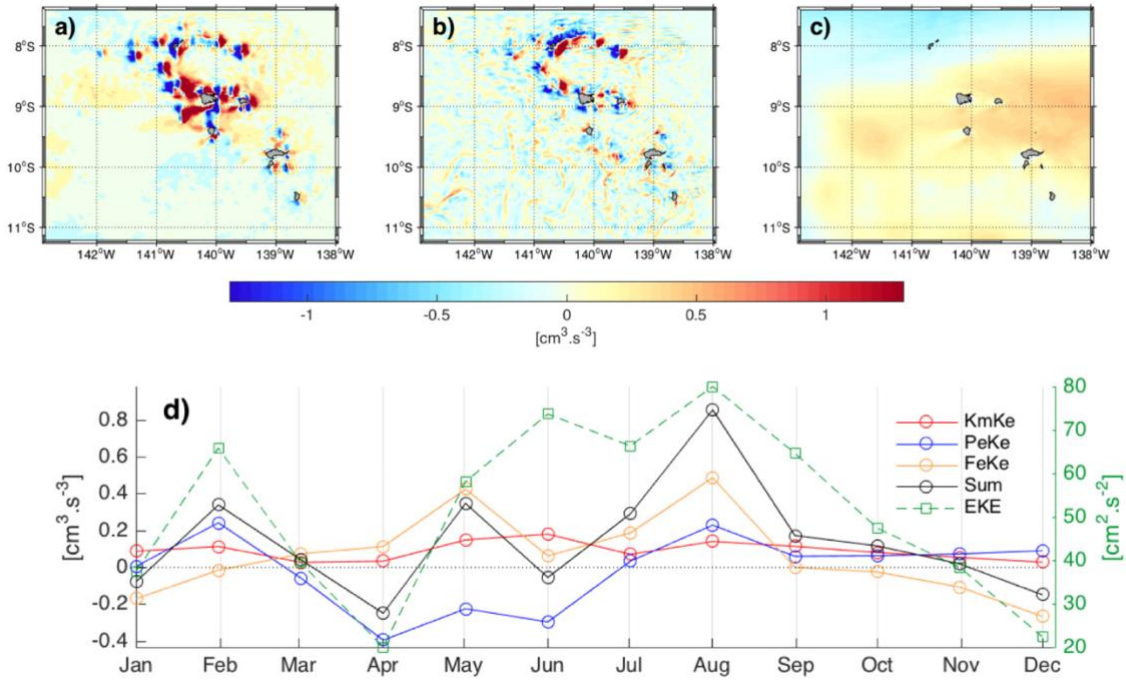

Figure III-7: Spatial distribution of the annual mean of the (a) barotropic (KmKe), (b) baroclinic (PeKe) energy conversion both integrated over the surface to 100 m and (c) the EKE generation due to transient wind, from year 4 to 10 of W13Q (units are in cm³ s⁻³). (d) Time series of wind work, baroclinic and barotropic energy (left axis), in yellow, blue and red, respectively. The sum of these three terms is indicated in black. The EKE (in cm² s⁻², right axis) spatially averaged over the child grid and at 10 m is represented in green.

III.3.4. Eddy activity

Detected eddies within the Marquesas archipelago are illustrated with green contours on relative vorticity maps from June 22 to July 22 during year 9 of W13Q (Figure III-8). Positive (negative) values reveal anticyclonic (cyclonic) circulation. The total number of detected eddies over the 7 years of integration is 1260, with a dominance of cyclonic (714) *vs*. anticyclonic eddies (546). This cyclonic eddy dominance (i.e., 56.7% of the total eddy number) is well illustrated (Figure III-8). On the other hand, positive patterns are unstable and tend to broaden and fragment inducing a weaker proportion of anticyclonic eddies. These observations are consistent with previous studies and are due to centrifugal instability occurring to anticyclonic eddies [*Dong et al.*, 2007; *Hasegawa et al.*, 2009; *Stegner*, 2014]. These snapshots reveal an important eddy activity in the archipelago which has never been investigated before. In particular, Figure III-8c shows the generation of cyclonic and anticyclonic eddies leeward Nuku

Hiva, the northern island, and likely producing SST small-scale patterns as observed in Figure III-2.

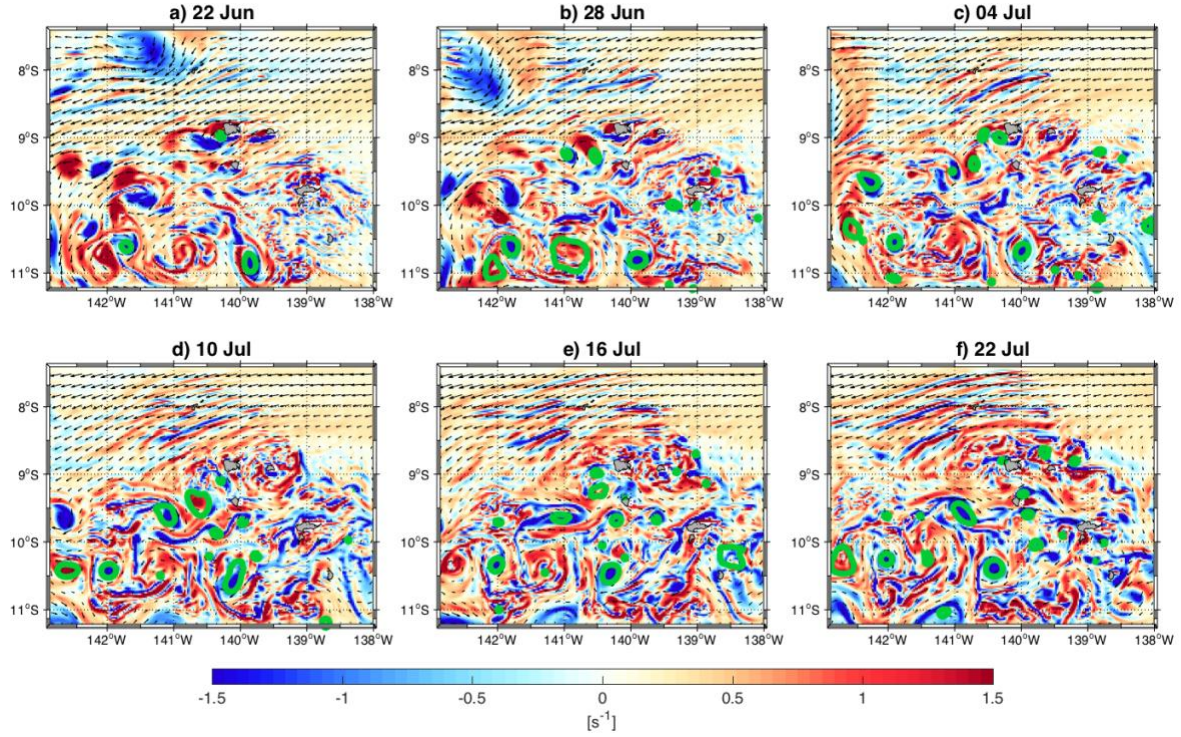

Figure III-8: Snapshots of relative vorticity at 10 m (units are in s^{-1}) from W13Q during Year 9 every 6 days (a-f). The detected eddies are represented by green contours (Nencioli et al. [2010] based algorithm). The animation of the vorticity from June to July is available in the auxiliary material.

To investigate where eddies are generated, the first eddy position determined by the detection algorithm is recorded and analysed. Most of eddies are generated leeward the archipelago highlighting the role of the topography (Figure III-9a). Part of these eddies are generated just behind the islands. Although the mean Reynolds number is larger than 40 only for Nuku Hiva, eddies are also generated behind the other islands. Indeed, when surface currents accelerate on the flanks of the other islands (Figure III-5), they induce a larger Re and create a decreasing pressure in the lee side associated with two opposite recirculation cells behind the islands. Anticyclonic eddies are generated on the equatorward side and cyclonic eddies on the poleward side. These eddies are emphasized behind Nuku Hiva and Ua Pou in the northern part of the archipelago where the SEC is the strongest, and Hiva Oa in the south which is the second biggest island of the Marquesas archipelago. Conversely, there is no eddy generation behind

Ua Huka (the northeastern most island) due to its small size inducing a too low Re (= 34) while there is a signature of the island wake on *EKE* (Figure III-6c), mean currents (Figure III-5), energy conversion rates (Figure III-7a) and vorticity (Figure III-8).

Eddies are also generated farther from the coasts, in the open ocean, where the flow presents complex structures as seen on Figure III-8. They are generated almost exclusively south-westward of the islands. A small number is also generated elsewhere, likely due to an eastward perturbation of the SEC during austral winter and referred as the Marquesas Counter Current [*Martinez et al.*, 2009]. Most of the eddies in the archipelago are generated during austral winter (July and August) when the wind stress and the *EKE* are maximum (Figure III-9b and Figure III-7c). Contrarily, eddies are barely detected in March and April when the wind stress and *EKE* are minimum. A strong correlation is found between eddy generation and the wind stress, with $r = 0.87$ ($p = 2.10^{-4}$). A high eddy generation occurs when the wind is strong (Figure III-9b). Indeed, not only the wind is responsible for a part of the *EKE* generation, but it also strengthens the surface currents, providing sufficient velocity to generate eddies behind the islands.

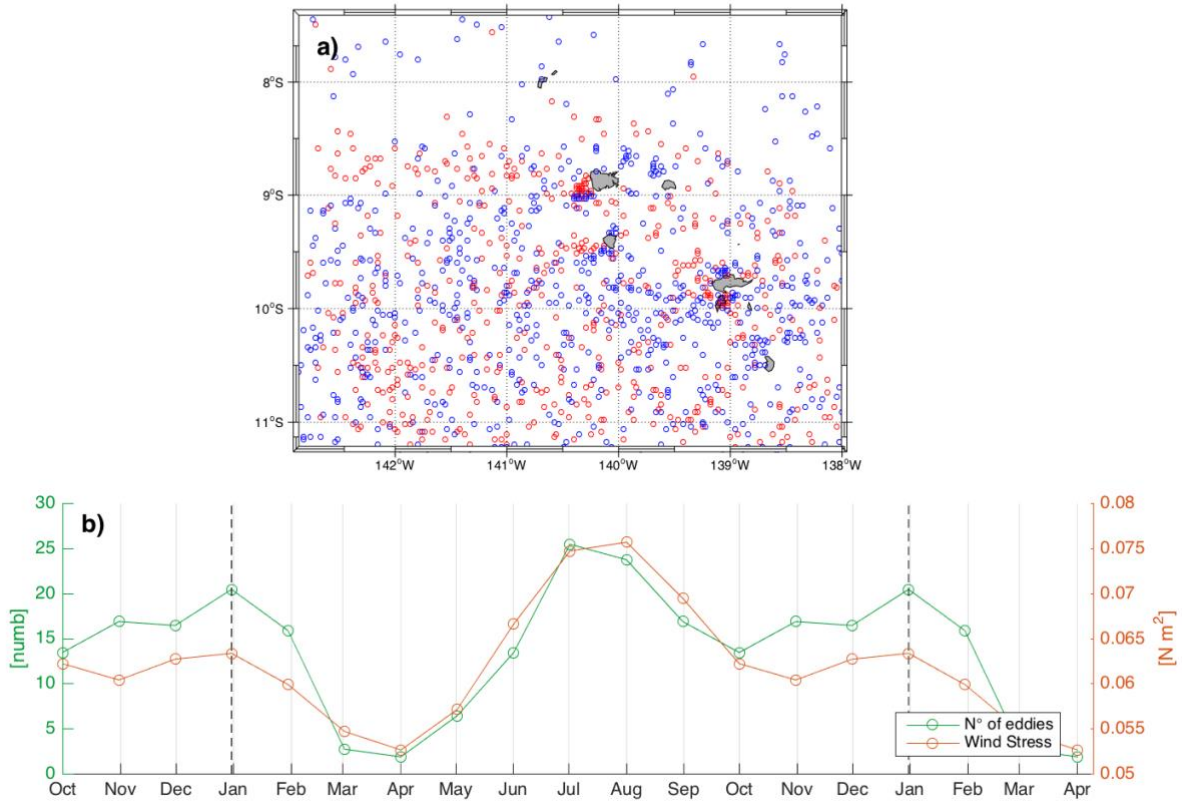

Figure III-9: (a) Location of eddy generation identified from W13Q over year 4 to 10. Anticyclonic and cyclonic eddies are represented by red and blue circles, respectively. (b)

Monthly mean number of generated eddies from W13Q from year 4 to 10 (green line) and wind stress issued from QuickSCAT in N.m^{-2} (orange line).

Investigating the maximum size of the detected eddies during their lifetime in W13Q shows that their distribution is similar to a Gaussian without an inferior tail due to resolution limitations (Figure III-10a, green bars). Most of the eddy radii are lower than 25 km and only a few are larger than 45 km. Indeed, size of eddies generated leeward the islands are approximately the same than the island dimensions, which can be explained by *Bu* larger than 1. The HYCOM eddy size distribution from January 2006 to December 2012 has been investigated within the child grid (Figure III-10a, black bars). In opposition with the W13Q results, a significant number of eddies larger than 20 km is present while smaller eddies are absent in HYCOM. The coarser spatial resolution of HYCOM prevents the resolution of such small structures. HYCOM larger eddies are suspected to be induced by the inter-annual forcing which is not represented in the present climatological W13Q configuration. In total, almost three times more eddies, are detected in our configuration than in HYCOM resulting from the higher resolution of our model.

Considering now the cyclonic *vs.* anticyclonic patterns, W13Q cyclonic eddies are dominant for all radius classes, except for the smallest ones (~10km) (Figure III-10b). Nevertheless, as previously mentioned, the generated anticyclonic structures are more unstable and form small structures with short lifetime (shorter than a week).

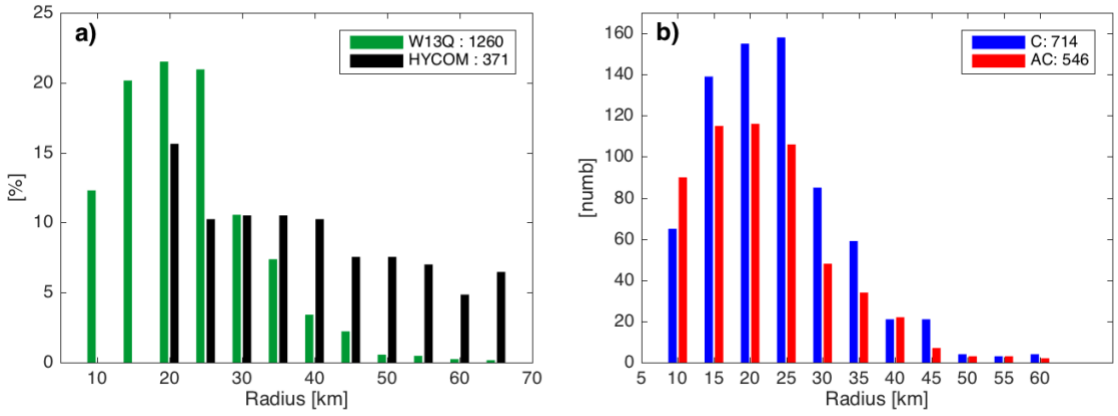

Figure III-10:(a) Distribution of the detected eddy radius from year 4 to 10 in W13Q (green) and from 2006 to 2012 in HYCOM (black). (b) Distribution of W13Q cyclonic (blue) vs. anticyclonic (red) eddies.

Focusing on these small eddies of interest, we further investigate trajectories of eddies with a maximum radius between 20 and 30 km, which represents about 50% of the eddies (Figure III-10a). As presented in Figure III-10b, anticyclonic eddies are less numerous than cyclonic ones for this radius range (Figure III-11a *vs*. 11b, respectively). Furthermore, the anticyclonic eddy trajectories are shorter than the cyclonic ones (Figure III-11b) because of the centrifugal instability that weakens anticyclonic eddies [*Dong et al.*, 2007]. While *Calil et al.* [2008] showed that cyclonic (anticyclonic) eddies tend to propagate poleward (equatorward) in the Hawaiian archipelago, trajectories of eddies generated leeward the Marquesas Islands are mostly zonal and do not present such a meridian trend. Indeed, while 61% (54.8%) of the cyclonic (anticyclonic) eddies propagate equatorward (southward), their meridian mean latitude change is only of 0.0163° (0.0182°). This might be explained by the lower latitude of the Marquesas archipelago inducing a weaker beta effect than in Hawaii.

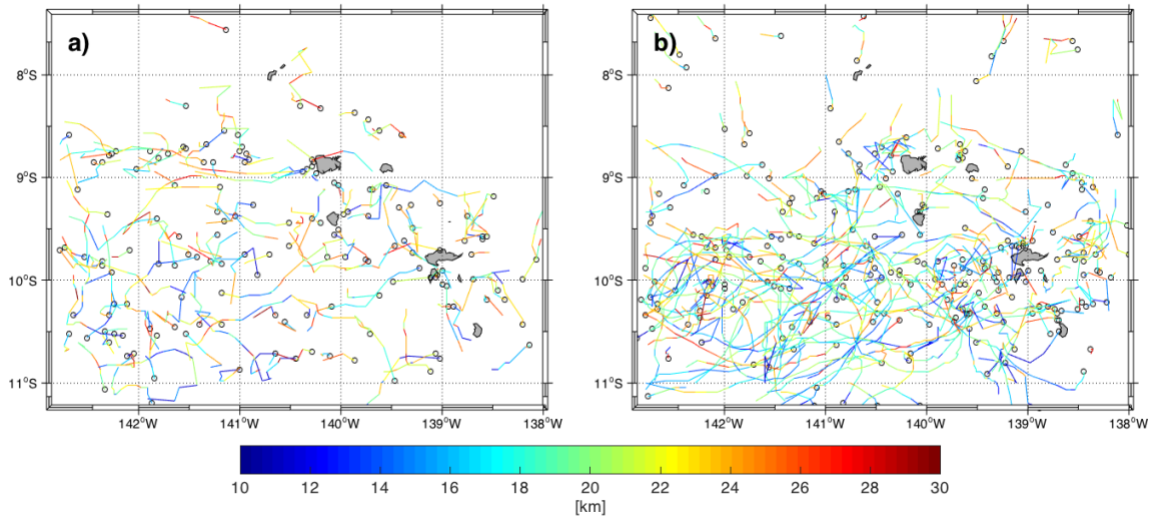

Figure III-11: Eddy generation sites (black circles) and their trajectories for (a) anticyclonic and (b) cyclonic eddies detected in W13Q and for a maximum radius over 20-30 km encountered over their lifetime. The size of the radius along the trajectory is given by the color bar (in km).

III.3.5. An insight to a possible eddy induced biological activity

Hasegawa et al. [2009] hypothesized that a combination of three processes can enrich the surface layer in island wakes: the propagation of coastal rich waters formed in the lee of the

islands by eddy shedding, the vertical advection of the Deep Chlorophyll Maximum (DCM) toward the surface in the island wake, and the uplift of nutrient rich deep waters by the strongest cyclonic eddies. We show that, when the SEC encounters the Marquesas Islands, it generates eddies in the lee of the archipelago (Figure III-9a). These eddies can trap and propagate inshore waters in the island wake. Thus, if these inshore waters have been previously enriched in proximity of the islands, the biological activity can be enhanced. An increase of the sea surface concentration of chlorophyll in the lee of an island could also be induced by the vertical advection of the DCM. During the "Pakaihi i te Moana" expedition, a correlation between the depth of the DCM and the mixed layer depth (MLD) has been reported in the archipelago [*Martinez et al.*, 2016]. On average, the DCM is deeper (shallower) in the northern (southern) region of the archipelago consistently with the MLD (60 m *vs*. 30 m). Our results show strong vertical velocities at the MLD associated with the eddies of the island wake (Figure III-12). This high vertical activity might induce the vertical advection of the DCM toward the surface. The evaluation of the impact of the fine scale dynamics on the nutricline is beyond the scope of the present study and will need further research. Indeed, to assess the uplift of nutrient-rich deep waters by cyclonic eddies and the associated biological activity, a coupled physical-biogeochemical model is required.

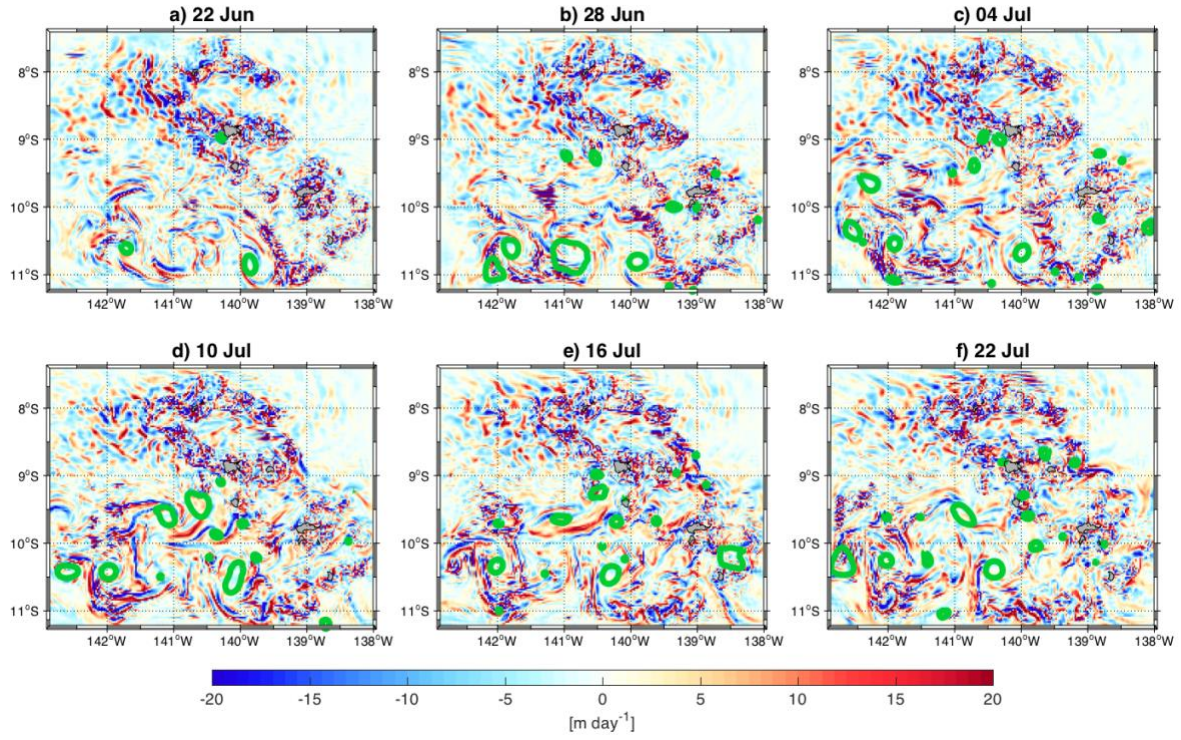

Figure III-12: Snapshots of vertical velocities (in m day^{-1}) as in Figure III-8, but at the mixed layer depth.

III.4. Conclusions and perspectives

The island wake in the Marquesas archipelago has been characterized in the present study, providing new insights into the spatial and seasonal variability of the fine-scale dynamics of this oceanic region. We based our analysis on the ocean circulation model ROMS-AGRIF with a 1/45° child grid resolution and forced by climatological mean fields. The high spatial and temporal resolution allows characterizing warm SST patterns just behind the Marquesas Islands. These patterns likely due to shadow zones of weak currents have been consistently observed leeward several islands [*Barton*, 2001; *Caldeira et al.*, 2002; *Chavanne et al.*, 2002]. Accordingly to a rough approximation of the local Reynolds number, only Nuku Hiva, the biggest island of the archipelago, would be expected to generate a wake of propagating eddies. However, the mean *EKE* and the use of an automated eddy detection algorithm reveals that eddy generation also occurs leeward the other islands, inshore and offshore. The energy budget analysis reveals that eddies are generated by a combination of wind power input, barotropic and baroclinic energy conversion. These generated eddies are cyclonic dominant due to the small size of the islands in comparison to the Rossby radius. Most of the eddies have their maximum radius between 20 and 30 km.

Our physical model results provide insight to explain the Marquesas biological enhancement. We suggest that the combination of at least two of the three processes proposed by *Hasegawa et al.* [2009] enriches surface layers via eddy activity: the propagation of rich waters formed in the lee of the islands by eddy shedding and the vertical advection of the DCM toward the surface in the island wake. To further investigate the third process, I.E. the possibility of an uplift of nutrient rich waters by the cyclonic eddies, new in situ data and the use of a coupled physical-biogeochemical numerical model are required.

Acknowledgments

We thank the government of French Polynesia for the financial support of the moana-maty project (convention n°6841/MTS) including the PhD grant of H. Raapoto. We also thank the OSU Pyheas that provided the cluster support.

The data used in this work are available from Moderate Resolution Imaging Spectroradiometer MODIS (http://oceandata.sci.gsfc.nasa.gov), In Situ Analysis System ISAS13 (http://www.seanoe.org/data/00348/45945/), Ocean Surface Current Analysis – Real time

OSCAR (http://www.oscar.noaa.gov/) and Hybrid Coordinate Ocean Model HYCOM (http://hycom.org/data/glbu0pt08/expt-19pt1). Please contact the corresponding author to obtain the data of the numerical model used in this paper.

References du Chapitre III

Alaee, M. J., G. Ivey, and C. Pattiaratchi (2004), Secondary circulation induced by flow curvature and Coriolis effects around headlands and islands, Ocean Dyn., 54(1), 27–38, doi:10.1007/s10236-003-0058-3.

Amores, A., S. Monserrat, and M. Marcos (2013), Vertical structure and temporal evolution of an anticyclonic eddy in the Balearic Sea (western Mediterranean), J. Geophys. Res. Ocean., 118(4), 2097–2106, doi:10.1002/jgrc.20150.

Andrade, I., P. Sangrà, S. Hormazabal, and M. Correa-Ramirez (2014), Island mass effect in the Juan Fernández Archipelago (33°S), Southeastern Pacific, Deep. Res. Part I Oceanogr. Res. Pap., 84, 86–99, doi:10.1016/j.dsr.2013.10.009.

Auad, G., A. Pares-Sierra, and G. K. Vallis (1991), Circulation and energetics of a model of the California Current system.pdf, J. Phys. Oceanogr., 21(10), 1534–1552.

Barton, E. D. (2001), Island wakes, Nature, 1–8, doi:10.1006/rwos.2001.0140.

Beckmann, A., and D. B. Haidvogel (1993), Numerical Simulation of Flow around a Tall Isolated Seamount. Part I: Problem Formulation and Model Accuracy, J. Phys. Oceanogr., 23(8), 1736–1753, doi:10.1175/1520-0485(1993)023<1736:NSOFAA>2.0.CO;2.

Bonjean, F., and G. S. E. Lagerloef (2002), Diagnostic model and analysis of the surface currents in the tropical Pacific Ocean, J. Phys. Oceanogr., 32(10), 2938–2954, doi:10.1175/1520-0485(2002)032<2938:DMAAOT>2.0.CO;2.

Caldeira, R. M. A., and P. Marchesiello (2002), Ocean response to wind sheltering in the Southern California Bight, Geophys. Res. Lett., 29(13), 1–4, doi:10.1029/2001GL014563.

Caldeira, R. M. A., S. Groom, P. Miller, D. Pilgrim, and N. P. Nezlin (2002), Sea-surface signatures of the island mass effect phenomena around Madeira Island, Northeast Atlantic, Remote Sens. Environ., 80(2), 336–360, doi:10.1016/S0034-4257(01)00316-9.

Calil, P. H. R., K. J. Richards, Y. Jia, and R. R. Bidigare (2008), Eddy activity in the lee of the Hawaiian Islands, Deep. Res. Part II Top. Stud. Oceanogr., 55(10–13), 1179–1194, doi:10.1016/j.dsr2.2008.01.008.

Chang, M. H., T. Y. Tang, C. R. Ho, and S. Y. Chao (2013), Kuroshio-induced wake in the lee of Green Island off Taiwan, J. Geophys. Res. Ocean., 118(3), 1508–1519, doi:10.1002/jgrc.20151.

Chavanne, C., P. Flament, R. Lumpkin, B. Dousset, and A. Bentamy (2002), Scatterometer observations of wind variations induced by oceanic islands: implications for wind-driven ocean circulation., Can. J. Remote Sens., 28(3), 466–474, doi:10.5589/m02-047.

Chelton, D. B., R. a. deSzoeke, M. G. Schlax, K. El Naggar, and N. Siwertz (1998), Geographical Variability of the First Baroclinic Rossby Radius of Deformation, J. Phys. Oceanogr., 28(3), 433–460, doi:10.1175/1520-0485(1998)028<0433:GVOTFB>2.0.CO;2.

Chen, R., A. F. Thompson, and G. R. Flierl (2016), Time-dependent eddy-mean energy diagrams and their application to the ocean, J. Phys. Oceanogr., 46(9), 2827–2850, doi:10.1175/JPO-D-16-0012.1.

Cummings, J. A., and O. M. Smedstad (2013), Variational Data Assimilation for the Global Ocean.

Debreu, L., and E. Blayo (2008), Two-way embedding algorithms: A review, Ocean Dyn., 58(5–6), 415–428, doi:10.1007/s10236-008-0150-9.

Debreu, L., P. Marchesiello, P. Penven, and G. Cambon (2012), Two-way nesting in split-explicit ocean models: Algorithms, implementation and validation, Ocean Model., 49–50, 1–21, doi:10.1016/j.ocemod.2012.03.003.

Dietrich, D., M. Bowman, and C. Lin (1996), Numerical studies of small island wakes in the ocean, Geophys. Astrophys. Fluid Dyn., 83(3–4), 195–231, doi:10.1080/03091929608208966.

DiGiacomo, P. M., and B. Holt (2001), Satellite observations of small coastal ocean eddies in the Southern California Bight, J. Geophys. Res., 106(10), 22,521-522,543, doi:10.1029/2000JC000728.

Doglioli, A. M., B. Blanke, S. Speich, and G. Lapeyre (2007), Tracking coherent structures in a regional ocean model with wavelet analysis: Application to Cape Basin eddies, J. Geophys. Res. Ocean., 112(5), 1–12, doi:10.1029/2006JC003952.

Dong, C., J. C. McWilliams, and A. F. Shchepetkin (2007), Island Wakes in Deep Water, J. Phys. Oceanogr., 37(4), 962–981, doi:10.1175/JPO3047.1.

Dong, C., X. Lin, Y. Liu, F. Nencioli, Y. Chao, Y. Guan, D. Chen, T. Dickey, and J. C. McWilliams (2012), Three-dimensional oceanic eddy analysis in the Southern California Bight from a numerical product, J. Geophys. Res. Ocean., 117(1), 1–17, doi:10.1029/2011JC007354.

Doty, M. S., & Oguri, M. (1956), The island mass effect, J. du Cons., 22(1), 33–37, doi:10.1093/icesjms/22.1.33.

Emery, W. J. (2003), Water Types and Water Masses Descriptive Tools : The TS Curve, in Ocean Circulation, pp. 1556–1567.

Gaillard, F., T. Reynaud, V. Thierry, N. Kolodziejczyk, and K. Von Schuckmann (2016), In

situ-based reanalysis of the global ocean temperature and salinity with ISAS: Variability of the heat content and steric height, J. Clim., 29(4), 1305–1323, doi:10.1175/JCLI-D-15-0028.1.

Halo, I., P. Penven, B. Backeberg, I. Ansorge, F. Shillington, and R. Roman (2014), Mesoscale eddy variability in the southern extension of the East Madagascar Current: Seasonal cycle, energy conversion terms, and eddymean properties, J. Geophys. Res. Ocean., 0, 7324–7356, doi:10.1002/2014JC009820.

Harrison, D. E., and A. R. Robinson (1978), Energy analysis of open regions of turbulent flows - mean eddy energetics of a numerical ocean circulation experiment, Dyn. Atmos. Ocean., 2(2), 185–211, doi:10.1016/0377-0265(78)90009-X.

Hasegawa, D., H. Yamazaki, R. G. Lueck, and L. Seuront (2004), How islands stir and fertilize the upper ocean, Geophys. Res. Lett., 31(16), 1–4, doi:10.1029/2004GL020143.

Hasegawa, D., H. Yamazaki, T. Ishimaru, H. Nagashima, and Y. Koike (2008), Apparent phytoplankton bloom due to island mass effect, J. Mar. Syst., 69(3–4), 238–246, doi:10.1016/j.jmarsys.2006.04.019.

Hasegawa, D., M. R. Lewis, and a. Gangopadhyay (2009), How islands cause phytoplankton to bloom in their wakes, Geophys. Res. Lett., 36(20), 1–4, doi:10.1029/2009GL039743.

Heywood, K. J., E. D. Barton, and J. H. Simpson (1990), The effects of flow disturbance by an oceanic island, J. Mar. Res., 48, 55–73, doi:10.1357/002224090784984623.

Heywood, K. J., D. P. Stevens, and G. R. Bigg (1996), Eddy formation behind the tropical island of Aldabra, Deep. Res. Part I Oceanogr. Res. Pap., 43(4), 555–578, doi:10.1016/0967-0637(96)00097-0.

Hristova, H. G., W. S. Kessler, J. C. McWilliams, and M. J. Molemaker (2014), Mesoscale variability and its seasonality in the Solomon and Coral Seas, J. Geophys. Res. Ocean., 119, 4669–4687, doi:10.1002/2013JC009741.

Jiménez, B., P. Sangrà, and E. Mason (2008), A numerical study of the relative importance of wind and topographic forcing on oceanic eddy shedding by tall, deep water islands, Ocean Model., 22(3–4), 146–157, doi:10.1016/j.ocemod.2008.02.004.

Kang, D., and E. N. Curchitser (2015), Energetics of Eddy-Mean Flow Interactions in the Gulf Stream Region, J. Phys. Oceanogr., 45, 1103–1120, doi:10.1175/JPO-D-14-0200.1.

Karnauskas, K. B., G. C. Johnson, and R. Murtugudde (2017), On the climate impacts of atolls in the central equatorial Pacific, Int. J. Climatol., 37(1), 197–203, doi:10.1002/joc.4697.

Kersalé, M., a. M. Doglioli, and a. a. Petrenko (2011), Sensitivity study of the generation of mesoscale eddies in a numerical model of Hawaii islands, Ocean Sci., 7(3), 277–291,

doi:10.5194/os-7-277-2011.

Large, W. G., J. C. McWilliams, and S. C. Doney (1994), Oceanic vertical mixing: A review and a model with a nonlocal boundary layer parameterization, Rev. Geophys., 32(4), 363, doi:10.1029/94RG01872.

Legeckis, R., C. W. Brown, F. Bonjean, and E. S. Johnson (2004), The influence of tropical instability waves on phytoplankton blooms in the wake of the Marquesas Islands during 1998 and on the currents observed during the drift of the Kon-Tiki in 1947, Geophys. Res. Lett., 31(23), 1–4, doi:10.1029/2004GL021637.

Liang, J. H., J. C. McWilliams, J. Kurian, F. Colas, P. Wang, and Y. Uchiyama (2012), Mesoscale variability in the northeastern tropical Pacific: Forcing mechanisms and eddy properties, J. Geophys. Res. Ocean., 117(7), 1–13, doi:10.1029/2012JC008008.

Liu, Y., C. Dong, Y. Guan, D. Chen, J. McWilliams, and F. Nencioli (2012), Eddy analysis in the subtropical zonal band of the North Pacific Ocean, Deep. Res. Part I Oceanogr. Res. Pap., 68, 54–67, doi:10.1016/j.dsr.2012.06.001.

Locarnini, R. A. et al. (2013), World Ocean Atlas 2013. Vol. 1: Temperature., S. Levitus, Ed.; A. Mishonov, Tech. Ed.; NOAA Atlas NESDIS, 73(September), 40, doi:10.1182/blood-2011-06-357442.

Lungu, T., and P. S. Callahan (2006), QuikSCAT science data product user's manual: Overview and geophysical data products, D-18053-Rev A, version, 3, 91.

Marchesiello, P., J. C. McWilliams, and A. Shchepetkin (2001), Open boundary conditions for long-term integration of regional oceanic models, Ocean Model., 3(1–2), 1–20, doi:10.1016/S1463-5003(00)00013-5.

Marchesiello, P., J. C. McWilliams, A. Shchepetkin, P. Physics, and L. Angeles (2003), Equilibrium Structure and Dynamics of the California Current System, J. Phys. Oceanogr., 33(4), 753–783, doi:10.1175/1520-0485(2003)33<753:ESADOT>2.0.CO;2.

Martinez, E., and K. Maamaatuaiahutapu (2004), Island mass effect in the Marquesas Islands: Time variation, Geophys. Res. Lett., 31(18), 1–4, doi:10.1029/2004GL020682.

Martinez, E., A. Ganachaud, J. Lefevre, and K. Maamaatuaiahutapu (2009), Central south pacific thermocline water circulation from a high-resolution ocean model validated against satellite data: seasonal variability and el niño 1997-1998 influence, J. Geophys. Res. Ocean., 114(5), 1–16, doi:10.1029/2008JC004824.

Martinez, E., M. Rodier, and K. Maamaatuaiahutapu (2016), Environnement océanique des Marquises, , 1–15.

Mkhinini, N., A., L. S. Coimbra, A. Stegner, T. Arsouze, I. Taupier-Letage, and K. Béranger

(2014), Long-lived mesoscale eddies in the easternMediterranean Sea: Analysis of 20 years of AVISO geostrophic velocities, J. Geophys. Res. Ocean., 119, 8603–8626, doi:10.1002/2014JC010176.

Neill, S. P., and A. J. Elliott (2004), Observations and simulations of an unsteady island wake in the Firth of Forth, Scotland, Ocean Dyn., 54(3–4), 324–332, doi:10.1007/s10236-003-0084-1.

Nencioli, F., C. Dong, T. Dickey, L. Washburn, and J. C. Mcwilliams (2010), A vector geometry-based eddy detection algorithm and its application to a high-resolution numerical model product and high-frequency radar surface velocities in the Southern California Bight, J. Atmos. Ocean. Technol., 27(3), 564–579, doi:10.1175/2009JTECHO725.1.

O'Connor, B. M., R. A. Fine, and D. B. Olson (2005), A global comparison of subtropical underwater formation rates, Deep. Res. Part I Oceanogr. Res. Pap., 52(9), 1569–1590, doi:10.1016/j.dsr.2005.01.011.

Palacios, D. M. (2002), Factors influencing the island-mass effect of the Galápagos Archipelago, Geophys. Res. Lett., 29(23), 1–4, doi:10.1029/2002GL016232.

Penven, P., P. Marchesiello, L. Debreu, and J. Lefèvre (2007), Software tools for pre- and post-processing of oceanic regional simulations, Environ. Model. Softw., 23(5), 660–662, doi:10.1016/j.envsoft.2007.07.004.

Qiu, B., and S. Chen (2004), Seasonal Modulations in the Eddy Field of the South Pacific Ocean, J. Phys. Oceanogr., 34(7), 1515–1527, doi:10.1175/1520-0485(2004)034<1515:SMITEF>2.0.CO;2.

Qu, T., S. Gao, and R. A. Fine (2013), Subduction of South Pacific Tropical Water and Its Equatorward Pathways as Shown by a Simulated Passive Tracer*, J. Phys. Oceanogr., 43(8), 1551–1565, doi:10.1175/JPO-D-12-0180.1.

Sangrà, P., G. Basterretxea, J. L. Pelegrí, and J. Arístegui (2001), Chlorophyll increase due to internal waves on the shelf break of Gran Canaria (Canary Islands)*, Signals, 65, 89–97, doi:http://digital.csic.es/bitstream/10261/5326/1/wave.pdf.

Sangrà, P., J. L. Pelegrí, A. Hernández-Guerra, I. Arregui, J. M. Martín, A. Marrero-Díaz, A. Martínez, A. W. Ratsimandresey, and A. Rodríguez-Santana (2005), Life history of an anticyclonic eddy, J. Geophys. Res. C Ocean., 110(3), 1–19, doi:10.1029/2004JC002526.

Shchepetkin, A. F., and J. C. McWilliams (2003), A method for computing horizontal pressure-gradient force in an oceanic model with nonaligned vertical coordinate, J. Geophys. Res., 108(C3), 1–34, doi:10.1029/2001JC001047.

Shchepetkin, A. F., and J. C. McWilliams (2005), The regional oceanic modeling system ({ROMS}): a split-explicit, free-surface, topography-following-coordinate oceanic model, Ocean~Model., 9, 347–404, doi:10.1016/j.ocemod.2004.08.002.

Signorini, S. R., C. R. McClain, and Y. Dandonneau (1999), Mixing and phytoplankton bloom in the wake of the Marquesas Islands, Geophys. Res. Lett., 26(20), 3121–3124, doi:10.1029/1999GL010470.

da Silva, A. M., C. C. Young, and S. Levitus (1994), Atlas of surface marine data 1994, vol. 4, Anomalies of fresh water fluxes, Noaa atlas nesdis, 9, 308.

Smith, W. H., and D. Sandwell (1997), Global Sea Floor Topography from Satellite Altimetry and Ship Depth Soundings, Science (80-.)., 277(5334), 1956–1962, doi:10.1126/science.277.5334.1956.

Stegner, A. (2014), Oceanic Island Wake Flows in the Laboratory, in Modeling Atmospheric and Oceanic Flows: Insights from Laboratory Experiments and Numerical Simulations, pp. 265–276.

Sun, Z., Z. Zhang, W. Zhao, and J. Tian (2016), Interannual modulation of eddy kinetic energy in the northeastern South China Sea as revealed by an eddy-resolving OGCM, J. Geophys. Res. Ocean., 121, 1–12, doi:10.1002/2015JC011497.

Tomczak, M. (1988), Island wakes in deep and shallow water, J. Geophys. Res., 93(8), 5153–5154.

Wolanksi, E., T. Asaeda, A. Tanaka, and E. Deleersnijder (1996), Three-dimensional island wakes in the field, laboratory experiments and numerical models, Cont. Shelf Res., 16(11), 1437–1452, doi:10.1016/0278-4343(95)00087-9.

Wyrtki, K. (1981), An Estimate of Equatorial Upwelling in the Pacific, J. Phys. Oceanogr., 11, 1205–1214.

Xu, Y., and R. B. Scott (2008), Subtleties in forcing eddy resolving ocean models with satellite wind data, Ocean Model., 20(3), 240–251, doi:10.1016/j.ocemod.2007.09.003.

Yan, X., C. Ho, Q. Zheng, and V. Klemas (1992), Temperature and Size Variabilities of the Western Pacific Warm Pool, Science (80-.)., 258(5088), 1643–1645.

Zweng, M. M., J. R. Reagan, J. I. Antonov, A. V. Mishonov, T. P. Boyer, H. E. Garcia, O. K. Baranova, D. R. Johnson, D. Seidov, and M. M. Bidlle (2013), World Ocean Atlas 2013, Volume 2: Salinity, NOAA Atlas NESDIS, 119(1), 227–237, doi:10.1182/blood-2011-06-357442.

Conclusion du Chapitre III

Dans cette étude, nous avons utilisé une configuration climatologique à haute-résolution du modèle ROMS-AGRIF (~2,5 km) pour étudier la dynamique dans l'archipel des Marquises. La robustesse de cette configuration, utilisant les forçages préalablement déterminés dans le chapitre II, a été évaluée en comparant les sorties du modèle avec des mesures satellites et *in situ* dans l'archipel. Ainsi, cette configuration réaliste a permis de mettre en évidence des processus physiques de fine échelle difficilement détectables sur les mesures satellites. En particulier, des zones de faible courant derrière les îles correspondent à des zones plus chaudes, qui sont visibles sur les mesures de températures de surface de la mer.
Une analyse préliminaire du nombre de Reynolds suggère que seule la plus grande île de l'archipel, Nuku Hiva, serait susceptible de générer une allée de tourbillons dans son sillage. Cependant, les résultats issus du modèle haute résolution révèlent une activité tourbillonnaire aussi derrière les autres îles. L'EKE et l'utilisation d'un algorithme de détection automatique de tourbillons montrent une génération de tourbillons proche des côtes et au large des îles. Ces tourbillons sont générés par une combinaison de forçages des vents, d'instabilités baroclines et barotropes. La taille des îles étant plus petite que le rayon de Rossby ambiant, la majorité de ces tourbillons sont cycloniques et ont un rayon maximum variant entre 20 et 30 km.

Ainsi, la mise en place d'une configuration physique à haute résolution pour l'archipel nous a permis de mettre en lumière une circulation secondaire difficilement décelable par les moyens actuels. En effet, les faibles résolutions spatiales et temporelles des données disponibles pour l'archipel ne permettaient pas, jusqu'à présent, d'identifier une telle activité tourbillonnaire derrière les îles. Les turbulences entrainées par ces tourbillons pourraient jouer un rôle important dans l'enrichissement des couches de surface et ainsi favoriser le développement de phytoplancton dans l'archipel. Cependant pour tester cette hypothèse, mais aussi pour déterminer si d'autres processus seraient à l'origine de la forte activité biologique observée aux Marquises, le recours au couplage du modèle physique avec un modèle biogéochimique est nécessaire. Ainsi, dans le chapitre suivant, nous utilisons les résultats obtenus jusqu'ici pour mettre en place le couplage ROMS-PISCES et étudier les processus qui pourraient être à l'origine de l'effet d'île Marquisien.

Chapitre IV

Modeling the biological enhancement of the Marquesas archipelago: impact of iron concentration

H. Raapoto[1], E. Martinez[1,2], A. Petrenko[3], A. M. Doglioli[3], R. Sauzède[4], K Maamaatuaihutapu[4], C. Menkes[5], T. Gorgues[2]

[1] IRD, UPF, ILM, Ifremer, Écosystèmes Insulaires Océaniens (EIO), Tahiti, French Polynesia.

[2] Université Brest, Ifremer, CNRS, IRD, Laboratoire d 'Océanographie Physique et Spatiale (LOPS), IUEM, Brest, France.

[3] Aix Marseille Univ, Université de Toulon, CNRS, IRD, OSU PYTHEAS, Mediterranean Institute of Oceanography MIO, UM 110, 13288, Marseille, Cedex 09, France.

[4] Laboratoire de Géosciences du Pacifique Sud, Université de la Polynésie française, Tahiti, French Polynesia

[5] Institut de Recherche pour le Développement, Nouméa, 98848, New Caledonia

---

Prêt à être soumis dans *Journal of Geophysical Research: Oceans*

RESUME

Un panache de chlorophylle très étendu est visible à la limite des eaux mésotrophes équatoriales et des eaux oligotrophes subéquatoriales au centre de l'océan Pacifique. Cette importante activité biologique est induite par l'effet d'île (EI) ayant lieu dans l'archipel des Marquises. Les eaux entourant ces îles présentent de fortes concentrations en macronutriments mais de faibles concentrations de fer. Dans cette étude, nous nous intéressons à l'origine de cet enrichissement biologique en utilisant la modélisation numérique. Pour cela, nous avons utilisé 4 simulations basées sur les mêmes forçages physique et biogéochimique à l'exception des concentrations et sources de fer. Les simulations prenant en compte un apport de fer depuis les sédiments présentent des distributions verticales et horizontales de chlorophylle proches des observations, mais avec des valeurs inférieures. Ainsi, il est déduit qu'un apport de fer depuis les îles est aussi nécessaire pour générer un EI. Les simulations n'utilisant que l'apport de fer depuis les frontières ont révélé l'implication de processus à l'échelle de l'archipel. Par exemple, le renforcement du courant induit une advection des eaux tropicales dans l'archipel, augmentant ainsi les concentrations de chlorophylle dans l'archipel. L'approfondissement hivernal de la couche de mélange permet aussi la remontée d'eaux riches en nutriments vers la surface. Enfin, l'apport local de fer via les sédiments, permet la production et la propagation de chlorophylle depuis les îles. Les variabilité spatiale de la distribution du panache de l'EI est ensuite modulée par les courants locaux.

ABSTRACT

A remarkable chlorophyll plume can be noticed at the boundary of the equatorial mesotrophic and the subtropical oligotrophic waters in the central Pacific Ocean. This important biological activity results from the Island Mass Effect (IME) occurring in the Marquesas archipelago. Waters surrounding these islands present high macronutrient concentrations but an iron depletion. In this study, we have investigated the origin of the biological enhancement using a modelling approach. We used 4 simulations based on identical physical and biogeochemical forcings but with different iron concentrations and sources. Simulations considering an iron input from the sediment present similar vertical and horizontal chlorophyll distributions with weaker values than observations. Thus, an iron input from the island is necessary to generate an IME. However, simulations with no other iron input than the boundary forcings revealed remote processes. The reinforcement of the main flow induces the advection of the rich equatorial waters through the archipelago, enhancing the chlorophyll in the archipelago. While the wintertime deepening of the mixed layer also provides nutrient rich waters toward the

surface. Then, the local iron contribution (sediment) allows the production of chlorophyll propagating from the islands. The spatial pattern of the IME is then modulated by the local currents.

IV.1. Introduction

For about three decades, iron (Fe) has been increasingly considered as a crucial element in regulating the ocean biological productivity [*Martin and Fitzwater*, 1988; *Boyd and Ellwood*, 2010]. Over approximately 20 to 50% of the global ocean primary productivity is limited by insufficient Fe concentrations for phytoplankton growth [*Boyd and Ellwood*, 2010]. Therefore, small changes in Fe concentrations are likely to induce significant impacts on phytoplankton growth affecting the productivity of ecosystems, the structure of the trophic food web and the efficiency of carbon sequestration. Fe can be supplied to the ocean by several external sources such as river input [*da Cunha and Buitenhuis*, 2013], hydrothermal input [*Tagliabue et al.*, 2010; *Guieu et al.*, 2018], dust deposition from the atmosphere [*Jickells et al.*, 2005] or sediment resuspension [*Johnson et al.*, 1999; *Elrod et al.*, 2004; *Dale et al.*, 2015]. However, substantial uncertainties on the Fe biogeochemical cycle and on the magnitude of these external sources remain.

Several studies have investigated Fe fertilization around islands in the Southern Ocean where phytoplankton blooms regularly occurs (Kerguelen, South Georgia and Crozet islands) [*Blain et al.*, 2007; *Planquette et al.*, 2007; *Maraldi et al.*, 2009; *D'Ovidio et al.*, 2015; *Robinson et al.*, 2016]. These blooms are particularly pronounced since these islands are localised in a high-nutrient low-chlorophyll (HNLC) region. Such localised increase of the biological activity around oceanic islands is refered to an island mass effect (IME) [*Doty and Oguri*, 1956]. Several physical processes can be involved in providing micro and macro-nutrient rich waters to the euphotic zone, thus allowing the development of phytoplankton. Vertical mixing induced by eddies, jets, coastal upwelling, Ekman pumping and internal wave breaking can play a key role in the input of nutrient rich water [*Heywood et al.*, 1990, 1996; *Barton*, 2001; *Sangrà et al.*, 2001; *Palacios*, 2002; *Benitez-Nelson and McGillicuddy*, 2008; *Hasegawa et al.*, 2009].

In the central South Pacific, the Marquesas archipelago (144°W-137°W/8°S-11°S, Figure IV-1) is also located in a HNLC environment, at the boundary between the oligotrophic subtropical gyre and the equatorial mesotrophic waters. While a remarkable plume of chlorophyll-a concentration (Chl, a proxy of phytoplankton biomass) can be observed leeward of the islands from satellite ocean color observations (Figure IV-1a) [*Signorini et al.*, 1999], *in situ* measurements are sparse in this area. In 2004, the oceanographic cruise BIOSOPE (BIogeochemistry and Optics South Pacific Experiment), which was devoted to study the biogeochemical properties in the South Pacific, crossed the Marquesas islands and performed vertical profiles of nutrient at one station (see star in Figure IV-1a) westward of Nuku Hiva

[*Raimbault et al.*, 2007; *Claustre et al.*, 2008; *Raimbault and Garcia*, 2008]. These profiles revealed high macronutrient concentrations in the surface layers with nitrate (NO3), phosphate (PO4) and silicate (Si) reaching 2, 0.4 and 1 µmol L^{-1}, respectively. These values do not seem to indicate a macronutrient depletion. On the other hand, Fe concentrations in the Marquesas were relatively weak ($0.15 < Fe < 0.41$ nmol L^{-1}) and a limitation of phytoplankton growth was suspected [*Blain et al.*, 2008]. In 2012, a second oceanographic cruise *Pakaihi i te Moana* (PM-12) also measured strong macronutrient concentrations in the archipelago. A contrast between the north and the south of the archipelago was reported with higher concentrations of macronutrient and Chl in the North than in the South [*Martinez et al.*, 2016].

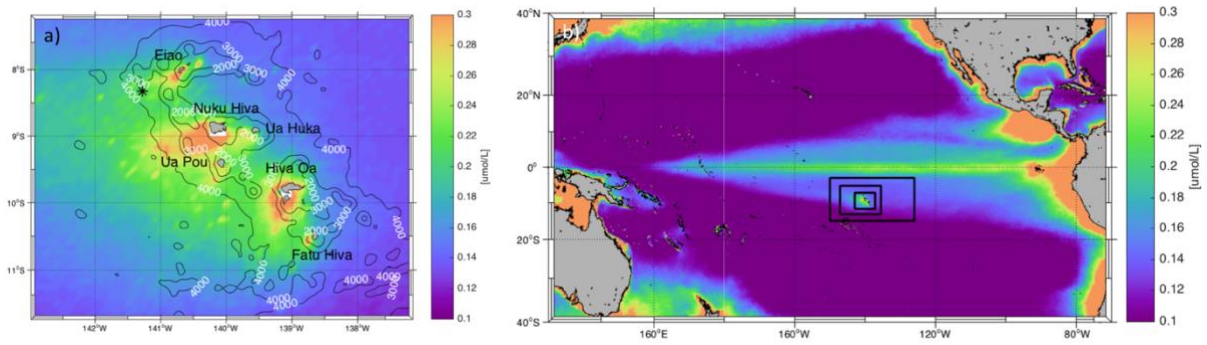

Figure IV-1: (a) Mean Chl from 1998 to 2010 over the Marquesas archipelago (in µmol L^{-1}). The black contours with the depth value in white (in m) represent the bottom topography from the 2-arc minute topography/bathymetry dataset ETOPO2 used in the model configuration. The star represents the MAR3 station from the BIOSOPE cruise. (b) Mean Chl over the Pacific Ocean over the same time period from SeaWIFS (in µmol L^{-1}). The three embedded grids used in the model are represented by the rectangular boxes.

The Marquesas archipelago is located in the northern part of French Polynesia where the South Equatorial Current (SEC) flows south-westward. It is composed by a dozen of small volcanic islands with no surrounded coral reefs. The islands are characterized by rugged steep cliffs and high volcanic mountains up to 1224m [*Maury et al.*, 2014]. The main four islands are Nuku Hiva (339 km^2), Ua Pou (105 km^2) and Ua Huka (83 km^2) in the northern part of the archipelago and Hiva Oa (320 km^2) in the southern region (Figure IV-1a). One of the only study investigating the Marquesan IME associated the occurrence of Chl blooms with an intensification of the surface current [*Martinez and Maamaatuaiahutapu*, 2004]. The authors

assumed that the mechanism at the origin of the blooms results from the interaction between the chain of islands and the mean flow, but they were unable to elucidate the relevant process. The present work aims at investigating the IME of the Marquesas islands and the physical processes that could explain the biological enhancement. The paper is organized as follows: Section 2 describes the physical-biological coupled numerical model, the data and the methodology. The seasonal variability of phytoplankton biomass as well as macro and micro nutrients is characterized, and the mechanisms are investigated in section 3. Finally, section 4 concludes this study.

IV.2. Data and methods

IV.2.1. ROMS-PISCES

The physical-biogeochemical model configuration used here is based on a physical model: ROMS (Regional Ocean Modeling System, https://www.myroms.org), coupled with a biogeochemical model: PISCES (Pelagic Interaction Scheme for Carbon and Ecosystem Studies) [*Aumont et al.*, 2015]. We used the ROMS-AGRIF (Adaptive Grid Refinement in Fortran) code provided by Debreu et al. [2012] and Penven et al. [2007]. The AGRIF version is especially suitable to study regional scale since it has the ability to manage an arbitrary number of fixed grids and embedding levels. We have configured the two-way embedding procedure. It means that the parent grid provides the boundary conditions for the child grid, and that the solution of the child grid is used to improve the larger scale parent grid solution for both physical and biogeochemical parameters. This allows a smooth and continuous interfacing between grid levels [*Debreu and Blayo*, 2008; *Debreu et al.*, 2012]. ROMS is a split-explicit, free surface and terrain-following vertical coordinate oceanic model [*Shchepetkin and McWilliams*, 2003, 2005]. PISCES is a biogeochemical model that simulates the first trophic levels of the marine ecosystem and the biogeochemical cycles of carbon and the main nutrients [*Aumont et al.*, 2015]. It has 24 compartments, of which 4 are living pools composed of 2 phytoplankton size-classes (nanophytoplankton and diatoms) and 2 zooplankton size-classes (microzooplankton and mesozooplankton). The phytoplankton growth is limited by 5 external nutrients: NO3, ammonium, PO4, Si and Fe. Chl from the 2 phytoplankton groups is parameterized using the photo-adaptive model of *Geider et al.* [1997]. Therefore, Chl in the model is hereafter defined as the sum of Chl in nanophytoplankton and diatoms.

The external physical forcings consist of monthly climatologies and are presented in *Raapoto et al.* [2018]. At the surface, the heat and fresh water fluxes are extracted on a monthly ½° grid from the Comprehensive Ocean-Atmosphere dataset (COADS) [*da Silva et al.*, 1994]. The wind forcing is issued from the QuikSCAT monthly climatology calculated over 1999-2009, on a ¼° grid [*Lungu and Callahan*, 2006]. The boundary conditions and initial state are based on the objective analysis of the World Ocean Atlas 2013 (WOA13) monthly climatology on a ¼° grid [*Locarnini et al.*, 2013; *Zweng et al.*, 2013]. Initial and boundary conditions for all the PISCES prognostic variables are derived from the monthly climatology WOA-PISCES [*Goyet et al.*, 2000; *Aumont and Bopp*, 2006].

The choice of these physical forcings that are the most suitable for the archipelago was investigate in Raapoto et al. (in rev). Then, the circulation in the archipelago using these forcings was investigated in *Raapoto et al.* [2018]. Compared to the setup presented in *Raapoto et al.* [2018], a third larger and coarser grid has been added to avoid biological enrichment artefacts at the eastern boundary. We defined the same embedded grids for all simulations: 1) the first grid extends from 126°W to 150°W and 3°S to 15°S; 2) the second grid extends from 135.47°W to 147.13°W and 5.24°S to 13.19°S; 3) the third grid extends from 137.16°W to 142.98°W and 7.18°S to 11.74°S (Figure IV-1b). The grid refinement rate is 3, implying a 1/5° (~22km), 1/15° (~7km) and 1/45° (~2.5 km) grid resolutions for the first, second and third grid, respectively. This allows a sufficient sampling of the island topography and of the fine-scale dynamics, as the first baroclinic Rossby radius of deformation is about 120 km in this region according to Chelton et al. (1998). The three grids have 32 vertical levels and the vertical s-coordinate is stretched for boundary layer resolution. The topography is derived from the 2' resolution ETOPO2 database provided by NOAA-NGDC [*Smith and Sandwell*, 1997]. The bathymetry field has been filtered to keep the slope parameter < 0.25 [*Beckmann and Haidvogel*, 1993].

IV.2.2. Set up of the 4 biological configurations

Prior to running the simulations, a comparison of the WOA-PISCES data was performed with the only available full set of micro- and macronutrient in situ measurements from station MAR3 of the BIOSOPE oceanographic campaign [*Blain et al.*, 2008] (Figure IV-2). Samples at MAR3, located at -141.2777°E; −8.3213°N (Figure IV-1a), were collected on 10-29-2004.

The BIOSOPE vertical profiles of NO3 and PO4 concentrations at MAR3 are close to the WOA-PISCES data in the upper 150 m (Figure IV-2). Values are high enough to not be limitant

as previously reported [*Signorini et al.*, 1999; *Raimbault et al.*, 2007; *Raimbault and Garcia*, 2008; *Martinez et al.*, 2016]. Fe concentrations are strongly underestimated in WOA-PISCES compared to the MAR3 data (Figure IV-2c). Nutrient profiles from two other stations around the archipelago also present the same patterns. Since it has been suggested that Fe is the limiting factor in the archipelago [*Blain et al.*, 2008], the impact of Fe in the Marquesas IME is here investigated through 4 simulations with different Fe concentration conditions:

- Run_{Ref}: is the reference simulation. It uses the WOA-PISCES Fe concentrations as initial and lateral boundary conditions;
- $Run_{Biosope}$: Fe concentrations from the surface to the Fe maximum gradient depth are increased by adding an Fe concentration of 0.14 10^{-3} nmol.L^{-1} to fit with the BIOSOPE observations (Figure IV-2c). These values are imposed over the entire domain for the initial conditions and at the boundaries for the lateral forcing.
- $Run_{Sed2.5}$: same as Run_{Ref} but a Fe flux of 2.5 µmol m^{-2} d^{-1} from the sediment is added.
- Run_{Sed5}: same as $Run_{Sed2.5}$ but applying a Fe flux of 5 µmol m^{-2} d^{-1}.

In the model, the Fe resuspension from the sediment is set using a constant flux on the first vertical level of parent and child grids.

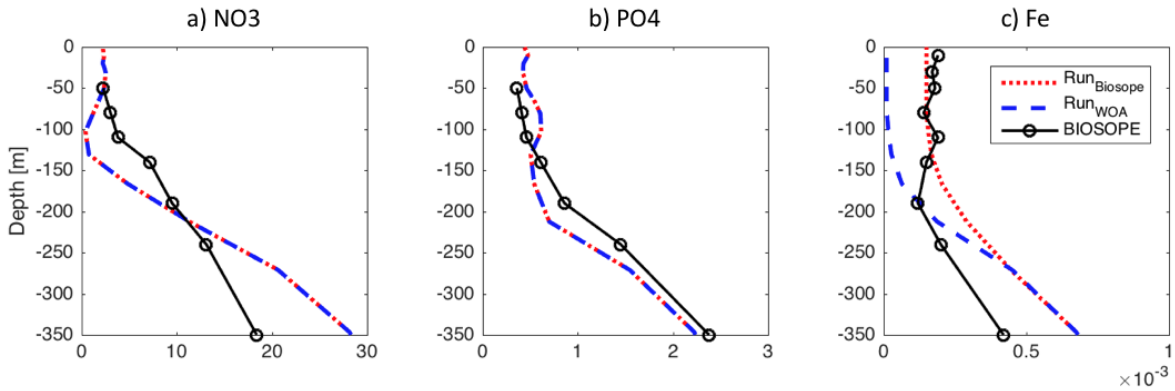

*Figure IV-2: Vertical profiles of (a) NO3, (b) PO4 and (c) Fe at MAR3 station the 10/29/2004 during BIOSOPE cruise (black curve - [*Blain et al.*, 2008]) and from the forcing files of Run_{WOA} (blue dashed curve) and $Run_{Biosope}$ (red dotted curve) at the same location than MAR3 for the month of October. MAR3 is represented by a star on Figure 1a.*

At the best of our knowledge, atmospheric dust deposition and river input data are not available. Using time variation of rainfall in the archipelago, *Martinez and Maamaatuaiahutapu* [2004] reported that nutrient inputs from land drainage seems to be negligible. Then, these three input are not considered in our simulations. Table IV-1 summarizes all the simulations performed.

	Run$_{Ref}$	**Run$_{Biosope}$**	**Run$_{Sed2.5}$**	**Run$_{Sed5}$**
Physical initial and boundary conditions	WOA 2013			
Physical surface forcing	QSCAT			
Heat and fresh water flux	COADS			
Biological initial and boundary conditions (except the Fe compartment)	WOA-PISCES			
Fe compartment	WOA-PISCES	Fit to BIOSOPE observations for the upper layer	WOA-PISCES + a constant 2.5 μmol m^{-2} d^{-1} Fe flux from sediment	WOA-PISCES + a constant 5 μmol m^{-2} d^{-1} Fe flux from sediment

Table IV-1: Summary of the ROMS-PISCES initial and boundary conditions used in the 4 simulations.

IV.2.3. In-situ and satellite observations

Model outputs are compared with observations issued from a Biogeochemical-Argo (BGC-Argo) float [*Johnson and Claustre*, 2016], identified from its World Meteorological Organization number 6900985. This float was equipped with a Seabird standard conductivity-temperature-depth (CTD), completed with additional sensor packages. The Satlantic OCR radiometer measures the downwelling irradiance at three wavelengths (380 nm, 410 nm and 490 nm). The WET Labs ECO Puck Triplet is composed of a chlorophyll *a* fluorometer, a Colored Dissolved Organic Matter (CDOM) fluorometer, and a sensor that measures the backscattering coefficient at 532 nm (excitation at 370; emission at 460nm). This float was deployed in August 2011 westward of Nuku Hiva and drifted over one year and a half within the archipelago. The profiles have a 1-meter vertical resolution and are recorded daily from 08-02-2011 to 09-23-2011 and every 5 days until 09-22-2012.

We also use satellite derived Chl from GlobColour (http://www.globcolour.info). The weighted average of single-sensor Level-2 Chl products merged from the SeaWiFS, MODIS, MERIS and VIIRS sensors instruments from 1998 to 2015 increases the data coverage in both time and space. We use eight-day composites with a spatial resolution of 4 km. Further details on the GlobColour data set can be found at: http://www.globcolour.info/CDR_Docs/GlobCOLOUR_PUG.pdf. The Chl signal derived from satellite is strongly modulated by intra- and inter-annual variability in the Marquesas archipelago [*Martinez et al.*, 2016]. The Chl seasonal signal has been obtained by filtering off the frequencies lower than the yearly signal in a Fourier transform analysis. This seasonal Chl signal is hereafter referred to as $Chl_{GlobColour}$.

Therefore, it is here irrelevant to calculate a monthly average to extract the seasonal signal. Thus, the Chl seasonal signal has been extracted performing a Fourier transform. All frequencies larger than a year have been removed and the seasonal cycle has been reconstructed and is hereafter referred to $Chl_{GlobColour}$.

IV.2.4. Dynamical and biogeochemical metrics

In this study, we define the eddy kinetic energy (EKE) as the kinetic energy due to transient dynamic given by: $EKE = \frac{1}{2}(u'^2 + v'^2)$, where $u' = u - \bar{u}$ and $v' = v - \bar{v}$, with u and v the zonal and meridional components of the velocity at 10 m, $\bar{u}$ and $\bar{v}$ their temporal mean from year 4 to 5.

The mixed layer depth (MLD) from the model is estimated according to the difference in potential density between 10 m and the base of the mixed layer using a threshold of 0.3 kg m^{-3}.

Remote sensing only allows the measurement of surface Chl in a layer defined from the surface to the first optical depth [*Gordon and McCluney*, 1975]. This layer represents approximately the fifth of the euphotic layer [*Morel and Berthon*, 1989]. To compare satellite derived $Chl_{GlobColour}$ and Chl from our models, we have computed a mean depth of penetration. For surface Chl between 0.1 and 0.2 mg m^{-3}, the depth of penetration is 17 and 13 m, respectively (calculated from *Morel and Berthon* [1989]). Therefore, $Chl_{GlobColour}$ is compared with model outputs averaged over the first 15 meters of the water column.

IV.3. Results and discussion

IV.3.1. Surface ocean dynamics

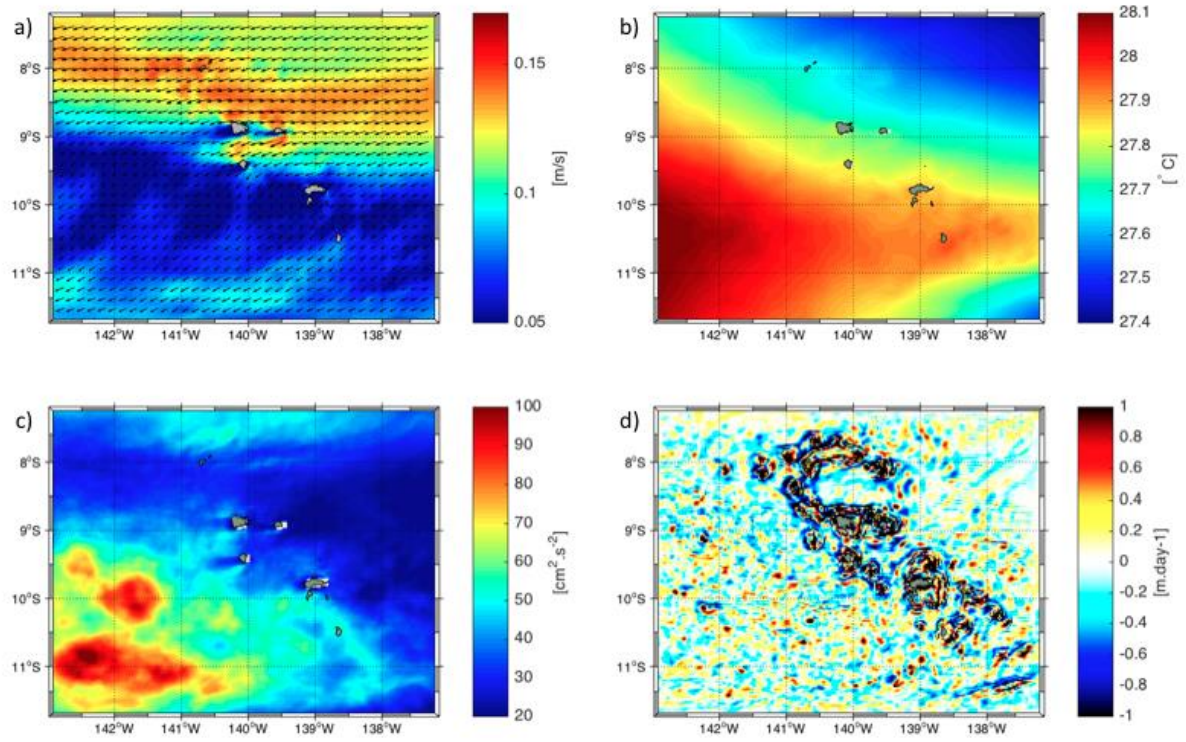

Figure IV-3: Annual mean over year 4 and 5 of (a) current, (b) temperature, (c) EKE and (d) vertical velocity at 10 m.

The 4 ROMS-PISCES simulations are initiated and forced with the same physical forcings as the ones used in *Raapoto et al.* [2018]. Therefore, the ocean dynamics in these 4 simulations are similar to the ones described in *Raapoto et al.* [2018]. Hence, the dynamical context is only briefly described here, and for Run_{Ref} only. For further details on the ocean dynamics, the reader is invited to read *Raapoto et al.* [2018].

The general surface circulation is characterized by the presence of a stronger South Equatorial Current (SEC) in the northern part of the archipelago than in the south (~15 cm s^{-1} *vs*. 6 cm s^{-1}, respectively; Figure IV-3a). In the north, the SEC accelerates on the flanks of the islands and a region of weak current is observed just downstream the islands. The SST annual average (Figure IV-3b) exhibits colder water in the north (≤ 27.5°C) as the imprint of the equatorial upwelling [*Wyrtki*, 1981] , and warmer water in the south (≥ 28°C) as the eastward signature of the western Pacific warm pool [*Yan et al.*, 1992]. The mean EKE (Figure IV-3c) is high in the

wake of the southern islands with values reaching up to 95 cm^2 s^{-2} and at the northern boundary, south of the equator with values up to 50 cm^2 s^{-2}. The eddy activity is weaker elsewhere, and noticeably in the wake of the northern islands. The mean vertical velocities (Figure IV-3d) are strong near the islands, suggesting a strong impact of the bathymetry.

IV.3.2. Comparison of biological simulations with observations

The annual means of $Chl_{GlobColour}$ and Chl from the 4 simulations are presented in Figure IV-4a,c-f, as well as their corresponding seasonal variability in Figure IV-4b. $Chl_{GlobColour}$ is high near the islands with a plume extending south-westward, downstream the SEC (Figure IV-4a). Its seasonal variability presents a maximum in April with a secondary increase in December, and a minimum in September-October (Figure IV-4b). The Run_{Ref} simulation does not exhibit any IME and presents low Chl_{Ref} values all over the archipelago (Figure IV-4c). Nevertheless, the model reproduces the $Chl_{GlobColour}$ seasonal cycle, although with a 1-month lag-time and weaker concentrations (Figure IV-4b, in blue). The $Run_{Biosope}$ does not generates an IME either (Figure IV-4d). Phytoplankton enriched waters can be observed north-east of the archipelago as a result of the higher $Fe_{Biosope}$ than Fe_{Ref} which forces the model at the north-eastern boundary and then flows southwestward along the SEC. As expected, the $Chl_{Biosope}$ seasonal variability presents higher values and amplitude than Chl_{Ref} (Figure IV-4b, in orange *vs*. blue, respectively). However, the seasonality of $Chl_{Biosope}$ differs from the 3 other simulations with high concentration from May to October. This difference may be due to a change in the biological activity near the boundaries induced by higher $Fe_{Biosope}$.

Adding Fe from the sediment in $Run_{Sed2.5}$ allows generating a small plume of $Chl_{Sed2.5}$ downstream the largest islands (Figure IV-4e). No plume of phytoplankton appears downstream the two smallest islands of Eiao, in the north, and Fatu Hiva, in the south, as the too coarse bathymetry, used in the model, prevents them to be represented. The $Chl_{Sed2.5}$ seasonal variability is similar to Chl_{Ref} but with a higher concentration, and hence is closer to the satellite observations (Figure IV-4b, in yellow). Finally, doubling the Fe input from the sediments allows Chl_{Sed5} to exhibit a stronger IME (Figure IV-4f). This spatial pattern is the closest to the one observed in remote sensing. The Chl_{Sed5} seasonal cycle is even closer to $Chl_{GlobColour}$ than Chl_{Ref} and $Chl_{Sed2.5}$. Nonetheless, the increase of Fe from sediment tends to damp the seasonal cycle of the signal. Here, the necessity of an Fe input from the sediments in the model is clearly highlighted to reproduce the IME observed in remote sensing.

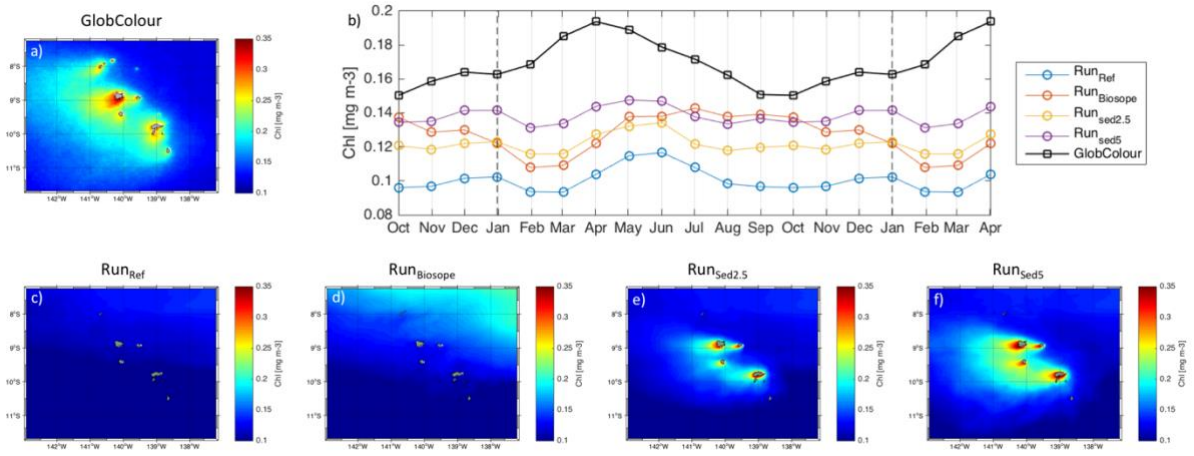

Figure IV-4: (a) Annual mean of surface $Chl_{GlobColour}$ in mg m^{-3}. (b) Seasonal variability of $Chl_{GlobColour}$ (1998 to 2015) and Chl from the 4 simulations (year 4 to 5). Annual mean of Chl for simulation (c) Run_{Ref}, (d) $Run_{Biosope}$, (e) $Run_{Sed2.5}$ and (f) Run_{Sed5}.

To provide an insight of the Chl vertical distribution within the archipelago, we use the only *in situ* vertical time series available (Figure IV-5a and b). These measurements were obtained from the BGC-Argo float released on 08-02-2011 leeward of Nuku Hiva. The float trajectory is given by the crosses represented in Figure IV-5a with the color corresponding to the date of its ascent (color bar under Figure IV-5b). During approximately 2 months (late-August to early-October 2011), the float stays in the lee of Nuku Hiva (Figure IV-5a and b). Indeed, as revealed by Figure IV-3a, currents in this region are weak. In this area, $Chl_{BGC\text{-}Argo}$ is high (> 0.5 mg m^{-3}) with peaks exceeding 1 mg m^{-3} and homogeneous from the surface down to 70 m (Figure IV-5b). Then, the float drifts southward away from Nuku Hiva, crossing the northern island wakes. Here again, $Chl_{BGC\text{-}Argo}$ vertical profiles remains homogenous with values around 0.5 mg m^{-3}. In late-February 2012, the $Chl_{BGC\text{-}Argo}$ pattern changes and starts presenting a deep chlorophyll maximum (DCM) around 50-100 m, characteristic of more oligotrophic waters [*Ras et al.*, 2008]. This change is concomitant with the transition from the northern to the southern islands of the archipelago (Figure IV-5a). Then $Chl_{BGC\text{-}Argo}$ alternates between a DCM and a homogeneous pattern with weaker values than in the north. This north-south difference was also observed during the oceanographic cruise PM-12 where in situ Chl were stronger and homogeneous in the northern region than in the south [*Martinez et al.*, 2016].

Sampling the model outputs along the same trajectory than the BGC-Argo float and for the corresponding climatological dates, we obtain Chl that are twice lower than the observations (Figure IV-5c-f). Chl_{Ref} presents a well-marked DCM over the whole trajectory with the highest

values reaching 0.22 mg m^{-3} (Figure IV-5c). $Chl_{Biosope}$ exhibits similar patterns with higher concentrations (~0.3 mg m^{-3}) due to higher Fe input at the boundaries (Figure IV-5d). When adding Fe from the sediment, vertical profiles differ from the two previous ones and are closer to the *in-situ* data (Figure IV-5e-f). $Chl_{Sed2.5}$ and Chl_{Sed5} are close with higher values for Run_{Sed5} due to the stronger Fe flux from the sediment. In the northern islands, $Chl_{Sed2.5}$ and Chl_{Sed5} profiles alternate between DCM and homogeneous patterns. In the southern region, concentrations are weaker and present a well-marked DCM.

Since Run_{Ref} and $Run_{Biosope}$ always exhibit a significant DCM, the two other simulations, with Fe input from the sediment, are closer to the BGC-Argo float. These two last simulations also allow to highlight the north – south differences. However, Chl obtained in the model still remains weaker than $Chl_{BGC\text{-}Argo}$.

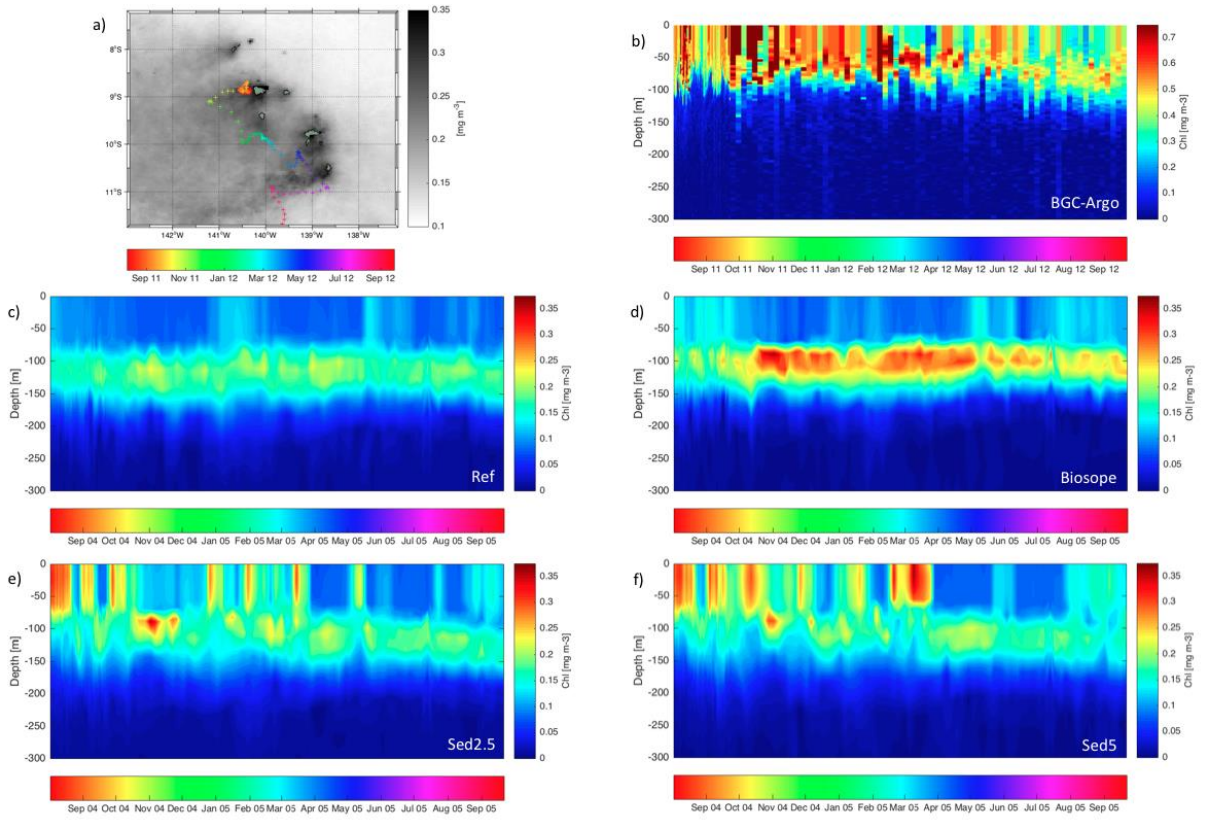

Figure IV-5: (a) Trajectory of the BGC-Argo float deployed west of Nuku-Hiva on 08-02-2011 and drifting out the area on 09-22-2012. The corresponding dates are given by the horizontal color bar. Satellite derived $Chl_{GlobColour}$ averaged over the whole-time period is shown with a gray scale. Chl vertical distribution (mg m^{-3}) (b) along the BGC-Argo float trajectory and for (c) Run_{Ref}, (d) $Run_{Biosope}$, (e) $Run_{Sed2.5}$ and (f) Run_{Sed5}. The horizontal color bar in (b) gives the date of the above corresponding vertical profiles. The one used for simulations (c) to (f) refers

to the climatological dates of the model. Note that, for clarity, the upper limit of the color bar used for the BGC-Argo float is twice larger than the one used for the simulations.

IV.3.3. Seasonal variability of phytoplankton growth

Here we explore the physical mechanisms involved in the seasonal Chl variability and the influence of the islands using Run_{Ref}. We investigate the physical and biogeochemical properties along a transect crossing the largest island, Nuku Hiva (the NH-transect on Figure IV-6a) following the main flow direction.

Run_{Ref} shows low mean surface Fe_{Ref} ($3\ 10^{-3}$ to $10\ 10^{-3}$ nmol L^{-1}; Figure IV-6a). A gradient with the highest values in the north-east is induced by the equatorial higher Fe, advected southwestward along the SEC. In Figure IV-6b, we consider the mean surface Chl_{Ref} upstream (North-East) and downstream (South-West) Nuku Hiva, along the NH-transect. Chl_{Ref} patterns are close upstream and downstream, indicating the absence of an IME. In average, Chl_{Ref} is low (~0.1 mg m^{-3}) with a clear increase in late-April and July up to 0.17 mg m^{-3}, and secondary peaks in October and November. The downstream time-series show a time lag of 1 to 2 weeks compared with the upstream ones. This time lag can be explained through the latitude-time diagram (Hovmöller diagram) of Chl_{Ref} (Figure IV-6c). Indeed, Chl_{Ref} increases earlier at the northern boundary, then propagates southward. The Chl_{Ref} increases are concomitant with those of Fe, NO3 and PO4 concentrations (Figure IV-6d-f). The Si concentration varies differently from the other nutrients, particularly during April and May when it remains relatively low (3 μmol L^{-1} - Figure IV-6g). Nevertheless, at that time, the weaker Si values do not prevent the increase of Chl_{Ref}. This is due to the minor contribution of diatoms, which are sensitive to Si, to the total phytoplankton biomass, largely dominated by nanophytoplankton (83.6 %). Moreover, macronutrient (NO3, PO4 and Si) concentrations represented in the model are consistent with in situ observations during BIOSOPE [*Blain et al.*, 2008; *Claustre et al.*, 2008] and PM-12 cruises [*Martinez et al.*, 2016].

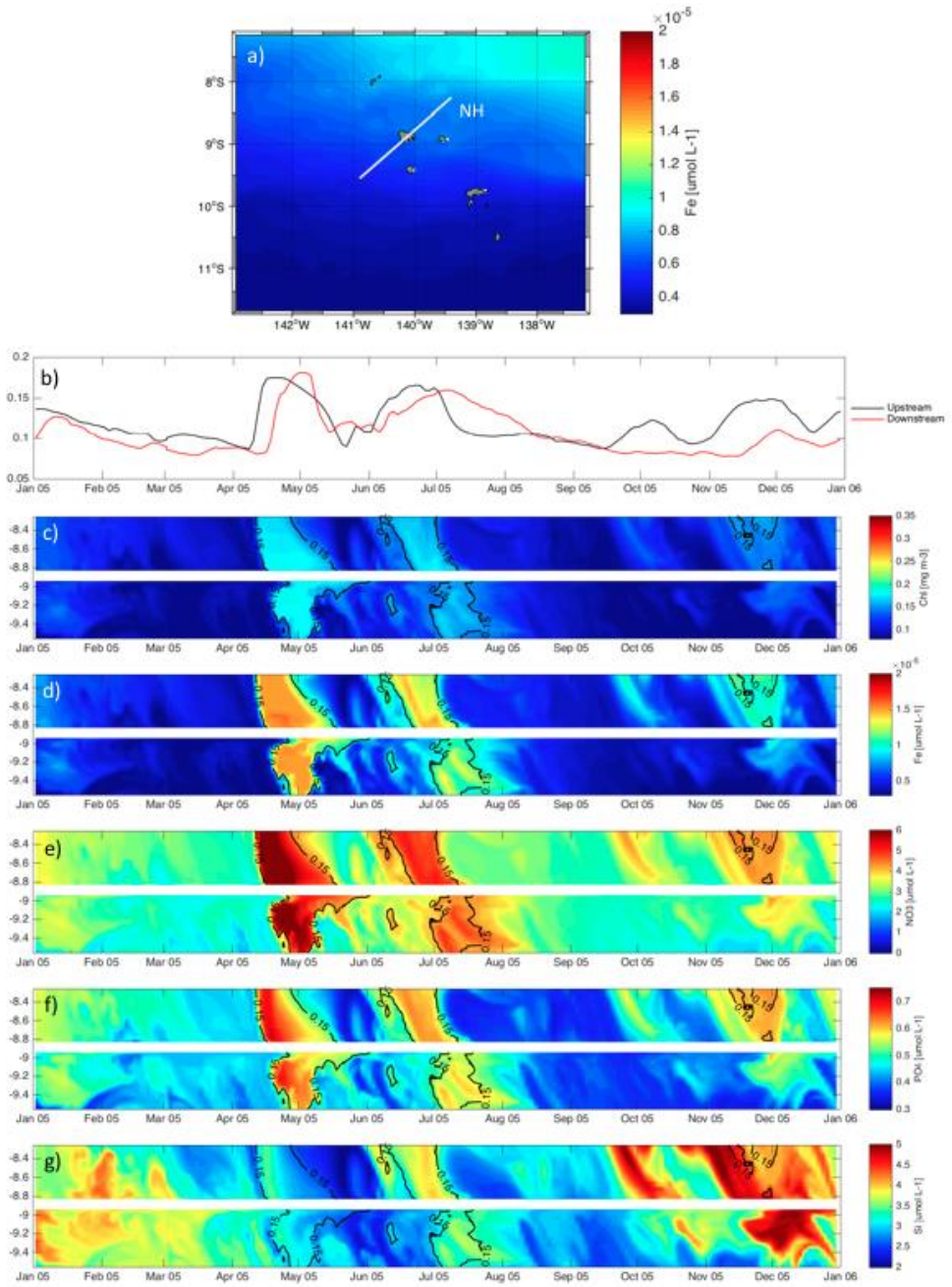

Figure IV-6: (a) Annual mean of Fe concentration in the archipelago during year 5 of Run$_{Ref}$ at 10 m. The NH-transect is represented by the white dashed line. (b) Mean Chl concentration upstream and downstream of the island along NH-transect at 10 m. Latitude-time diagrams of (c) Chl, (d) Fe, (e) NO3, (f) PO4 and (g) Si along NH-transect during the fifth year of simulation at 10 m (units are in mg m^{-3} for Chl and µmol L^{-1} for all the nutrients). The 0.15 mg m^{-3} iso-contour of Chl is also drawn on the latitude-time diagrams.

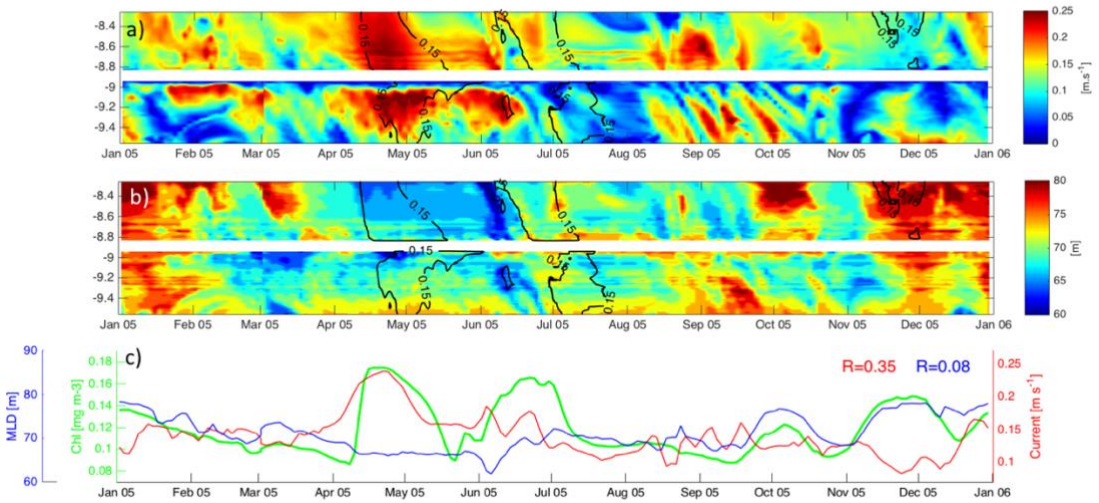

Figure IV-7: Latitude-time diagram of (a) current intensity at -10 m (units in m s^{-1}) and (b) MLD (units in m) along NH-transect during the fifth year of Run_{Ref}. The 0.15 mg m^{-3} iso-contour of Chl_{Ref} is also drawn on the two latitude-time diagrams. (c) Average of Chl_{Ref}, MLD and current upstream of NH-transect.

Physical mechanisms forcing the ocean dynamics at the archipelago scale are likely to impact the phytoplankton seasonal variability. Among them, horizontal advection of nutrient-rich waters from the equatorial area could bring nutrients toward the archipelago allowing phytoplankton growth. The latitude-time diagram of current intensities on the NH-transect shows strong currents reaching above 20 cm s^{-1} when Chl_{Ref} and nutrients also increase (Figure IV-7a). The strengthening of the SEC reveals an important role of the current in this configuration. The advection of nutrients from equatorial rich water through the islands allows the enhancement of the local biological parameters. Hence, the concomitant increase of the surface current and Chl_{Ref} in the archipelago are consistent with satellite observations in *Martinez and Maamaatuaiahutapu* [2004]. The wintertime convection associated with deeper mixed layer uplifting nutrients from the nutricline toward the surface could also allow phytoplankton growth. In June, the MLD is at its shallowest (60 m – Figure IV-7b). While in late-November, it deepens at its maximum (80 m) and induces an increase of nutrient (Figure IV-6d-g). However, during this period, Fe_{Ref} increase is weak and is likely limiting the Chl_{Ref}. In summary, this configuration suggests that nutrients are supplied by both the advection of northern waters by the SEC and the deepening of the MLD. Both processes are well marked upstream of the island as seen in Figure IV-7c and also correspond with the seasonal variability observed in Figure IV-4b. Chl_{Ref} increases in late-April and June are well correlated with

current strengthening while the one at the end of the year is well correlated with the deepening of the MLD. The first mechanism was suggested by *Signorini et al.* [1999] and observed by [*Martinez and Maamaatuaiahutapu* [2004] while the second one has never been investigated before in this area. However, if we only consider these two processes, Chl values are too weak and do not allow the generation of IME, as seen in Figure IV-4a.

A similar investigation is performed for $Run_{Biosope}$ along the NH-transect (Figure IV-8). Mean $Fe_{Biosope}$ in this configuration closely follows the same spatial pattern as for Run_{Ref} (Figure IV-6a) with values twice higher at the north-eastern boundary, induced by the new Fe lateral forcing (not shown). This increase of Fe directly impacts $Chl_{Biosope}$ with higher values than Run_{Ref} and a seasonal maximum exceeding 0.2 mg m^{-3} upstream and downstream the transect crossing Nuku-Hiva (Figure IV-8a and b). The main difference between $Run_{Biosope}$ and Run_{Ref} affects the first bloom in late-April. The $Chl_{Biosope}$ values remain high from late-April to early-June while Chl_{Ref} decrease earlier (early-May), simultaneously with Fe_{Ref}, $NO3_{Ref}$ and $PO4_{Ref}$. In $Run_{Biosope}$ macronutrients are consumed by $Chl_{Biosope}$ and their concentrations start decreasing, while $Fe_{Biosope}$ remains higher than 2 10^{-3} nmol L^{-1}. Although $NO3_{Biosope}$ and $PO4_{Biosope}$ decrease, $Chl_{Biosope}$ follows the $Fe_{Biosope}$ variation and remains higher than 0.2 mg m^{-3}. It only starts decreasing in early-June, after the macro- and micronutrient depletion. After that, the surface layer replenishes itself in macronutrients. However, $Chl_{Biosope}$ remains low, as well as $Fe_{Biosope}$, highlighting the Fe limitation in the archipelago.
In this simulation, Fe at the boundaries have been risen to fit the BIOSOPE measurements. However, concentrations obtained in the model outputs are still ten times inferior to the observations (Figure IV-8c *vs.* Figure IV-2a). For the macronutrients, values along the NH-transect are weaker than in Run_{Ref}. Indeed, high $Fe_{Biosope}$ in these Fe depleted waters allows phytoplankton growth and the consumption of macronutrients. Here again, this configuration does not allow the generation of an IME but raises concerns on the Fe sources. Although we increase Fe concentrations at the boundaries, $Fe_{Biosope}$ remains weak in the archipelago. This suggests the contribution of a local Fe source as proposed by *Blain et al.* [2008].

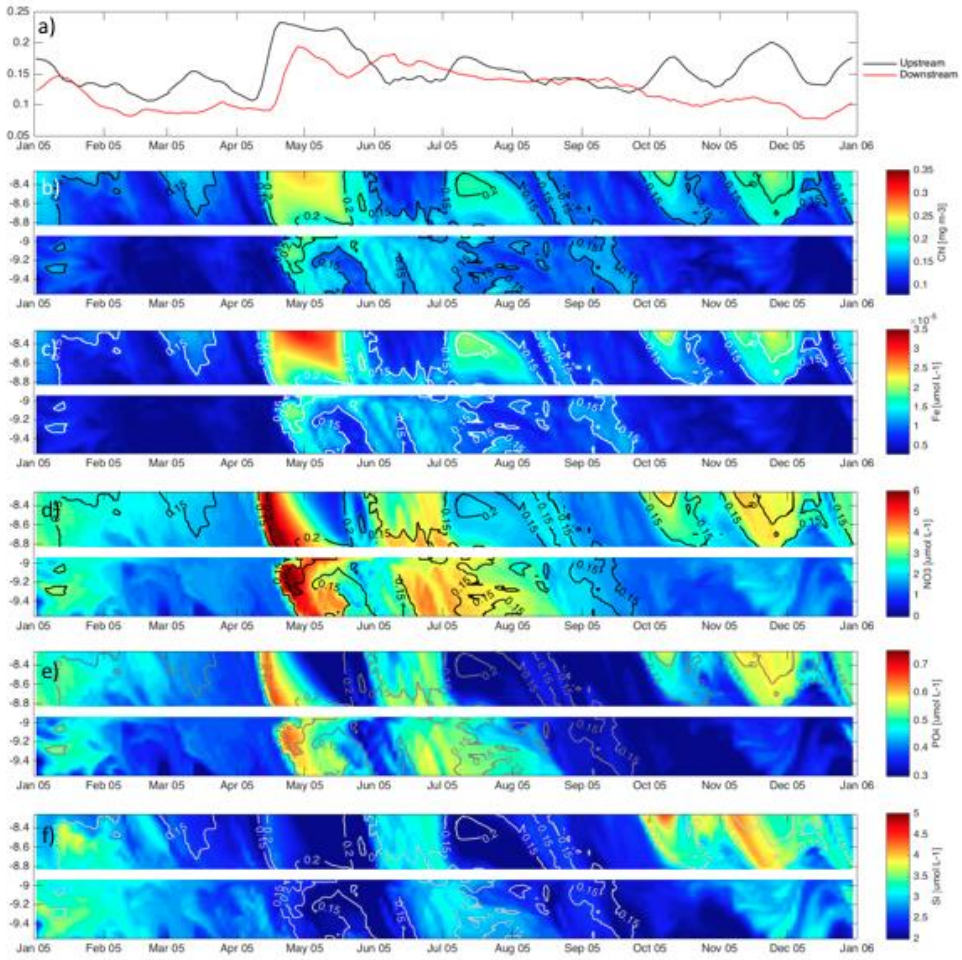

Figure IV-8: (a) Mean Chl concentration upstream and downstream of the island along NH-transect at -10 m for $Run_{Biosope}$*. Latitude-time diagram of (b) Chl, (c) Fe, (d) NO3, (e) PO4 and (f) Si along NH-transect during the fifth year of simulation at -10 m (units are in mg* m^{-3} *for Chl and µmol* L^{-1} *for all the nutrients). The 0.15 and 0.2 mg* m^{-3} *iso-contours of* $Chl_{Biosope}$ *are drawn on the latitude-time diagrams.*

IV.3.4. Sediment enrichment

The previous two simulations do not reproduce any IME but reveal an enrichment due to the deepening of the MLD and the advection of northern waters through the archipelago. They also highlight the importance of Fe for Chl growth in the archipelago and suggest a local Fe source. Therefore, an additional input of Fe from sediment in $Run_{Sed2.5}$ and Run_{Sed5} was considered. Run_{Sed5} presents similar patterns than $Run_{Sed2.5}$, but with closer results to the satellite observations. Therefore, we only present here results from Run_{Sed5}.

Along the NH-transect, noticeable differences between the upstream and downstream Chl_{Sed5} averages are observed (Figure IV-9a). Upstream of the island, Chl_{Sed5} is relatively low (0.15 mg m^{-3}). Values observed on the latitude-time diagram exhibit a strong variability in the north-east (Figure IV-9b). Upstream of the island, two increases of Chl_{Sed5} and Fe_{Sed5} appears during late-April and July in parallel to the strengthening of the SEC, as in the $Run_{Ref.}$ A weaker increase of Chl_{Sed5} due to the MLD also appears in late-November. Unlike Run_{Ref} and $Run_{Biosope}$, Chl_{Sed5} and Fe_{Sed5} increase in December. At the same time, the meridional current becomes strongly positive inducing a northward current (Figure IV-9e) and the transport of nutrients upstream the island. Consistently, all over the year, Chl_{Sed5} is high very close to the shore upstream the island, this is strongly correlated with local northward veins of current also shown in Figure IV-9e.

Downstream Nuku Hiva, the input of Fe from the sediments allows a strong Chl_{Sed5} growth (0.25 mg m^{-3} - Figure IV-9a), highlighting an IME. Both Chl_{Sed5} and Fe_{Sed5} distributions are strongly correlated on the latitude-time diagram (Figure IV-9b-c) and reveal the advection of Fe southward from the island (Figure IV-9d). However, even in the Run_{Sed5}, the Fe_{Sed5} in the surface water is still inferior but comparable with surface measures from the profile at MAR3 in BIOSOPE (Figure IV-9c vs Figure IV-2a). In the very close shore downstream the island, Chl_{Sed5} remains high all over the year while the currents are weak. This area corresponds to the calm zone identified in Figure IV-3a and by *Raapoto et al.* [2018]. When surface currents strengthen downstream of Nuku Hiva, Fe_{Sed5} is advected away from the island and Chl_{Sed5} downstream decreases (as in April to June – Figure IV-9b-d). Conversely, high Chl_{Sed5} and Fe_{Sed5} veins can be observed southward along the transect (as in March and July) concomitantly with weak current. Vertical velocities do not present specific patterns (Figure IV-9f). Though, they are generally positive very close to the island inducing an uplift of Fe to the surface along the southern coast.

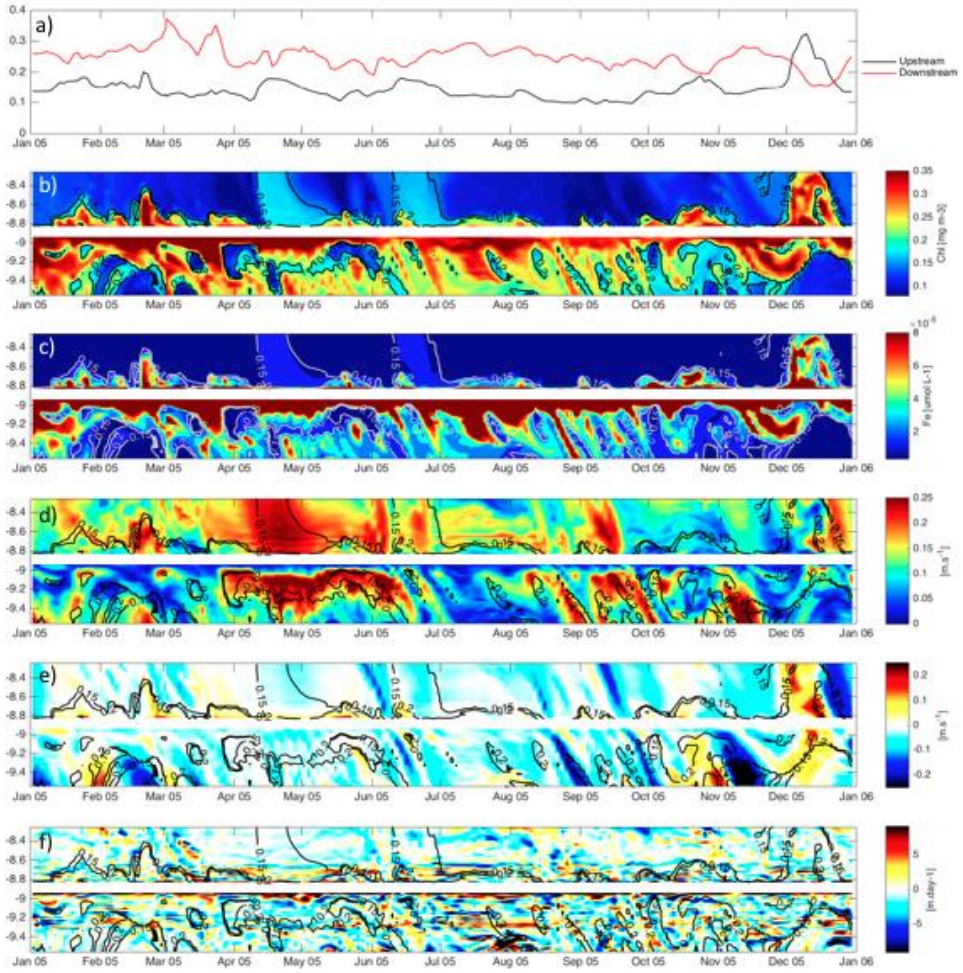

Figure IV-9: (a) Mean Chl concentration upstream and downstream of the island along NH-transect at -10 m for Run_{Sed5}*. Latitude-time diagram of (b) Chl (mg* m^{-3}*), (c) Fe (µmol* L^{-1}*), (d) current intensity (m* s^{-1}*), (e) meridional current (m* s^{-1}*) and (f) vertical velocity (m* day^{-1}*) along NH-transect during the fifth year of simulation at -10 m. The 0.15 and 0.2 mg* m^{-3} *iso-contours of* Chl_{Sed5} *is also drawn on the latitude-time diagrams.*

The biological enrichment observed in the Marquesas archipelago can be influenced by inter-annual events such as ENSO (El Niño Southern Oscillation) [*Signorini et al.*, 1999; *Legeckis et al.*, 2004; *Radenac et al.*, 2012; *Martinez et al.*, 2018]. However, the model simulations presented here are based on seasonal climatology only and do not take into account inter-annual processes. Hence, the satellite derived surface $Chl_{GlobColour}$ along the NH-transect is shown from 2003, which is a neutral ENSO year (Figure IV-10). Along the transect, model and observations have fairly close patterns (Figure IV-9b vs Figure IV-10). $Chl_{GlobColour}$ values downstream the island are strong all year round with weaker values from May to July while some patches are sometimes observed upstream. The IME is relatively well represented within Run_{Sed5} although

Chl_{Sed5} values are globally lower than the observations on the downstream side (Figure IV-9b and Figure IV-10). In the observations, Chl values exceeding 0.35 mg m^{-3} extent southwestward over a longer distance than what is obtained in the model. In Run_{Sed5}, these high values remain near the island likely due to an insufficient Fe input.

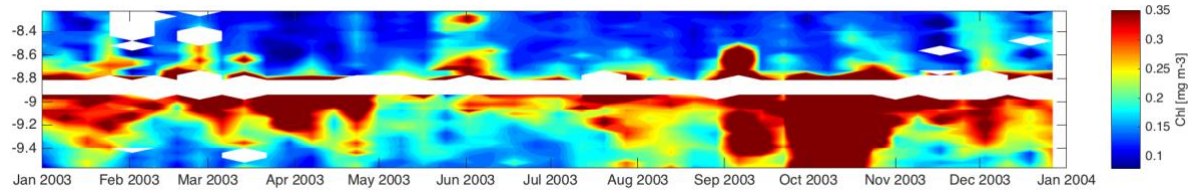

Figure IV-10: Latitude-time diagram of $Chl_{GlobColour}$ (mg m^{-3}) during 2003.

IV.4. Conclusion and perspectives

In the present study, we have investigated the origin and the seasonal variability of the IME occurring in the Marquesas archipelago climatological coupled ROMS-PISCES simulations. The 4 simulations use the same physical and biogeochemical forcings except the Fe compartment. The first one is based on the WOA-PISCES data. The second one use higher Fe concentration at the surface. And a constant iron flux from the sediment is added in the third and fourth simulations. The annual mean of Chl from satellite derived ocean color exhibits a remarkable plume generated downstream the islands. This enrichment is depicted in the simulations using an Fe input from the sediments. The seasonal variability observed from remote sensing is reproduced by the models, although the intensity is weaker. We also compared vertical profiles from a BGC-Argo float released downstream of the biggest island (Nuku Hiva) with our simulations. Along the float trajectory, profiles alternate from homogenous high Chl in the northern archipelago upper layer to profiles associated with a DCM-like structure in the southern region. Here again, similar Chl patterns are only observed in simulations using Fe input from the sediments, with also weaker values than the observations. The comparison of the model outputs with observations reveals that an Fe input from the island is necessary to generate an IME in the archipelago.

We have used the different simulation to investigate the origin of the biological enhancement in the Marquesas islands. The numerical outputs allow revealing remote and local origins for the archipelago enrichments. The two first simulations were used to highlight the remote processes implicated in the Chl enhancement. The southwestward advection of rich waters from

the equator and the wintertime deepening of the mixed layer induce an increase of the phytoplankton biomass in the Marquesas. These processes are also depicted in the simulations where the Fe from the sediment is considered. However, the IME spatial pattern of Chl, comparable to $Chl_{GlobColour}$ although with a weaker amplitude, only appears in the model with the local injection of Fe from sediments. The spatial patterns of Chl are modulated by local currents.

Using 4 different simulations, we have demonstrated that the Marquesan IME only occurs when an Fe input from the sediment is considered. However, remote forcings such as the advection of the equatorial waters and the seasonal deepening of the MLD also plays an important role in modulating the Chl in the archipelago.

Several improvements may be considered regarding the Fe fluxes. First, the Fe flux from the sediments was set constant along time and no seasonality of is considered here. Thus, several processes can be implied in the Fe input with important seasonality (eg, river discharge, internal wave breaking, hydrothermal fluxes, …). Particularly, the land drainage likely enhancing Fe in the nearshore waters is expected to be stronger during the January to August rainy season [*Laurent et al.*, 2004]. Nevertheless, quantitative investigations are needed to optimize these Fe fluxes in the model. Second, a strong constant sediment Fe flux induces a strong constant nearshore Chl growth. The stronger this flux is, the stronger the mean Chl signal is, and thus the more dampened the seasonal signal is (Figure IV-4f). Third, dissolved Fe is traditionally considered as the only available form for phytoplankton growth, while the role of the particulate Fe has been neglected. However, a recent study has highlighted the role of terrigenous particle dissolutions as a slow release of Fe at ocean margins [*Jeandel and Oelkers*, 2015]. In the PISCES model the particulate fraction is not considered and could explain the $Chl_{GlobColour}$ *vs*. Chl_{Sed5} spatial and amplitude differences of the plume.

The simulations used in this study are based on climatological forcings with spatial coarse resolutions. The use of a higher resolution may induce more realistic dynamics in the archipelago. The bathymetry could also play an important role in the intensity and shape of the IME. The one used in our configurations is not sufficient to let emerge the smallest islands. As opposed to other islands in French Polynesia, the Marquesas islands do not have coral reefs [*Montaggioni et al.*, 2016]. The absence of lagoons directly exposes the coasts to the open ocean. This configuration may also influence the Fe transport from the island to the ocean and may induce stronger Fe fluxes that could be underestimated in our simulations.

Finally, our study focuses on the Marquesas IME seasonal variability. To further investigate this remarkable IME, an inter-annual simulation of the coupled ROMS-PISCES model is currently ongoing. This last configuration would allow to understand the impact of ENSO events on the modulation of the biological enrichment in the Marquesas archipelago [*Signorini et al.*, 1999; *Radenac et al.*, 2012; *Martinez et al.*, 2018].

Acknowledgments

We thank the government of French Polynesia for the financial support of the moana-maty project (convention n°6841/MTS) including the PhD grant of H. Raapoto. We also thank the OSU Pyheas that provided the cluster support.

References du Chapitre IV

Aumont, O., and L. Bopp (2006), Globalizing results from ocean in situ iron fertilization studies, Global Biogeochem. Cycles, 20(2), n/a-n/a, doi:10.1029/2005GB002591.

Aumont, O., C. Ethé, a. Tagliabue, L. Bopp, and M. Gehlen (2015), PISCES-v2: an ocean biogeochemical model for carbon and ecosystem studies, Geosci. Model Dev. Discuss., 8(2), 1375–1509, doi:10.5194/gmdd-8-1375-2015.

Barton, E. D. (2001), Island wakes, Encycl. Ocean Sci., 3, 1397–1403, doi:10.1006/rwos.2001.0140.

Beckmann, A., and D. B. Haidvogel (1993), Numerical Simulation of Flow around a Tall Isolated Seamount. Part I: Problem Formulation and Model Accuracy, J. Phys. Oceanogr., 23(8), 1736–1753, doi:10.1175/1520-0485(1993)023<1736:NSOFAA>2.0.CO;2.

Benitez-Nelson, C. R., and D. J. McGillicuddy (2008), Mesoscale physical–biological–biogeochemical linkages in the open ocean: An introduction to the results of the E-Flux and EDDIES programs, Deep Sea Res. Part II Top. Stud. Oceanogr., 55(10–13), 1133–1138, doi:10.1016/j.dsr2.2008.03.001.

Blain, S. et al. (2007), Effect of natural iron fertilization on carbon sequestration in the Southern Ocean, Nature, 446(7139), 1070–1074, doi:10.1038/nature05700.

Blain, S., S. Bonnet, and C. Guieu (2008), Dissolved iron distribution in the tropical and sub tropical South Eastern Pacific, Biogeosciences, 5(1), 269–280, doi:10.5194/bgd-4-2845-2007.

Boyd, P. W., and M. J. Ellwood (2010), The biogeochemical cycle of iron in the ocean, Nat. Geosci., 3(10), 675–682, doi:10.1038/ngeo964.

Chelton, D. B., R. a. deSzoeke, M. G. Schlax, K. El Naggar, and N. Siwertz (1998), Geographical Variability of the First Baroclinic Rossby Radius of Deformation, J. Phys. Oceanogr., 28(3), 433–460, doi:10.1175/1520-0485(1998)028<0433:GVOTFB>2.0.CO;2.

Claustre, H., A. Sciandra, and D. Vaulot (2008), Introduction to the special section bio-optical and biogeochemical conditions in the South East Pacific in late 2004: the BIOSOPE program, Biogeosciences, 5, 679–691, doi:10.5194/bgd-5-605-2008.

da Cunha, L. C., and E. T. Buitenhuis (2013), Riverine influence on the tropical Atlantic Ocean biogeochemistry, Biogeosciences, 10(10), 6357–6373, doi:10.5194/bg-10-6357-2013.

D'Ovidio, F., A. Della Penna, T. W. Trull, F. Nencioli, M. I. Pujol, M. H. Rio, Y. H. Park, C. Cotté, M. Zhou, and S. Blain (2015), The biogeochemical structuring role of horizontal

stirring: Lagrangian perspectives on iron delivery downstream of the Kerguelen Plateau, Biogeosciences, 12(19), 5567–5581, doi:10.5194/bg-12-5567-2015.

Dale, A. W., L. Nickelsen, F. Scholz, C. Hensen, A. Oschlies, and K. Wallmann (2015), A revised global estimate of dissolved iron fluxes from marine sediments, Global Biogeochem. Cycles, 29(5), 691–707, doi:10.1002/2014GB005017.

Debreu, L., and E. Blayo (2008), Two-way embedding algorithms: A review, Ocean Dyn., 58(5–6), 415–428, doi:10.1007/s10236-008-0150-9.

Debreu, L., P. Marchesiello, P. Penven, and G. Cambon (2012), Two-way nesting in split-explicit ocean models: Algorithms, implementation and validation, Ocean Model., 49–50, 1–21, doi:10.1016/j.ocemod.2012.03.003.

Doty, M. S., and M. Oguri (1956), The Island Mass Effect, ICES J. Mar. Sci., doi:10.1093/icesjms/22.1.33.

Elrod, V. A., W. M. Berelson, K. H. Coale, and K. S. Johnson (2004), The flux of iron from continental shelf sediments: A missing source for global budgets, Geophys. Res. Lett., 31(12), 2–5, doi:10.1029/2004GL020216.

Geider, R. J., H. L. MacIntyre, and T. M. Kana (1997), Dynamic model of phytoplankton growth and acclimation: Responses of the balanced growth rate and the chlorophyll a:carbon ratio to light, nutrient-limitation and temperature, Mar. Ecol. Prog. Ser., 148(1–3), 187–200, doi:10.3354/meps148187.

Gordon, H. R., and W. R. McCluney (1975), Estimation of the Depth of Sunlight Penetration in the Sea for Remote Sensing, Appl. Opt., 14(2), 413, doi:10.1364/AO.14.000413.

Goyet, C., R. Healy, J. Ryan, and A. Kozyr (2000), Global distribution of total inorganic carbon and total alkalinity below the deepest winter mixed layer depths,

Guieu, C., S. Bonnet, A. Petrenko, C. Menkes, V. Chavagnac, K. Desboeufs, C. Maes, and T. Moutin (2018), Iron from a submarine source impacts the productive layer of the Western Tropical South Pacific (WTSP), Sci. Rep., 8(1), 9075, doi:10.1038/s41598-018-27407-z.

Hasegawa, D., M. R. Lewis, and a. Gangopadhyay (2009), How islands cause phytoplankton to bloom in their wakes, Geophys. Res. Lett., 36(20), 1–4, doi:10.1029/2009GL039743.

Heywood, K. J., E. D. Barton, and J. H. Simpson (1990), The effects of flow disturbance by an oceanic island, J. Mar. Res., 48, 55–73, doi:10.1357/002224090784984623.

Heywood, K. J., D. P. Stevens, and G. R. Bigg (1996), Eddy formation behind the tropical island of Aldabra, Deep. Res. Part I Oceanogr. Res. Pap., 43(4), 555–578, doi:10.1016/0967-0637(96)00097-0.

Jeandel, C., and E. H. Oelkers (2015), The influence of terrigenous particulate material

dissolution on ocean chemistry and global element cycles, Chem. Geol., 395, 50–66, doi:10.1016/j.chemgeo.2014.12.001.

Jickells, T. D. et al. (2005), Global iron connections between desert dust, ocean biogeochemistry, and climate., Science, 308(5718), 67–71, doi:10.1126/science.1105959.

Johnson, K., and H. Claustre (2016), Bringing Biogeochemistry into the Argo Age, Eos (Washington. DC)., doi:10.1029/2016EO062427.

Johnson, K. S., F. P. Chavez, and G. E. Friederich (1999), Continental-shelf sediment as a primary source of iron for coastal phytoplankton, Nature, 398(6729), 697–700, doi:10.1038/19511.

Laurent, V., K. Maamaatuaiahutapu, J. Maiau, and P. Varney (2004), Atlas Climatologique de la Polynésie Française, Météo Fran.

Legeckis, R., C. W. Brown, F. Bonjean, and E. S. Johnson (2004), The influence of tropical instability waves on phytoplankton blooms in the wake of the Marquesas Islands during 1998 and on the currents observed during the drift of the Kon-Tiki in 1947, Geophys. Res. Lett., 31(23), 1–4, doi:10.1029/2004GL021637.

Locarnini, R. A. et al. (2013), World Ocean Atlas 2013. Vol. 1: Temperature., S. Levitus, Ed.; A. Mishonov, Tech. Ed.; NOAA Atlas NESDIS, 73(September), 40, doi:10.1182/blood-2011-06-357442.

Lungu, T., and P. S. Callahan (2006), QuikSCAT science data product user's manual: Overview and geophysical data products, D-18053-Rev A, version, 3, 91.

Maraldi, C., M. Mongin, R. Coleman, and L. Testut (2009), The influence of lateral mixing on a phytoplankton bloom: Distribution in the Kerguelen Plateau region, Deep. Res. Part I Oceanogr. Res. Pap., 56(6), 963–973, doi:10.1016/j.dsr.2008.12.018.

Martin, J. H., and S. E. Fitzwater (1988), Iron deficiency limits phytoplankton growth in the north-east Pacific subarctic, Nature, 331(6154), 341–343, doi:10.1038/331341a0.

Martinez, E., and K. Maamaatuaiahutapu (2004), Island mass effect in the Marquesas Islands: Time variation, Geophys. Res. Lett., 31(18), 1–4, doi:10.1029/2004GL020682.

Martinez, E., M. Rodier, and K. Maamaatuaiahutapu (2016), Environnement océanique des Marquises, in Biodiversité terrestre et marine des îles Marquises, Polynésie Française, edited by R. Galzin, S.-D. Duron, and J.-Y. Meyer, pp. 123–136, Société française d'Ichtyologie, Paris.

Martinez, E., H. Raapoto, C. Maes, and K. Maamaatuaihutapu (2018), Influence of Tropical Instability Waves on Phytoplankton Biomass near the Marquesas Islands, , 1–12, doi:10.3390/rs10040640.

Maury, R. C., G. Guille, G. Hervé, C. Catherine, C. Legendre, P. Rossi, S. Blais, C. Pallares, D. Sébastien, and A. Marabal (2014), Géologie des Marquises : des volcans boucliers intra-océaniques effondrés issus d ' un point chaud atypique Géologie des Marquises : des volcans boucliers intra-océaniques effondrés issus d ' un point chaud atypique, Géologie la Fr., 1(8), 111–135.

Montaggioni, L., S. Etienne, and C. Seard (2016), Récifs coralliens et paysages géomorphologiques littoraux des îles Marquises géomorphologiques littoraux des îles, in Biodiversité terrestre et marine des îles Marquises, Polynésie Française, edited by R. Galzin, S.-D. Duron, and J.-Y. Meyer, pp. 79–104, Société française d'Ichtyologie, Paris.

Morel, A., and J.-F. Berthon (1989), Surface pigments, algal biomass profiles, and potential production of the euphotic layer: Relationships reinvestigated in view of remote-sensing applications, Limnol. Oceanogr., 34(8), 1545–1562, doi:10.4319/lo.1989.34.8.1545.

Palacios, D. M. (2002), Factors influencing the island-mass effect of the Galápagos Archipelago, Geophys. Res. Lett., 29(23), 1–4, doi:10.1029/2002GL016232.

Penven, P., P. Marchesiello, L. Debreu, and J. Lefèvre (2007), Software tools for pre- and post-processing of oceanic regional simulations, Environ. Model. Softw., 23(5), 660–662, doi:10.1016/j.envsoft.2007.07.004.

Planquette, H. et al. (2007), Dissolved iron in the vicinity of the Crozet Islands, Southern Ocean, Deep. Res. Part II Top. Stud. Oceanogr., 54(18–20), 1999–2019, doi:10.1016/j.dsr2.2007.06.019.

Raapoto, H., E. Martinez, A. Petrenko, A. M. Doglioli, and C. Maes (2018), Modeling the Wake of the Marquesas Archipelago, J. Geophys. Res. Ocean., doi:10.1002/2017JC013285.

Radenac, M. H., F. Léger, A. Singh, and T. Delcroix (2012), Sea surface chlorophyll signature in the tropical Pacific during eastern and central Pacific ENSO events, J. Geophys. Res. Ocean., 117(4), 1–15, doi:10.1029/2011JC007841.

Raimbault, P., and N. Garcia (2008), Evidence for efficient regenerated production and dinitrogen fixation in nitrogen-deficient waters of the South Pacific Ocean: impact on new and export production estimates, Biogeosciences, 5(2), 323–338, doi:10.5194/bg-5-323-2008.

Raimbault, P., N. Garcia, and F. Cerutti (2007), Distribution of inorganic and organic nutrients in the South Pacific Ocean - evidence for long-term accumulation of organic matter in nitrogen-depleted waters, Biogeosciences Discuss., 4(1), 3041–3087, doi:10.5194/bg-5-281-2008.

Ras, J., H. Claustre, and J. Uitz (2008), Spatial variability of phytoplankton pigment

distributions in the Subtropical South Pacific Ocean: Comparison between in situ and predicted data, Biogeosciences, 5(2), 353–369, doi:10.5194/bg-5-353-2008.

Robinson, J., E. E. Popova, M. A. Srokosz, and A. Yool (2016), A tale of three islands: Downstream natural iron fertilization in the Southern Ocean, J. Geophys. Res. Ocean., 121(5), 3350–3371, doi:10.1002/2015JC011319.

Sangrà, P., G. Basterretxea, J. L. Pelegrí, and J. Arístegui (2001), Chlorophyll increase due to internal waves on the shelf break of Gran Canaria (Canary Islands)*, Signals, 65, 89–97, doi:http://digital.csic.es/bitstream/10261/5326/1/wave.pdf.

Shchepetkin, A. F., and J. C. McWilliams (2003), A method for computing horizontal pressure-gradient force in an oceanic model with nonaligned vertical coordinate, J. Geophys. Res., 108(C3), 1–34, doi:10.1029/2001JC001047.

Shchepetkin, A. F., and J. C. McWilliams (2005), The regional oceanic modeling system (ROMS): a split-explicit, free-surface, topography-following-coordinate oceanic model, Ocean~Model., 9, 347–404, doi:10.1016/j.ocemod.2004.08.002.

Signorini, S. R., C. R. McClain, and Y. Dandonneau (1999), Mixing and phytoplankton bloom in the wake of the Marquesas Islands, Geophys. Res. Lett., 26(20), 3121–3124, doi:10.1029/1999GL010470.

da Silva, A. M., C. C. Young, and S. Levitus (1994), Atlas of surface marine data 1994, vol. 4, Anomalies of fresh water fluxes, Noaa atlas nesdis, 9, 308.

Smith, W. H., and D. Sandwell (1997), Global Sea Floor Topography from Satellite Altimetry and Ship Depth Soundings, Science (80-.)., 277(5334), 1956–1962, doi:10.1126/science.277.5334.1956.

Tagliabue, A. et al. (2010), Hydrothermal contribution to the oceanic dissolved iron inventory, Nat. Geosci., 3(4), 252–256, doi:10.1038/ngeo818.

Wyrtki, K. (1981), An Estimate of Equatorial Upwelling in the Pacific, J. Phys. Oceanogr., 11, 1205–1214.

Yan, X., C. Ho, Q. Zheng, and V. Klemas (1992), Temperature and Size Variabilities of the Western Pacific Warm Pool, Science (80-.)., 258(5088), 1643–1645.

Zweng, M. M., J. R. Reagan, J. I. Antonov, A. V. Mishonov, T. P. Boyer, H. E. Garcia, O. K. Baranova, D. R. Johnson, D. Seidov, and M. M. Bidlle (2013), World Ocean Atlas 2013, Volume 2: Salinity.

Conclusion du Chapitre IV

Dans cette dernière étude, nous avons mis en place plusieurs simulations climatologiques couplées physique/biogéochimique (ROMS-PISCES). Les forçages physiques utilisés ont été déduits des résultats des chapitres précédents. Ainsi, toutes les simulations lancées dans ce chapitre utilisent les conditions initiales et forçages aux bords WOA 2013, et les forçages de surface QuikSCAT. Les conditions aux bords de la partie biogéochimique, issues des données WOA-PISCES, sont elles aussi les mêmes pour ces simulations, à l'exception du compartiment fer. La première simulation utilise les concentrations issues des données WOA-PISCES (Run_{Ref}). La deuxième est basée sur ce même jeu de données mais les concentrations en fer de la surface jusqu'à la profondeur de gradient maximum de fer ont été augmentées pour se rapprocher des observations réalisées durant la campagne océanographique BIOSOPE ($Run_{Biosope}$). Les deux dernières simulations utilisent les concentrations en fer issues de WOA-PISCES, mais un apport depuis les sédiments est pris en compte avec des flux constants, mais différents dans chaque simulation : l'une avec un flux de 2,5 μmol m^{-2} d^{-1} ($Run_{Sed2.5}$) et l'autre un flux de 5 μmol m^{-2} d^{-1} (Run_{Sed5}).

Les concentrations moyennes de Chl mesurées par satellite dans l'archipel révèlent un panache de Chl orienté vers le Sud-Ouest, le long de l'écoulement du SEC. Seules les simulations prenant en compte un apport de fer depuis les sédiments ($Run_{Sed2.5}$ et Run_{Sed5}) permettent de retrouver un panache de Chl généré derrière les îles. Celles ne prenant pas en compte les sédiments (Run_{Ref} et $Run_{Biosope}$) ne montrent pas d'enrichissement au niveau des îles mais un gradient nord-est/sud-ouest avec les eaux riches au niveau de l'upwelling équatorial. La saisonnalité de la Chl des simulations sont proches de celle des mesures satellites mais les valeurs restent inférieures aux observations. L'apport de fer depuis les sédiments permet d'obtenir des valeurs plus proches des observations satellites.

Les simulations $Run_{Sed2.5}$ et Run_{Sed5} permettent de reproduire les structures verticales observées par le flotteur profileur BGC-Argo mis à l'eau dans l'archipel en août 2011. Ainsi, ces deux simulations permettent d'observer une différence Nord-Sud, avec des couches de Chl mélangées dans le Nord de l'archipel et la formation d'un maximum de chlorophylle en profondeur (DCM) dans la partie Sud.

Les processus intervenant dans l'enrichissement biologique de l'archipel sont étudiés en se basant sur un transect le long de l'écoulement du SEC et traversant la plus grande île de l'archipel, Nuku-Hiva. Les simulations ne prenant pas en compte l'émission de fer depuis les sédiments ont permis de mettre en évidence la limitation en micronutriments dans la zone mais

aussi de révéler des enrichissements par des processus à l'échelle de l'archipel. En effet, les deux premières simulations ont permis de montrer des enrichissements dû à l'advection d'eaux plus riches venant de la zone équatoriale mais aussi dû à l'approfondissement hivernal de la couche de mélange. En plus de ces processus, l'apport local de fer depuis les sédiments dans les simulations $Run_{Sed2.5}$ et Run_{Sed5} ont permis d'observer des panaches de Chl proches de ceux observés par les images de couleur de la mer. Le SEC permet de moduler la forme et l'intensité des panaches.

Perspectives du Chapitre IV

Dans ce chapitre, le couplage des modèles de physique et de biogéochimie a permis de révéler des processus responsables de la génération de l'effet d'île Marquisien. Cependant, le chapitre précédent soulevait la possibilité d'un enrichissement induit par la circulation secondaire des tourbillons qui sont générés et propagés dans l'archipel. En effet, les tourbillons cycloniques ont pour effet général d'enrichir les eaux de surface grâce à la remontée d'eau induite par la circulation secondaire. Pour étudier cette hypothèse, nous nous sommes intéressés à la simulation Run_{Ref}, afin de vérifier la présence ou l'absence d'impact des tourbillons sur la remonté de nutriments. Un diagnostic préliminaire a été réalisé en utilisant le même algorithme de détection automatique de tourbillons que dans le Chapitre III [*Nencioli et al.*, 2010]. L'ensemble des tourbillons généré dans la simulation Run_{Ref} a été répertorié selon leur sens de rotation (cyclonique ou anticyclonique). Puis, une moyenne de la température et de la Chl le long de transects Nord-Sud passant par leur centre et sur une distance faisant 3 fois leur rayon a été réalisé au milieu de leur temps de vie, lorsque leur intensité est maximale [*Liu et al.*, 2012]. Cette moyenne est soustraite à chaque transect et permet ainsi d'obtenir une anomalie de température et de Chl pour chaque tourbillon. Ainsi, la moyenne de ces anomalies permet d'obtenir des composites d'anomalies et permet de traduire l'effet des tourbillons cycloniques et anticycloniques (Figure IV-11). Une anomalie positive traduit une augmentation et une anomalie négative une diminution de chaque paramètre.

Les composites d'anomalies de température des tourbillons cycloniques (anticycloniques) révèlent un faible refroidissement (réchauffement) de l'ordre de 0,05°C autour de 100 m de profondeur (Figure IV-11a et b). Ces anomalies de températures sont observées à une profondeur proche de celle de la couche de mélange (Figure IV-7). Les patterns observés sur la Chl (Figure IV-11c et d) sont contre-intuitifs avec un appauvrissement (enrichissement) des

eaux de surface pour les tourbillons cycloniques (anticycloniques). Cependant, les anomalies générées sont elles faibles avec des valeurs de l'ordre de 3 10^{-3} mg m^{-3}.

Ainsi, les tourbillons générés dans l'archipel ont, au premier abord, un impact faible sur l'enrichissement biologique de l'archipel. Cependant, ce constat s'applique pour l'ensemble des tourbillons générés, sans distinction de taille, d'âge, etc, … Une étude s'appuyant sur des critères plus sélectifs serait intéressante à effectuer et permettrait, par exemple, d'évaluer l'influence de la taille des tourbillons sur ces possibles enrichissements. En effet, le chapitre précédent révélait des tailles de tourbillons variables et pourrait probablement indiquer des intensités variables selon leur taille. Pour ces différentes raisons, l'impact des tourbillons n'a pas été considéré dans ce chapitre. Une étude plus approfondie est donc nécessaire, et les résultats pourraient faire l'objet d'un prochain article en considérant aussi les effets que pourraient avoir les tourbillons sur la propagation des eaux riches formées juste derrière les îles.

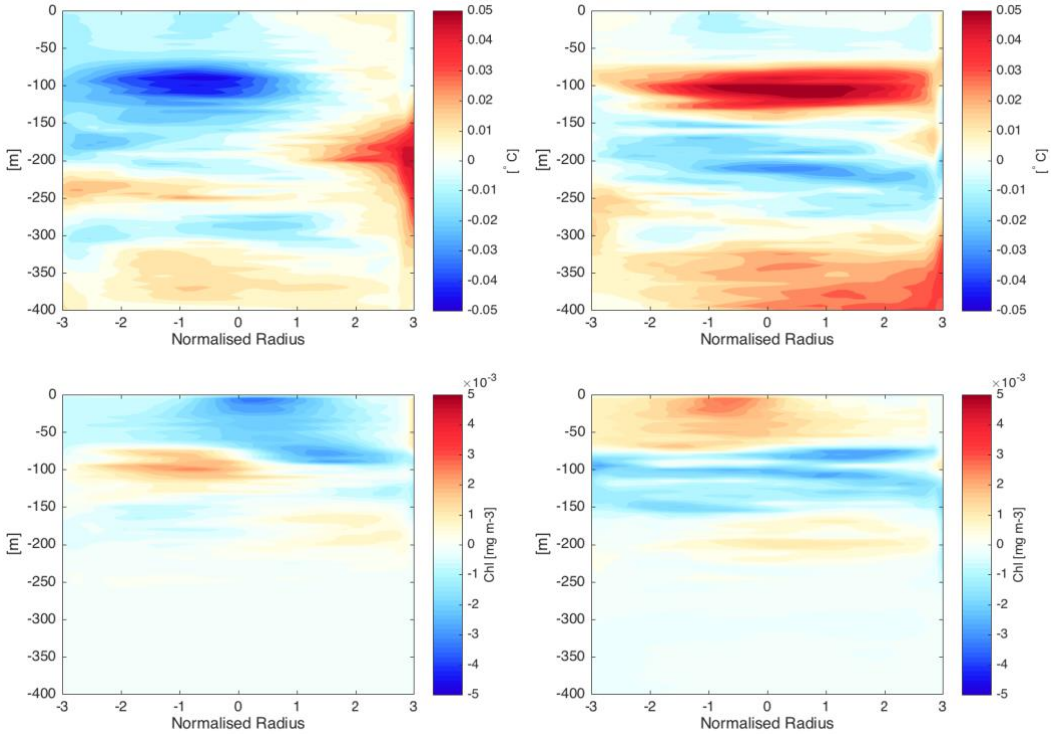

Figure IV-11 : Composites d'anomalies de température pour les tourbillons (a) cycloniques et (b) anticycloniques. Les composites d'anomalies de Chl pour les tourbillons (c) cycloniques et (d) anticycloniques.

Chapitre V

Conclusion et Perspectives

V.1. Une étude pionnière

Le travail qui a été présenté ici est une avancée majeure dans la compréhension des processus océaniques physiques et biogéochimiques de l'archipel des Marquises, et en particulier, de ceux impliqués dans l'effet d'îles aux Marquises. En effet, l'EI marquisien, bien que remarquable à l'échelle du bassin Pacifique, n'a été que peu étudié et documenté jusqu'à présent.

Les mesures satellites, qui sont pourtant un outil standard pour ce type d'étude, présentent une résolution spatio-temporelle insuffisante au regard de la petite taille des îles de l'archipel et rendent difficile l'étude des processus dynamiques à plus fines échelles. En effet (voir annexe A), à l'aide de mesures satellites et de sorties d'un modèle global (i.e., disponible à l'échelle de la planète avec une résolution spatio-temporelle moyenne), nous avons pu mettre en évidence l'influence de phénomènes de méso-échelles sur l'enrichissement biologique au sein de l'archipel. Durant les évènements La Niña de 1998 et 2010, les TIWs peuvent apporter des eaux riches depuis la zone de l'upwelling équatorial vers les Marquises et ainsi favoriser le développement du phytoplancton. Cependant, la seule influence de ces TIWs ne pouvait expliquer l'enrichissement remarquable observé dans l'archipel. L'utilisation de ces données (satellites et modèles globaux) ne permettait donc pas d'étudier les processus à l'échelle de l'archipel qui peuvent entrainer une augmentation de Chl.

De plus, le manque de mesures *in situ* ne permet pas non plus d'aborder une analyse des processus aussi bien sur la verticale que dans le temps. Par conséquent, la mise en place d'un modèle numérique à haute résolution (suffisante pour prendre en compte la présence des îles) se révèle indispensable pour aborder les questions soulevées par cet EI.

Tout d'abord, un travail de modélisation de la circulation océanique a donc été mis en place autour des îles Marquises afin d'étudier les processus physiques capables d'induire un apport de sels nutritifs, par exemple depuis les eaux plus riches en profondeur, et de caractériser leur saisonnalité. S'agissant d'implémenter un modèle régional et avec frontières ouvertes, plusieurs choix de forçages et de conditions aux frontières étaient disponibles. Il a donc été nécessaire dans un premier temps d'effectuer une étude comparative afin de vérifier le réalisme des sorties de modèles obtenues. Pour cela, nous avons comparé ces dernières aux mesures satellites disponibles à l'échelle de l'archipel selon différents diagnostiques. Il a été montré que les propriétés thermohalines (température et salinité) obtenues par les différentes configurations du

modèle sont proches des observations, indiquant les bonnes performances du modèle, et que les forçages ayant la résolution la plus haute permettent d'obtenir des niveaux d'énergies en accord avec les observations satellites de courantologie. Une fois identifiée la meilleure configuration, il a été possible de démarrer l'investigation de l'EI marquisien.

La mise en place et la validation du modèle de dynamique océanique ad 'hoc pour l'archipel des Marquises nous a permis d'étudier certains processus physiques pouvant entraîner un enrichissement de la couche euphotique. Parmi ces processus, la génération et la propagation de tourbillons derrière les îles a été plus particulièrement analysée. Cette activité tourbillonnaire, qui est difficilement perceptible sur les observations satellites, a pu être mise en évidence pour la première fois dans cette étude. Une dominance de tourbillons cycloniques a ainsi pu être établie. L'origine de ces tourbillons a aussi été analysée en caractérisant les processus de conversions d'énergies. Ces derniers révèlent une contribution de l'énergie cinétique, potentielle et aussi des vents de surface avec des saisonnalités différentes. La remontée d'eaux au niveau des côtes, c'est à dire le mécanisme d'upwelling, ne semble pas être présent/prédominant dans l'archipel. En effet, l'absence de la signature de ces remontées d'eaux (qui devraient donc être plus froides au niveau des côtes), et à contrario des températures de surfaces plus chaudes au niveau des îles indiqueraient non seulement une absence d'upwelling, mais plutôt une zone d'accalmie à l'abri du vent.

L'étude de l'effet d'île de l'archipel des Marquises d'un point de vue biogéochimique a été réalisée en mettant en place le couplage du modèle physique avec celui de biogéochimie, en se basant sur l'ensemble des résultats précédents. Les eaux étant limitantes en micronutriments, une série de tests de sensibilité sur l'intensité et les sources des apports en fer dans l'archipel ont permis de montrer la nécessité d'implémenter un apport terrigène dans le modèle couplé physique-biogéochimique pour pouvoir générer un enrichissement biologique au niveau des îles. Aussi, il a été démontré que les augmentations de concentration de chlorophylle sont liées aussi bien à des processus dynamiques ayant lieu à l'échelle du bassin qu'à des échelles plus locales. En effet, l'advection des eaux provenant de l'équateur et l'approfondissement hivernal de la couche de mélange permettent saisonnièrement l'apport d'eaux plus riches en sels nutritifs dans l'archipel. A ces deux processus, il faut ajouter l'apport de fer depuis les sédiments pour obtenir dans le modèle la génération du panache de chlorophylle tel qu'observé par satellite.

Dans le travail présenté ici, la dynamique au sein de l'archipel des Marquises mais aussi les propriétés biogéochimiques ont été analysées en grande partie à l'aide d'un modèle numérique haute résolution adapté à la région. Les observations satellites et les mesures *in situ* ont, elles aussi, été utilisées dans ces travaux, notamment pour être comparées avec les sorties de modèle. Ainsi, certains processus responsables de l'enrichissement de la couche euphotique en sels nutritifs et du développement de la biomasse phytoplanctonique ont pu être mis en évidence.

V.2. Perspectives

Cette étude a permis de caractériser la dynamique océanique dans l'archipel des Marquises ainsi que de mettre en évidence certains processus à l'origine de l'enrichissement biologique de ces îles. Cependant, seule l'échelle saisonnière a été considérée ici, et d'autres pistes sont à évaluer pour une compréhension plus complète de ce remarquable EI :

- Autres processus impliqués dans la variabilité saisonnière de l'EI :

Des simulations supplémentaires devront être lancées pour étudier d'autres processus qui pourraient être impliqués dans la génération de l'EI marquisien. En particulier, les marées et le déferlement des ondes internes n'étant pas pris en compte dans les précédentes simulations, il sera intéressant d'étudier leur importance dans l'enrichissement biologique observé dans la zone. Il serait, par exemple, possible de lancer des simulations identiques à celles du Chapitre IV mais en prenant en compte les ondes internes et les marées. Il sera alors relativement simple de déterminer l'impact de ces forçages en analysant les différences avec les sorties des simulations présentées précédemment. Aussi, comme discuté dans le Chapitre IV, d'autres sources de fer devront être prises en compte pour améliorer le réalisme des simulations. L'hypothèse d'un apport de fer par le drainage des terres et les rivières pourra par exemple être évalué. En se basant sur la méthodologie du Chapitre IV, il serait intéressant de lancer différentes simulations qui considèreraient ces différentes sources de fer. Puis, les différences obtenues entre ces sorties de modèle et la simulation de référence de l'étude précédente permettront de déterminer le rôle de ces sources dans l'EI Marquisien. Le rôle des tourbillons pourra être lui aussi étudié pour révéler s'ils interviennent dans l'enrichissement en nutriment des eaux de surface ou seulement pour moduler le panache de chlorophylle par le piégeage des eaux riches proches des iles. Pour cela, un travail plus rigoureux sur les composites d'anomalies des tourbillons pourrait être réalisé en utilisant une sélection plus adaptée, comme détaillée dans la conclusion du chapitre précédent.

- Processus physiques et biogéochimiques impliqués dans la variabilité interannuelle

Jusqu'à présent, les simulations réalisées ne se sont focalisées que sur l'échelle saisonnière. Cependant, les processus impliqués dans l'enrichissement peuvent être différents aux échelles interannuelles. Plus spécifiquement, l'influence des évènements ENSO à l'échelle du bassin océanique sur l'activité biologique aux Marquises devra être caractérisée plus en détail. L'impact des changements de la profondeur de la pycnocline/nutricline (zone de gradient maximum de la densité et des nutriments, respectivement), des vents et des courants sur la biomasse et les communautés phytoplanctoniques pendant les événements ENSO devra être étudié. Pour ce travail, des diagnostiques similaires à ceux réalisés pour les sorties de modèle climatologique pourront être lancés. Dans un premier temps, il sera intéressant de voir l'influence d'ENSO sur les processus physiques dans l'archipel des Marquises. En particulier, une étude sur la génération et propagation des tourbillons sera facilement réalisable à l'aide des outils développés au cours de cette thèse. Dans un second temps, il sera possible d'évaluer l'impact des phénomènes ENSO sur l'évolution du panache de chlorophylle. Il sera particulièrement intéressant de mettre en évidence si la forte variabilité observée sur les mesures satellites peut être retrouvée à l'aide du modèle. Pour cela, une simulation couplée utilisant des forçages réalistes issues des sorties de modèles globaux, tel que GLORYS, pourra être lancée. Cependant, les temps de calculs et le volume considérable des sorties (4 To minimum) seront une des difficultés à prendre en compte pour cette partie. La mise en place de cette simulation sera réalisée après la soutenance ainsi qu'une analyse préliminaire. Toutefois, les sorties de cette simulation pourront, par la suite, faire l'objet d'un travail de stage de master.

- Processus physiques et biogéochimiques impliqués dans la variabilité décennale

De la même manière que pour les échelles interannuelles, l'impact des cycles décennaux sur les processus impliqués dans l'EI Marquisien, et donc sur la signature de l'EI pourrait être étudiée. Notamment, la variabilité du panache de phytoplancton ainsi que les mécanismes physiques et biogéochimiques pendant les phases chaudes et froides de l'IPO (Interdecadal Pacific Oscillation) pourront être analysés. Pour y arriver, deux climatologies correspondant à la phase chaude de l'IPO et à sa phase froide pourront être utilisées pour le forçage du modèle couplée ROMS-PISCES. Les sorties du modèle couplé pourront être analysé de la même manière que les sorties du modèle interannuel et une attention particulière sera portée sur les différences obtenues entre les deux phases.

- Impacts sur les ressources pélagiques

Par la suite, il sera possible d'étudier l'impact de l'EI sur la disponibilité et/ou la diversité des ressources pélagiques autour des Marquises puis de déterminer l'impacts des changements climatiques. En effet, la pêche représente une activité majeure pour les populations locales. Il serait intéressant de comprendre l'impact que pourrait avoir les différents processus sur la distribution de la ressource et ainsi appréhender les impacts du changement climatique. Pour cette partie applicative, le modèle SEAPODYM [*Lehodey et al.*, 2008] qui permet d'étudier la dynamique d'espèces pélagiques (tels que les thonidés) à partir de données environnementales pourrait être mis en place pour l'archipel. De la même manière que pour cette thèse, une simulation climatologique pourrait permettre d'étudier la variabilité saisonnière puis une simulation interannuelle permettrait d'étudier la variabilité interannuelle.

- Campagnes océanographiques

Enfin, il serait bien évidemment nécessaire de mettre en place des campagnes océanographiques autour des îles Marquises. Bien que la modélisation permette de comprendre les processus impliqués dans cet EI, les mesures *in situ* permettraient quant à elles d'observer et de caractériser l'environnement océanique physique et biogéochimique dans l'archipel et pourraient servir à la validation des résultats obtenues à partir des modèles. En particulier, une meilleure connaissance de la distribution de micronutriment ainsi que leurs possibles sources dans l'archipel pourront être étudiées. Ces avancées permettront, par ailleurs, de valider le précédent couplage des modèles physique et biogéochimique mais aussi de mettre en place une nouvelle configuration plus réaliste. C'est dans cette optique que la prochaine campagne océanographique MOANA-MATY doit se dérouler à la fin du mois de septembre 2018.

Annexe A.

Influence of Tropical Instability Waves on Phytoplankton Biomass near the Marquesas Islands

E. Martinez [a,b], H. Raapoto[a], C. Maes[b] and K Maamaatuaihutapu[c]

[a] IRD, UPF, ILM, Ifremer, Écosystèmes Insulaires Océaniens (EIO), Tahiti, French Polynesia

[b] Université Brest, Ifremer, CNRS, IRD, Laboratoire d'Océanographie Physique et Spatiale (LOPS), IUEM, Brest, France

[c] Laboratoire de Géosciences du Pacifique Sud, Université de la Polynésie française, Tahiti, French Polynesia

Publié dans *Remote Sensing*

Martinez, E., Raapoto, H., Maes, C., & Maamaatuaiahutapu, K. (2018). Influence of Tropical Instability Waves on Phytoplankton Biomass near the Marquesas Islands. *Remote Sensing*, 10(4), 640

RESUME

L'archipel des Marquises situé dans le Pacifique Central Sud est formé de petites îles isolées et présente une activité biologique quasi-permanente. Durant les évènements La Niña, une augmentation considérable de la concentration en chlorophylle-a est observée. Cette forte activité a longtemps été supposée provenir de l'advection des eaux riches en fer provenant de la région équatoriale vers l'archipel des Marquises par les ondes d'instabilités tropical (TIWs). Nous examinons ici cette hypothèse sur 18 années en combinant des observations satellites, des réanalyses de données de l'océan et des diagnostiques lagrangiens. Durant cette période, quatre évènements La Niña d'intensité modéré à fort ont eu lieu. Nos résultats montrent que la génération du panache de Chl au niveau des îles peut effectivement être influencée par l'advection depuis l'équateur mais seulement durant les évènements La Niña de forte intensité en 1998 et 2010. Les schémas spatio-temporels de Chl durant les épisodes de TIWs suggèrent plutôt des interactions de forçage à grande échelle tels qu'une remonté de la thermocline ou l'intensification d'upwelling côtier entrainant ainsi une augmentation de la biomasse phytoplanctonique dans les eaux de surface. Globalement, quelques soient les conditions, cette analyse suggère que l'influence des TIWs est de moduler la forme du panache de phytoplancton existant.

ABSTRACT

The Marquesas form an isolated group of small islands in the Central South Pacific where quasi-permanent biological activity is observed. During La Niña events, this biological activity, shown by a net increase of chlorophyll-a concentration (Chl, a proxy of phytoplankton biomass), is particularly strong. It has been hypothesized that this strong activity is due to iron-rich waters advected from the equatorial region to the Marquesas by tropical instability waves (TIWs). Here we investigate this hypothesis over 18 years by combining satellite observations, re-analyses of ocean data, and Lagrangian diagnostics. Four La Niña events ranging from moderate to strong intensity occurred during this period, and our results show that the Chl plume within the archipelago can be indeed influenced by such equatorial advection, but this was observed during the strong 1998 and 2010 La Niña conditions only. Chl spatio-temporal patterns during the occurrence of other TIWs rather suggest the interaction of large-scale forcing events such as an uplift of the thermocline or the enhancement of coastal upwelling induced by the tropical strengthening of the trades with the islands leading to enhancement of phytoplankton biomass within the surface waters. Overall, whatever the conditions, our

analyses suggest that the influence of the TIWs is to disperse, stir, and, therefore, modulate the shape of the existing phytoplankton plume.

Keywords: tropical instability waves; La Niña; chlorophyll-a concentration variability; ocean colour; island mass effect; Marquesas islands; oceanography; satellite observations

A.1. Introduction

Over the next century, the frequency of extreme La Niña events is expected to nearly double from one in every 23 years to one in every 13 years [*Cai et al.*, 2015]. In the Pacific Ocean, a La Niña event induces an increase of phytoplankton biomass along the eastern and central equatorial/tropical band through the uplift of the thermocline and hence of nutrients [*Radenac et al.*, 2001, 2012; *Masotti et al.*, 2011; *Shi and Wang*, 2014], but also more locally around islands [*Signorini et al.*, 1999; *Legeckis et al.*, 2004; *Messié et al.*, 2006; *Lo-Yat et al.*, 2011; *Martinez et al.*, 2016]. In such an island context, biological variability can be directly influenced by local processes such as land drainage, dust deposition, changes occurring at basin/regional scale (i.e., basin-scale thermocline depth and wind variability), and/or can be impacted by remote forcing, such as the horizontal advection of cold nutrient-rich waters upwelled along the Equator due to tropical instability waves (TIWs) [*Barber R. T et al.*, 1996; *Foley et al.*, 1997; *Strutton et al.*, 2001]. Tropical instability waves are cusp-shaped oceanic perturbations of currents and temperature [*Legeckis*, 1977]. They are generated either by the baroclinic instability associated with sea surface temperature (SST) fronts or the barotropic instability associated with the ocean current shears between the eastward Equatorial Undercurrent (EUC) and the opposing westward flowing South Equatorial Current (SEC) [*Philander*, 1978]. During La Niña events, the trade winds drive the enhancement of the equatorial currents, hence, TIW activity is maximized [*Yu and Liu*, 2003].

The Marquesas islands are located in the Central South Pacific (11°S–8°S/142°W–139°W) in high nutrient low chlorophyll (HNLC) waters south of the equatorial upwelling region (Figure A-1). HNLC waters present some moderate oligotrophic characteristics associated with significant amounts of nitrate ([*Claustre et al.*, 2008] and references therein). The archipelago extends over about 350 km and islands rise steeply from the abyssal plain at 4000 m. Hence, deep channels between the islands (40 to 100 km wide) allow the SEC to flow unobstructed south-westward, while the dozens of islands themselves divert the flow as they are 10–25 km-wide obstacles embedded in the SEC. A strong biological enhancement referred to as an island mass effect (IME, [*Doty and Oguri*, 1956]) occurs in the location of these small islands. An annual mean of 0.2 mg/m^3 of surface chlorophyll-a concentration (Chl, a proxy of phytoplankton biomass) has been reported [*Martinez and Maamaatuaiahutapu*, 2004]. The authors also reported a strong correlation between this IME and the total (Ekman plus geostrophic) surface current. However, the relevant process at the origin of the blooms was not identified. During La Niña events in 1998 and 2000, Chl rose to 0.3 and 0.5 mg/m^3,

respectively. The 1998 Chl increase was associated with a plume extending up to 800 km in the lee of the islands [*Signorini et al.*, 1999]. To explain the phytoplankton enhancement during the 1998 La Niña event, two hypotheses have been proposed. Firstly, it could be attributed to local sources of iron and the interactions of the Marquesas with the La Niña-enhanced SEC [*Signorini et al.*, 1999; *Martinez and Maamaatuaiahutapu*, 2004]. Secondly, a progression of cooler bands of equatorial waters that extend far to the south and can reach the Marquesas islands has been associated with TIW fronts [*Legeckis et al.*, 2004]. Hence, these authors have suggested that the upwelled equatorial waters rich in iron generating phytoplankton blooms could be advected downstream along TIWs.

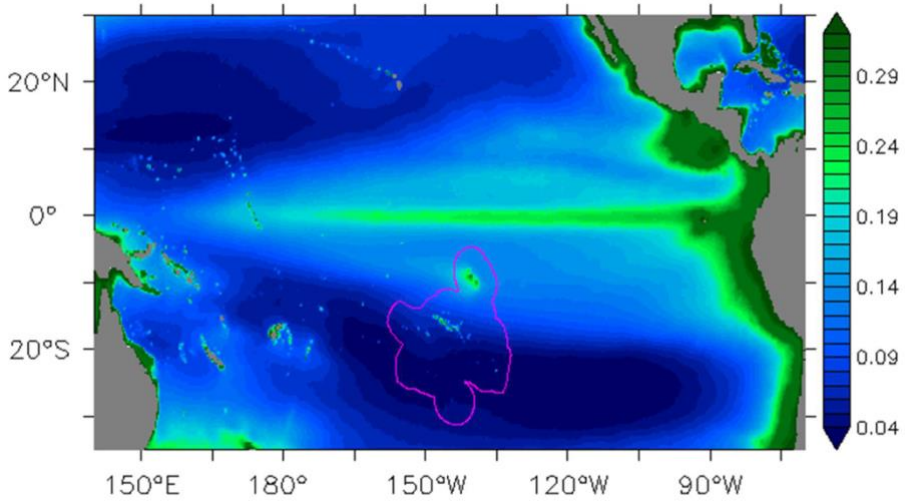

Figure A-1: The 1998–2014 annual average of chlorophyll-a concentrations (Chl, mg/m^3) from the satellite-derived GlobColour Chl AVE product. The purple line delineates the French Polynesian Exclusive Economic Zone (EEZ).

This second hypothesis has been proposed for 1998 only, a year when a strong La Niña event occurred [*Legeckis et al.*, 2004]. Hence, here we investigate the consistency of this hypothesis over a longer period (18 years) and under different La Niña conditions. In order to detect TIWs and to follow their propagations, we used satellite observations combining ocean colour, SST, altimetric surface currents and fronts, and transport barrier information derived from altimetric surface currents, along with estimates of the density field issued from a re-analysed ocean model.

A.2. Materials and Methods

We used the Chl AVE GlobColour data set developed, validated, and distributed by ACRI-ST France [*Fanton d'Andon et al.*, 2009] (http://globcolour.info). This product merges derived-Chl from L3 Ocean Colour products derived from four different sensors (Sea-viewing Wide Field-of-view Sensor, Moderate Resolution Imaging Spectroradiometer Aqua, Medium-Resolution Imaging Spectrometer, and Visible Infrared Imaging Radiometer Suite) to produce a long-time series with a better spatio-temporal coverage than that provided by each individual ocean colour mission. Weekly surface data, from September 1997 to December 2014, were available on a 4-km horizontal grid.

Sea surface temperature was used to detect the cold water associated with TIWs. Data were provided by the AVHRR Pathfinder Project v4.1 (1985–2002) and AVHRR GAC (2003–present) (https://www.class.ngdc.noaa.gov/data_available/avhrr/index.htm). Weekly data on a 9 km horizontal grid were downloaded for the 1997–2014 period (http://oceanwatch.pifsc.noaa.gov).

In order to investigate the possible pathways and connectivity between the Equator and the Marquesas islands and, hence, the possible surface advection of phytoplankton or iron-rich waters by TIWs, we used passive Lagrangian diagnostics, with Finite-Size Lyapunov Exponents (FSLEs), derived from ocean surface currents (e.g., [*d'Ovidio et al.*, 2004]). Finite-size lyapunov exponents enable us to study the relative dispersion between initially close particles, thus providing information on fronts and transport barriers, and on horizontal stirring by surface currents. Finite-size lyapunov exponents provided by AVISO+ (https://www.aviso.altimetry.fr/en/home.html) every 4 days on a 1/25° horizontal grid were derived from delayed-time global ocean absolute geostrophic currents (DUACS2014 *DT MADT* UV products). Parameters of the FSLE computations were defined to characterize the mesoscale features of the flow with an initial separation of 0.04 degrees and final separation of 0.6 degrees. We assumed here that FSLEs are representative of convergent structures and small-scale fronts that are relevant for the biological conditions and Chl variability [*d'Ovidio et al.*, 2010; *Lévy et al.*, 2012; *D'Ovidio et al.*, 2015].

Surface density was used to identify the signature of the TIW waters around the Marquesas archipelago. Surface density was provided daily from January 1998 to December 2012 by the ocean reanalyses from the HYbrid Coordinate Ocean Model (HYCOM; the more precise values originating from the GLBu0.08/expt_19.1 experiment, http://hycom.org) at the 1/12° horizontal resolution.

Finally, in order to demonstrate a possible arrival of the equatorial particles at the Marquesas, Lagrangian trajectories were directly calculated using satellite derived surface current velocities. The Ocean Surface Current Analysis Real-time (OSCAR) data set was provided every 5 days with a 1/3° spatial resolution (http://dx.doi.org/10.5067/OSCAR-03D01). A fourth-order Runge–Kutta technique was used to integrate the Lagrangian equations. The south-westward SEC was considered, and after some trials, it clearly appears that the water particles that could reach the Marquesas area come from the north-east. Hence, water particle departure points were taken every degree over the area 4°S–1°S/130°W–120°W. Since we were interested in knowing whether particles can reach the Marquesas and contribute to the local phytoplankton enhancement, the maximum time drift of the particles was chosen from 30 to 120 days. The shorter duration is the minimum time to drift from the Equator to the archipelago. The longer one is assumed to be just long enough for the equatorial iron and phytoplankton to be consumed and grazed, respectively. Particles were launched every five days and the number of particles within the Marquesas area (11°S–8°S/142°W–138°W) after the maximum time drift (corresponding to the chosen simulation) was recorded.

A.3. Results

A.3.1. The case of the 1998 La Niña event

Finite-size lyapunov exponents were first used to identify large-scale regions characterized by different dynamical regimes. The 1998–2014 mean FSLE shows a weak dynamical activity area over 9°S–6°S/150°W–130°W, contrasting with the two higher dynamical regions located in the north along the Equator, and south of 10°S (Figure A-2a). The Marquesas archipelago lies within the calm area where fronts and transport barriers are barely noticeable. From a dynamical point of view, the Marquesas area is associated with weaker surface currents, warmer and lighter waters than waters flowing from the equatorial region northeast of the islands (Figure A-2b–d). The boundary of the oligotrophic and mesotrophic areas is noticeable southwest of the archipelago with low Chl (<0.1 mg/m^3; Figure A-1 and Figure A-2d).

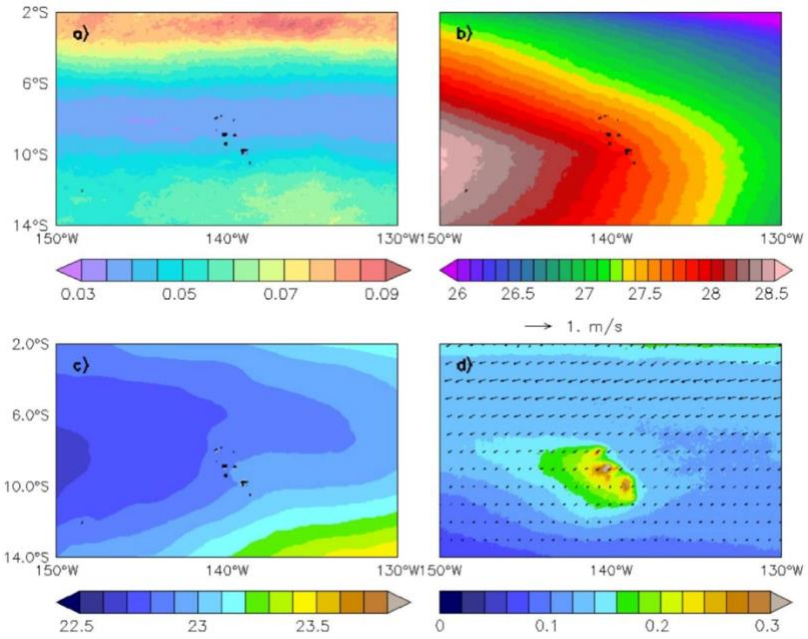

Figure A-2: Annual average conditions calculated over the whole-time period for the Marquesas physical and biological environment. (a) Finite-size lyapunov exponents (FSLEs) (d^{-1}); (b) Sea surface temperature (SST) (°C); (c) surface sigma (kg/m^3); (d) Chl (mg/m^3) and surface current (m/s). The islands are shown in black.

However, the weak dynamical activity within the Marquesas can be temporarily disrupted such as during the strong 1998–1999 La Niña. During this event, the FLSE annual root mean square (RMS) shows several individual paths of fronts induced by horizontal transport crossing the archipelago (Figure A-3). This disturbance in the FSLE dynamic could be attributed to the intrusion of TIWs in 1998 as reported by *Legeckis et al.* [2004].

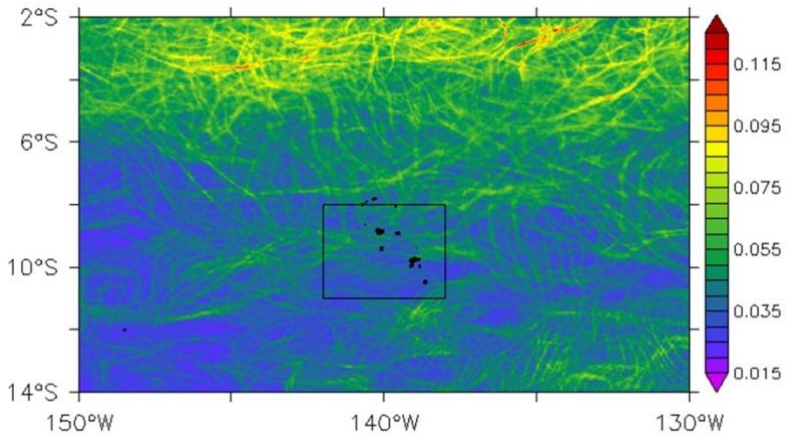

Figure A-3: Root mean square (RMS) of FLSEs in 1998. The black box delineates the area over which data are averaged to provide time-series of Figure A-6. The islands are shown in black.

The particular event occurring in September 1998 illustrates how one of these TIWs reaches the archipelago along a north-east/south-west axis in association with low SST (as in *Legeckis et al.* [2004]), a well-marked FSLE (Figure A-4, left column), and high-density waters flowing from the Equator (Figure A-4, centre column). This intrusion is most evident on 22 September 1998. Along the Equator, the highest Chl values (Figure A-4, right column) are associated with SST approximately lower than 23 °C. Within the archipelago, a Chl plume was already noticeable prior to the arrival of the TIW (not shown), likely due to the IME. However, the equatorial band seems to be connected to the northern islands of the Marquesas through a region of strong FSLE gradient and higher Chl pathway than the surrounding waters. This higher Chl plume down to 8°S could be associated with an uptake of nutrient which is likely to reach the northern part of the archipelago. The eastern boundary of the region of strong gradient of FSLE is delimited by strong surface currents, associated with low Chl patterns. Not only is there is no apparent increase of Chl in this part of the archipelago, but the outer area of the TIW is associated with a stirred low Chl plume. This pattern also reflects the differences between the interior and the exterior of the TIW in terms of Chl, SST, and surface density.

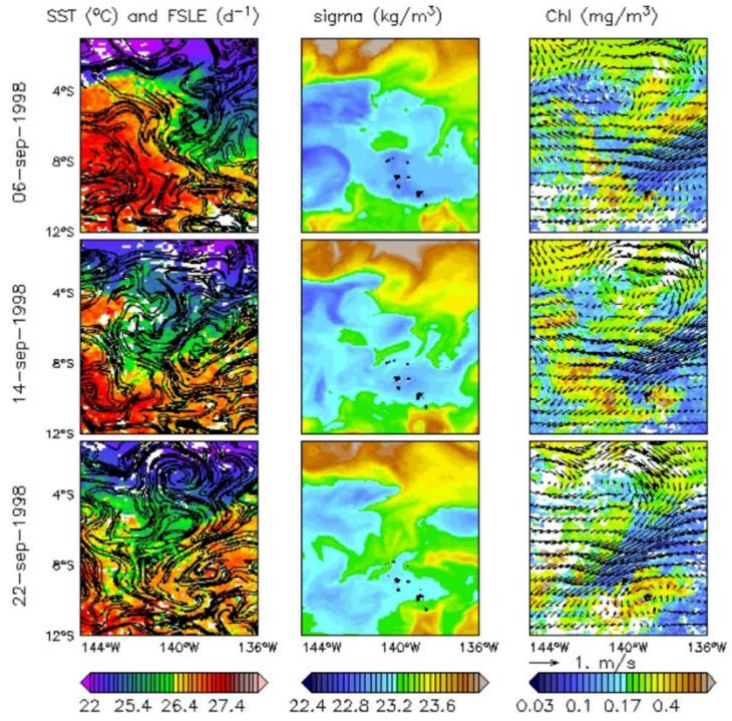

Figure A-4: (Left) SST (°C) and FSLEs (d^{-1}, isocontours are plotted from 0.07 to 1 every 0.1); (Centre) surface sigma (kg/m^3); (Right) Chl (mg/m^3) and surface current (m/s) on 6, 14, and 22 September 1998 (top to bottom, respectively). The islands are shown in black.

A.3.2. Investigating the 1997-2014 Period

Considering the annual RMS values, FLSEs also have a characteristic signal in the Marquesas archipelago during other moderate to strong La Niña years (Figure A-5). Consistently, the FSLE monthly anomalies ($FSLE_{ano}$) averaged over the archipelago (11°S–8°S and 142°W–138°W) are negatively correlated with the El Niño Southern Oscillation (ENSO) ($r_{El\ Nino34\text{-}FSLEano} = -0.42$; $p < 0.001$; Figure A-6b blue line vs. Figure A-6a). The weak dynamical activity within the archipelago is typical of neutral and El Niño years while during moderate to strong La Niña years (as defined with an index threshold of −1 in Figure A-6a), the FSLE activity increases. SST monthly anomalies (SST_{ano}) in this area are also correlated with ENSO ($r_{El\ Nino34\text{-}SSTano} = 0.73$; $p < 0.001$; Figure A-6b black line). During La Niña events, when the equatorial cold tongue and the related current shear are intense, TIWs become unusually vigorous (e.g., [*Evans et al.*, 2009; *Strutton et al.*, 2011]). Hence, cold anomalies associated with a high FSLE activity could be consistent with the passage of TIWs through the archipelago. However, the $FSLE_{ano}$ increase within the archipelago is not solely related to the strength of La Niña events. Indeed, $FSLE_{ano}$is stronger in late 1998 than in 1999, 2008, or 2010, while SST_{ano} is weaker and the El Niño 3.4 index is similar over these four years.

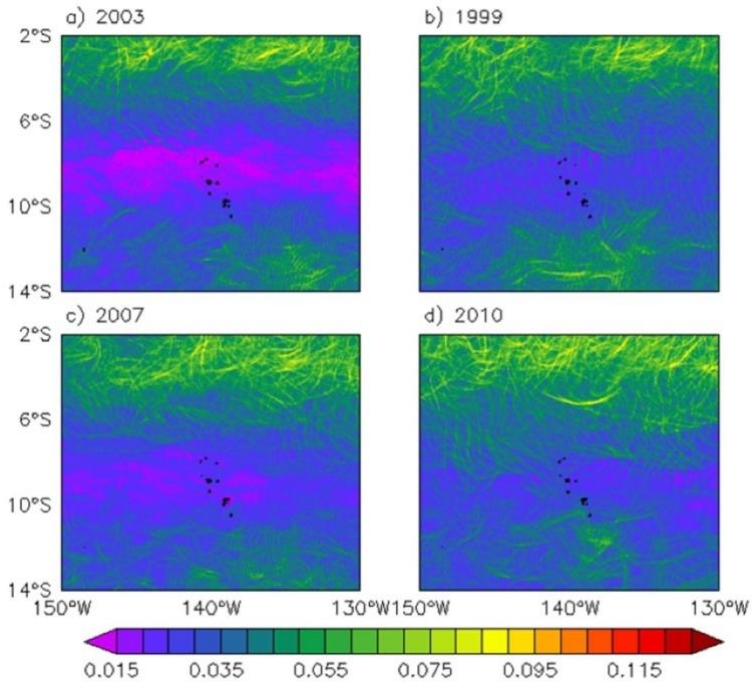

Figure A-5: Annual RMS of FLSE for (a) a neutral year (as in 2003); and during La Niña events as in (b) 1999; (c) 2007; and (d) 2010.

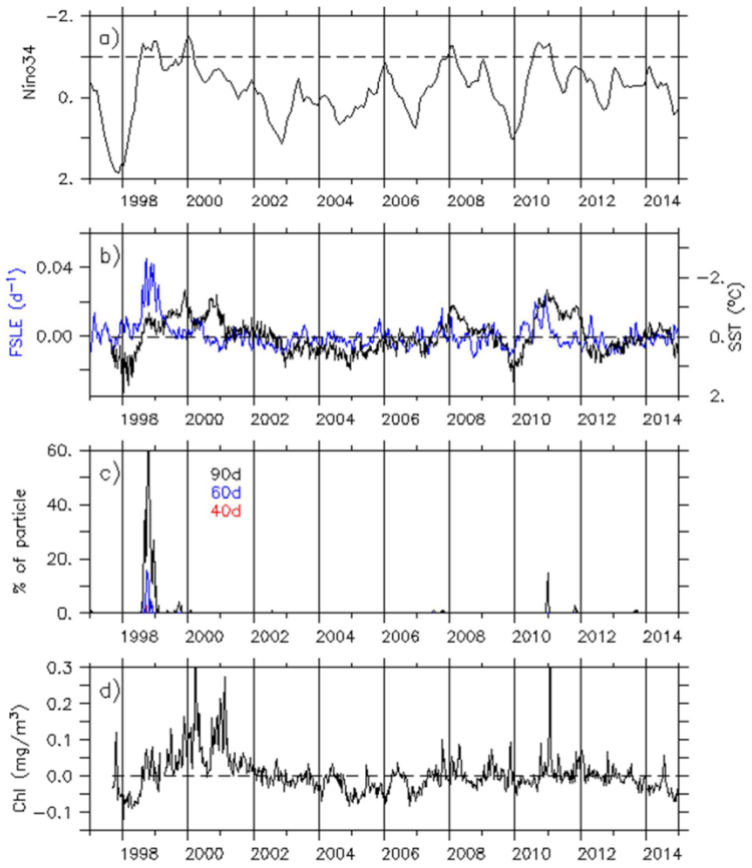

Figure A-6: Time series of (a) El Niño 3–4 index provided by the Climate Prediction Center (CPC)/National Centers for Environmental Prediction (NCEP) services (the y-axis is inverted). Values lower than the −1 threshold (dash line) highlight moderate to strong La Niña years; (b) FSLE (d^{-1}; blue line and left axis) and SST (°C; black line and right axis) monthly anomalies averaged over the Marquesas archipelago (11°S–18°S/142°W–138°W); (c) Number of particles launched from the northeastern equatorial area and reaching the Marquesas after 40, 60, and 90 days of drift (red, blue, and black lines, respectively); (d) Chl monthly anomalies (mg/m^3) averaged over the same area as in (b).

To further investigate the possibility of equatorial particles reaching the Marquesas, Lagrangian drift simulations were set up. After 30 days of drift, no particle reached the archipelago. It appears that the 1998 La Niña event is rather unique. Indeed, most particles reached the area after 40 to 60 days of drift for this 1998 event (Figure A-6c). During the 2010 La Niña event some particles reached the archipelago after 3 to 4 months. These Equator–Marquesas connections in 1998 and 2010 can be related to the two strongest peaks in FSLE activity and TIW pathways.

According to Legeckis et al., an enhancement of the Marquesas IME should be expected [*Legeckis et al.*, 2004]. However, Chl monthly anomalies (Chl_{ano}) increase only moderately following the FSLE and particle arrival in 1998, while the increase in 2010 is much stronger. The two strongest Chl_{ano} increases occurred around March 2000, and from mid-2000 to the beginning of 2001, strong and moderate La Niña years, respectively. While high Chl_{ano} in March 2000 might be related with a heavy rain event and induced island run-off, there is no explanation for the strong increase occurring in the end of 2000 [*Martinez and Maamaatuaiahutapu*, 2004]. However, in both cases these Chl_{ano} increases do not seem to be related with FSLE (and hence TIW) activity. Considering the whole-time series, it is clear that no correlation exits between the strength of Chl_{ano} changes and FSLEs ($r_{Chlano\text{-}FSLEano}$ = 0.09, Figure A-6d vs. Figure A-6b).

A.4. Discussion

The lack of systematic blooms following the arrival of TIWs in the Marquesas archipelago suggests that the TIWs may not bring (or may not bring enough) equatorial iron-rich waters to the islands for them to be responsible for increased biological activity. This is in agreement with several studies based on modelling. Indeed, the authors of *Gorgues et al.* [2005] showed that TIWs induce a decrease of iron concentration by 20% at the equator and by about 3% over the region 5°S–5°N and 180°W–90°W, hence inducing a Chl decrease of 10% and 1%, respectively. Consistent with our results, the authors of *Hasegawa et al.* [2009] reported that high Chl, in three regions north of the upwelling zone (2°N–7°N), does not result from increased TIW activity. On the contrary, Chl was particularly low during periods of strong TIW activity.

This result is illustrated hereafter with snapshots corresponding to $FSLE_{ano}$ peaks during the four strong to moderate La Niña events occurring over 1997–2014 (Figure A-7). First, high values of $FSLE_{ano}$ are clearly associated with TIWs. Second, the inner part of the TIWs associated with regions of strong gradient of FSLE has low Chl patterns, whereas the outer part of the TIWs is associated with a stirred plume of Chl. The Chl plume from the Equator down to 8°S along the TIWs and FSLEs is noticeable only in September 1998 (Figure A-4). In contrast, the FSLE fronts during other La Niña events rather reflect a local stirring of the Chl plume. In addition to the Lagrangian drift results, this suggests that the increase of Chl reported in the archipelago during La Niña may rather be the local signature of large-scale forcing such as an uplift of the thermocline or the enhancement of coastal upwelling induced by the

strengthening of the trades, uplifting nutrients. Because these two mechanisms have an imprint on SST, this is consistent with the Chl_{ano} and SST_{ano} correlation in the archipelago ($r_{SSTano-Chlano} = -0.44$, $p < 0.001$), although it is possible that a cold SST_{ano} could also partly reflect the pathway of TIWs.

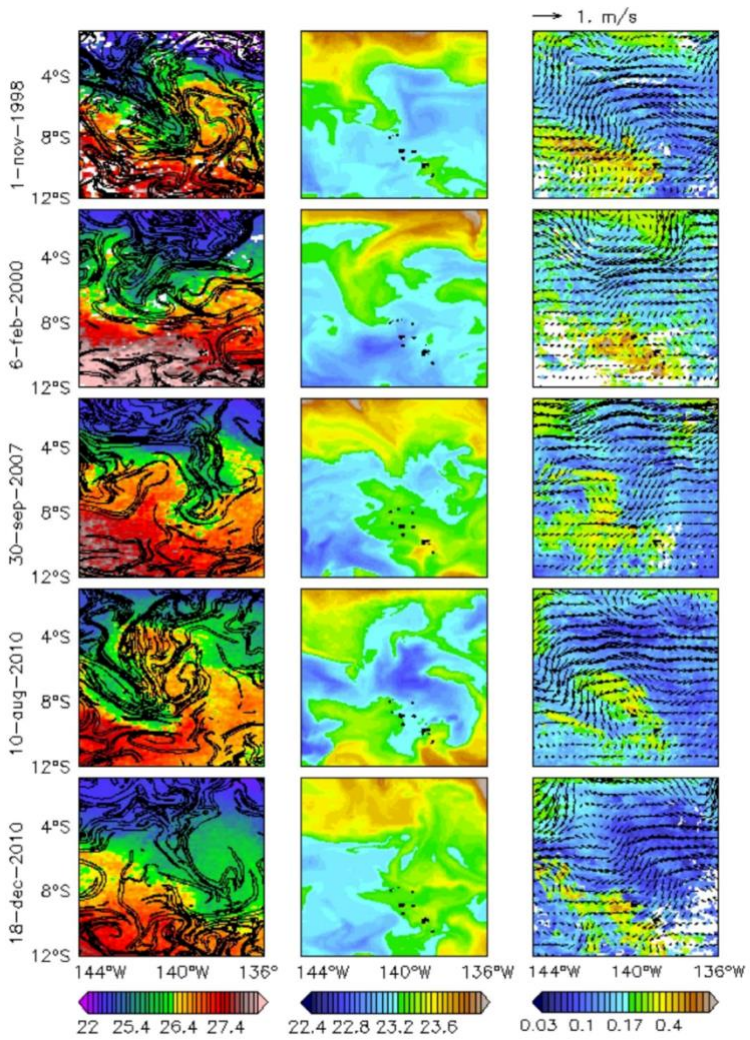

Figure A-7: (Left) SST (°C) and FSLEs (d^{-1}, isocontours are plotted from 0.07 to 1 every 0.1); (Centre) surface sigma (kg/m^3); (Right) Chl (mg/m^3) and surface current (m/s) during the five moderate to strong La Niña events over 1997–2014 (top to bottom). The islands are shown in black.

The present study also highlights the importance of small-scale processes and fronts in the local stirring and mixing around the Marquesas archipelago. *Martinez and Maamaatuaiahutapu* [2004] assumed that the mechanism at the origin of the IME is the result of the interaction between the chain of islands and the mean flow. However, the relevant process/processes, such

as wind-driven upwelling process or mixing due to friction, were not identified. While current satellite observations place the archipelago within a dynamically low region (Figure A-2a and Figure A-6b), this may be due to the fact that the spatial resolution of these products is limited. The use of a high-resolution model taking into account the topographic forcing (presence of the islands) emphasizes a high mean eddy kinetic energy (EKE) leeward of the islands (compare Figure A-8a vs. Figure A-8b). A dipole is formed behind the three northern islands where the flow is stronger than around the southern islands. A Von Karman-like eddy street can be seen on the relative vorticity map (Figure A-8c). Dipoles of cyclonic vs. anticyclonic structures are formed in the immediate lee of the islands, related to the EKE dipole pattern. Then, they detach and flow away south-westward. The cyclonic vortex (blue patches in Figure A-8c) leeward of the islands could be at the origin of upwelled rich waters, enhancing local primary production in the euphotic layer as also reported in *Hasegawa et al.* [2009]. These small-scale EKE and vorticity patterns in the wake of the islands may contribute to the local enrichment of Chl, which also shows small-scale structures (Figure A-8d).

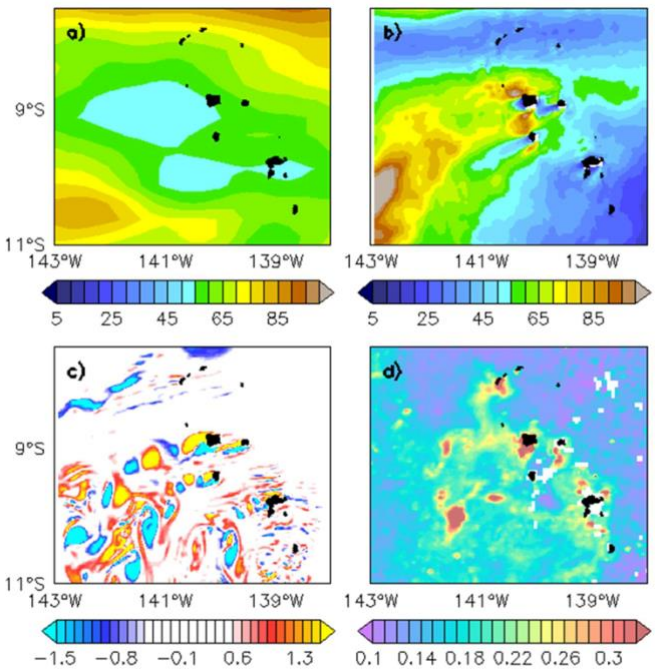

Figure A-8: Annual mean of eddy kinetic energy (EKE; cm²/s²) issued from (a) the Geostrophic and Ekman Current Observatory (GECKO) climatology with a ¼° spatial resolution [*Sudre et al.*, 2013] *and (b) a climatological 1/45° resolution simulation from the Regional Ocean Modeling System (ROMS model) (see* [*Raapoto et al.*, 2018]*); (c) Daily vorticity field (10^{-5}/s^{1}) at 10 m for 14 June of Year 6 from the ROMS climatological simulation; (d) Chl (mg/m^3) for 20 July 2006, from the satellite-derived Chl AVE GlobColour product.*

A.5. Conclusions

In this study, we investigated whether the iron-rich equatorial waters could reach the Marquesas archipelago during La Niña events by advection of tropical instability waves. Our study relied on a combination of ocean colour, temperature, and surface current satellite observations and modelled density with some estimates of small-scale structures as derived from large-scale ocean observed currents. While the authors of *Legeckis et al.* [2004] concluded that TIWs along the Equator may transport iron and influence the Marquesan phytoplankton blooms, we showed that this hypothesis could not be generalized to all La Niña events over the period 1997–2014. Indeed, an increase of Chl in the Marquesas is not systematically associated with the arrival of a TIW. Only the case in 1998, as initially suggested by *Legeckis et al.* [2004], seems to be related to iron advection from the Equator, and, to a lesser extent, a possible second one in 2010. However, how long it takes for phytoplankton to uptake iron probably flowing from the Equator remains an open question. Moreover, it is not possible to distinguish, at this moment, which part of the Chl plume enhancement in the Marquesas is due to a local IME, or to the potential advection of equatorial iron by the TIWs. Indeed, besides iron advection, the impacts of the TIWs with strong small-scale fronts and associated vertical dynamics could mix upward subsurface waters already enriched by the IME and, consequently, increase the bloom intensity. It appears that the water transported from the Equator to the Marquesas by the TIWs is able to disperse and stir the local waters, shaping the features of the plume of Chl and revealing the existence of strong frontal structures.

Finally, our study highlights the necessity to combine high resolution observations and coupled physical–biogeochemical numerical modelling as well as a regional/basin-scale overview to investigate the origin, patterns, and variability of the Marquesas IME. An effort to understand the potential impact of upwelled waters rich in iron associated with the local mesoscale eddies is currently underway.

Acknowledgments

We thank the government of French Polynesia for the financial support of the moana-maty project (convention n°6841/MTS), as well as A. Petrenko and A. Doglioli for the co-supervision of H. Raapoto. This work has also been supported by the OCEANS department from IRD. The data used are listed in the references and figures. We warmly thank Hilary Todd for correcting

the English. We would like to also acknowledge the four anonymous reviewers for their helpful comments.

References de l'Annexe A

Barber R. T, M. P. Sanderson, S. T. Lindley, F. Chai, J. Newton, C. C. Trees, D. G. Foley, and F. P. Chavez (1996), Primary productivity and its regulation in the equatorial Pacific during and following the 1991-92 El Ni{ñ}o, Deep. Res. Part II, 43(4–6), 933–969, doi:10.1016/0967-0645(96)00035-5.

Cai, W. et al. (2015), Increased frequency of extreme La Nina events under greenhouse warming, Nat. Clim. Chang., 5(2), 132–137, doi:10.1038/nclimate2492.

Claustre, H., A. Sciandra, and D. Vaulot (2008), Introduction to the special section bio-optical and biogeochemical conditions in the South East Pacific in late 2004: the BIOSOPE program, Biogeosciences, 5, 679–691, doi:10.5194/bgd-5-605-2008.

d'Ovidio, F., V. Fernández, E. Hernández-García, and C. López (2004), Mixing structures in the Mediterranean Sea from finite-size Lyapunov exponents, Geophys. Res. Lett., 31(17), doi:10.1029/2004GL020328.

d'Ovidio, F., S. De Monte, S. Alvain, Y. Dandonneau, and M. Levy (2010), Fluid dynamical niches of phytoplankton types, Proc. Natl. Acad. Sci., 107(43), 18366–18370, doi:10.1073/pnas.1004620107.

D'Ovidio, F., A. Della Penna, T. W. Trull, F. Nencioli, M. I. Pujol, M. H. Rio, Y. H. Park, C. Cotté, M. Zhou, and S. Blain (2015), The biogeochemical structuring role of horizontal stirring: Lagrangian perspectives on iron delivery downstream of the Kerguelen Plateau, Biogeosciences, 12(19), 5567–5581, doi:10.5194/bg-12-5567-2015.

Doty, M. S., and M. Oguri (1956), The Island Mass Effect, ICES J. Mar. Sci., doi:10.1093/icesjms/22.1.33.

Evans, W., P. G. Strutton, and F. P. Chavez (2009), Impact of tropical instability waves on nutrient and chlorophyll distributions in the equatorial Pacific, Deep. Res. Part I Oceanogr. Res. Pap., 56(2), 178–188, doi:10.1016/j.dsr.2008.08.008.

Fanton d'Andon, O., A. Mangin, S. Lavender, D. Antoine, S. Maritorena, A. Morel, G. Barrot, J. Demaria, and S. Pinnock (2009), GlobColour-the European Service for Ocean Colour, in Proceedings from 2009 IEEE International Geoscience & Remote Sensing Symposium (IGARSS).

Foley, D. G., T. D. Dickey, M. J. McPhaden, R. R. Bidigare, M. R. Lewis, R. T. Barber, S. T. Lindley, C. Garside, D. V. Manov, and J. D. McNeil (1997), Longwaves and primary productivity variations in the equatorial Pacific at 0°, 140°W, Deep. Res. Part II Top. Stud. Oceanogr., 44(9–10), 1801–1826, doi:10.1016/S0967-0645(97)00080-5.

Gorgues, T., C. Menkes, O. Aumont, J. Vialard, Y. Dandonneau, and L. Bopp (2005), Biogeochemical impact of tropical instability waves in the equatorial Pacific, Geophys. Res. Lett., 32(24), L24615, doi:10.1029/2005GL024110.

Hasegawa, D., M. R. Lewis, and a. Gangopadhyay (2009), How islands cause phytoplankton to bloom in their wakes, Geophys. Res. Lett., 36(20), 1–4, doi:10.1029/2009GL039743.

Legeckis, R. (1977), Long waves in the eastern equatorial Pacific Ocean: A view from a geostationary satellite, Science (80-.)., 197(4309), 1179–1181, doi:10.1126/science.197.4309.1179.

Legeckis, R., C. W. Brown, F. Bonjean, and E. S. Johnson (2004), The influence of tropical instability waves on phytoplankton blooms in the wake of the Marquesas Islands during 1998 and on the currents observed during the drift of the Kon-Tiki in 1947, Geophys. Res. Lett., 31(23), 1–4, doi:10.1029/2004GL021637.

Lévy, M., R. Ferrari, P. J. S. Franks, A. P. Martin, and P. Rivière (2012), Bringing physics to life at the submesoscale, Geophys. Res. Lett., 39(14), doi:10.1029/2012GL052756.

Lo-Yat, A., S. D. Simpson, M. Meekan, D. Lecchini, E. Martinez, and R. Galzin (2011), Extreme climatic events reduce ocean productivity and larval supply in a tropical reef ecosystem, Glob. Chang. Biol., 17(4), 1695–1702, doi:10.1111/j.1365-2486.2010.02355.x.

Martinez, E., and K. Maamaatuaiahutapu (2004), Island mass effect in the Marquesas Islands: Time variation, Geophys. Res. Lett., 31(18), 1–4, doi:10.1029/2004GL020682.

Martinez, E., M. Rodier, and K. Maamaatuaiahutapu (2016), Environnement océanique des Marquises, in Biodiversité terrestre et marine des îles Marquises, Polynésie Française, edited by R. Galzin, S.-D. Duron, and J.-Y. Meyer, pp. 123–136, Société française d'Ichtyologie, Paris.

Masotti, I., C. Moulin, S. Alvain, L. Bopp, A. Tagliabue, and D. Antoine (2011), Large-scale shifts in phytoplankton groups in the Equatorial Pacific during ENSO cycles, Biogeosciences, 8(3), 539–550, doi:10.5194/bg-8-539-2011.

Messié, M., M. H. Radenac, J. Lefèvre, and P. Marchesiello (2006), Chlorophyll bloom in the western Pacific at the end of the 1997-1998 El Niño: The role of the Kiribati Islands, Geophys. Res. Lett., 33(14), 1–5, doi:10.1029/2006GL026033.

Philander, S. G. H. (1978), Instabilities of zonal equatorial currents, 2, J. Geophys. Res., 83(C7), 3679, doi:10.1029/JC083iC07p03679.

Raapoto, H., E. Martinez, A. Petrenko, A. M. Doglioli, and C. Maes (2018), Modeling the Wake of the Marquesas Archipelago, J. Geophys. Res. Ocean., doi:10.1002/2017JC013285.

Radenac, M.-H., C. Menkes, J. Vialard, C. Moulin, Y. Dandonneau, T. Delcroix, C. Dupouy, A. Stoens, and P.-Y. Deschamps (2001), Modeled and observed impacts of the 1997-1998 El Niño on nitrate and new production in the equatorial Pacific, J. Geophys. Res. Ocean., 106(C11), 26879–26898, doi:10.1029/2000JC000546.

Radenac, M. H., F. Léger, A. Singh, and T. Delcroix (2012), Sea surface chlorophyll signature in the tropical Pacific during eastern and central Pacific ENSO events, J. Geophys. Res. Ocean., 117(4), 1–15, doi:10.1029/2011JC007841.

Shi, W., and M. Wang (2014), Satellite-observed biological variability in the equatorial Pacific during the 2009-2011 ENSO cycle, Adv. Sp. Res., 54(9), 1913–1923, doi:10.1016/j.asr.2014.07.003.

Signorini, S. R., C. R. McClain, and Y. Dandonneau (1999), Mixing and phytoplankton bloom in the wake of the Marquesas Islands, Geophys. Res. Lett., 26(20), 3121–3124, doi:10.1029/1999GL010470.

Strutton, P. G., J. P. Ryan, and F. P. Chavez (2001), Enhanced chlorophyll associated with tropical instability waves in the equatorial Pacific, Geophys. Res. Lett., 28(10), 2005–2008, doi:10.1029/2000GL012166.

Strutton, P. G., A. P. Palacz, R. C. Dugdale, F. Chai, A. Marchi, A. E. Parker, V. Hogue, and F. P. Wilkerson (2011), The impact of equatorial Pacific tropical instability waves on hydrography and nutrients: 2004-2005, Deep. Res. Part II Top. Stud. Oceanogr., 58(3–4), 284–295, doi:10.1016/j.dsr2.2010.08.015.

Sudre, J., C. Maes, and V. Garçon (2013), On the global estimates of geostrophic and Ekman surface currents, Limnol. Oceanogr. Fluids Environ., 3(1), 1–20, doi:10.1215/21573689-2071927.

Yu, J.-Y., and W. T. Liu (2003), A linear relationship between ENSO intensity and tropical instability wave activity in the eastern Pacific Ocean, Geophys. Res. Lett., 30(14), doi:10.1029/2003GL017176.

Conclusion de l'Annexe A

Dans leur étude, Legeckis et al. (2004) ont émis l'hypothèse que les ondes d'instabilités tropicales (Tropical Instability Waves, TIW) permettraient de transporter des eaux riches en fer depuis l'équateur et enrichiraient l'archipel des Marquises durant les événements La Niña. Cependant, comme nous avons pu le montrer dans ce chapitre, cette hypothèse ne peut être généralisée à tous les évènements La Niña. En effet, les augmentations de Chl dans l'archipel ne sont pas systématiquement corrélées avec l'arrivée de TIWs. L'enrichissement en fer depuis l'équateur semble possible uniquement pendant les évènements La Niña de 1998 et 2010. Il apparait également que les TIWs peuvent influencer la forme du panache de Chl dans l'archipel. Cependant, la dynamique générée par la présence des îles Marquises au milieu de l'écoulement du courant équatorial sud parait jouer un rôle prédominant dans l'enrichissement de l'archipel.

Cette étude menée sur l'impact des TIWs sur les îles Marquises reste cependant limitée à la dynamique de surface, et avec des résolutions spatio-temporelles insuffisante au regard des processus impliqués ici. De la même manière, l'utilisation des sorties d'un modèle global tel que celui utilisé dans cette étude (HYCOM) reste, elle aussi, limitée par la faible résolution de ces produits.

Références

Alaee, M. J., G. Ivey, and C. Pattiaratchi (2004), Secondary circulation induced by flow curvature and Coriolis effects around headlands and islands, *Ocean Dyn.*, *54*(1), 27–38, doi:10.1007/s10236-003-0058-3.

Amores, A., S. Monserrat, and M. Marcos (2013), Vertical structure and temporal evolution of an anticyclonic eddy in the Balearic Sea (western Mediterranean), *J. Geophys. Res. Ocean.*, *118*(4), 2097–2106, doi:10.1002/jgrc.20150.

Andrade, I., P. Sangrà, S. Hormazabal, and M. Correa-Ramirez (2014), Island mass effect in the Juan Fernández Archipelago (33°S), Southeastern Pacific, *Deep. Res. Part I Oceanogr. Res. Pap.*, *84*, 86–99, doi:10.1016/j.dsr.2013.10.009.

Antonov, J., D. Seidov, T. Boyer, and R. Locarnini (2010), World Ocean Atlas 2009, vol. 2: Salinity, edited by: Levitus, *S., NOAA Atlas NESDIS*.

Auad, G., A. Pares-Sierra, and G. K. Vallis (1991), Circulation and energetics of a model of the California Current system.pdf, *J. Phys. Oceanogr.*, *21*(10), 1534–1552.

Aumont, O., and L. Bopp (2006), Globalizing results from ocean in situ iron fertilization studies, *Global Biogeochem. Cycles*, *20*(2), n/a-n/a, doi:10.1029/2005GB002591.

Aumont, O., C. Ethé, a. Tagliabue, L. Bopp, and M. Gehlen (2015), PISCES-v2: an ocean biogeochemical model for carbon and ecosystem studies, *Geosci. Model Dev. Discuss.*, *8*(2), 1375–1509, doi:10.5194/gmdd-8-1375-2015.

Barber R. T, M. P. Sanderson, S. T. Lindley, F. Chai, J. Newton, C. C. Trees, D. G. Foley, and F. P. Chavez (1996), Primary productivity and its regulation in the equatorial Pacific during and following the 1991-92 El Ni{ñ}o, *Deep. Res. Part II*, *43*(4–6), 933–969, doi:10.1016/0967-0645(96)00035-5.

Barton, E. D. (2001), Island wakes, *Encycl. Ocean Sci.*, *3*, 1397–1403, doi:10.1006/rwos.2001.0140.

Beckmann, A., and D. B. Haidvogel (1993), Numerical Simulation of Flow around a Tall Isolated Seamount. Part I: Problem Formulation and Model Accuracy, *J. Phys. Oceanogr.*, *23*(8), 1736–1753, doi:10.1175/1520-0485(1993)023<1736:NSOFAA>2.0.CO;2.

Bell, J. D., M. Kronen, A. Vunisea, W. J. Nash, G. Keeble, A. Demmke, S. Pontifex, and S. Andréfouët (2009), Planning the use of fish for food security in the Pacific, *Mar. Policy*, *33*(1), 64–76, doi:10.1016/j.marpol.2008.04.002.

Benitez-Nelson, C. R., and D. J. McGillicuddy (2008), Mesoscale physical–biological–biogeochemical linkages in the open ocean: An introduction to the results of the E-Flux

and EDDIES programs, *Deep Sea Res. Part II Top. Stud. Oceanogr.*, *55*(10–13), 1133–1138, doi:10.1016/j.dsr2.2008.03.001.

Blain, S. et al. (2007), Effect of natural iron fertilization on carbon sequestration in the Southern Ocean, *Nature*, *446*(7139), 1070–1074, doi:10.1038/nature05700.

Blain, S., S. Bonnet, and C. Guieu (2008), Dissolved iron distribution in the tropical and sub tropical South Eastern Pacific, *Biogeosciences*, *5*(1), 269–280, doi:10.5194/bgd-4-2845-2007.

Bonjean, F., and G. S. E. Lagerloef (2002), Diagnostic model and analysis of the surface currents in the tropical Pacific Ocean, *J. Phys. Oceanogr.*, *32*(10), 2938–2954, doi:10.1175/1520-0485(2002)032<2938:DMAAOT>2.0.CO;2.

Boyd, P. W., and M. J. Ellwood (2010), The biogeochemical cycle of iron in the ocean, *Nat. Geosci.*, *3*(10), 675–682, doi:10.1038/ngeo964.

Cai, W. et al. (2015), Increased frequency of extreme La Nina events under greenhouse warming, *Nat. Clim. Chang.*, *5*(2), 132–137, doi:10.1038/nclimate2492.

Caldeira, R. M. A., and P. Marchesiello (2002), Ocean response to wind sheltering in the Southern California Bight, *Geophys. Res. Lett.*, *29*(13), 1–4, doi:10.1029/2001GL014563.

Caldeira, R. M. A., S. Groom, P. Miller, D. Pilgrim, and N. P. Nezlin (2002), Sea-surface signatures of the island mass effect phenomena around Madeira Island, Northeast Atlantic, *Remote Sens. Environ.*, *80*(2), 336–360, doi:10.1016/S0034-4257(01)00316-9.

Calil, P. H. R., K. J. Richards, Y. Jia, and R. R. Bidigare (2008), Eddy activity in the lee of the Hawaiian Islands, *Deep. Res. Part II Top. Stud. Oceanogr.*, *55*(10–13), 1179–1194, doi:10.1016/j.dsr2.2008.01.008.

Chang, M. H., T. Y. Tang, C. R. Ho, and S. Y. Chao (2013), Kuroshio-induced wake in the lee of Green Island off Taiwan, *J. Geophys. Res. Ocean.*, *118*(3), 1508–1519, doi:10.1002/jgrc.20151.

Chavanne, C., P. Flament, R. Lumpkin, B. Dousset, and A. Bentamy (2002), Scatterometer observations of wind variations induced by oceanic islands: implications for wind-driven ocean circulation., *Can. J. Remote Sens.*, *28*(3), 466–474, doi:10.5589/m02-047.

Chelton, D. B., R. a. deSzoeke, M. G. Schlax, K. El Naggar, and N. Siwertz (1998), Geographical Variability of the First Baroclinic Rossby Radius of Deformation, *J. Phys. Oceanogr.*, *28*(3), 433–460, doi:10.1175/1520-0485(1998)028<0433:GVOTFB>2.0.CO;2.

Chen, R., A. F. Thompson, and G. R. Flierl (2016), Time-dependent eddy-mean energy diagrams and their application to the ocean, *J. Phys. Oceanogr.*, *46*(9), 2827–2850,

doi:10.1175/JPO-D-16-0012.1.

Claustre, H., A. Sciandra, and D. Vaulot (2008), Introduction to the special section bio-optical and biogeochemical conditions in the South East Pacific in late 2004: the BIOSOPE program, *Biogeosciences*, *5*, 679–691, doi:10.5194/bgd-5-605-2008.

Cummings, J. A., and O. M. Smedstad (2013), Variational Data Assimilation for the Global Ocean, in *Data Assimilation for Atmospheric, Oceanic and Hydrologic Applications (Vol. II)*, vol. II, edited by Springer, pp. 303–343, Berlin, Heidelberg.

da Cunha, L. C., and E. T. Buitenhuis (2013), Riverine influence on the tropical Atlantic Ocean biogeochemistry, *Biogeosciences*, *10*(10), 6357–6373, doi:10.5194/bg-10-6357-2013.

d'Ovidio, F., V. Fernández, E. Hernández-García, and C. López (2004), Mixing structures in the Mediterranean Sea from finite-size Lyapunov exponents, *Geophys. Res. Lett.*, *31*(17), doi:10.1029/2004GL020328.

d'Ovidio, F., S. De Monte, S. Alvain, Y. Dandonneau, and M. Levy (2010), Fluid dynamical niches of phytoplankton types, *Proc. Natl. Acad. Sci.*, *107*(43), 18366–18370, doi:10.1073/pnas.1004620107.

D'Ovidio, F., A. Della Penna, T. W. Trull, F. Nencioli, M. I. Pujol, M. H. Rio, Y. H. Park, C. Cotté, M. Zhou, and S. Blain (2015), The biogeochemical structuring role of horizontal stirring: Lagrangian perspectives on iron delivery downstream of the Kerguelen Plateau, *Biogeosciences*, *12*(19), 5567–5581, doi:10.5194/bg-12-5567-2015.

Dale, A. W., L. Nickelsen, F. Scholz, C. Hensen, A. Oschlies, and K. Wallmann (2015), A revised global estimate of dissolved iron fluxes from marine sediments, *Global Biogeochem. Cycles*, *29*(5), 691–707, doi:10.1002/2014GB005017.

Debreu, L., and E. Blayo (2008), Two-way embedding algorithms: A review, *Ocean Dyn.*, *58*(5–6), 415–428, doi:10.1007/s10236-008-0150-9.

Debreu, L., P. Marchesiello, P. Penven, and G. Cambon (2012), Two-way nesting in split-explicit ocean models: Algorithms, implementation and validation, *Ocean Model.*, *49–50*, 1–21, doi:10.1016/j.ocemod.2012.03.003.

Dietrich, D. E., M. J. Bowmanb, C. A. Lin, and A. Mestas-nunezd (1996), Numerical studies of small island wakes in the ocean, *Geophys. Astrophys. Fluid Dyn.*, *83*(3–4), 195–231, doi:10.1080/03091929608208966.

DiGiacomo, P. M., and B. Holt (2001), Satellite observations of small coastal ocean eddies in the Southern California Bight, *J. Geophys. Res.*, *106*(10), 22,521-522,543, doi:10.1029/2000JC000728.

Doglioli, A. M., B. Blanke, S. Speich, and G. Lapeyre (2007), Tracking coherent structures in

a regional ocean model with wavelet analysis: Application to Cape Basin eddies, *J. Geophys. Res. Ocean.*, *112*(5), 1–12, doi:10.1029/2006JC003952.

Dong, C., and J. C. McWilliams (2007), A numerical study of island wakes in the Southern California Bight, *Cont. Shelf Res.*, *27*(9), 1233–1248, doi:10.1016/j.csr.2007.01.016.

Dong, C., J. C. McWilliams, and A. F. Shchepetkin (2007), Island Wakes in Deep Water, *J. Phys. Oceanogr.*, *37*(4), 962–981, doi:10.1175/JPO3047.1.

Dong, C., X. Lin, Y. Liu, F. Nencioli, Y. Chao, Y. Guan, D. Chen, T. Dickey, and J. C. McWilliams (2012), Three-dimensional oceanic eddy analysis in the Southern California Bight from a numerical product, *J. Geophys. Res. Ocean.*, *117*(1), 1–17, doi:10.1029/2011JC007354.

Doty, M. S., and M. Oguri (1956), The Island Mass Effect, *ICES J. Mar. Sci.*, doi:10.1093/icesjms/22.1.33.

Elrod, V. A., W. M. Berelson, K. H. Coale, and K. S. Johnson (2004), The flux of iron from continental shelf sediments: A missing source for global budgets, *Geophys. Res. Lett.*, *31*(12), 2–5, doi:10.1029/2004GL020216.

Emery, W. J. (2001), Water Types and Water Masses, *Encycl. Ocean Sci. Second Ed.*, *6*, 3179–3187, doi:10.1006/rwos.2001.0108.

Emery, W. J. (2003), Water Types and Water Masses Descriptive Tools : The TS Curve, in *Ocean Circulation*, pp. 1556–1567.

Evans, W., P. G. Strutton, and F. P. Chavez (2009), Impact of tropical instability waves on nutrient and chlorophyll distributions in the equatorial Pacific, *Deep. Res. Part I Oceanogr. Res. Pap.*, *56*(2), 178–188, doi:10.1016/j.dsr.2008.08.008.

Fanton d'Andon, O., A. Mangin, S. Lavender, D. Antoine, S. Maritorena, A. Morel, G. Barrot, J. Demaria, and S. Pinnock (2009), GlobColour-the European Service for Ocean Colour, in *Proceedings from 2009 IEEE International Geoscience & Remote Sensing Symposium (IGARSS)*.

Foley, D. G., T. D. Dickey, M. J. McPhaden, R. R. Bidigare, M. R. Lewis, R. T. Barber, S. T. Lindley, C. Garside, D. V. Manov, and J. D. McNeil (1997), Longwaves and primary productivity variations in the equatorial Pacific at 0°, 140°W, *Deep. Res. Part II Top. Stud. Oceanogr.*, *44*(9–10), 1801–1826, doi:10.1016/S0967-0645(97)00080-5.

Folland, C. K., J. A. Renwick, M. J. Salinger, and A. B. Mullan (2002), Relative influences of the Interdecadal Pacific Oscillation and ENSO on the South Pacific Convergence Zone, *Geophys. Res. Lett.*, *29*(13), 2–5, doi:10.1029/2001GL014201.

Gaillard, F., T. Reynaud, V. Thierry, N. Kolodziejczyk, and K. Von Schuckmann (2016), In

situ-based reanalysis of the global ocean temperature and salinity with ISAS: Variability of the heat content and steric height, *J. Clim.*, *29*(4), 1305–1323, doi:10.1175/JCLI-D-15-0028.1.

Geider, R. J., H. L. MacIntyre, and T. M. Kana (1997), Dynamic model of phytoplankton growth and acclimation: Responses of the balanced growth rate and the chlorophyll a:carbon ratio to light, nutrient-limitation and temperature, *Mar. Ecol. Prog. Ser.*, *148*(1–3), 187–200, doi:10.3354/meps148187.

Gordon, H. R., and W. R. McCluney (1975), Estimation of the Depth of Sunlight Penetration in the Sea for Remote Sensing, *Appl. Opt.*, *14*(2), 413, doi:10.1364/AO.14.000413.

Gorgues, T., C. Menkes, O. Aumont, J. Vialard, Y. Dandonneau, and L. Bopp (2005), Biogeochemical impact of tropical instability waves in the equatorial Pacific, *Geophys. Res. Lett.*, *32*(24), L24615, doi:10.1029/2005GL024110.

Goyet, C., R. Healy, J. Ryan, and A. Kozyr (2000), Global distribution of total inorganic carbon and total alkalinity below the deepest winter mixed layer depths,

Guieu, C., S. Bonnet, A. Petrenko, C. Menkes, V. Chavagnac, K. Desboeufs, C. Maes, and T. Moutin (2018), Iron from a submarine source impacts the productive layer of the Western Tropical South Pacific (WTSP), *Sci. Rep.*, *8*(1), 9075, doi:10.1038/s41598-018-27407-z.

Halo, I., P. Penven, B. Backeberg, I. Ansorge, F. Shillington, and R. Roman (2014), Mesoscale eddy variability in the southern extension of the East Madagascar Current: Seasonal cycle, energy conversion terms, and eddymean properties, *J. Geophys. Res. Ocean.*, *00000*, 7324–7356, doi:10.1002/2014JC009820.

Harrison, D. E., and A. R. Robinson (1978), Energy analysis of open regions of turbulent flows - mean eddy energetics of a numerical ocean circulation experiment, *Dyn. Atmos. Ocean.*, *2*(2), 185–211, doi:10.1016/0377-0265(78)90009-X.

Hasegawa, D., H. Yamazaki, R. G. Lueck, and L. Seuront (2004), How islands stir and fertilize the upper ocean, *Geophys. Res. Lett.*, *31*(16), 1–4, doi:10.1029/2004GL020143.

Hasegawa, D., H. Yamazaki, T. Ishimaru, H. Nagashima, and Y. Koike (2008), Apparent phytoplankton bloom due to island mass effect, *J. Mar. Syst.*, *69*(3–4), 238–246, doi:10.1016/j.jmarsys.2006.04.019.

Hasegawa, D., M. R. Lewis, and a. Gangopadhyay (2009), How islands cause phytoplankton to bloom in their wakes, *Geophys. Res. Lett.*, *36*(20), 1–4, doi:10.1029/2009GL039743.

Hastings, D. A., and W. J. Emery (1992), The advanced very high resolution radiometer (AVHRR): a brief reference guide., *Photogramm. Eng. Remote Sensing.*, *58*(8), 1183–1188.

Henley, B. J., J. Gergis, D. J. Karoly, S. Power, J. Kennedy, and C. K. Folland (2015), A Tripole Index for the Interdecadal Pacific Oscillation, *Clim. Dyn.*, *45*(11–12), 3077–3090, doi:10.1007/s00382-015-2525-1.

Hernández-León, S., M. Gómez, M. Pagazaurtundua, A. Portillo-Hahnefeld, I. Montero, and C. Almeida (2001), Vertical distribution of zooplankton in Canary Island waters: implications for export flux, *Deep Sea Res. Part I Oceanogr. Res. Pap.*, *48*(4), 1071–1092, doi:10.1016/S0967-0637(00)00074-1.

Heywood, K. J., E. D. Barton, and J. H. Simpson (1990), The effects of flow disturbance by an oceanic island, *J. Mar. Res.*, *48*, 55–73, doi:10.1357/002224090784984623.

Heywood, K. J., D. P. Stevens, and G. R. Bigg (1996), Eddy formation behind the tropical island of Aldabra, *Deep. Res. Part I Oceanogr. Res. Pap.*, *43*(4), 555–578, doi:10.1016/0967-0637(96)00097-0.

Hristova, H. G., W. S. Kessler, J. C. McWilliams, and M. J. Molemaker (2014), Mesoscale variability and its seasonality in the Solomon and Coral Seas, *J. Geophys. Res. Ocean.*, *119*, 4669–4687, doi:10.1002/2013JC009741.

Jeandel, C., and E. H. Oelkers (2015), The influence of terrigenous particulate material dissolution on ocean chemistry and global element cycles, *Chem. Geol.*, *395*, 50–66, doi:10.1016/j.chemgeo.2014.12.001.

Jickells, T. D. et al. (2005), Global iron connections between desert dust, ocean biogeochemistry, and climate., *Science*, *308*(5718), 67–71, doi:10.1126/science.1105959.

Jiménez, B., P. Sangrà, and E. Mason (2008), A numerical study of the relative importance of wind and topographic forcing on oceanic eddy shedding by tall, deep water islands, *Ocean Model.*, *22*(3–4), 146–157, doi:10.1016/j.ocemod.2008.02.004.

Johnson, K., and H. Claustre (2016), Bringing Biogeochemistry into the Argo Age, *Eos (Washington. DC).*, doi:10.1029/2016EO062427.

Johnson, K. S., F. P. Chavez, and G. E. Friederich (1999), Continental-shelf sediment as a primary source of iron for coastal phytoplankton, *Nature*, *398*(6729), 697–700, doi:10.1038/19511.

Kang, D., and E. N. Curchitser (2015), Energetics of Eddy-Mean Flow Interactions in the Gulf Stream Region, *J. Phys. Oceanogr.*, *45*, 1103–1120, doi:10.1175/JPO-D-14-0200.1.

Von Karman, T., and W. R. Sears (1938), Airfoil Theory for Non-Uniform Motion, *J. Aeronaut. Sci.*, *5*(10), 379–390, doi:10.2514/8.674.

Karnauskas, K. B., G. C. Johnson, and R. Murtugudde (2017), On the climate impacts of atolls in the central equatorial Pacific, *Int. J. Climatol.*, *37*(1), 197–203, doi:10.1002/joc.4697.

Kersalé, M., a. M. Doglioli, and a. a. Petrenko (2011), Sensitivity study of the generation of mesoscale eddies in a numerical model of Hawaii islands, *Ocean Sci.*, *7*(3), 277–291, doi:10.5194/os-7-277-2011.

Large, W. G., J. C. McWilliams, and S. C. Doney (1994), Oceanic vertical mixing: A review and a model with a nonlocal boundary layer parameterization, *Rev. Geophys.*, *32*(4), 363, doi:10.1029/94RG01872.

Laurent, V., K. Maamaatuaiahutapu, J. Maiau, and P. Varney (2004), *Atlas Climatologique de la Polynésie Française*, Météo Fran.

Legeckis, R. (1977), Long waves in the eastern equatorial Pacific Ocean: A view from a geostationary satellite, *Science (80-.).*, *197*(4309), 1179–1181, doi:10.1126/science.197.4309.1179.

Legeckis, R., C. W. Brown, F. Bonjean, and E. S. Johnson (2004), The influence of tropical instability waves on phytoplankton blooms in the wake of the Marquesas Islands during 1998 and on the currents observed during the drift of the Kon-Tiki in 1947, *Geophys. Res. Lett.*, *31*(23), 1–4, doi:10.1029/2004GL021637.

Lehodey, P., I. Senina, and R. Murtugudde (2008), A spatial ecosystem and populations dynamics model (SEAPODYM) – Modeling of tuna and tuna-like populations, *Prog. Oceanogr.*, *78*(4), 304–318, doi:10.1016/j.pocean.2008.06.004.

Lehodey, P. et al. (2011), Vulnerability of oceanic fisheries in the tropical Pacific to climate change, *Vulnerability Trop. Pacific Fish. Aquac. to Clim. Chang.*, 433–492.

Lévy, M., R. Ferrari, P. J. S. Franks, A. P. Martin, and P. Rivière (2012), Bringing physics to life at the submesoscale, *Geophys. Res. Lett.*, *39*(14), doi:10.1029/2012GL052756.

Liang, J. H., J. C. McWilliams, J. Kurian, F. Colas, P. Wang, and Y. Uchiyama (2012), Mesoscale variability in the northeastern tropical Pacific: Forcing mechanisms and eddy properties, *J. Geophys. Res. Ocean.*, *117*(7), 1–13, doi:10.1029/2012JC008008.

Liu, Y., C. Dong, Y. Guan, D. Chen, J. McWilliams, and F. Nencioli (2012), Eddy analysis in the subtropical zonal band of the North Pacific Ocean, *Deep. Res. Part I Oceanogr. Res. Pap.*, *68*, 54–67, doi:10.1016/j.dsr.2012.06.001.

Lo-Yat, A., S. D. Simpson, M. Meekan, D. Lecchini, E. Martinez, and R. Galzin (2011), Extreme climatic events reduce ocean productivity and larval supply in a tropical reef ecosystem, *Glob. Chang. Biol.*, *17*(4), 1695–1702, doi:10.1111/j.1365-2486.2010.02355.x.

Locarnini, R., A. Mishonov, J. Antonov, T. Boyer, and H. Garcia (2010), World Ocean Atlas 2009, vol. 1, Temperature, edited by S. Levitus, 184 pp, *US Gov. Print. Off.*

Locarnini, R. A. et al. (2013), World Ocean Atlas 2013. Vol. 1: Temperature., *S. Levitus, Ed.; A. Mishonov, Tech. Ed.; NOAA Atlas NESDIS*, *73*(September), 40, doi:10.1182/blood-2011-06-357442.

Lungu, T., and P. S. Callahan (2006), QuikSCAT science data product user's manual: Overview and geophysical data products, *D-18053-Rev A, version*, *3*, 91.

Maraldi, C., M. Mongin, R. Coleman, and L. Testut (2009), The influence of lateral mixing on a phytoplankton bloom: Distribution in the Kerguelen Plateau region, *Deep. Res. Part I Oceanogr. Res. Pap.*, *56*(6), 963–973, doi:10.1016/j.dsr.2008.12.018.

Marchesiello, P., J. C. McWilliams, and A. Shchepetkin (2001), Open boundary conditions for long-term integration of regional oceanic models, *Ocean Model.*, *3*(1–2), 1–20, doi:10.1016/S1463-5003(00)00013-5.

Marchesiello, P., J. C. McWilliams, A. Shchepetkin, P. Physics, and L. Angeles (2003), Equilibrium Structure and Dynamics of the California Current System, *J. Phys. Oceanogr.*, *33*(4), 753–783, doi:10.1175/1520-0485(2003)33<753:ESADOT>2.0.CO;2.

Martin, J. H., and S. E. Fitzwater (1988), Iron deficiency limits phytoplankton growth in the north-east Pacific subarctic, *Nature*, *331*(6154), 341–343, doi:10.1038/331341a0.

Martinez, E., and K. Maamaatuaiahutapu (2004), Island mass effect in the Marquesas Islands: Time variation, *Geophys. Res. Lett.*, *31*(18), 1–4, doi:10.1029/2004GL020682.

Martinez, E., A. Ganachaud, J. Lefevre, and K. Maamaatuaiahutapu (2009), Central south pacific thermocline water circulation from a high-resolution ocean model validated against satellite data: seasonal variability and el niño 1997-1998 influence, *J. Geophys. Res. Ocean.*, *114*(5), 1–16, doi:10.1029/2008JC004824.

Martinez, E., M. Rodier, and K. Maamaatuaiahutapu (2016), Environnement océanique des Marquises, in *Biodiversité terrestre et marine des îles Marquises, Polynésie Française*, edited by R. Galzin, S.-D. Duron, and J.-Y. Meyer, pp. 123–136, Société française d'Ichtyologie, Paris.

Martinez, E., H. Raapoto, C. Maes, and K. Maamaatuaihutapu (2018), Influence of Tropical Instability Waves on Phytoplankton Biomass near the Marquesas Islands, , 1–12, doi:10.3390/rs10040640.

Masotti, I., C. Moulin, S. Alvain, L. Bopp, A. Tagliabue, and D. Antoine (2011), Large-scale shifts in phytoplankton groups in the Equatorial Pacific during ENSO cycles, *Biogeosciences*, *8*(3), 539–550, doi:10.5194/bg-8-539-2011.

Maury, R. C., G. Guille, G. Hervé, C. Catherine, C. Legendre, P. Rossi, S. Blais, C. Pallares, D. Sébastien, and A. Marabal (2014), Géologie des Marquises : des volcans boucliers

intra-océaniques effondrés issus d ' un point chaud atypique Géologie des Marquises : des volcans boucliers intra-océaniques effondrés issus d ' un point chaud atypique, *Géologie la Fr.*, *1*(8), 111–135.

McPhaden, M. J. (1999), Genesis and Evolution of the 1997-98 El Niño, *Science (80-.).*, *283*, 950–954, doi:10.1126/science.283.5404.950.

McPhaden, M. J. (2015), Playing hide and seek with El Niño, *Nat. Clim. Chang.*, *5*(9), 791–795, doi:10.1038/nclimate2775.

McPhaden MJ (1993), TOGA-TAO and the 1991 93 El Nino Southern Oscillation event, *Oceanography*, *6,No. 2*(2), 36 44, doi:10.2307/43924639.

Menzel, D. W., and J. H. Ryther (1961), Annual variations in primary productivity of the Sargasso Sea off Bermuda, *Deep. Res. I*, *7*(1119), 282–288.

Messié, M., and F. P. Chavez (2012), A global analysis of ENSO synchrony: The oceans' biological response to physical forcing, *J. Geophys. Res. Ocean.*, *117*(C9), n/a-n/a, doi:10.1029/2012JC007938.

Messié, M., M. H. Radenac, J. Lefèvre, and P. Marchesiello (2006), Chlorophyll bloom in the western Pacific at the end of the 1997-1998 El Niño: The role of the Kiribati Islands, *Geophys. Res. Lett.*, *33*(14), 1–5, doi:10.1029/2006GL026033.

Mkhinini, N., A., L. S. Coimbra, A. Stegner, T. Arsouze, I. Taupier-Letage, and K. Béranger (2014), Long-lived mesoscale eddies in the easternMediterranean Sea: Analysis of 20 years of AVISO geostrophic velocities, *J. Geophys. Res. Ocean.*, *119*, 8603–8626, doi:10.1002/2014JC010176.

Montaggioni, L., S. Etienne, and C. Seard (2016), Récifs coralliens et paysages géomorphologiques littoraux des îles Marquises géomorphologiques littoraux des îles, in *Biodiversité terrestre et marine des îles Marquises, Polynésie Française*, edited by R. Galzin, S.-D. Duron, and J.-Y. Meyer, pp. 79–104, Société française d'Ichtyologie, Paris.

Morel, A., and J.-F. Berthon (1989), Surface pigments, algal biomass profiles, and potential production of the euphotic layer: Relationships reinvestigated in view of remote-sensing applications, *Limnol. Oceanogr.*, *34*(8), 1545–1562, doi:10.4319/lo.1989.34.8.1545.

Neill, S. P., and A. J. Elliott (2004), Observations and simulations of an unsteady island wake in the Firth of Forth, Scotland, *Ocean Dyn.*, *54*(3–4), 324–332, doi:10.1007/s10236-003-0084-1.

Nencioli, F., C. Dong, T. Dickey, L. Washburn, and J. C. Mcwilliams (2010), A vector geometry-based eddy detection algorithm and its application to a high-resolution numerical model product and high-frequency radar surface velocities in the Southern

California Bight, *J. Atmos. Ocean. Technol.*, *27*(3), 564–579, doi:10.1175/2009JTECHO725.1.

O'Connor, B. M., R. A. Fine, and D. B. Olson (2005), A global comparison of subtropical underwater formation rates, *Deep. Res. Part I Oceanogr. Res. Pap.*, *52*(9), 1569–1590, doi:10.1016/j.dsr.2005.01.011.

Olmedo, E., J. Martinez, M. Umbert, N. Hoareau, M. Portabella, J. Ballabrera-Poy, and A. Turiel (2016), Improving time and space resolution of SMOS salinity maps using multifractal fusion, *Remote Sens. Environ.*, *180*, 246–263, doi:10.1016/j.rse.2016.02.038.

Palacios, D. M. (2002), Factors influencing the island-mass effect of the Galápagos Archipelago, *Geophys. Res. Lett.*, *29*(23), 1–4, doi:10.1029/2002GL016232.

Pattiaratchi, C., A. James, and M. Collins (1987), Island wakes and headland eddies: A comparison between remotely sensed data and laboratory experiments, *J. Geophys. Res. Ocean.*, *92*(C1), 783–794, doi:10.1029/JC092iC01p00783.

Penven, P., P. Marchesiello, L. Debreu, and J. Lefèvre (2007), Software tools for pre- and post-processing of oceanic regional simulations, *Environ. Model. Softw.*, *23*(5), 660–662, doi:10.1016/j.envsoft.2007.07.004.

Philander, S. G. H. (1978), Instabilities of zonal equatorial currents, 2, *J. Geophys. Res.*, *83*(C7), 3679, doi:10.1029/JC083iC07p03679.

Planquette, H. et al. (2007), Dissolved iron in the vicinity of the Crozet Islands, Southern Ocean, *Deep. Res. Part II Top. Stud. Oceanogr.*, *54*(18–20), 1999–2019, doi:10.1016/j.dsr2.2007.06.019.

Power, S., T. Casey, C. Folland, A. Colman, and V. Mehta (1999), Inter-decadal modulation of the impact of ENSO on Australia, *Clim. Dyn.*, *15*(5), 319–324, doi:10.1007/s003820050284.

Qiu, B., and S. Chen (2004), Seasonal Modulations in the Eddy Field of the South Pacific Ocean, *J. Phys. Oceanogr.*, *34*(7), 1515–1527, doi:10.1175/1520-0485(2004)034<1515:SMITEF>2.0.CO;2.

Qu, T., S. Gao, and R. A. Fine (2013), Subduction of South Pacific Tropical Water and Its Equatorward Pathways as Shown by a Simulated Passive Tracer*, *J. Phys. Oceanogr.*, *43*(8), 1551–1565, doi:10.1175/JPO-D-12-0180.1.

Raapoto, H., E. Martinez, A. Petrenko, A. M. Doglioli, and C. Maes (2018), Modeling the Wake of the Marquesas Archipelago, *J. Geophys. Res. Ocean.*, doi:10.1002/2017JC013285.

Radenac, M.-H., C. Menkes, J. Vialard, C. Moulin, Y. Dandonneau, T. Delcroix, C. Dupouy, A. Stoens, and P.-Y. Deschamps (2001), Modeled and observed impacts of the 1997-1998

El Niño on nitrate and new production in the equatorial Pacific, *J. Geophys. Res. Ocean.*, *106*(C11), 26879–26898, doi:10.1029/2000JC000546.

Radenac, M. H., F. Léger, A. Singh, and T. Delcroix (2012), Sea surface chlorophyll signature in the tropical Pacific during eastern and central Pacific ENSO events, *J. Geophys. Res. Ocean.*, *117*(4), 1–15, doi:10.1029/2011JC007841.

Raimbault, P., and N. Garcia (2008), Evidence for efficient regenerated production and dinitrogen fixation in nitrogen-deficient waters of the South Pacific Ocean: impact on new and export production estimates, *Biogeosciences*, *5*(2), 323–338, doi:10.5194/bg-5-323-2008.

Raimbault, P., N. Garcia, and F. Cerutti (2007), Distribution of inorganic and organic nutrients in the South Pacific Ocean - evidence for long-term accumulation of organic matter in nitrogen-depleted waters, *Biogeosciences Discuss.*, *4*(1), 3041–3087, doi:10.5194/bg-5-281-2008.

Ras, J., H. Claustre, and J. Uitz (2008), Spatial variability of phytoplankton pigment distributions in the Subtropical South Pacific Ocean: Comparison between in situ and predicted data, *Biogeosciences*, *5*(2), 353–369, doi:10.5194/bg-5-353-2008.

Ridgway, K. R., J. R. Dunn, and J. L. Wilkin (2002), Ocean interpolation by four-dimensional weighted least squares - Application to the waters around Australasia, *J. Atmos. Ocean. Technol.*, *19*(9), 1357–1375, doi:10.1175/1520-0426(2002)019<1357:OIBFDW>2.0.CO;2.

Robinson, J., E. E. Popova, M. A. Srokosz, and A. Yool (2016), A tale of three islands: Downstream natural iron fertilization in the Southern Ocean, *J. Geophys. Res. Ocean.*, *121*(5), 3350–3371, doi:10.1002/2015JC011319.

Rodier, M., and E. Martinez (2012), Rapport de Campagne « Pakaihi i te moana », Partie « biodiversité hauturière » du 2 au 22 février 2012,

Salinger, M. J., J. A. Renwick, and A. B. Mullan (2001), Interdecadal Pacific Oscillation and South Pacific climate, *Int. J. Climatol.*, *21*(14), 1705–1721, doi:10.1002/joc.691.

Sangrà, P., G. Basterretxea, J. L. Pelegrí, and J. Arístegui (2001), Chlorophyll increase due to internal waves on the shelf break of Gran Canaria (Canary Islands)*, *Signals*, *65*, 89–97, doi:http://digital.csic.es/bitstream/10261/5326/1/wave.pdf.

Sangrà, P., J. L. Pelegrí, A. Hernández-Guerra, I. Arregui, J. M. Martín, A. Marrero-Díaz, A. Martínez, A. W. Ratsimandresy, and A. Rodríguez-Santana (2005), Life history of an anticyclonic eddy, *J. Geophys. Res. C Ocean.*, *110*(3), 1–19, doi:10.1029/2004JC002526.

Shchepetkin, A. F., and J. C. McWilliams (2003), A method for computing horizontal pressure-

gradient force in an oceanic model with nonaligned vertical coordinate, *J. Geophys. Res.*, *108*(C3), 1–34, doi:10.1029/2001JC001047.

Shchepetkin, A. F., and J. C. McWilliams (2005), The regional oceanic modeling system (ROMS): a split-explicit, free-surface, topography-following-coordinate oceanic model, *Ocean~Model.*, *9*, 347–404, doi:10.1016/j.ocemod.2004.08.002.

Shi, W., and M. Wang (2014), Satellite-observed biological variability in the equatorial Pacific during the 2009-2011 ENSO cycle, *Adv. Sp. Res.*, *54*(9), 1913–1923, doi:10.1016/j.asr.2014.07.003.

Signorini, S. R., C. R. McClain, and Y. Dandonneau (1999), Mixing and phytoplankton bloom in the wake of the Marquesas Islands, *Geophys. Res. Lett.*, *26*(20), 3121–3124, doi:10.1029/1999GL010470.

da Silva, A. M., C. C. Young, and S. Levitus (1994), Atlas of surface marine data 1994, vol. 4, Anomalies of fresh water fluxes, *Noaa atlas nesdis*, *9*, 308.

Smith, W. H., and D. Sandwell (1997), Global Sea Floor Topography from Satellite Altimetry and Ship Depth Soundings, *Science (80-.).*, *277*(5334), 1956–1962, doi:10.1126/science.277.5334.1956.

Stegner, A. (2014), Oceanic Island Wake Flows in the Laboratory, in *Modeling Atmospheric and Oceanic Flows: Insights from Laboratory Experiments and Numerical Simulations*, edited by T. von Larcher and P. D. Williams, pp. 265–276, John Wiley & Sons,Inc., Hoboken, New Jersey.

Strutton, P. G., J. P. Ryan, and F. P. Chavez (2001), Enhanced chlorophyll associated with tropical instability waves in the equatorial Pacific, *Geophys. Res. Lett.*, *28*(10), 2005–2008, doi:10.1029/2000GL012166.

Strutton, P. G., A. P. Palacz, R. C. Dugdale, F. Chai, A. Marchi, A. E. Parker, V. Hogue, and F. P. Wilkerson (2011), The impact of equatorial Pacific tropical instability waves on hydrography and nutrients: 2004-2005, *Deep. Res. Part II Top. Stud. Oceanogr.*, *58*(3–4), 284–295, doi:10.1016/j.dsr2.2010.08.015.

Sudre, J., C. Maes, and V. Garçon (2013), On the global estimates of geostrophic and Ekman surface currents, *Limnol. Oceanogr. Fluids Environ.*, *3*(1), 1–20, doi:10.1215/21573689-2071927.

Sun, Z., Z. Zhang, W. Zhao, and J. Tian (2016), Interannual modulation of eddy kinetic energy in the northeastern South China Sea as revealed by an eddy-resolving OGCM, *J. Geophys. Res. Ocean.*, *121*, 1–12, doi:10.1002/2015JC011497.

Tagliabue, A. et al. (2010), Hydrothermal contribution to the oceanic dissolved iron inventory,

Nat. Geosci., *3*(4), 252–256, doi:10.1038/ngeo818.

Talley, L. D. (2002), Salinity Patterns in the Ocean, *Earth Syst. Phys. Chem. Dimens. Glob. Environ. Chang.*, *1*, 629–640.

Teinturier, S., A. Stegner, H. Didelle, and S. Viboud (2010), Small-scale instabilities of an island wake flow in a rotating shallow-water layer, *Dyn. Atmos. Ocean.*, *49*(1), 1–24, doi:10.1016/j.dynatmoce.2008.10.006.

Tian, R. . et al. (2000), Effects of pelagic food-web interactions and nutrient remineralization on the biogeochemical cycling of carbon: a modeling approach, *Deep Sea Res. Part II Top. Stud. Oceanogr.*, *47*(3–4), 637–662, doi:10.1016/S0967-0645(99)00121-6.

Tomczak, M. (1988), Island wakes in deep and shallow water, *J. Geophys. Res.*, *93*(8), 5153–5154.

Williams, R. G., and M. J. Follows (1998), The Ekman transfer of nutrients and maintenance of new production over the North Atlantic, *Deep. Res. Part I Oceanogr. Res. Pap.*, *45*(2–3), 461–489, doi:10.1016/S0967-0637(97)00094-0.

Williams, R. G., and M. J. Follows (2003), Physical Transport of Nutrients and the Maintenance of Biological Production, in *Ocean Biogeochemistry*, pp. 19–51, Springer Berlin Heidelberg, Berlin, Heidelberg.

Wilson, C., and D. Adamec (2001), Correlations between surface chlorophyll and sea surface height in the tropical Pacific during the 1997–1999 El Niño-Southern Oscillation event, *J. Geophys. Res.*, *106*(C12), 31175, doi:10.1029/2000JC000724.

Wolanksi, E., T. Asaeda, A. Tanaka, and E. Deleersnijder (1996), Three-dimensional island wakes in the field, laboratory experiments and numerical models, *Cont. Shelf Res.*, *16*(11), 1437–1452, doi:10.1016/0278-4343(95)00087-9.

Wolanski, E., J. Imberger, and M. L. Heron (1984), Island wakes in shallow waters, *J. Geophys. Res.*, *89*(C6), 553–569, doi:10.1029/JC093iC02p01335.

Wyrtki, K. (1981), An Estimate of Equatorial Upwelling in the Pacific, *J. Phys. Oceanogr.*, *11*, 1205–1214.

Xu, Y., and R. B. Scott (2008), Subtleties in forcing eddy resolving ocean models with satellite wind data, *Ocean Model.*, *20*(3), 240–251, doi:10.1016/j.ocemod.2007.09.003.

Yan, X., C. Ho, Q. Zheng, and V. Klemas (1992), Temperature and Size Variabilities of the Western Pacific Warm Pool, *Science (80-.).*, *258*(5088), 1643–1645.

Yoder, J. A., and M. A. Kennelly (2003), Seasonal and ENSO variability in global ocean phytoplankton chlorophyll derived from 4 years of SeaWiFS measurements, *Global Biogeochem. Cycles*, *17*(4), n/a-n/a, doi:10.1029/2002GB001942.

Yu, J.-Y., and W. T. Liu (2003), A linear relationship between ENSO intensity and tropical instability wave activity in the eastern Pacific Ocean, *Geophys. Res. Lett.*, *30*(14), doi:10.1029/2003GL017176.

Zweng, M. M., J. R. Reagan, J. I. Antonov, A. V. Mishonov, T. P. Boyer, H. E. Garcia, O. K. Baranova, D. R. Johnson, D. Seidov, and M. M. Bidlle (2013), *World Ocean Atlas 2013, Volume 2: Salinity*.

Alaee, M. J., G. Ivey, and C. Pattiaratchi (2004), Secondary circulation induced by flow curvature and Coriolis effects around headlands and islands, *Ocean Dyn.*, *54*(1), 27–38, doi:10.1007/s10236-003-0058-3.

Amores, A., S. Monserrat, and M. Marcos (2013), Vertical structure and temporal evolution of an anticyclonic eddy in the Balearic Sea (western Mediterranean), *J. Geophys. Res. Ocean.*, *118*(4), 2097–2106, doi:10.1002/jgrc.20150.

Andrade, I., P. Sangrà, S. Hormazabal, and M. Correa-Ramirez (2014), Island mass effect in the Juan Fernández Archipelago (33°S), Southeastern Pacific, *Deep. Res. Part I Oceanogr. Res. Pap.*, *84*, 86–99, doi:10.1016/j.dsr.2013.10.009.

Antonov, J., D. Seidov, T. Boyer, and R. Locarnini (2010), World Ocean Atlas 2009, vol. 2: Salinity, edited by: Levitus, *S., NOAA Atlas NESDIS*.

Auad, G., A. Pares-Sierra, and G. K. Vallis (1991), Circulation and energetics of a model of the California Current system.pdf, *J. Phys. Oceanogr.*, *21*(10), 1534–1552.

Aumont, O., and L. Bopp (2006), Globalizing results from ocean in situ iron fertilization studies, *Global Biogeochem. Cycles*, *20*(2), n/a-n/a, doi:10.1029/2005GB002591.

Aumont, O., C. Ethé, a. Tagliabue, L. Bopp, and M. Gehlen (2015), PISCES-v2: an ocean biogeochemical model for carbon and ecosystem studies, *Geosci. Model Dev. Discuss.*, *8*(2), 1375–1509, doi:10.5194/gmdd-8-1375-2015.

Barber R. T, M. P. Sanderson, S. T. Lindley, F. Chai, J. Newton, C. C. Trees, D. G. Foley, and F. P. Chavez (1996), Primary productivity and its regulation in the equatorial Pacific during and following the 1991-92 El Ni{ñ}o, *Deep. Res. Part II*, *43*(4–6), 933–969, doi:10.1016/0967-0645(96)00035-5.

Barton, E. D. (2001), Island wakes, *Encycl. Ocean Sci.*, *3*, 1397–1403, doi:10.1006/rwos.2001.0140.

Beckmann, A., and D. B. Haidvogel (1993), Numerical Simulation of Flow around a Tall Isolated Seamount. Part I: Problem Formulation and Model Accuracy, *J. Phys. Oceanogr.*, *23*(8), 1736–1753, doi:10.1175/1520-0485(1993)023<1736:NSOFAA>2.0.CO;2.

Bell, J. D., M. Kronen, A. Vunisea, W. J. Nash, G. Keeble, A. Demmke, S. Pontifex, and S.

Andréfouët (2009), Planning the use of fish for food security in the Pacific, *Mar. Policy*, *33*(1), 64–76, doi:10.1016/j.marpol.2008.04.002.

Benitez-Nelson, C. R., and D. J. McGillicuddy (2008), Mesoscale physical–biological–biogeochemical linkages in the open ocean: An introduction to the results of the E-Flux and EDDIES programs, *Deep Sea Res. Part II Top. Stud. Oceanogr.*, *55*(10–13), 1133–1138, doi:10.1016/j.dsr2.2008.03.001.

Blain, S. et al. (2007), Effect of natural iron fertilization on carbon sequestration in the Southern Ocean, *Nature*, *446*(7139), 1070–1074, doi:10.1038/nature05700.

Blain, S., S. Bonnet, and C. Guieu (2008), Dissolved iron distribution in the tropical and sub tropical South Eastern Pacific, *Biogeosciences*, *5*(1), 269–280, doi:10.5194/bgd-4-2845-2007.

Bonjean, F., and G. S. E. Lagerloef (2002), Diagnostic model and analysis of the surface currents in the tropical Pacific Ocean, *J. Phys. Oceanogr.*, *32*(10), 2938–2954, doi:10.1175/1520-0485(2002)032<2938:DMAAOT>2.0.CO;2.

Boyd, P. W., and M. J. Ellwood (2010), The biogeochemical cycle of iron in the ocean, *Nat. Geosci.*, *3*(10), 675–682, doi:10.1038/ngeo964.

Cai, W. et al. (2015), Increased frequency of extreme La Nina events under greenhouse warming, *Nat. Clim. Chang.*, *5*(2), 132–137, doi:10.1038/nclimate2492.

Caldeira, R. M. A., and P. Marchesiello (2002), Ocean response to wind sheltering in the Southern California Bight, *Geophys. Res. Lett.*, *29*(13), 1–4, doi:10.1029/2001GL014563.

Caldeira, R. M. A., S. Groom, P. Miller, D. Pilgrim, and N. P. Nezlin (2002), Sea-surface signatures of the island mass effect phenomena around Madeira Island, Northeast Atlantic, *Remote Sens. Environ.*, *80*(2), 336–360, doi:10.1016/S0034-4257(01)00316-9.

Calil, P. H. R., K. J. Richards, Y. Jia, and R. R. Bidigare (2008), Eddy activity in the lee of the Hawaiian Islands, *Deep. Res. Part II Top. Stud. Oceanogr.*, *55*(10–13), 1179–1194, doi:10.1016/j.dsr2.2008.01.008.

Chang, M. H., T. Y. Tang, C. R. Ho, and S. Y. Chao (2013), Kuroshio-induced wake in the lee of Green Island off Taiwan, *J. Geophys. Res. Ocean.*, *118*(3), 1508–1519, doi:10.1002/jgrc.20151.

Chavanne, C., P. Flament, R. Lumpkin, B. Dousset, and A. Bentamy (2002), Scatterometer observations of wind variations induced by oceanic islands: implications for wind-driven ocean circulation., *Can. J. Remote Sens.*, *28*(3), 466–474, doi:10.5589/m02-047.

Chelton, D. B., R. a. deSzoeke, M. G. Schlax, K. El Naggar, and N. Siwertz (1998), Geographical Variability of the First Baroclinic Rossby Radius of Deformation, *J. Phys.*

Oceanogr., *28*(3), 433–460, doi:10.1175/1520-0485(1998)028<0433:GVOTFB>2.0.CO;2.

Chen, R., A. F. Thompson, and G. R. Flierl (2016), Time-dependent eddy-mean energy diagrams and their application to the ocean, *J. Phys. Oceanogr.*, *46*(9), 2827–2850, doi:10.1175/JPO-D-16-0012.1.

Claustre, H., A. Sciandra, and D. Vaulot (2008), Introduction to the special section bio-optical and biogeochemical conditions in the South East Pacific in late 2004: the BIOSOPE program, *Biogeosciences*, *5*, 679–691, doi:10.5194/bgd-5-605-2008.

Cummings, J. A., and O. M. Smedstad (2013), Variational Data Assimilation for the Global Ocean, in *Data Assimilation for Atmospheric, Oceanic and Hydrologic Applications (Vol. II)*, vol. II, edited by Springer, pp. 303–343, Berlin, Heidelberg.

da Cunha, L. C., and E. T. Buitenhuis (2013), Riverine influence on the tropical Atlantic Ocean biogeochemistry, *Biogeosciences*, *10*(10), 6357–6373, doi:10.5194/bg-10-6357-2013.

d'Ovidio, F., V. Fernández, E. Hernández-García, and C. López (2004), Mixing structures in the Mediterranean Sea from finite-size Lyapunov exponents, *Geophys. Res. Lett.*, *31*(17), doi:10.1029/2004GL020328.

d'Ovidio, F., S. De Monte, S. Alvain, Y. Dandonneau, and M. Levy (2010), Fluid dynamical niches of phytoplankton types, *Proc. Natl. Acad. Sci.*, *107*(43), 18366–18370, doi:10.1073/pnas.1004620107.

D'Ovidio, F., A. Della Penna, T. W. Trull, F. Nencioli, M. I. Pujol, M. H. Rio, Y. H. Park, C. Cotté, M. Zhou, and S. Blain (2015), The biogeochemical structuring role of horizontal stirring: Lagrangian perspectives on iron delivery downstream of the Kerguelen Plateau, *Biogeosciences*, *12*(19), 5567–5581, doi:10.5194/bg-12-5567-2015.

Dale, A. W., L. Nickelsen, F. Scholz, C. Hensen, A. Oschlies, and K. Wallmann (2015), A revised global estimate of dissolved iron fluxes from marine sediments, *Global Biogeochem. Cycles*, *29*(5), 691–707, doi:10.1002/2014GB005017.

Debreu, L., and E. Blayo (2008), Two-way embedding algorithms: A review, *Ocean Dyn.*, *58*(5–6), 415–428, doi:10.1007/s10236-008-0150-9.

Debreu, L., P. Marchesiello, P. Penven, and G. Cambon (2012), Two-way nesting in split-explicit ocean models: Algorithms, implementation and validation, *Ocean Model.*, *49–50*, 1–21, doi:10.1016/j.ocemod.2012.03.003.

Dietrich, D. E., M. J. Bowmanb, C. A. Lin, and A. Mestas-nunezd (1996), Numerical studies of small island wakes in the ocean, *Geophys. Astrophys. Fluid Dyn.*, *83*(3–4), 195–231, doi:10.1080/03091929608208966.

DiGiacomo, P. M., and B. Holt (2001), Satellite observations of small coastal ocean eddies in the Southern California Bight, *J. Geophys. Res.*, *106*(10), 22,521-522,543, doi:10.1029/2000JC000728.

Doglioli, A. M., B. Blanke, S. Speich, and G. Lapeyre (2007), Tracking coherent structures in a regional ocean model with wavelet analysis: Application to Cape Basin eddies, *J. Geophys. Res. Ocean.*, *112*(5), 1–12, doi:10.1029/2006JC003952.

Dong, C., and J. C. McWilliams (2007), A numerical study of island wakes in the Southern California Bight, *Cont. Shelf Res.*, *27*(9), 1233–1248, doi:10.1016/j.csr.2007.01.016.

Dong, C., J. C. McWilliams, and A. F. Shchepetkin (2007), Island Wakes in Deep Water, *J. Phys. Oceanogr.*, *37*(4), 962–981, doi:10.1175/JPO3047.1.

Dong, C., X. Lin, Y. Liu, F. Nencioli, Y. Chao, Y. Guan, D. Chen, T. Dickey, and J. C. McWilliams (2012), Three-dimensional oceanic eddy analysis in the Southern California Bight from a numerical product, *J. Geophys. Res. Ocean.*, *117*(1), 1–17, doi:10.1029/2011JC007354.

Doty, M. S., and M. Oguri (1956), The Island Mass Effect, *ICES J. Mar. Sci.*, doi:10.1093/icesjms/22.1.33.

Elrod, V. A., W. M. Berelson, K. H. Coale, and K. S. Johnson (2004), The flux of iron from continental shelf sediments: A missing source for global budgets, *Geophys. Res. Lett.*, *31*(12), 2–5, doi:10.1029/2004GL020216.

Emery, W. J. (2001), Water Types and Water Masses, *Encycl. Ocean Sci. Second Ed.*, *6*, 3179–3187, doi:10.1006/rwos.2001.0108.

Emery, W. J. (2003), Water Types and Water Masses Descriptive Tools : The TS Curve, in *Ocean Circulation*, pp. 1556–1567.

Evans, W., P. G. Strutton, and F. P. Chavez (2009), Impact of tropical instability waves on nutrient and chlorophyll distributions in the equatorial Pacific, *Deep. Res. Part I Oceanogr. Res. Pap.*, *56*(2), 178–188, doi:10.1016/j.dsr.2008.08.008.

Fanton d'Andon, O., A. Mangin, S. Lavender, D. Antoine, S. Maritorena, A. Morel, G. Barrot, J. Demaria, and S. Pinnock (2009), GlobColour-the European Service for Ocean Colour, in *Proceedings from 2009 IEEE International Geoscience & Remote Sensing Symposium (IGARSS)*.

Foley, D. G., T. D. Dickey, M. J. McPhaden, R. R. Bidigare, M. R. Lewis, R. T. Barber, S. T. Lindley, C. Garside, D. V. Manov, and J. D. McNeil (1997), Longwaves and primary productivity variations in the equatorial Pacific at 0°, 140°W, *Deep. Res. Part II Top. Stud. Oceanogr.*, *44*(9–10), 1801–1826, doi:10.1016/S0967-0645(97)00080-5.

Folland, C. K., J. A. Renwick, M. J. Salinger, and A. B. Mullan (2002), Relative influences of the Interdecadal Pacific Oscillation and ENSO on the South Pacific Convergence Zone, *Geophys. Res. Lett.*, *29*(13), 2–5, doi:10.1029/2001GL014201.

Gaillard, F., T. Reynaud, V. Thierry, N. Kolodziejczyk, and K. Von Schuckmann (2016), In situ-based reanalysis of the global ocean temperature and salinity with ISAS: Variability of the heat content and steric height, *J. Clim.*, *29*(4), 1305–1323, doi:10.1175/JCLI-D-15-0028.1.

Geider, R. J., H. L. MacIntyre, and T. M. Kana (1997), Dynamic model of phytoplankton growth and acclimation: Responses of the balanced growth rate and the chlorophyll a:carbon ratio to light, nutrient-limitation and temperature, *Mar. Ecol. Prog. Ser.*, *148*(1–3), 187–200, doi:10.3354/meps148187.

Gordon, H. R., and W. R. McCluney (1975), Estimation of the Depth of Sunlight Penetration in the Sea for Remote Sensing, *Appl. Opt.*, *14*(2), 413, doi:10.1364/AO.14.000413.

Gorgues, T., C. Menkes, O. Aumont, J. Vialard, Y. Dandonneau, and L. Bopp (2005), Biogeochemical impact of tropical instability waves in the equatorial Pacific, *Geophys. Res. Lett.*, *32*(24), L24615, doi:10.1029/2005GL024110.

Goyet, C., R. Healy, J. Ryan, and A. Kozyr (2000), Global distribution of total inorganic carbon and total alkalinity below the deepest winter mixed layer depths,

Guieu, C., S. Bonnet, A. Petrenko, C. Menkes, V. Chavagnac, K. Desboeufs, C. Maes, and T. Moutin (2018), Iron from a submarine source impacts the productive layer of the Western Tropical South Pacific (WTSP), *Sci. Rep.*, *8*(1), 9075, doi:10.1038/s41598-018-27407-z.

Halo, I., P. Penven, B. Backeberg, I. Ansorge, F. Shillington, and R. Roman (2014), Mesoscale eddy variability in the southern extension of the East Madagascar Current: Seasonal cycle, energy conversion terms, and eddymean properties, *J. Geophys. Res. Ocean.*, *00000*, 7324–7356, doi:10.1002/2014JC009820.

Harrison, D. E., and A. R. Robinson (1978), Energy analysis of open regions of turbulent flows - mean eddy energetics of a numerical ocean circulation experiment, *Dyn. Atmos. Ocean.*, *2*(2), 185–211, doi:10.1016/0377-0265(78)90009-X.

Hasegawa, D., H. Yamazaki, R. G. Lueck, and L. Seuront (2004), How islands stir and fertilize the upper ocean, *Geophys. Res. Lett.*, *31*(16), 1–4, doi:10.1029/2004GL020143.

Hasegawa, D., H. Yamazaki, T. Ishimaru, H. Nagashima, and Y. Koike (2008), Apparent phytoplankton bloom due to island mass effect, *J. Mar. Syst.*, *69*(3–4), 238–246, doi:10.1016/j.jmarsys.2006.04.019.

Hasegawa, D., M. R. Lewis, and a. Gangopadhyay (2009), How islands cause phytoplankton

to bloom in their wakes, *Geophys. Res. Lett.*, *36*(20), 1–4, doi:10.1029/2009GL039743.

Hastings, D. A., and W. J. Emery (1992), The advanced very high resolution radiometer (AVHRR): a brief reference guide., *Photogramm. Eng. Remote Sensing.*, *58*(8), 1183–1188.

Henley, B. J., J. Gergis, D. J. Karoly, S. Power, J. Kennedy, and C. K. Folland (2015), A Tripole Index for the Interdecadal Pacific Oscillation, *Clim. Dyn.*, *45*(11–12), 3077–3090, doi:10.1007/s00382-015-2525-1.

Hernández-León, S., M. Gómez, M. Pagazaurtundua, A. Portillo-Hahnefeld, I. Montero, and C. Almeida (2001), Vertical distribution of zooplankton in Canary Island waters: implications for export flux, *Deep Sea Res. Part I Oceanogr. Res. Pap.*, *48*(4), 1071–1092, doi:10.1016/S0967-0637(00)00074-1.

Heywood, K. J., E. D. Barton, and J. H. Simpson (1990), The effects of flow disturbance by an oceanic island, *J. Mar. Res.*, *48*, 55–73, doi:10.1357/002224090784984623.

Heywood, K. J., D. P. Stevens, and G. R. Bigg (1996), Eddy formation behind the tropical island of Aldabra, *Deep. Res. Part I Oceanogr. Res. Pap.*, *43*(4), 555–578, doi:10.1016/0967-0637(96)00097-0.

Hristova, H. G., W. S. Kessler, J. C. McWilliams, and M. J. Molemaker (2014), Mesoscale variability and its seasonality in the Solomon and Coral Seas, *J. Geophys. Res. Ocean.*, *119*, 4669–4687, doi:10.1002/2013JC009741.

Jeandel, C., and E. H. Oelkers (2015), The influence of terrigenous particulate material dissolution on ocean chemistry and global element cycles, *Chem. Geol.*, *395*, 50–66, doi:10.1016/j.chemgeo.2014.12.001.

Jickells, T. D. et al. (2005), Global iron connections between desert dust, ocean biogeochemistry, and climate., *Science*, *308*(5718), 67–71, doi:10.1126/science.1105959.

Jiménez, B., P. Sangrà, and E. Mason (2008), A numerical study of the relative importance of wind and topographic forcing on oceanic eddy shedding by tall, deep water islands, *Ocean Model.*, *22*(3–4), 146–157, doi:10.1016/j.ocemod.2008.02.004.

Johnson, K., and H. Claustre (2016), Bringing Biogeochemistry into the Argo Age, *Eos (Washington. DC).*, doi:10.1029/2016EO062427.

Johnson, K. S., F. P. Chavez, and G. E. Friederich (1999), Continental-shelf sediment as a primary source of iron for coastal phytoplankton, *Nature*, *398*(6729), 697–700, doi:10.1038/19511.

Kang, D., and E. N. Curchitser (2015), Energetics of Eddy-Mean Flow Interactions in the Gulf Stream Region, *J. Phys. Oceanogr.*, *45*, 1103–1120, doi:10.1175/JPO-D-14-0200.1.

Von Karman, T., and W. R. Sears (1938), Airfoil Theory for Non-Uniform Motion, *J. Aeronaut. Sci.*, *5*(10), 379–390, doi:10.2514/8.674.

Karnauskas, K. B., G. C. Johnson, and R. Murtugudde (2017), On the climate impacts of atolls in the central equatorial Pacific, *Int. J. Climatol.*, *37*(1), 197–203, doi:10.1002/joc.4697.

Kersalé, M., a. M. Doglioli, and a. a. Petrenko (2011), Sensitivity study of the generation of mesoscale eddies in a numerical model of Hawaii islands, *Ocean Sci.*, *7*(3), 277–291, doi:10.5194/os-7-277-2011.

Large, W. G., J. C. McWilliams, and S. C. Doney (1994), Oceanic vertical mixing: A review and a model with a nonlocal boundary layer parameterization, *Rev. Geophys.*, *32*(4), 363, doi:10.1029/94RG01872.

Laurent, V., K. Maamaatuaiahutapu, J. Maiau, and P. Varney (2004), *Atlas Climatologique de la Polynésie Française*, Météo Fran.

Legeckis, R. (1977), Long waves in the eastern equatorial Pacific Ocean: A view from a geostationary satellite, *Science (80-.).*, *197*(4309), 1179–1181, doi:10.1126/science.197.4309.1179.

Legeckis, R., C. W. Brown, F. Bonjean, and E. S. Johnson (2004), The influence of tropical instability waves on phytoplankton blooms in the wake of the Marquesas Islands during 1998 and on the currents observed during the drift of the Kon-Tiki in 1947, *Geophys. Res. Lett.*, *31*(23), 1–4, doi:10.1029/2004GL021637.

Lehodey, P., I. Senina, and R. Murtugudde (2008), A spatial ecosystem and populations dynamics model (SEAPODYM) – Modeling of tuna and tuna-like populations, *Prog. Oceanogr.*, *78*(4), 304–318, doi:10.1016/j.pocean.2008.06.004.

Lehodey, P. et al. (2011), Vulnerability of oceanic fisheries in the tropical Pacific to climate change, *Vulnerability Trop. Pacific Fish. Aquac. to Clim. Chang.*, 433–492.

Lévy, M., R. Ferrari, P. J. S. Franks, A. P. Martin, and P. Rivière (2012), Bringing physics to life at the submesoscale, *Geophys. Res. Lett.*, *39*(14), doi:10.1029/2012GL052756.

Liang, J. H., J. C. McWilliams, J. Kurian, F. Colas, P. Wang, and Y. Uchiyama (2012), Mesoscale variability in the northeastern tropical Pacific: Forcing mechanisms and eddy properties, *J. Geophys. Res. Ocean.*, *117*(7), 1–13, doi:10.1029/2012JC008008.

Liu, Y., C. Dong, Y. Guan, D. Chen, J. McWilliams, and F. Nencioli (2012), Eddy analysis in the subtropical zonal band of the North Pacific Ocean, *Deep. Res. Part I Oceanogr. Res. Pap.*, *68*, 54–67, doi:10.1016/j.dsr.2012.06.001.

Lo-Yat, A., S. D. Simpson, M. Meekan, D. Lecchini, E. Martinez, and R. Galzin (2011), Extreme climatic events reduce ocean productivity and larval supply in a tropical reef

ecosystem, *Glob. Chang. Biol.*, *17*(4), 1695–1702, doi:10.1111/j.1365-2486.2010.02355.x.

Locarnini, R., A. Mishonov, J. Antonov, T. Boyer, and H. Garcia (2010), World Ocean Atlas 2009, vol. 1, Temperature, edited by S. Levitus, 184 pp, *US Gov. Print. Off.*

Locarnini, R. A. et al. (2013), World Ocean Atlas 2013. Vol. 1: Temperature., *S. Levitus, Ed.; A. Mishonov, Tech. Ed.; NOAA Atlas NESDIS*, *73*(September), 40, doi:10.1182/blood-2011-06-357442.

Lungu, T., and P. S. Callahan (2006), QuikSCAT science data product user's manual: Overview and geophysical data products, *D-18053-Rev A, version*, *3*, 91.

Maraldi, C., M. Mongin, R. Coleman, and L. Testut (2009), The influence of lateral mixing on a phytoplankton bloom: Distribution in the Kerguelen Plateau region, *Deep. Res. Part I Oceanogr. Res. Pap.*, *56*(6), 963–973, doi:10.1016/j.dsr.2008.12.018.

Marchesiello, P., J. C. McWilliams, and A. Shchepetkin (2001), Open boundary conditions for long-term integration of regional oceanic models, *Ocean Model.*, *3*(1–2), 1–20, doi:10.1016/S1463-5003(00)00013-5.

Marchesiello, P., J. C. McWilliams, A. Shchepetkin, P. Physics, and L. Angeles (2003), Equilibrium Structure and Dynamics of the California Current System, *J. Phys. Oceanogr.*, *33*(4), 753–783, doi:10.1175/1520-0485(2003)33<753:ESADOT>2.0.CO;2.

Martin, J. H., and S. E. Fitzwater (1988), Iron deficiency limits phytoplankton growth in the north-east Pacific subarctic, *Nature*, *331*(6154), 341–343, doi:10.1038/331341a0.

Martinez, E., and K. Maamaatuaiahutapu (2004), Island mass effect in the Marquesas Islands: Time variation, *Geophys. Res. Lett.*, *31*(18), 1–4, doi:10.1029/2004GL020682.

Martinez, E., A. Ganachaud, J. Lefevre, and K. Maamaatuaiahutapu (2009), Central south pacific thermocline water circulation from a high-resolution ocean model validated against satellite data: seasonal variability and el niño 1997-1998 influence, *J. Geophys. Res. Ocean.*, *114*(5), 1–16, doi:10.1029/2008JC004824.

Martinez, E., M. Rodier, and K. Maamaatuaiahutapu (2016), Environnement océanique des Marquises, in *Biodiversité terrestre et marine des îles Marquises, Polynésie Française*, edited by R. Galzin, S.-D. Duron, and J.-Y. Meyer, pp. 123–136, Société française d'Ichtyologie, Paris.

Martinez, E., H. Raapoto, C. Maes, and K. Maamaatuaihutapu (2018), Influence of Tropical Instability Waves on Phytoplankton Biomass near the Marquesas Islands, , 1–12, doi:10.3390/rs10040640.

Masotti, I., C. Moulin, S. Alvain, L. Bopp, A. Tagliabue, and D. Antoine (2011), Large-scale

shifts in phytoplankton groups in the Equatorial Pacific during ENSO cycles, *Biogeosciences*, *8*(3), 539–550, doi:10.5194/bg-8-539-2011.

Maury, R. C., G. Guille, G. Hervé, C. Catherine, C. Legendre, P. Rossi, S. Blais, C. Pallares, D. Sébastien, and A. Marabal (2014), Géologie des Marquises : des volcans boucliers intra-océaniques effondrés issus d ' un point chaud atypique Géologie des Marquises : des volcans boucliers intra-océaniques effondrés issus d ' un point chaud atypique, *Géologie la Fr.*, *1*(8), 111–135.

McPhaden, M. J. (1999), Genesis and Evolution of the 1997-98 El Niño, *Science (80-.).*, *283*, 950–954, doi:10.1126/science.283.5404.950.

McPhaden, M. J. (2015), Playing hide and seek with El Niño, *Nat. Clim. Chang.*, *5*(9), 791–795, doi:10.1038/nclimate2775.

McPhaden MJ (1993), TOGA-TAO and the 1991�93 El Nino�Southern Oscillation event, *Oceanography*, *6,No. 2*(2), 36�44, doi:10.2307/43924639.

Menzel, D. W., and J. H. Ryther (1961), Annual variations in primary productivity of the Sargasso Sea off Bermuda, *Deep. Res. I*, *7*(1119), 282–288.

Messié, M., and F. P. Chavez (2012), A global analysis of ENSO synchrony: The oceans' biological response to physical forcing, *J. Geophys. Res. Ocean.*, *117*(C9), n/a-n/a, doi:10.1029/2012JC007938.

Messié, M., M. H. Radenac, J. Lefèvre, and P. Marchesiello (2006), Chlorophyll bloom in the western Pacific at the end of the 1997-1998 El Niño: The role of the Kiribati Islands, *Geophys. Res. Lett.*, *33*(14), 1–5, doi:10.1029/2006GL026033.

Mkhinini, N., A., L. S. Coimbra, A. Stegner, T. Arsouze, I. Taupier-Letage, and K. Béranger (2014), Long-lived mesoscale eddies in the easternMediterranean Sea: Analysis of 20 years of AVISO geostrophic velocities, *J. Geophys. Res. Ocean.*, *119*, 8603–8626, doi:10.1002/2014JC010176.

Montaggioni, L., S. Etienne, and C. Seard (2016), Récifs coralliens et paysages géomorphologiques littoraux des îles Marquises géomorphologiques littoraux des îles, in *Biodiversité terrestre et marine des îles Marquises, Polynésie Française*, edited by R. Galzin, S.-D. Duron, and J.-Y. Meyer, pp. 79–104, Société française d'Ichtyologie, Paris.

Morel, A., and J.-F. Berthon (1989), Surface pigments, algal biomass profiles, and potential production of the euphotic layer: Relationships reinvestigated in view of remote-sensing applications, *Limnol. Oceanogr.*, *34*(8), 1545–1562, doi:10.4319/lo.1989.34.8.1545.

Neill, S. P., and A. J. Elliott (2004), Observations and simulations of an unsteady island wake in the Firth of Forth, Scotland, *Ocean Dyn.*, *54*(3–4), 324–332, doi:10.1007/s10236-003-

0084-1.

Nencioli, F., C. Dong, T. Dickey, L. Washburn, and J. C. Mcwilliams (2010), A vector geometry-based eddy detection algorithm and its application to a high-resolution numerical model product and high-frequency radar surface velocities in the Southern California Bight, *J. Atmos. Ocean. Technol.*, *27*(3), 564–579, doi:10.1175/2009JTECHO725.1.

O'Connor, B. M., R. A. Fine, and D. B. Olson (2005), A global comparison of subtropical underwater formation rates, *Deep. Res. Part I Oceanogr. Res. Pap.*, *52*(9), 1569–1590, doi:10.1016/j.dsr.2005.01.011.

Olmedo, E., J. Martinez, M. Umbert, N. Hoareau, M. Portabella, J. Ballabrera-Poy, and A. Turiel (2016), Improving time and space resolution of SMOS salinity maps using multifractal fusion, *Remote Sens. Environ.*, *180*, 246–263, doi:10.1016/j.rse.2016.02.038.

Palacios, D. M. (2002), Factors influencing the island-mass effect of the Galápagos Archipelago, *Geophys. Res. Lett.*, *29*(23), 1–4, doi:10.1029/2002GL016232.

Pattiaratchi, C., A. James, and M. Collins (1987), Island wakes and headland eddies: A comparison between remotely sensed data and laboratory experiments, *J. Geophys. Res. Ocean.*, *92*(C1), 783–794, doi:10.1029/JC092iC01p00783.

Penven, P., P. Marchesiello, L. Debreu, and J. Lefèvre (2007), Software tools for pre- and post-processing of oceanic regional simulations, *Environ. Model. Softw.*, *23*(5), 660–662, doi:10.1016/j.envsoft.2007.07.004.

Philander, S. G. H. (1978), Instabilities of zonal equatorial currents, 2, *J. Geophys. Res.*, *83*(C7), 3679, doi:10.1029/JC083iC07p03679.

Planquette, H. et al. (2007), Dissolved iron in the vicinity of the Crozet Islands, Southern Ocean, *Deep. Res. Part II Top. Stud. Oceanogr.*, *54*(18–20), 1999–2019, doi:10.1016/j.dsr2.2007.06.019.

Power, S., T. Casey, C. Folland, A. Colman, and V. Mehta (1999), Inter-decadal modulation of the impact of ENSO on Australia, *Clim. Dyn.*, *15*(5), 319–324, doi:10.1007/s003820050284.

Qiu, B., and S. Chen (2004), Seasonal Modulations in the Eddy Field of the South Pacific Ocean, *J. Phys. Oceanogr.*, *34*(7), 1515–1527, doi:10.1175/1520-0485(2004)034<1515:SMITEF>2.0.CO;2.

Qu, T., S. Gao, and R. A. Fine (2013), Subduction of South Pacific Tropical Water and Its Equatorward Pathways as Shown by a Simulated Passive Tracer*, *J. Phys. Oceanogr.*, *43*(8), 1551–1565, doi:10.1175/JPO-D-12-0180.1.

Raapoto, H., E. Martinez, A. Petrenko, A. M. Doglioli, and C. Maes (2018), Modeling the Wake of the Marquesas Archipelago, *J. Geophys. Res. Ocean.*, doi:10.1002/2017JC013285.

Radenac, M.-H., C. Menkes, J. Vialard, C. Moulin, Y. Dandonneau, T. Delcroix, C. Dupouy, A. Stoens, and P.-Y. Deschamps (2001), Modeled and observed impacts of the 1997-1998 El Niño on nitrate and new production in the equatorial Pacific, *J. Geophys. Res. Ocean.*, *106*(C11), 26879–26898, doi:10.1029/2000JC000546.

Radenac, M. H., F. Léger, A. Singh, and T. Delcroix (2012), Sea surface chlorophyll signature in the tropical Pacific during eastern and central Pacific ENSO events, *J. Geophys. Res. Ocean.*, *117*(4), 1–15, doi:10.1029/2011JC007841.

Raimbault, P., and N. Garcia (2008), Evidence for efficient regenerated production and dinitrogen fixation in nitrogen-deficient waters of the South Pacific Ocean: impact on new and export production estimates, *Biogeosciences*, *5*(2), 323–338, doi:10.5194/bg-5-323-2008.

Raimbault, P., N. Garcia, and F. Cerutti (2007), Distribution of inorganic and organic nutrients in the South Pacific Ocean - evidence for long-term accumulation of organic matter in nitrogen-depleted waters, *Biogeosciences Discuss.*, *4*(1), 3041–3087, doi:10.5194/bg-5-281-2008.

Ras, J., H. Claustre, and J. Uitz (2008), Spatial variability of phytoplankton pigment distributions in the Subtropical South Pacific Ocean: Comparison between in situ and predicted data, *Biogeosciences*, *5*(2), 353–369, doi:10.5194/bg-5-353-2008.

Ridgway, K. R., J. R. Dunn, and J. L. Wilkin (2002), Ocean interpolation by four-dimensional weighted least squares - Application to the waters around Australasia, *J. Atmos. Ocean. Technol.*, *19*(9), 1357–1375, doi:10.1175/1520-0426(2002)019<1357:OIBFDW>2.0.CO;2.

Robinson, J., E. E. Popova, M. A. Srokosz, and A. Yool (2016), A tale of three islands: Downstream natural iron fertilization in the Southern Ocean, *J. Geophys. Res. Ocean.*, *121*(5), 3350–3371, doi:10.1002/2015JC011319.

Rodier, M., and E. Martinez (2012), Rapport de Campagne « Pakaihi i te moana », Partie « biodiversité hauturière » du 2 au 22 février 2012,

Salinger, M. J., J. A. Renwick, and A. B. Mullan (2001), Interdecadal Pacific Oscillation and South Pacific climate, *Int. J. Climatol.*, *21*(14), 1705–1721, doi:10.1002/joc.691.

Sangrà, P., G. Basterretxea, J. L. Pelegrí, and J. Arístegui (2001), Chlorophyll increase due to internal waves on the shelf break of Gran Canaria (Canary Islands)*, *Signals*, *65*, 89–97, doi:http://digital.csic.es/bitstream/10261/5326/1/wave.pdf.

Sangrà, P., J. L. Pelegrí, A. Hernández-Guerra, I. Arregui, J. M. Martín, A. Marrero-Díaz, A. Martínez, A. W. Ratsimandresey, and A. Rodríguez-Santana (2005), Life history of an anticyclonic eddy, *J. Geophys. Res. C Ocean.*, *110*(3), 1–19, doi:10.1029/2004JC002526.

Shchepetkin, A. F., and J. C. McWilliams (2003), A method for computing horizontal pressure-gradient force in an oceanic model with nonaligned vertical coordinate, *J. Geophys. Res.*, *108*(C3), 1–34, doi:10.1029/2001JC001047.

Shchepetkin, A. F., and J. C. McWilliams (2005), The regional oceanic modeling system (ROMS): a split-explicit, free-surface, topography-following-coordinate oceanic model, *Ocean~Model.*, *9*, 347–404, doi:10.1016/j.ocemod.2004.08.002.

Shi, W., and M. Wang (2014), Satellite-observed biological variability in the equatorial Pacific during the 2009-2011 ENSO cycle, *Adv. Sp. Res.*, *54*(9), 1913–1923, doi:10.1016/j.asr.2014.07.003.

Signorini, S. R., C. R. McClain, and Y. Dandonneau (1999), Mixing and phytoplankton bloom in the wake of the Marquesas Islands, *Geophys. Res. Lett.*, *26*(20), 3121–3124, doi:10.1029/1999GL010470.

da Silva, A. M., C. C. Young, and S. Levitus (1994), Atlas of surface marine data 1994, vol. 4, Anomalies of fresh water fluxes, *Noaa atlas nesdis*, *9*, 308.

Smith, W. H., and D. Sandwell (1997), Global Sea Floor Topography from Satellite Altimetry and Ship Depth Soundings, *Science (80-.).*, *277*(5334), 1956–1962, doi:10.1126/science.277.5334.1956.

Stegner, A. (2014), Oceanic Island Wake Flows in the Laboratory, in *Modeling Atmospheric and Oceanic Flows: Insights from Laboratory Experiments and Numerical Simulations*, edited by T. von Larcher and P. D. Williams, pp. 265–276, John Wiley & Sons,Inc., Hoboken, New Jersey.

Strutton, P. G., J. P. Ryan, and F. P. Chavez (2001), Enhanced chlorophyll associated with tropical instability waves in the equatorial Pacific, *Geophys. Res. Lett.*, *28*(10), 2005–2008, doi:10.1029/2000GL012166.

Strutton, P. G., A. P. Palacz, R. C. Dugdale, F. Chai, A. Marchi, A. E. Parker, V. Hogue, and F. P. Wilkerson (2011), The impact of equatorial Pacific tropical instability waves on hydrography and nutrients: 2004-2005, *Deep. Res. Part II Top. Stud. Oceanogr.*, *58*(3–4), 284–295, doi:10.1016/j.dsr2.2010.08.015.

Sudre, J., C. Maes, and V. Garçon (2013), On the global estimates of geostrophic and Ekman surface currents, *Limnol. Oceanogr. Fluids Environ.*, *3*(1), 1–20, doi:10.1215/21573689-2071927.

Sun, Z., Z. Zhang, W. Zhao, and J. Tian (2016), Interannual modulation of eddy kinetic energy in the northeastern South China Sea as revealed by an eddy-resolving OGCM, *J. Geophys. Res. Ocean.*, *121*, 1–12, doi:10.1002/2015JC011497.

Tagliabue, A. et al. (2010), Hydrothermal contribution to the oceanic dissolved iron inventory, *Nat. Geosci.*, *3*(4), 252–256, doi:10.1038/ngeo818.

Talley, L. D. (2002), Salinity Patterns in the Ocean, *Earth Syst. Phys. Chem. Dimens. Glob. Environ. Chang.*, *1*, 629–640.

Teinturier, S., A. Stegner, H. Didelle, and S. Viboud (2010), Small-scale instabilities of an island wake flow in a rotating shallow-water layer, *Dyn. Atmos. Ocean.*, *49*(1), 1–24, doi:10.1016/j.dynatmoce.2008.10.006.

Tian, R. . et al. (2000), Effects of pelagic food-web interactions and nutrient remineralization on the biogeochemical cycling of carbon: a modeling approach, *Deep Sea Res. Part II Top. Stud. Oceanogr.*, *47*(3–4), 637–662, doi:10.1016/S0967-0645(99)00121-6.

Tomczak, M. (1988), Island wakes in deep and shallow water, *J. Geophys. Res.*, *93*(8), 5153–5154.

Williams, R. G., and M. J. Follows (1998), The Ekman transfer of nutrients and maintenance of new production over the North Atlantic, *Deep. Res. Part I Oceanogr. Res. Pap.*, *45*(2–3), 461–489, doi:10.1016/S0967-0637(97)00094-0.

Williams, R. G., and M. J. Follows (2003), Physical Transport of Nutrients and the Maintenance of Biological Production, in *Ocean Biogeochemistry*, pp. 19–51, Springer Berlin Heidelberg, Berlin, Heidelberg.

Wilson, C., and D. Adamec (2001), Correlations between surface chlorophyll and sea surface height in the tropical Pacific during the 1997–1999 El Niño-Southern Oscillation event, *J. Geophys. Res.*, *106*(C12), 31175, doi:10.1029/2000JC000724.

Wolanksi, E., T. Asaeda, A. Tanaka, and E. Deleersnijder (1996), Three-dimensional island wakes in the field, laboratory experiments and numerical models, *Cont. Shelf Res.*, *16*(11), 1437–1452, doi:10.1016/0278-4343(95)00087-9.

Wolanski, E., J. Imberger, and M. L. Heron (1984), Island wakes in shallow waters, *J. Geophys. Res.*, *89*(C6), 553–569, doi:10.1029/JC093iC02p01335.

Wyrtki, K. (1981), An Estimate of Equatorial Upwelling in the Pacific, *J. Phys. Oceanogr.*, *11*, 1205–1214.

Xu, Y., and R. B. Scott (2008), Subtleties in forcing eddy resolving ocean models with satellite wind data, *Ocean Model.*, *20*(3), 240–251, doi:10.1016/j.ocemod.2007.09.003.

Yan, X., C. Ho, Q. Zheng, and V. Klemas (1992), Temperature and Size Variabilities of the

Western Pacific Warm Pool, *Science (80-.).*, *258*(5088), 1643–1645.

Yoder, J. A., and M. A. Kennelly (2003), Seasonal and ENSO variability in global ocean phytoplankton chlorophyll derived from 4 years of SeaWiFS measurements, *Global Biogeochem. Cycles*, *17*(4), n/a-n/a, doi:10.1029/2002GB001942.

Yu, J.-Y., and W. T. Liu (2003), A linear relationship between ENSO intensity and tropical instability wave activity in the eastern Pacific Ocean, *Geophys. Res. Lett.*, *30*(14), doi:10.1029/2003GL017176.

Zweng, M. M., J. R. Reagan, J. I. Antonov, A. V. Mishonov, T. P. Boyer, H. E. Garcia, O. K. Baranova, D. R. Johnson, D. Seidov, and M. M. Bidlle (2013), *World Ocean Atlas 2013, Volume 2: Salinity*.

Liste des Figures

Liste des tableaux

Liste des abréviations

AGRIF : Adaptive Grid Refinement in Fortran

Chl : Chlorophylle a

DCM : Deep Chlorophyll Maximum

EI : Effet d'île

EKE : Eddy Kinetic Energy

ENSO : El Niño – Southern Oscillation

Fe : Fer

FSLE : Finite-Size Lyapunov Exponents

HNLC : High Nutrient Low Chlorophyll

IME : Island mass effect

IPO : Interdecadal Pacific Oscillation

KE : Kinetic Energy

MLD : Mixed Layer Depth

NO3 : Nitrates

PISCES : Pelagic Interactions Scheme for Carbon and Ecosystem Studies

PO4 : Phosphates

PP : Production primaire

RMS : Root Mean Square

ROMS : Regional Ocean Modeling System

SDP : Spatial Difference Parameter

SEC : South Equatorial Current

Si : Silicates

SSS : Sea Surface Salinity

SST : Sea Surface Temperature

TDP : Temporal Difference Parameter

TIW : Tropical Instability Wave

Glossaire

Couche de mélange : couche à la surface des océans qui est chaude et homogène en température

Downwelling : phénomène de plongée d'eau de surface vers les couches plus profondes

Nutricline : zone de fort gradient vertical en nutriment séparant les eaux pauvres de surface et riches en profondeur

Production primaire : production de matière organique végétale (biomasse), issue de la photosynthèse, par des organismes autotrophes

Stratification : se dit d'un profil vertical avec diverses masses d'eaux formant des couches empêchant le mélange vertical

Thermocline : zone de fort gradient vertical de température séparant les eaux de surface et de profondeur

Thermocline permanente : zone qui sépare grossièrement les eaux de surfaces des eaux profondes (situé généralement à quelques centaines de mètres)

Thermohaline : qui dépend conjointement de la température et de la salinité

Upwelling : phénomène de remontée d'eau des couches plus profondes vers la surface

Zone HNLC : Région où les concentrations en sels nutritifs sont élevées avec de faibles concentrations de phytoplancton dû à une limitation en un des nutriment (généralement le fer)